Universiteit Leiden
The Netherlands

Planet formation through the lens of dynamics

Huang, S.

Citation
Huang, S. (2026, June 19). *Planet formation through the lens of dynamics*. Retrieved from https://hdl.handle.net/1887/4306860

Version:	Publisher's Version
License:	Licence agreement concerning inclusion of doctoral thesis in the Institutional Repository of the University of Leiden
Downloaded from:	https://hdl.handle.net/1887/4306860

Note: To cite this publication please use the final published version (if applicable).

Planet Formation through the Lens of Dynamics

Proefschrift

ter verkrijging van
de graad van doctor aan de Universiteit Leiden,
op gezag van rector magnificus prof. dr. S. de Rijcke,
volgens besluit van het college voor promoties
te verdedigen op vrijdag 19 juni 2026
klokke 11:30 uur

door

Shuo Huang

geboren te Hefei, China
in 1998

Promotor:

Prof. dr. S. Portegies Zwart

Co-promotor:

Prof. dr. C. Ormel	Tsinghua University

Promotiecommissie:

Prof. dr. I. A. G. Snellen	
Dr. M. Kenworthy	
Prof. dr. E. Kokubo	National Astronomical Observatory of Japan
Dr. Y. Miguel	
Prof. dr. C. Dominik	University of Amsterdam
Prof. dr. A. Petit	Côte d'Azur Observatory

ISBN: 978-94-6534-449-2

Cover: Illustration of a planetary system before and after a giant impact, generated with the assistance of ChatGPT (OpenAI), based on an input image created by Shuo Huang using PowerPoint.

We all learn at different stages and speeds, and each of us has our own strengths and areas of expertise.

– Han Yu (c. 768–824), Tang dynasty

Contents

1 Introduction **1**
1.1 Planet formation . . . 2
1.1.1 Protoplanet disk . . . 3
1.1.2 Planet migration . . . 4
1.2 Mean motion resonance . . . 5
1.3 Planet architecture . . . 7
1.3.1 Exoplanet systems . . . 7
1.3.2 The Solar System . . . 9
1.4 This Thesis . . . 9
1.5 Outlook: confirm and characterize broken chains . . . 11

2 When, where, and how many exoplanets end up in orbital resonances? **15**
2.1 Introduction . . . 16
2.2 Methodology . . . 17
2.2.1 Disc model . . . 18
2.2.2 Type I migration . . . 19
2.2.3 Dynamics of resonance trapping . . . 19
2.2.4 Mass-radius relations . . . 20
2.2.5 A statistical model of resonant and non-resonant planets . . . 22
2.3 Resonance Trapping criterion for the restricted 3-body problem . . . 24
2.3.1 Theoretical Derivation . . . 24
2.3.2 Comparison with simulation . . . 25
2.4 MCMC analysis . . . 27
2.4.1 Sample selection . . . 27
2.4.2 Implication on planet-disc interaction from MCMC . . . 29
2.5 Implications for planet formation . . . 31
2.5.1 Fraction of resonant pairs . . . 32
2.5.2 Upper limit on the disc surface density at resonance trapping . . . 35
2.5.3 Migration barrier reflects the disc inner rim . . . 36
2.6 Discussion . . . 38
2.7 Conclusions . . . 40
Appendices . . . 41
2.A Results of the General disc model . . . 41
2.B MCMC performance examination . . . 42
2.B.1 Tests without assuming a disc structure . . . 43
2.B.2 Tests assuming a disc structure . . . 45

3 The dynamics of the special resonance chain systems and their formation: TRAPPIST-1 47
3.1 Introduction . . . 48
3.2 Model . . . 50
3.2.1 Preliminaries and Terminology . . . 50
3.2.2 Numerical integration . . . 52
3.2.3 Planet-disc interaction . . . 53
3.2.4 Tidal dissipation . . . 56
3.3 Preliminary simulations . . . 57
3.3.1 Planet b at the cavity edge (bC) . . . 57
3.3.2 Formation imprints for planet c and g (bCcgI) . . . 59
3.3.3 Planet d at the cavity edge (dCcgI) . . . 60
3.3.4 Parameter variation for Objective I (dCcgI) . . . 62
3.4 Trapping and escape of planets in 3BRs . . . 63
3.4.1 Crossing and trapping of the three-body resonances (dCcgIcT) . . . 65
3.4.2 Long term tidal dissipation (dCcgIcT) . . . 67
3.5 Early cavity infall (dCcgIcL) . . . 68
3.5.1 Disc repulsion on planets in the cavity . . . 69
3.5.2 Parameter study (dCcgIcL) . . . 70
3.6 Analysis . . . 72
3.6.1 Trapping under convergent migration in MMRs . . . 72
3.6.2 Eccentricity-period relation in 3BRs . . . 73
3.7 Discussion . . . 74
3.7.1 Model Assessment . . . 74
3.7.2 Resonances Establishing and Breaking . . . 75
3.7.3 Application to other systems . . . 76
3.8 Conclusions . . . 76
Appendices . . . 78
3.A Lindblad torque . . . 78

4 The dynamics of the broken resonance chain systems and their formation: the Solar System 79
4.1 Introduction and motivation . . . 80
4.2 Model . . . 82
4.2.1 Initial conditions . . . 82
4.2.2 Giant planet instability . . . 83
4.2.3 Theia and proto-Earth mass-radius calculation . . . 83
4.3 Comparison with Solar system . . . 85
4.4 Implications . . . 88
4.5 Conclusions . . . 89
Appendices . . . 90
4.A Formation of a resonant chain in the pebble accretion and planetesimal accretion models . . . 90
4.B Parameter sensitivity . . . 94
4.C Venus-Mars period ratio in the late collisional growth scenario . . . 96

5 Birth stellar cluster dynamics matters: planet population synthesis with external photo-evaporation 99
5.1 Introduction . . . 100
5.2 Methods . . . 101
5.2.1 Cluster evolution . . . 101
5.2.2 Disk model . . . 103
5.2.3 Planet growth . . . 104
5.2.4 Planet migration . . . 107
5.3 Initial conditions and parameter choices . . . 107
5.4 Results . . . 109
5.4.1 Planet formation for two example stars . . . 109
5.4.2 Planet population: Isolated versus clustered . . . 111
5.4.3 Co-evolution between CJ formation and the cluster . . . 113
5.5 Analytical criteria for CJ formation in the cluster . . . 114
5.6 Discussion . . . 115
5.6.1 Model assessment . . . 115
5.6.2 Cold Jupiter and Neptune in observation . . . 117
5.7 Conclusions . . . 118
Appendices . . . 118
5.A Planet population in isolated stars and a star cluster . . . 118

6 ALMA signature of closely-spaced pebble-accreting protoplanets in Transition disks 121
6.1 Introduction . . . 122
6.2 Methods . . . 123
6.2.1 Dust transport including pebble accretion . . . 123
6.2.2 Initial conditions . . . 124
6.3 Pebble flux reduction . . . 124
6.3.1 Pebble accretion efficiency . . . 124
6.3.2 Dust cavity and ring structure . . . 126
6.4 Two groups of planet-hosting transition disks . . . 129
6.4.1 Below pebble isolation mass: GM Aur . . . 130
6.4.2 Above pebble isolation mass: PDS 70 . . . 131
6.4.3 A sample of transition disks . . . 132
6.5 Discussion . . . 135
6.5.1 Model assessment . . . 135
6.5.2 Feasibility of the "sweet spot" on the accretion map . . . 136
6.5.3 Emerging the planet formation story in transition disks . . . 137
6.5.4 Consequence for planet detection . . . 138
6.6 Conclusions . . . 138
Appendices . . . 139
6.A Numerical treatment of pebble flux reduction . . . 139
6.B Evaluating dust diffusion during pebble accretion . . . 139
6.C Simulated continuum of GM Aur with three planets . . . 140
6.D Profile of the gap opened by planet . . . 141
6.E Quantify the morphology of dust rings . . . 142

Bibliography 142

Summary **163**

Nederlandse samenvatting **167**

List of Publications **171**

Curriculum Vitæ **173**

Acknowledgments **175**

1

Introduction

Since the first detection of exoplanet 51 Pegasi b, the discoveries have been boosted significantly. Till now, about 6,000 exoplanets have been found (Fig. 1.1), but Earth remains the only known planet that hosts life. This contrast forces upon us fundamental questions: Are we really alone in the Universe? What is the origin of life?

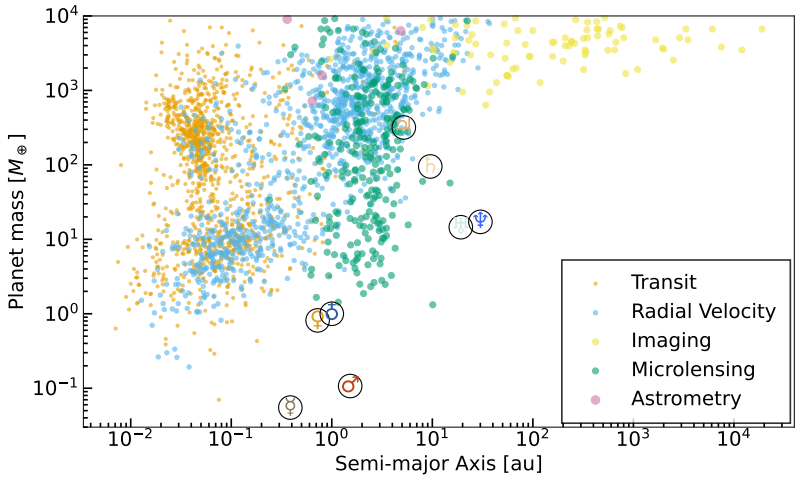


Figure 1.1. Planet mass versus semi-major axis for all confirmed exoplanets (NASA Exoplanet Archive, retrieved January 2026). Exoplanets are color- and size-coded by discovery method. The Solar System planets are indicated with their astronomical symbols.

However, our view of the exoplanet population is intrinsically incomplete and distorted. The observations are biased in different ways, depending on which exoplanet detection method is used. **Transit Photometry** detects the eclipsing behavior of a planet passing in front of its host star. It is heavily biased toward planets on short-period orbits, as they transit more frequently and have a higher geometric probability of alignment with our line of sight. **Radial Velocity** measures the star's Doppler shift in its light caused by the gravitational pull of an orbiting planet. It is most sensitive to massive planets in moderately close orbits, as these induce a larger and more rapid stellar motion. **Direct Imaging** directly captures light from the planet itself. It is biased toward massive, young planets on very wide orbits.

Young planets are sufficiently hot (after accretion) and bright, and the wide separations help to avoid stellar glare. **Astrometry** tracks the star's spatial shift on the sky due to the orbital motion of massive companions. It is most effective for massive planets at intermediate orbital distances, where the stellar wobble is both significant and occurs over an observable timescale. **Microlensing** can detect foreground planets due to their gravitational lensing effect, which magnifies the light of a background star when temporarily passing through it. It probes planets, including cold super-Earths, at orbital distances typically near or beyond 1 AU. But the detailed orbital characterization remains challenging in this way.

Therefore, current observations alone cannot determine whether Earth is intrinsically rare or common. While the construction of larger, more sensitive telescopes represents the definitive long-term path forward, the essential near-term work lies in understanding planet formation processes as much as possible based on the present observational abilities.

1.1 Planet formation

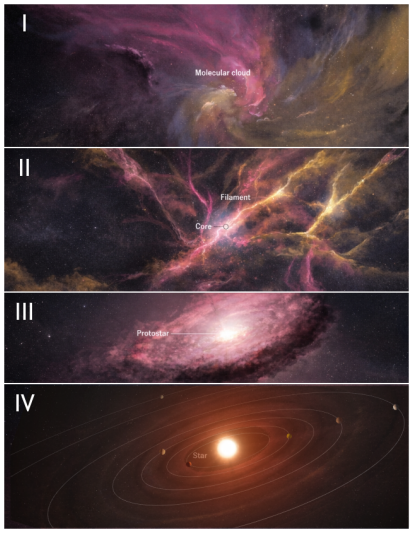


Figure 1.2. Simple illustration of star formation stages. Stage I, molecular cloud. Stage II, stars form during core collapse. Stage III, circumstellar disk around a protostar. Stage IV, mature planet system. Credit: Matthew Twombly (Panel I, II, III) and NASA/Daniel Rutter (Panel IV)

The formation of a planet system begins with the gravitational collapse of a cold, dense region within a giant molecular cloud. As shown in Fig. 1.2, this collapse fragments the cloud, with the most massive central core accreting the bulk of the material to form a protostar. Some smaller fragments may directly collapse into isolated planetary-mass objects, denoting an early, direct formation pathway. Once the central protostar has obtained sufficient mass, its thermodynamic feedback halts further large-scale infall (Jeans 1902). Then, conservation of angular momentum forces the remaining material into a flattened, rotating protoplanetary disk. This disk is the perfect birthplace for planets. The Solar System also had such a disk 4.5 Gyr ago, often called the Solar Nebula.

1.1.1 Protoplanet disk

Protoplanetary disks are mostly composed of gas, initially 10% of the host mass, with about 1% solids. As the disk cools down, the local gravity becomes important and planets can form. This process is called Gravitational Instability. Similar to star formation, but the fragment of the protoplanet disk needs to balance Keplerian shearing additionally (Toomre 1964). GI might be happening violently in some disks like AB Aurigae (Speedie et al. 2024; Calcino et al. 2025).

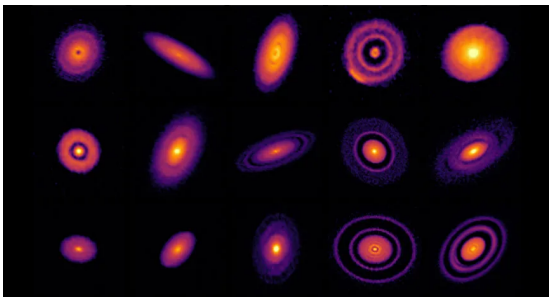


Figure 1.3. Continuum gallery of Dsharp disks imaged by ALMA (Andrews et al. 2018).

Planets also form through the alternative, bottom-up pathway of core accretion. Within the disk, microscopic dust grains collide and coalesce, gradually building larger bodies from planetesimals to planetary embryos. Embryos as small as the Moon can efficiently accrete pebbles (Ormel & Klahr 2010; Lambrechts & Johansen 2012), while closer to the star (within ~1 au), shorter collisional timescales allow for the accretion of numerous kilometre-sized planetesimals (Kokubo & Ida 1998). Upon reaching a critical mass of ~10 Earth masses, an embryo begins to accrete a gaseous envelope. When this envelope mass rivals the solid core mass, runaway gas accretion is triggered (Pollack et al. 1996), rapidly forming a gas giant. Concurrently, stellar radiation (Owen et al. 2012), disk viscosity (Shakura & Sunyaev 1976), and winds (Bai & Stone 2013) dissipate the remaining gas over several million years, leaving behind a mature planetary system whose architecture is dictated by the disk's initial temperature, density, and chemical gradients.

The advent of advanced facilities like ALMA, the VLT, and JWST now allows us to directly image protoplanetary disks in our galactic neighbourhood. Millimeter-wavelength observations, such as those from the DSHARP survey shown in Fig. 1.3, reveal that disks are not smooth; they are richly structured with rings and gaps. The most compelling interpretation for these substructures is the presence of embedded, accreting protoplanets. However, alternative explanations like pressure bumps exist, highlighting the need for multi-wavelength observations to confirm the planet candidates.

To date, dozens of candidate protoplanets have been identified, with confirmed detections in two young, solar-type systems, as shown in Fig. 1.4. The protoplanets PDS 70 b and c and WISEA 2 b are located at substantial distances of approximately 20, 30, and 50 AU from their host stars, respectively. In both systems, the planets are confirmed because they are actively accreting surrounding disk material, a process so vigorous that it generates detectable Hα emission induced by accretion shocks. In both systems, the protoplanets are gas giants. Their strong gravity clears the disk at their orbits and opens deep gaps.

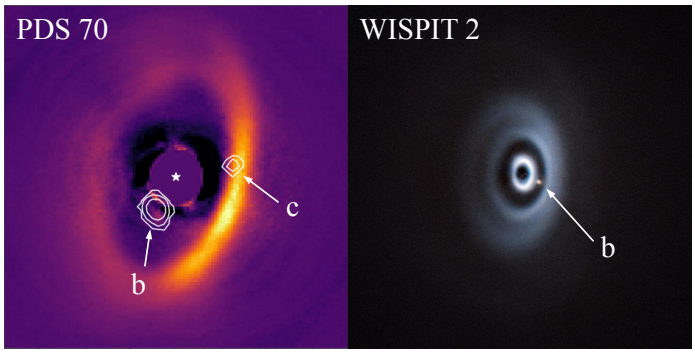


Figure 1.4. Protoplanets in PDS 70 (Haffert et al. 2019) and WISPIT 2 (van Capelleveen et al. 2025). The disk data are collected via VLT/SPHERE.

1.1.2 Planet migration

Planets do not remain at their birth locations. While embedded in a gaseous protoplanetary disk, gravitational interactions between a planet and the surrounding gas exchange angular momentum, causing the planetary orbit to evolve — a process known as planet migration. This mechanism fundamentally shapes the final architecture of planetary systems and provides a natural explanation for close-in exoplanets observed today.

Depending on the planet's mass and local disk conditions, migration proceeds in distinct dynamical regimes. Low-mass planets that do not strongly perturb the gas structure undergo Type I migration, a linear regime in which the migration rate scales with both the disk surface density and the planet's mass. As planets grow and become gas giants, they carve deep, cleared gaps in the disk, transitioning into Type II migration. In this regime, migration is significantly slower because the flow of disk material across the gap is suppressed by the strong planet gravity (Kanagawa et al. 2017). In the following sections, I outline the primary physical torques responsible for this angular momentum exchange.

Lindblad Torque

The dominant contribution to planet migration arises from spiral density waves launched by the planet at Lindblad resonances in the disk. These resonances occur where the gas orbital frequency satisfies a simple commensurability with the planet's orbital frequency (e.g. Lin & Papaloizou 1979). At these locations, the planet excites trailing spiral waves that propagate radially, exchanging angular momentum.

The torque exerted by the disk can be decomposed into contributions from the inner and outer disk. The inner disk typically exerts a positive torque on the planet, while the outer disk exerts a negative torque. In most disk models, the outer torque dominates, resulting in a net negative torque known as the differential Lindblad torque. The magnitude and direction of the Lindblad torque depend primarily on the disk surface density and temperature gradients, as well as the planet's mass and the disk scale height. In locally isothermal disks, the Lindblad torque is almost always negative, leading to inward migration.

Corotation Torque

In addition to Lindblad torques, planets exchange angular momentum with gas in their co-orbital region, near the planet's orbital radius. Gas in this region executes horseshoe-shaped trajectories corotating with the planet. The leading horseshoe gives angular momentum to the planets, while the trailing horseshoe takes away angular momentum. The resulting net

corotation torque can either slow down, halt, or even reverse migration depending on the gradients of vortensity (vorticity divided by surface density) and entropy across the horseshoe region (Paardekooper & Papaloizou 2009; Paardekooper et al. 2010).

However, the corotation torque is prone to saturation. In low-viscosity or weakly diffusive disks, the horseshoe region becomes phase-mixed, erasing the gradients that sustain the torque. Viscosity and thermal diffusion are therefore essential to maintain an unsaturated corotation torque.

New Torques and the disk inner edge

Beyond the classical Lindblad and corotation torques, recent theoretical and numerical work has identified additional torque components that can significantly alter migration behaviour.

One is the heating torque. Actively accreting planets release gravitational energy as localized heating, which modifies the gas density asymmetrically around the planet and produces an additional positive torque. This can slow or even reverse inward migration for low-mass, rapidly accreting planets (Benítez-Llambay et al. 2015; Masset 2017), and is especially relevant during early growth phases.

A recent study by Chrenko et al. (2024) has also shown that the process of pebble accretion can produce a significant outward torque on a planet, known as the pebble torque. As a planet accretes drifting pebbles, it creates an imbalance in the pebble distribution around its orbit. This asymmetry gives the planet angular momentum and can often reverse the typical inward migration driven by the gas disk, depending on the disk mass, pebble sizes, and planet mass.

The inner edge of the protoplanetary disk, where gas density drops abruptly, can act as a migration trap for low-mass planets. This halt occurs because the sharp density gradient at the edge generates an almost one-sided, strong, positive corotation torque, which can balance the outer one-sided negative Lindblad torque (Liu et al. 2017). In contrast, gap-opening gas giants are largely decoupled from the local disk structure. Their deep gaps reduce gas–planet interaction, allowing them to cross the inner edge and migrate into the cavity region (Ataiee & Kley 2021).

1.2 Mean motion resonance

The study of mean motion resonance (MMR) originated with the work of Pierre-Simon Laplace, who first explained the resonant orbital architecture of Jupiter's Galilean moons. Celestial mechanics has since formalized the dynamics of orbital resonance Murray & Dermott (1999). In recent decades, the discovery of numerous resonant exoplanet systems and the detection of resonant substructures in protoplanetary disks have placed MMRs within the modern context of planet formation.

Planet migration naturally leads to mean motion resonances. When planets undergo convergent migration, where the outer planet migrates inward faster than the inner planet, they are driven toward orbital commensurabilities (or integer period ratios). If the mutual migration is sufficiently slow and eccentricity damping is moderate, the planets can be gravitationally captured into a resonance. The specific resonance attained depends on the migration rate, eccentricity damping timescales, and planet masses.

The left panel of Fig. 1.5 uses three N-body simulations to show how different migration speeds lead to capture into different resonances. Faster migration typically produces more compact orbital resonances. If a pair of planets is in a p:q mean motion resonance, their

orbital period ratio must satisfy

$$\frac{P_2}{P_1} \approx \frac{p}{q}, \tag{1.1}$$

where p and q are small integers, and subscripts 1 and 2 denote the inner and outer planets, respectively. Equivalently, the mean motions $n_i = 2\pi/P_i$ satisfy

$$pn_2 - qn_1 \approx 0. \tag{1.2}$$

In such configurations, gravitational perturbations accumulate coherently over many orbital periods.

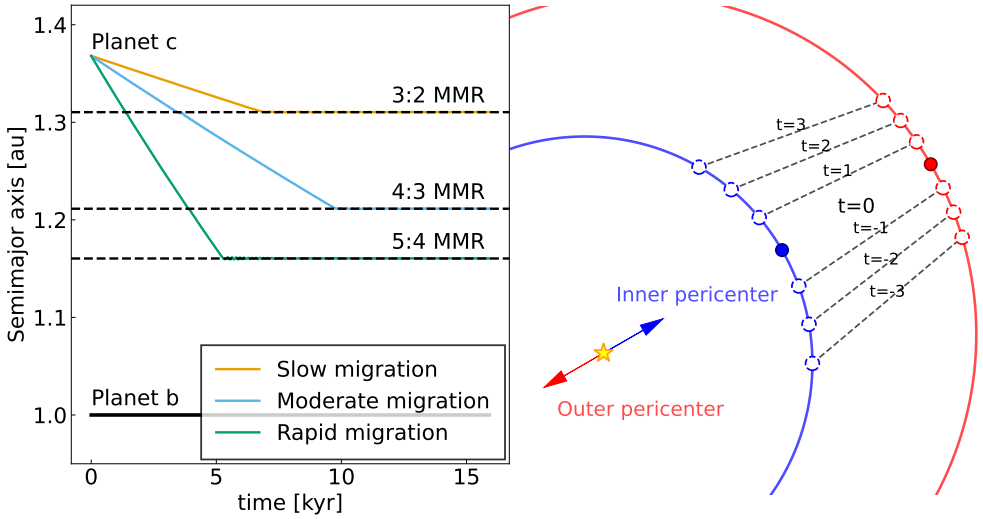


Figure 1.5. Left panel: Three restricted N-body simulations of resonant trapping for a low-mass planet cc migrating inward toward a massive perturber b. Colored tracks show the orbital evolution of planet c under different migration timescales. Dashed vertical lines mark the nominal locations of mean-motion resonances with planet b. In this setup, planet b is treated as a fixed, massive central body whose orbit is not perturbed by planet c. Right panel: Schematic geometry of two planets locked in a mean-motion resonance. Planet conjunctions occur at a fixed phase, typically either aligned near the pericenter of the inner planet's orbit or the apocenter of the outer planet's orbit. This phase-locking enables stable, long-term angular momentum exchange that maintains the resonant configuration.

The defining feature of a mean motion resonance is the libration of one or more resonant angles. For a first-order resonance (p:$p-1$), a commonly used resonant angle is

$$\phi = p\lambda_2 - (p-1)\lambda_1 - \varpi_{1/2} = p(\lambda_2 - \varpi_{1/2}) - (p-1)(\lambda_1 - \varpi_{1/2}), \tag{1.3}$$

where $\lambda = M + \varpi$ is the mean longitude, M is the mean anomaly, and ϖ is the longitude of pericenter. Additional resonant angles involving ϖ_2 may also librate, depending on the system parameters.

The geometric interpretation of liberating resonance angles is that the conjunction longitude is fixed with respect to the planetary pericenters. As shown in Fig. 1.5 right panel, close encounters between the planets occur repeatedly at nearly the same orbital phase, typically near the pericenter (of the inner orbit) or the apocenter (of the outer orbit). If the encounter point is slightly off the pericenter or apocenter, the asymmetric torque between

the planets will shift the next conjunction backwards. This phase-locking allows angular momentum exchange to occur coherently, maintaining the commensurability between the orbital periods while preventing too close encounters.

Planets locked in such a resonant configuration are significantly more stable than non-resonant planets (circulating resonance angles) with integer period ratios (Hu et al. 2025b). Resonance capture thus represents a fundamental mechanism for sculpting stable, long-lived planetary architectures.

Three-Body Resonance

In systems containing three or more planets, resonant interactions can involve all planets simultaneously. A three-body mean motion resonance occurs when the orbital periods of three planets satisfy a single commensurability relation. A classic example is again the Laplace resonance among Jupiter's moons Io, Europa, and Ganymede, which satisfies

$$n_1 - 3n_2 + 2n_3 \approx 0, \tag{1.4}$$

where $n_i = 2\pi/P_i$ is the mean motion of the $i-th$ planet.

Three-body resonances are characterized by the libration of a three-body resonant angle. Taking an example of zero-order three-body resonance, the form of the angle is

$$\phi_{3b} = -p\lambda_1 + q\lambda_2 - r\lambda_3 = q(\lambda_2 - \lambda_1) - r(\lambda_3 - \lambda_1), \tag{1.5}$$

where p, q, and r are integers satisfying $p - q + r = 0$. This angle can be derived from two body resonance angles by simply eliminating the pericenter term. If each adjacent pair of planets in a triplet is in resonance (with liberating two-body resonance angles), the three planets are by definition in three-body resonance. Unlike two-body resonances, these angles do not explicitly involve the longitudes of pericenter and can remain dynamically important even for nearly circular orbits. The characterization of three-body resonances is therefore also much easier than that of two-body resonances.

However, three-body resonance is not simply the addition of two two-body MMRs. But the physical picture of three-body resonance can be understood as two-body resonance in a corotating frame of the innermost planet (Petit et al. 2020). Three-body resonances can also arise naturally during convergent migration, particularly in compact multi-planet systems where planets are sequentially captured into two-body resonances, forming resonant chains. But in some cases, individual two-body resonances may be disrupted while the three-body resonance persists, continuing to provide long-term dynamical protection and stability following a track in period ratio space (Papaloizou et al. 2018; Charalambous et al. 2018):

$$p\frac{P_2}{P_1} + r\frac{P_2}{P_3} = q, \tag{1.6}$$

and it is the time derivative of the mean-motion condition Eq. (1.4).

1.3 Planet architecture

1.3.1 Exoplanet systems

The dynamical complexity of a planetary system generally increases with the number of planets it contains. Multi-planet systems offer a rich laboratory to study planet formation and orbital evolution. Because as one more planet is introduced,

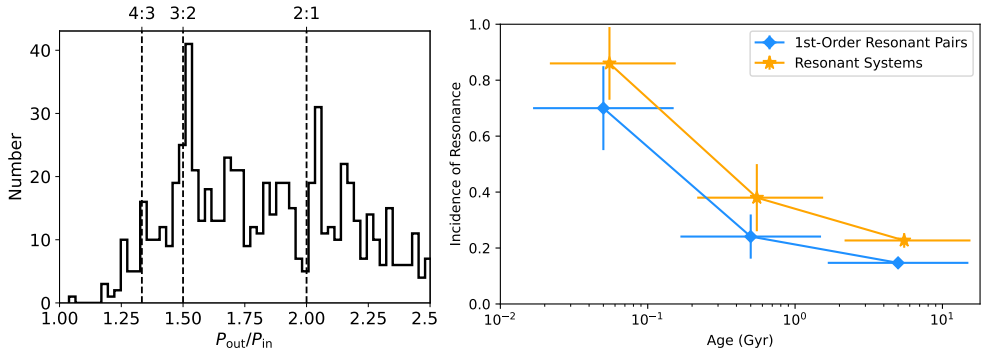


Figure 1.6. Left panel: Period ratio distribution of transiting exoplanets. Vertical dashed lines denote the resonant period ratios. Right panel: The fraction of planetary systems with at least one resonant pair (1st-order resonance in blue and 2nd-order resonance in orange) across three age bins. Figure adopted from Dai et al. (2024).

The architecture of exoplanet systems is very diverse. There are some planet systems in resonance: TRAPPIST-1, TOI-178, HR8799, PDS 70, etc. Most other planet systems do not exhibit resonance chains.

Fig. 1.6 (left panel) shows the period ratio distribution of transiting exoplanets. While most planet pairs lie just outside exact resonances, the presence of peaks near commensurate period ratios indicates that a certain fraction ($\approx$ 10%) of planets are captured into or have passed through mean motion resonances. These statistics have sparked considerable debate about the dominant pathways of planet formation:

1. The first school of thought argues that planets underwent substantial gas-driven migration and were initially trapped in resonance, but that roughly 80% of these chains later destabilized, potentially during the dispersal of the gaseous disk (Izidoro et al. 2017, 2021). Recent works further suggest that secular perturbations from an outer Earth-sized embryo (Ogihara & Kunitomo 2026), high-order resonance in the chain (Li et al. 2024), and planetesimal flybys (Li et al. 2025) can break an inner resonant chain.

2. A second view holds that many planets formed in gas-poor disks, where migration was inefficient (Ogihara et al. 2018; Choksi & Chiang 2020). In this scenario, large-scale resonant capture and the subsequent violent breaking of chains are largely absent.

3. A third perspective proposes that planets largely formed in situ after gas-disk dissipation. Clement et al. (2025) showed that terrestrial planet systems assembled in debris disks can reproduce the observed exoplanet statistics around M-dwarfs, an approach also applied to the Solar System's terrestrial planets (e.g., Clement et al. 2023). Alternatively, Wu et al. (2024a) argue that the observed period-ratio and eccentricity distributions can be reproduced by starting from a uniform distribution of embryos and then allowing resonant kicks—gravitational scattering during brief resonant encounters—to dynamically rearrange the orbits into the observed configuration.

Recent observations provide mounting support for the broken-chain scenario. The right panel of Fig. 1.6 reveals that young planetary systems (age $\lesssim$ 100 Myr) exhibit a high fraction (80–90%) of planet pairs near commensurate period ratios, whereas older systems show a much lower resonant fraction (roughly 10%). Moreover, Leleu et al. (2024) found that planets

far from resonance tend to be more massive than those that remain in resonance. These trends are consistent with a picture in which planets initially migrate into resonant chains, but subsequently break resonance through violent dynamical scattering and merger events.

1.3.2 The Solar System

Compared to many observed exoplanetary systems, the planets of the Solar System present a somewhat similar configuration in terms of resonance: None of the eight planets is currently locked in mean motion resonances, similar to many compact, evolved exoplanetary systems. The study on the formation of the Solar System started earlier due to more observations than the exoplanet systems.

In the Nice model, the giant planets (Jupiter, Saturn, Uranus, Neptune, often with an additional ice giant) are initially assumed to form in a multi-resonant configuration (Tsiganis et al. 2005). Subsequent interactions with a residual planetesimal disk Griveaud et al. (2024), photoevaporative disk front (Liu et al. 2022), or star flybys (Kaib & Raymond 2025) destabilize the primordial resonances, leading to a period of orbital rearrangement and planet scattering that shapes the current architecture. This scenario provides a natural explanation for the current spacing and eccentricities of the outer planets, Kuiper belt distribution, and some other features in the outer Solar System.

The formation of the Solar System's inner terrestrial planets started with a well-known puzzle: the small Mars problem. Classical in-situ accretion models consistently produce a Mars that is too massive and fail to replicate the stark mass contrast between Earth and Mars. Then a breakthrough came with the idea that the terrestrial planets accreted from a narrow annulus of planetesimals situated roughly between 0.7 and 1.0 au, rather than from a broad disk extending to the present orbit of Mars. This confined initial distribution, when combined with perturbations from the outer giant planets, naturally truncates the outer disk. It leaves insufficient material to form a large Mars and successfully reproduces the observed planetary masses and orbital spacing (Walsh et al. 2011).

More recent work has further refined this picture by introducing a two-ring model of terrestrial planet formation. This approach is motivated by the desire to place planet formation within a more physically realistic, earlier phase of the solar nebula. In the two-ring model, planetesimals form concurrently in distinct inner and outer rings, separated by a gap likely created by silicate sublimation or other processes in the young, gas-rich disk. This structure provides a more natural initial condition consistent with astrophysical disk models and allows terrestrial accretion to begin earlier, during the nebular phase. Many of the protoplanets are also formed in resonance chains. As demonstrated by Nesvorný et al. (2025), this framework can additionally match the terrestrial planet oxidation states compared to single-ring models. But the ground truth of the terrestrial planet formation origin is still under active debate (Morbidelli et al. 2024; Johansen et al. 2024).

1.4 This Thesis

To understand the complex nature of planet formation, one obvious thing to do is to study planet architectures, which preserve imprints of planet evolution histories. The work presented in this dissertation focuses on unraveling the dynamical history of planet systems in resonance and potential broken resonance chains, with N-body simulations, statistics, and planet formation modeling. This Thesis covers the three exoplanet system categories in Fig. 1.7: perfect resonance chains, special resonance chains and broken resonance chains.

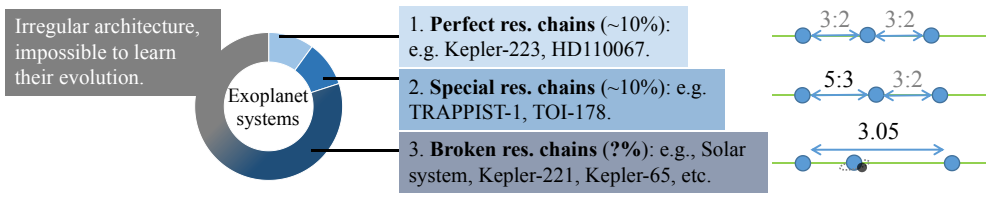


Figure 1.7. Classifying planet system architectures by how pristine their resonance chains are.

When, where, and how many exoplanets end up in orbital resonances?

Protoplanetary disks are the birthplaces of planets. As protoplanets exchange angular momentum with the surrounding disk, they migrate. Migration can capture two planets in a stable mean motion resonance, as observed in systems such as PDS70 (2:1 resonance Bae et al. 2019) and TRAPPIST-1 (resonance chain Luger et al. 2017). However, too rapidly migrating planets result in resonance crossing instead of trapping. Here, I have derived the critical migration rate delineating the transition between resonance trapping and crossing, providing a tool for the community to diagnose the birth disk mass of perfect resonance chain planets. Because fast migration typically entails the existence of a massive disk, I also calculated that near-resonant exoplanets were formed in disks with masses comparable to the Minimum Mass Solar Nebula. Around the same time that I archived my paper, Batygin & Petit (2023a) independently derived an equivalent resonance-trapping criterion using a different approach.

The dynamics of special chain systems and their formation: TRAPPIST-1

Higher-order resonance chains allow us to constrain planet formation timescales. For example, in the TRAPPIST-1 system, the high-order 8:5 and 5:3 resonances of its inner three planets are near-impossible to replicate if the planets stayed within the disk (Teyssandier et al. 2022; Burn et al. 2021). These resonances can only be obtained when the inner planets migrated into a gas-free magnetospheric cavity, where disk torques expand their original 3:2 resonances to the observed higher-order resonances. In addition, the outer planets d, e, and f can neither form too fast nor too slow, otherwise the planets would result in a configuration incompatible with observation. In this way, I offered an approach to constrain the formation timescales of exoplanets from their present-day architectures. Recent magnetohydrodynamic simulations (Romanova et al. 2025) confirmed our proposed cavity migration mechanism. Our proposed pathway for TRAPPIST-1 is also applicable to other resonance chain systems, e.g., TOI-178, and HD158259.

The dynamics of broken chain systems and their formation: the Solar System

While many systems exhibit resonances, others, including our Solar System, do not. Various mechanisms, such as disk dispersal (Izidoro et al. 2021), stellar flybys (Maas et al. 2025), and planetesimal collisions (Li et al. 2024; Yi et al. 2025a), can disrupt primordial resonances. In the Solar System, the giant planet instability (Morbidelli et al. 2005) perturbs inner terrestrial planets through secular interactions (Kaib & Chambers 2016). Here, the present-day dynamical structure of the Solar terrestrial planets naturally emerges when these planets started in a resonance chain that was destabilized during the giant planet instability, resulting in the Moon-forming impact. Our findings support the view that the Solar terrestrial planets formed early, in a gas-rich disk, analogous to exoplanet systems. It also offers a new testable way for multi-planet systems to break primordial resonances, as most planet systems exhibit.

Suppression of giant planet formation in star cluster environments
Observation already revealed that the birth environment of stars significantly impacts the planet-forming disks. The examples are the observed Proplyds in the Orion Nebula (Berné et al. 2024) as well as numerical simulations (Wilhelm et al. 2023). This study introduces a simplified planet population synthesis code that simulates planet formation in the proplyds in an Orion-like cluster, incorporating factors such as pebble accretion and the effects of nearby stellar radiation on protoplanetary disks. The simulations show that clustered environments hinder the formation of giant planets, especially around low-mass stars. Neptune-sized planets on wide orbits are formed instead. The reason is that the short disk life time halt both planet gas accretion and migration. The large population of Neptune-sized planets at Jupiter-like orbits is consistent with recent Microlensing discoveries (Zang et al. 2025).

Signature of closely-spaced pebble-accreting protoplanets in ALMA disks
While exoplanets on wide orbits are relatively common, not so many protoplanets have been found. It has been shown that the occurrence rate of substructures in disks is comparable to the occurrence rate of exoplanets (van der Marel & Mulders 2021). This study propose many of the protoplanets are too small to be detected. The transition disks are categorized into two distinct groups based on their properties and the types of planets they may host. In Group A, massive gas giants create deep gaps in the gas disk, while in Group B, multiple smaller Neptunian-like planets contribute to the formation of inner dust cavities without creating substantial gas gaps. The characteristics of the dust rings formed in these disks—such as sharp inner edges—can provide critical insights into the underlying planet formation processes. The observational implications of these findings suggest that high-resolution imaging techniques, particularly with the Atacama Large Millimeter/submillimeter Array (ALMA), could further validate these models and enhance our understanding of planet formation in various disk environments.

1.5 Outlook: confirm and characterize broken chains

This thesis has shown that compact systems without strong external perturbations can preserve their primordial resonant chains over ~Gyr timescales (e.g., Tamayo et al. 2017). In contrast, the breakage of such a chain is driven by post-formation perturbations, resulting in a Solar terrestrial planet-like configuration (see Fig. 1.8). Both intact and broken resonant chains encode valuable information about a system's migration and evolution history. However, while intact chains are relatively straightforward to identify through period commensurabilities, broken chains are far more observationally elusive. Their identification represents a significant challenge, but also a compelling opportunity, in exoplanet science. The detection and characterization of such systems would address many fundamental questions in planet formation theories. To advance this search, future work should pursue two complementary lines of evidence: Orbital architecture and planetary composition.

Broken resonance chains in exoplanet systems
Disrupted resonance chains are much harder to identify than intact ones, but near-integer period ratios can act as dynamical relics of primordial resonances (Cambioni et al. 2025). Analogous to the 3.05 period ratio between Venus and Mars, several *Kepler* systems show similar signatures. For example, in Kepler-48 the inner pair lies near a 2:1 commensurability, while an outer giant planet may have disrupted the original chain. In Kepler-65, the b–d pair lies close to a 15:4 ratio, consistent with the remnant of an original 2:1–3:2–4:3 chain in

which planet c plausibly formed via a merger. The Kepler-221 system exhibits a comparable architecture (Yi et al. 2025a).

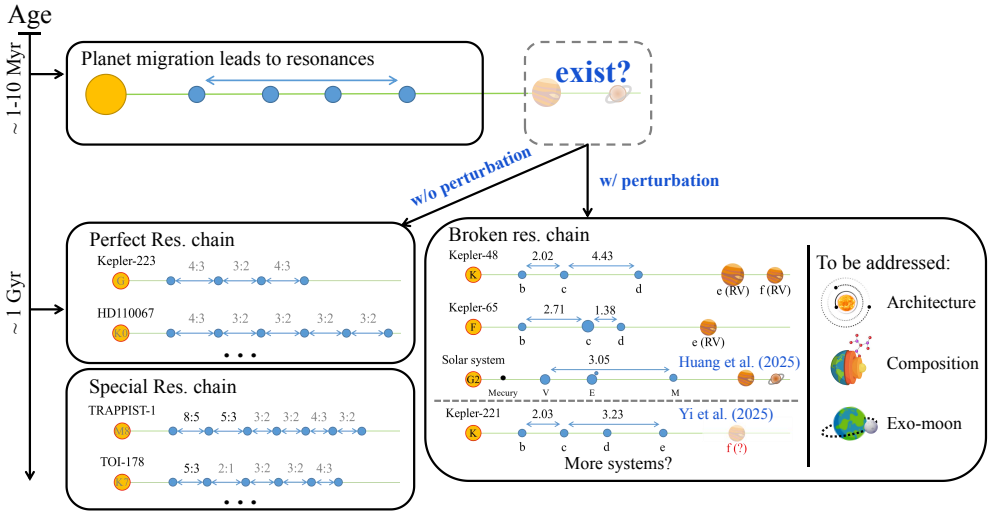


Figure 1.8. Sketch of the dichotomy evolution of a primordial resonance chain. If there are no external perturbations, the resonance chains are preserved (left). The resonances of each adjacent planet pair are labeled. If there are perturbations, the resonance chains are destabilized (right). The relevant period ratios are labeled.

A natural extension of my PhD work is to conduct a systematic survey of the ~330 known multi-planet systems, using analytical criteria and N-body simulations to determine whether their present architectures can arise from initially resonant chains that were later destabilized. This will generalize the framework developed in Yi et al. (2025a) and Huang et al. (2025) to a population-level test. For systems that show evidence of disruption but lack detected outer giants, dynamical modeling can be used to infer whether unseen companions are required, a prediction that can be tested with forthcoming Gaia DR4 astrometry.

Compositional signatures of chain disruption

Chain destabilization is expected to trigger close encounters and giant impacts, leaving observable imprints on planetary radii, densities, and atmospheres. In Kepler-65, for instance, planet c ($2.5\,R_\oplus$) is substantially larger than its neighbors b and d ($\sim 1.5\,R_\oplus$), consistent with a merger origin and possible post-impact atmosphere loss (Biersteker & Schlichting 2021). More generally, planets that experienced giant impacts should be denser and more depleted in primordial volatiles or even host moons, like the Earth-Moon system.

By combining N-body simulations with models of impact outcomes based on smoothed-particle hydrodynamics (Emsenhuber et al. 2024; Dou et al. 2024), I will identify the most likely post-impact planets in broken-chain systems. These predictions can be tested through precise mass measurements from radial-velocity surveys and atmospheric characterization with JWST, allowing the broken-chain scenario to be probed from both dynamical and compositional perspectives.

Looking further ahead, a powerful suite of next-generation facilities will enable the systematic characterization of smaller exoplanets. This includes ground-based giants like the Extremely Large Telescope (ELT), Giant Magellan Telescope (GMT), and Thirty Meter Telescope (TMT), alongside space-based observatories such as the Habitable Worlds Observatory,

PLATO, ARIEL, and the Roman Space Telescope. Together, they will probe atmospheric biosignatures and habitability, bringing us closer to answering the ultimate questions of how common Solar System–like architectures are and how we came to be here.

2

When, where, and how many exoplanets end up in orbital resonances?

The theory of Type I migration has been widely used in many studies. Transiting multi-planet systems offer us the opportunity to examine the consistency between observation and theory, especially for those systems harbouring planets in Mean Motion Resonance (MMR). The displacement these resonant pairs show from exact commensurability provides us with information on their migration and eccentricity-damping histories. Here, we adopt a probabilistic approach, characterized by two distributions – appropriate for either the resonant or non-resonant planets – to fit the observed planet period ratio distribution. With the Markov chain Monte Carlo (MCMC) method, we find that ≈15% of exoplanets are in first order (j+1:j) MMRs, the ratio of eccentricity-to-semi-major axis damping is too high to allow overstable librations and that the results are by-and-large consistent with Type-I migration theory. In addition, our modeling finds that a small fraction of resonant pairs is captured into resonance during migration, implying late planet formation (gas-poor). Most of the resonant pairs park themselves at the migration barrier, indicating early planet formation (gas-rich). Furthermore, after improving the criterion on two-body resonant trapping, we obtain an upper limit of the disc surface density at the time the planets are locked in resonance.

S. Huang★, C. W. Ormel (2023) When, where, and how many planets end up in first-order resonances? MNRAS, 522, 828

2.1 Introduction

Since the first discovery of exoplanets around solar-type stars (Mayor & Queloz 1995), the number of exoplanets has ballooned in the last three decades, exceeding 5 200 as of the present day. It is therefore appropriate to conduct population-level analyses to examine planet formation theories (Mordasini et al. 2015; Zhu & Dong 2021). When independent mass and radius measurements are available, planet bulk density and their composition can be inferred (Fortney et al. 2007; Seager et al. 2007; Piaulet et al. 2022), with which their mass accretion history and post-formation evolution can be constrained. The core accretion model successfully predicted the so-called "planet dessert" (Ida & Lin 2004), which refers to the paucity of planets with tens of Earth-mass within 3 au. The "radius valley" (Fulton et al. 2017) is manifested at a planet radius $\sim 2R_\oplus$, which has been attributed to photoevaporation-driven mass loss (Owen & Wu 2013, 2017), planet formation location with respect to snow line (Luque & Pallé 2022; Izidoro et al. 2022), or core-powered mass loss (Ginzburg et al. 2018).

The physical principles underlying migration of low-mass planets in gaseous discs (Type I migration) have long been established (Goldreich & Tremaine 1979; Lin & Papaloizou 1979). The total torque exerted on planets by the surrounding disc is typically negative, resulting in inward planet migration on time-scales shorter than the disc lifetimes (e.g., Ward 1997; Tanaka et al. 2002; Ribas et al. 2014; Winter et al. 2019). However, the direction of migration can be reversed at special locations where conditions materialize that render a net positive torque, resulting in migration traps. These locations include the region where the horseshoe saturates, i.e when the (positive) co-rotation torque compensates the (negative) Lindblad torque (Goldreich & Tremaine 1980; Ward 1991; Paardekooper et al. 2010, 2011), the disc inner edge (Liu et al. 2017; Romanova et al. 2019; Ataiee & Kley 2021) where the torque becomes one-sided, and the regions where the disc switches from optically thin to optically thick (0.1 – 1 au) (Masset et al. 2006). In addition, in the pebble accretion paradigm, the infalling dust can efficiently induce (positive) thermal torque onto the planets (Benítez-Llambay et al. 2015; Masset 2017; Guilera et al. 2019, 2021).

Although the present close-in positions of exoplanets indirectly hint at planet migration, it is hard to quantitatively test the theory based only on single-planet systems. Instead, multi-planet systems, especially those with planet pairs in Mean Motion Resonance (MMR) leave richer dynamical imprints against which the theory can be tested (Snellgrove et al. 2001; Papaloizou & Szuszkiewicz 2005). It is likely that such resonant architecture results from migration in a gas-rich environment (i.e., the disc) as energy dissipation is needed to trap planets in resonance (Terquem & Papaloizou 2007; Raymond et al. 2008; Rein 2012; Batygin 2015). One famous example is PDS 70, which harbours two directly imaged near-resonance planets in its protoplanetary disc (Bae et al. 2019; Benisty et al. 2021). Besides, a chain of planets in resonance might sculpt the asymmetry disc structure in HD 163296 (Isella et al. 2018; Garrido-Deutelmoser et al. 2023a). In particular, there tends to be an excess of systems with planets' period ratio just wide of commensurability (Fabrycky et al. 2014; Steffen & Hwang 2015), indicating that a certain fraction of planet pairs are truly in resonance.

Formally, two planets are said to be in $(j+1) : j$ resonance if at least one of their resonance angles ($\phi_{1,2} = (j+1)\lambda_2 - j\lambda_1 - \varpi_{1,2}$, with λ_i the mean longitudes and ϖ_i the longitude of pericentres) librate around a fixed value. However, the values of the resonance angles are poorly constrained because it is hard to constrain ϖ_i for near-circular orbits. We therefore

turn our attention to their period ratios and define the dimensionless parameter

$$\Delta = \frac{P_2}{P_1} - \frac{j+1}{j} \tag{2.1}$$

to measure the offset of the period ratio away from a first-order $(j+1) : j$ commensurability. Here, P_1 is the period of the inner planet and P_2 that of the outer. If two planets are in a $(j+1) : j$ resonance, the offset Δ must be close to zero. Xie (2014) and Ramos et al. (2017) emphasize that the exact value of Δ is determined by migration and eccentricity damping, linking the observed quantity Δ to planet migration (Charalambous et al. 2022). It offers us an opportunity to examine planet-disc interaction histories through planets in MMR in multi-planet systems. The migration history of such specific multi-planet systems like TRAPPIST-1 (Gillon et al. 2017; Luger et al. 2017; Huang & Ormel 2022), K2-24 (Petigura et al. 2018; Teyssandier & Libert 2020) and TOI-1136 (Dai et al. 2022), can be reconstructed.

Yet, most exoplanets are obviously not in resonance because of their large offsets Δ. Various scenarios have been proposed to explain the overall observed non-resonant planetary architecture statistically. These include dynamical instability (Izidoro et al. 2017, 2021), disc winds (Ogihara et al. 2018), *in situ* formation of sub-Netunes (Dawson et al. 2015; Choksi & Chiang 2020), planetesimal scattering (Chatterjee & Ford 2015; Ghosh & Chatterjee 2022), stellar tides (Lithwick & Wu 2012; Delisle & Laskar 2014; Xie 2014; Sánchez et al. 2020), and stochastic forces (Rein & Papaloizou 2009; Goldberg & Batygin 2022). However, many of these works introduce additional free parameters in order to match the only observed quantity – the period ratio distribution. Overfitting may occur. One way to improve on this is to include more observational quantities. For example, Goldberg & Batygin (2022) and Choksi & Chiang (2022) find that by additionally accounting for the TTV signatures of hundreds of Kepler planets, a laminar disc alone cannot reproduce the observed TTV features. Either additional planets (perturbers) are required (Choksi & Chiang 2022) or their birth proto-discs are turbulent (Goldberg & Batygin 2022).

In this work, we introduce a statistical approach to study all transiting exoplanets and try to answer when, where, and how many planets are captured in resonance. The observed planetary radii, orbital periods, and host stellar masses are taken into account. By assuming that the period ratio distribution is characterized by two distributions, representing both resonant and non-resonant planets, the probability that a planets pair is in resonance is evaluated. Whether the migration and eccentricity damping is consistent with migration theory is determined. In addition, our approach allows us to constrain the timing and the location, of the resonance trapping, which implies the pathway of planet formation.

The paper is structured as follows: We first introduce our statistical model in Sect. 2.2. Using the MCMC method, we constrain the relation between eccentricity damping time-scale and migration time-scale in Sect. 2.4. Along with the resonance trapping criterion that we improve on (Sect. 2.3), we address when, where, and how many planets are in resonance Sect. 2.5. The discussion and conclusion of this study are presented in Sect. 2.6 and Sect. 2.7, respectively.

2.2 Methodology

In this section, we describe our disc model and migration (Type I), and construct the likelihood function needed for the Monte Carlo Markov Chain (MCMC) simulations of Sect. 2.4. Since our migration model is linear with planet mass (Type I), we focus on the planets with relatively low planet-to-star mass ratios which are not likely to open a gap when they are in

the protoplanet disc. We assume that the relevant disc quantities follow power-law distribution (Sect. 2.2.1). We describe the migration model in Sect. 2.2.2. The equilibrium dynamics of planets trapping in resonance are described in Sect. 2.2.3. The masses of observed planets are calculated from a mass-radius (M-R) relationship. Its prescription is given in Sect. 2.2.4. The total log-likelihood function we construct for the MCMC is detailed in Sect. 2.2.5.

2.2.1 Disc model

As most observed transiting planets are located within ∼1 au of their host star, we will describe the possible structures of the inner disc. We assume that the gas surface density always follows a power-law distribution:

$$\Sigma(r) = \Sigma_{1\mathrm{au}} \left(\frac{r}{1\,\mathrm{au}}\right)^{s}, \tag{2.2}$$

where $\Sigma_{1\mathrm{au}}$ is the gas surface density at 1 au and s is its slope. The gas aspect ratio also follows a power-law distribution:

$$h(r) = h_{1\mathrm{au}} \left(\frac{r}{1\,\mathrm{au}}\right)^{q} \tag{2.3}$$

where $h_{1\mathrm{au}}$ is the gas aspect ratio at 1 au and q is its slope. Different assumptions about the disc structure, e.g., heating mechanisms, result in distinct values of s, q, $\Sigma_{1\mathrm{au}}$, and $h_{1\mathrm{au}}$. Typically, the inner disc is optically thick and the main heating energy comes from viscous dissipation (Ruden & Lin 1986), while the outer disc is optically thin and stellar irradiation mainly heat the disc onto its surface layer (Chiang & Goldreich 1997).

For discs dominated by stellar radiation, we make use of the disc structure from Liu et al. (2019). The gas surface density is:

$$\Sigma_{\mathrm{g,irr}} = 250 \left(\frac{\dot{M}_g}{10^{-8} M_\odot/\mathrm{yr}}\right) \left(\frac{M_\star}{M_\odot}\right)^{\frac{9}{14}} \left(\frac{L_\star}{L_\odot}\right)^{-\frac{2}{7}} \left(\frac{r}{\mathrm{au}}\right)^{-\frac{15}{14}} \mathrm{g\,cm^{-2}} \tag{2.4}$$

where $\dot{M}_g$ is stellar accretion rate and $L_\star$ is the star luminosity. The aspect ratio is:

$$h_{\mathrm{g,irr}} = 0.0245 \left(\frac{M_\star}{1 M_\odot}\right)^{-4/7} \left(\frac{L_\star}{1 L_\odot}\right)^{1/7} \left(\frac{r}{1\,\mathrm{au}}\right)^{2/7}. \tag{2.5}$$

For stars of mass between $0.43 M_\odot$ and $2 M_\odot$, which covers most of our star sample, the mass-luminosity relation is well represented by $L_\star/L_\odot = (M_\star/M_\odot)^4$ (Duric 2004). Therefore, the disc aspect ratio simplifies to:

$$h_{\mathrm{g,irr}} = 0.0245 \left(\frac{r}{1\,\mathrm{au}}\right)^{2/7} \tag{2.6}$$

independent of stellar mass.

If the inner disc is dominated by viscous heating, its temperature structure is highly related to the viscous accretion rate and opacity. Following Liu et al. (2019), s and q are taken to be $-3/8$ and $-1/16$, while $\Sigma_{1\mathrm{au}}$ and $h_{1\mathrm{au}}$ are not specified.

2.2.2 Type I migration

In the Type I migration regime, planet migration is the result of a net torque $\Gamma_{\rm net}$ consisting of the Lindblad (Ward 1986, 1997), corotation (Goldreich & Tremaine 1979; Ward 1992) and thermal torques (Benítez-Llambay et al. 2015; Masset 2017; Guilera et al. 2019, 2021), etc. Usually, the net torque is negative and the planet migrates inward. In the Type I limit the migration speed is proportional to disc mass and planet mass. In the limit of a locally isothermal disc, which implies that temperature is a function of radius only, $T(r)$, the type I migration time-scale for the i-th planet at distance r_i is:

$$\tau_{a_i} = \frac{L_i}{\Gamma_{\rm net}} = \frac{\gamma_I \tau_{w_i}}{h(r_i)^2}, \tag{2.7}$$

where L_i is the angular momentum of the planet, $\gamma_I = (2.7 - 1.1s)^{-1}$ (Tanaka et al. 2002) is the Type I migration prefactor (D'Angelo & Lubow 2010), and $h(r_i)$ is the disc gas aspect ratio at r_i. The characteristic time of the orbital evolution (Tanaka & Ward 2004) is:

$$\tau_{w_i} = \frac{1}{\mu_i} \frac{M_\star}{\Sigma(r_i) r_i^2} \frac{h(r_i)^4}{\Omega_K(r_i)}, \tag{2.8}$$

where μ_i is the mass ratio of the i-th planet over its host star and $\Omega_K(r_i) = \sqrt{GM_\star/r_i^3}$ is the Keplerian angular velocity at distance r_i. The eccentricity damping rate is proportional to the local surface density and planet mass. It is given by:

$$\tau_{e_i} = \frac{C_e \tau_{w_i}}{0.78} = \frac{C_e}{0.78\gamma_I} h^2 \tau_a, \tag{2.9}$$

where C_e stands for eccentricity damping efficiency. Although Cresswell & Nelson (2008) gives $C_e \approx 1$, lower values are needed in other studies to reproduce specific systems. TRAPPIST-1 planets demand $C_e \approx 0.1$ (Huang & Ormel 2022) and K2-24 requires $C_e \approx 0.28$ (Teyssandier & Libert 2020). A recently discovered ~100 Myr old exoplanet system TOI-1136, on the other hand, suggest $C_e \sim 10$ (Dai et al. 2022). We are therefore agnostic about the value of C_e, which value we intend to constrain through our MCMC fitting.

2.2.3 Dynamics of resonance trapping

Resonance trapping is a natural outcome of convergent disc migration and eccentricity damping, especially for first-order resonances $(j+1):j$. When two planets are in first-order resonance, their eccentricities and period ratio librate around their equilibrium values. Such equilibrium has been studied by Goldreich & Schlichting (2014) and Terquem & Papaloizou (2019). They both give the equilibrium eccentricity (the eccentricity where tidal damping equals resonant excitation) of the inner planet:

$$e^2_{1,\rm eq} = \frac{\tau_{e_1}/\tau_{a_2} - \tau_{e_1}/\tau_{a_1}}{2(j+1)\left(1 + \frac{j}{j+1}\frac{\mu_1}{\alpha\mu_2}\right)\left[1 + \frac{\mu_1}{\alpha\mu_2}\left(\frac{j}{j+1}\right)^2 \left(\frac{f_2'}{f1}\right)^2 \frac{\tau_{e_1}}{\tau_{e_2}}\right]} \tag{2.10}$$

where α is ratio of the inner-to-outer semi-major axis . Here, and in the following, the subscription '1' stands for the inner planet and '2' for the outer planet. The relationship between the eccentricities of the inner and outer planets is:

$$\frac{e_2^2}{e_1^2} = \left(\frac{\mu_1}{\alpha\mu_2}\frac{j}{j+1}\frac{f_2'}{f_1}\right)^2, \tag{2.11}$$

where f_1 and f_2' are coefficients tabulated in Terquem & Papaloizou (2019, their Table A1). The equilibrium value for the offset from exact resonance is:

$$\Delta_{\rm eq} = -f_2' \mu_1 \frac{1}{j} \frac{1}{e_{2,\rm eq}}. \tag{2.12}$$

At this distance, the resonance repulsion equals the Type-I inward migration.

In order to calculate the period ratios for planets in resonance, we need to know what their equilibrium eccentricities are. This calculation can be done only after the values of τ_{e_1}/τ_{e_2}, τ_{e_1}/τ_{a_2} and τ_{e_1}/τ_{a_1} are known. Combining the disc model and migration model, we have

$$\frac{\tau_{e_1}}{\tau_{e_2}} = \frac{\mu_2}{\mu_1} \left(\frac{r_1}{r_2}\right)^{4q-s-0.5} \tag{2.13}$$

and

$$\frac{\tau_{e_1}}{\tau_{a_2}} = \frac{\tau_{e_2}}{\tau_{a_2}} \frac{\tau_{e_1}}{\tau_{e_2}} = \frac{C_e h(r_2)^2}{0.78\gamma_I} \frac{\mu_2}{\mu_1} \left(\frac{r_1}{r_2}\right)^{4q-s-0.5} \tag{2.14}$$

where s and q are gas surface density and aspect ratio gradient.

For the eccentricity-to-semi-major axis damping of the inner planet, we distinguish it between two cases:

1. `Migrating` pair. If resonances are formed during migration and the ambient disc disperses before the planet pairs reach a migration barrier, planet migration and eccentricity damping follow Eq. (2.7) and Eq. (2.9). Therefore,

   $$\frac{\tau_{e_1}}{\tau_{a_1}} = \frac{C_e h(r_1)^2}{0.78\gamma_I} \tag{2.15}$$

   It requires that the outer planet migrates faster than the inner planet to guarantee convergent migration.

2. `Braking` pair. On the other hand, if resonances are formed before/after the inner planet's migration is halted by a barrier (could be disc inner edge or the radius where reverse migration occurs), there is no net torque on the two planets. Angular momentum conservation gives $\tau_{a_1}/\tau_{a_2} = -\sqrt{\mu_1 r_1/\mu_2 r_2}$. Hence,

   $$\begin{aligned} \frac{\tau_{e_1}}{\tau_{a_1}} &= -\frac{C_e h(r_2)^2}{0.78\gamma_I} \left(\frac{\mu_2}{\mu_1}\right)^{\frac{3}{2}} \left(\frac{r_1}{r_2}\right)^{4q-s-1} \\ &= -\frac{C_e h(r_1)^2}{0.78\gamma_I} \left(\frac{\mu_2}{\mu_1}\right)^{\frac{3}{2}} \left(\frac{r_1}{r_2}\right)^{2q-s-1} \end{aligned} \tag{2.16}$$

For the outer planet $\tau_{e_2}/\tau_{a_2} = C_e h(r_2)^2/0.78\gamma_I$ is always true. It is also apparent that the resonant equilibrium does not depend on disc mass ($\Sigma_{1\rm au}$) but on power law indices and aspect ratio (s, q, and $h_{1\rm au}$).

2.2.4 Mass-radius relations

Planets' masses are also needed to calculate the equilibrium period ratios in resonance. However, most transiting planets have poorly constrained masses compared to their radii.

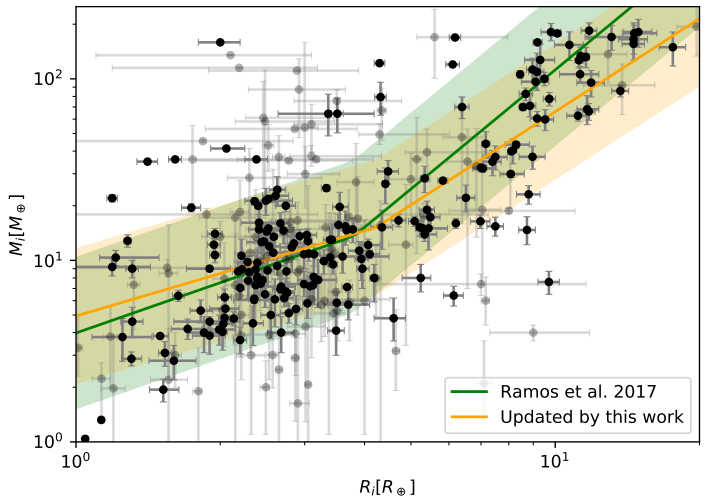


Figure 2.1. Mass-radius (M-R) relationship for exoplanets. Planets are selected based on the data of transiting planets in the NASA Exoplanet Archive. Only planets with mass lower than $200M_\oplus$, radii smaller than $20R_\oplus$ and periods longer than 5 days are included in the sample. Planets' masses and radii are indicated by black dots, with 1σ error bars. The green colour indicates the fit result from Ramos et al. (2017), orange colour is the updated fit result by this work (Eq. (2.17)). The values within their 1σ dispersion ($\sigma_\mathrm{m} = 0.374$ for our fit) are contained within the light green and orange region respectively.

If the planet mass is not yet constrained from e.g., Transit Timing Variation (TTV Agol et al. 2005) or Radial Velocity (RV), we then obtain the planet mass using a mass-radius relation. The planet sample for fitting the mass-radius relation is based on the data of transiting planets from the NASA Exoplanet Archive[1]. Planets with masses lower than $200M_\oplus$, radii smaller than $20R_\oplus$, or periods longer than 5 days (see Sect. 2.4.1) are selected while planets with periods shorter than 5 days are excluded.

Our fitting approach is identical to Ramos et al. (2017). They use a broken power law expression, which fits two different power law relations for larger bodies ($R > R_\mathrm{crit}$) and smaller bodies ($R < R_\mathrm{crit}$).

$$\log_{10}\left(\frac{\overline{M_i}}{M_\oplus}\right) = \begin{cases} a + b\log_{10}\left(\frac{R_i}{R_\oplus}\right) & \text{if } R_i \leq R_\mathrm{crit} \\ c + d\log_{10}\left(\frac{R_i}{R_\oplus}\right) & \text{if } R_i > R_\mathrm{crit} \end{cases} \tag{2.17}$$

where M_i and R_i is the mass and radius of the i-th planet. We make use of the Maximum Likelihood Estimator (MLE) to maximize a Gaussian likelihood centered at Eq. (2.17). The critical radius R_crit is also fitted. It estimates that: $a = 0.69$, $b = 0.78$, $c = 0.11$, $d = 1.7$, $R_\mathrm{crit} = 4.23R_\oplus$ and the corresponding dispersion $\sigma_m = 0.374$. The best-fitting relation is shown in Fig. 2.1 in comparison with the relation fitted by Ramos et al. (2017). They do not differ significantly. The estimated value for R_crit is consistent with Teske et al. (2021) who suggest a single power law relation for planets with $R < 3.25R_\oplus$.

Equation (2.17) allows us to calculate the planet mass and therefore the resonance offset (Eq. (2.12)). Moreover, the log-normal dispersion in planet mass enables us to check our model consistency. The reason is that any uncertainty in the mass, will propagate, through

[1] `https://exoplanetarchive.ipac.caltech.edu`

Eq. (2.10) and Eq. (2.12). Therefore, we expect that the obtained value for σ_Δ from MCMC fitting is similar to, or exceeds, σ_m.

The log-normal dispersion in planet mass significantly simplifies our analysis. There are arguably more sophisticated forms of M-R relationships, e.g., the one given by Wolfgang et al. (2016) and improved by Teske et al. (2021). However, they assume planet mass follows a normal dispersion instead of a log-normal. In that case, the resulting Δ would follow a complicated form of the ratio distribution[2].

2.2.5 A statistical model of resonant and non-resonant planets

We define the posterior distribution as: $p(\boldsymbol{\theta}|\Delta_{\mathrm{obs},k}, \boldsymbol{X}_k) = p(\Delta_{\mathrm{obs},k}|\boldsymbol{\theta}, \boldsymbol{X}_k)p(\boldsymbol{\theta}|\boldsymbol{X}_{\mathrm{obs},k})$. If the disc structure is not specified (without knowing the specific values of s, q in Eq. (2.2) and Eq. (2.3)), the unknown model parameters are $\boldsymbol{\theta} = (\log_{10}(C_e h_{1\mathrm{au}}^2), \sigma_\Delta, s, q)$ and the known parameters $\boldsymbol{X}_k = (M_\star, M_1, M_2, r_1, r_2, j)$. The index k indicates the k-th planet pair. If a disc structure is specified, the unknown model parameters are $\boldsymbol{\theta} = (\log_{10} C_e, \sigma_\Delta)$ for the irradiation disc and $\boldsymbol{\theta} = (\log_{10}(C_e h_{1\mathrm{au}}^2), \sigma_\Delta)$ for the viscous disc, and the known parameters are $\boldsymbol{X}_k = (M_\star, M_1, M_2, r_1, r_2, j, h_{1\mathrm{au}}, s, q)$. We assume that the prior $p(\boldsymbol{\theta}|\boldsymbol{X}_k)$ follows a uniform distribution (Table 2.1). The resonance index j is regarded as one of the known parameters such that we can analyse all pairs at once.

As mentioned, resonance trapping naturally results from convergent migration: either two planets get trapped into resonance during migration (both inward) with the outer planet migrating faster than the inner one, or the inner planet reaches a migration barrier with the outer planet arriving at a later time. Following the discussion in Sect. 2.2.4, we assume that the period ratio of a planet pair that is in resonance obeys a log-normal distribution $\log_{10}\Delta \sim \mathcal{N}(\log_{10}\Delta_{\mathrm{m/s}}(\boldsymbol{\theta}, \boldsymbol{X}_k), \sigma_\Delta^2)$:

$$\begin{aligned} &p_{\mathrm{res,m/s}}(\Delta|\boldsymbol{\theta}, \boldsymbol{X}_k) d\log_{10}\Delta \\ &= \frac{1}{\sqrt{2\pi\sigma_\Delta^2}} \exp\left[-\frac{[\log_{10}\Delta - \log_{10}\Delta_{\mathrm{m/s}}(\boldsymbol{\theta}, \boldsymbol{X}_k)]^2}{2\sigma_\Delta^2}\right] d\log_{10}\Delta, \end{aligned} \tag{2.18}$$

where $\Delta_{\mathrm{m/s}}$ indicates the resonance commensurability calculated by Eq. (2.12). The resonance offset Δ_{m} indicates the value calculated for `Migrating` pairs using Eq. (2.15), while Δ_{s} is for `Braking` pairs and is calculated using Eq. (2.16).

In the Type I migration regime, if the inner planet is more massive (migrates faster), convergent migration can only occur when the inner planet has reached the migration barrier. On the other hand, if the inner planet's migration is slower than the outer, migration is always convergent. In that case, trapping can occur when both planets migrate inward or when the inner planet has reached the migration barrier. For ease of the likelihood calculation, we further divide the resonant planet pairs into three categories:

Group 1: The inner planet migrated slower ($\tau_{a_1} > \tau_{a_2}$) and it did not reach a migration barrier (N_1);

Group 2: The inner planet migrated slower ($\tau_{a_1} > \tau_{a_2}$) and it reached a migration barrier (N_2);

Group 3: The inner planets migrated faster ($\tau_{a_1} \leq \tau_{a_2}$) and it reached a migration barrier (N_3).

[2] If variables X and Y follow a dependent (independent) normal distribution with nonzero mean values, the new variable $Z = X/Y$ follows correlated (uncorrelated) non-central normal ratio distribution (Hinkley 1969; Hayya et al. 1975).

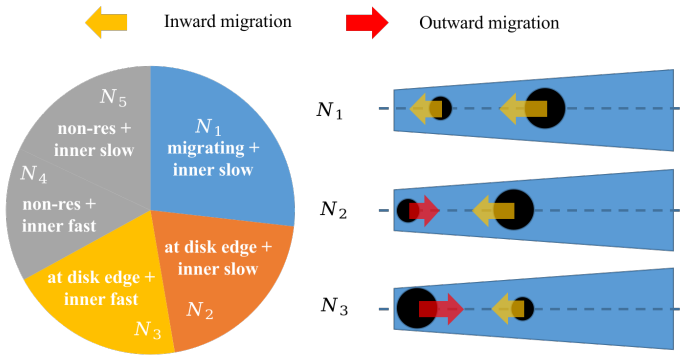


Figure 2.2. Classification of resonant and non-resonant planet pairs. In the pie chart, 'migrating' means the pairs lock into resonance before reaching a migration barrier, whereas "at disc edge" indicates planets lock into resonance at a planet migration trap. "Inner slow" ("fast") means that the inner planet has a longer (shorter) migration time-scale than its outer planet. $N_{\rm res}$ is the number of resonant pairs. N_1, N_2, and N_5 are the numbers of `Migrating`, `Braking`, and non- resonant pairs in the pairs with the inner planets migrating slower than the outer. N_3 and N_4 are the numbers of `Braking` and non-resonant pairs among the pairs with inner planets migrating faster than the outer.

N_1, N_2 and N_3 represent the number of resonant planet pairs corresponding to each type of resonance. In addition, N_4 (N_5) represents the number of pairs that are not in resonance with the inner planet migrating faster (slower) than the outer planet. We provide a sketch to explain the five classes in Fig. 2.2.

If the inner planets migrate faster ($\tau_{a_1} \leq \tau_{a_2}$), those pairs in resonance must be `Braking` pairs. However, if the inner planets migrate slower, they could either be `Migrating` pairs or `Braking` pairs. The $\log_{10}\Delta$ distribution of planets in resonance is therefore (hereafter, $p_{\rm res}(\Delta)$ represents $p_{\rm res}(\Delta_{\rm obs}|\boldsymbol{\theta}, \boldsymbol{X}_k)$, etc):

$$p_{\rm res}(\Delta) = \begin{cases} p_{\rm res,s}(\Delta) & \text{if } \tau_{a_1} \leq \tau_{a_2}, \\ \left[p_{\rm res,s}(\Delta) + p_{\rm res,m}(\Delta)\right] & \text{if } \tau_{a_1} > \tau_{a_2}. \end{cases} \tag{2.19}$$

The period ratio of planet pairs that are not in resonance is assumed to follow a uniform distribution:

$$p_{\rm n-res}(\Delta) d\log_{10}\Delta = \frac{(\ln 10)\Delta}{\Delta_{\rm max}} d\log_{10}\Delta \tag{2.20}$$

where $\Delta_{\rm max}$ is the value above which a planet pair with $\Delta_{\rm obs}$ is not considered in resonance. We use $\Delta_{\rm max} = (3j+2)/(3j-1) - (j+1)/j$ which is the distance from the first order $(j+1):j$ resonance to its closest external 3rd order $(3j+2):(3j-1)$ resonance.

Finally, the total log-likelihood is written as:

$$\ln\mathcal{L} = \sum_{k=1}^{N_{\rm pairs}} \ln\left[p_{\rm res}(\Delta_{{\rm obs},k}) + p_{\rm n-res}(\Delta_{{\rm obs},k})\right], \tag{2.21}$$

where $N_{\rm pairs}$ is the number of planet pairs in our sample.

Parameter	Prior		
	General	Irradiation	Viscous
$\log_{10}(C_e h_{1\mathrm{au}}^2)$	$\mathcal{U}(-8,0)$	–	$\mathcal{U}(-8,0)$
$\log_{10} C_e$	–	$\mathcal{U}(-2,2)$	–
σ_Δ	$\mathcal{U}(0,1)$	$\mathcal{U}(0,1)$	$\mathcal{U}(0,1)$
s	$\mathcal{U}(-5,2.4)$	$-15/14$	$-3/8$
q	$\mathcal{U}(-2,2)$	$2/7$	$-1/16$
$h_{1\mathrm{au}}$	–	0.0245	–

Table 2.1. Prior bounds or values for the disc parameters of the three models. All priors follow a uniform distribution $\mathcal{U}$.

2.3 Resonance Trapping criterion for the restricted 3-body problem

In this section, we improve and numerically verify the two-body resonance trapping criterion. This new trapping condition will be used in Sect. 2.5.2 to further constrain the statistical results of Sect. 2.4.2.[3]

2.3.1 Theoretical Derivation

In the restricted three-body problem, the outer planet is on a fixed circular orbit. The inner planet moves outward and its semi-major axis and eccentricity are damped on time-scales of τ_a and τ_e, respectively. Lagrange's planetary equation for the mean motion (n) then reads:

$$\dot{n}_1 = -3j\alpha f_1 \mu_2 e_1 n_1^2 \sin\phi_1 - \frac{3n_1}{2\tau_a} + \frac{p e_1^2 n_1}{\tau_e}, \tag{2.22}$$

where $\alpha = a_1/a_2$, ϕ_1, e_1 and f_1 are the semi-major axis ratio, resonance angle, the eccentricity of the inner planet, and f_1 is a numerical factor that depends on the resonance index j (Murray & Dermott 1999; Terquem & Papaloizou 2019). By definition, $p = 3$ holds when the eccentricity damping operates at constant angular momentum (Teyssandier & Terquem 2014). Lagrange's planetary equation for eccentricity is:

$$\dot{e}_1 = -\alpha f_1 \mu_2 n_1 \sin\phi_1 - \frac{e_1}{\tau_{e_1}}, \tag{2.23}$$

When two planets are in resonance, the values of different orbital properties e.g., e_1, α and ϕ_1 librate around their equilibrium values. The equilibrium eccentricity (Goldreich & Schlichting 2014; Terquem & Papaloizou 2019) is derived by putting $\dot{e} = \dot{a} = 0$ and eliminating $\sin\phi_1$ in Eq. (2.22) and Eq. (2.23):

$$e_{1,\mathrm{eq}} = \sqrt{\frac{\tau_{e_1}}{2(j+1)\tau_{a_1}}}. \tag{2.24}$$

By inserting the equilibrium eccentricity $e_{1,\mathrm{eq}}$ and $\alpha_{\mathrm{eq}} \approx [j/(j+1)]^{2/3}$ into Eq. (2.23), $\sin\phi_1$ follows:

$$\sin\phi_{1,\mathrm{eq}} = -\frac{1}{\alpha f_1 \mu_2 n_1}\sqrt{\frac{1}{2(j+1)\tau_{e_1}\tau_{a_1}}} \tag{2.25}$$

[3] Batygin & Petit (2023b) have recently presented an analysis with a trapping condition also predicated on the equilibrium phase angle, Eq. (2.25), like in this Section. Their findings are consistent with ours.

Naturally, its absolute value cannot exceed 1. Otherwise, for $|\sin\phi_1| > 1$, no steady state exists and the planets will cross the resonance. Combining, $\dot{e}_1 = 0$, Eq. (2.23) and Eq. (2.24) we can write the resonance trapping condition:

$$\tau_{a_1}\tau_{e_1} \geq \frac{1}{2(j+1)(\alpha f_1 \mu_2 n_1)^2}. \tag{2.26}$$

The classical theory about the resonance trapping criterion is that the time for the planet to migrate across the libration width is shorter than the libration time-scale (Ogihara & Kobayashi 2013; Batygin 2015). For comparison, we also provide the criterion derived from the classical pendulum model (Murray & Dermott 1999; Ogihara & Kobayashi 2013; Huang & Ormel 2022):

$$\tau_{a_1}\tau_{e_1} \geq \frac{\pi(j+1)}{4(\alpha f_1 \mu_2 n_1)^2}. \tag{2.27}$$

Compared to Eq. (2.27), the new criterion (Eq. (2.26)) has the same dependence on planet-to-star mass ratio μ_2 and the orbital frequency n_1 but differs regarding the resonance index j.

2.3.2 Comparison with simulation

We compare the new resonance trapping criterion above against the numerical simulation. The fiducial accelerations accounting for migration and eccentricity of planets in the simulations are expressed by:

$$\boldsymbol{a}_{\rm m} = -\frac{\boldsymbol{v}}{2\tau_a}, \tag{2.28}$$

$$\boldsymbol{a}_{\rm e} = -2\frac{(\boldsymbol{v}\cdot\boldsymbol{r})\boldsymbol{r}}{2r^2\tau_e} \tag{2.29}$$

(Papaloizou & Larwood 2000; Cresswell & Nelson 2006, 2008). We make use of the `WHfast` integrator of the open-source N-body code REBOUND (Rein 2012). The migration and eccentricity damping on planets are implemented through REBOUNDx (Tamayo et al. 2020).

We fix the outer planet on a circular orbit at $[(j+1)/j]^{2/3}$ au. The inner planet starts to migrate outward at 0.8 au on a time-scale of τ_a. Its eccentricity is damped on a time-scale of τ_e. The planet mass is fixed at $10\,M_\oplus$ and the host mass is $1\,M_\odot$. We vary two parameters in the simulation: τ_a from 10^4 yr (fast migration) to 10^7 yr (slow migration), and τ_a/τ_e ranging from 10^1 (inefficient eccentricity damping) to 10^4 (efficient eccentricity damping). Each parameter is sampled by 100 grid points evenly distributed in log-space. In order to capture the probabilistic behavior of resonance trapping, we run five simulations for each point in the τ_a/τ_e–τ_a parameter space, where we evenly sample the initial longitude of the inner planet.

We conduct simulations for $j = 1$ (2:1 resonance) and $j = 2$ (3:2 resonance). We run the simulation until $t = \tau_a$, but we take a snapshot at $t = 0.2\tau_a$. If the period ratio P_2/P_1 decreases below $(j+1)/j$, we classify the simulation outcome as a resonance crossing. The results are shown in Fig. 2.3 and Fig. 2.4 for $j = 1$ and $j = 2$ respectively. Resonance crossing cases are in white and resonance trapping cases are in green. The red dashed line indicates the boundary below which the trapping solution becomes overstable,

$$\left(\frac{\tau_a}{\tau_e}\right)_{\rm overstable} = \frac{1}{8(j+1)}\left(-\frac{3j^2}{\alpha f_1 \mu_2}\right)^{2/3} \tag{2.30}$$

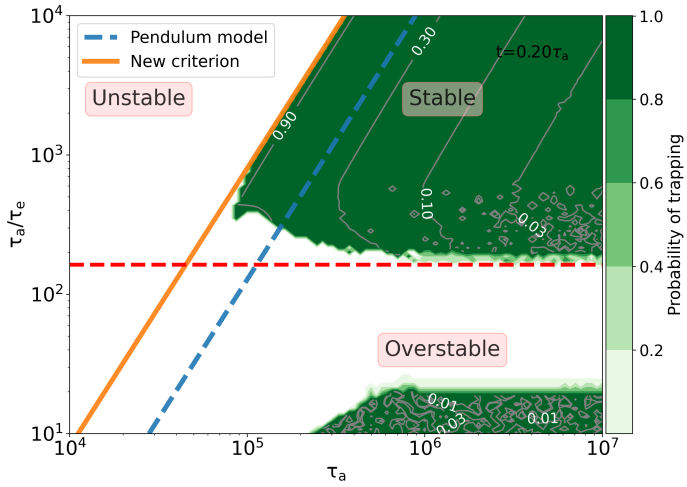


Figure 2.3. Resonance trapping and crossing for the 2:1 resonance. For each point in the parameter space, we run five simulations with different initial conditions to obtain the probabilistic result of resonance trapping (green shading). The blue line is the resonance trapping criterion derived from the pendulum model (Eq. (2.27)) while the orange line is our newly derived criterion (Eq. (2.26)). The grey solid lines are the contours of $\sin\phi_1$, with corresponding values labelled in white. The red dashed line (Eq. (2.30)) corresponds to the transition from stable resonance trapping (above) to overstable resonance (below). Below this line, the simulations progressively evolve into the overstable territory, see `https://raw.githubusercontent.com/shuohuangGIT/Infer-migration-history/main/q1.mp4`.

(Goldreich & Schlichting 2014), which evaluates to $\tau_a/\tau_e \approx 170$ for $\mu_2 = 3\times10^{-5}$, both for $j = 1$ and 2. Above this line, all systems are either trapped in resonance or not. The top-right corner indicates the parameter space where the two planets both get captured and permanently stay in resonance and the top-left indicates resonance crossing. Below this line, some systems are still evolving and resonance trapping is only temporary.

We indicate the trapping criterion derived from the pendulum model in blue and the improved trapping criterion (Eq. (2.26)) with the orange line. From Fig. 2.3 and 2.4 it is clear that the pendulum model criterion for resonance trapping (blue line) fails to quantitatively match the numerical simulations. Our new criterion (orange line), however, fits the simulations perfectly. The equilibrium value of $\sin\phi_1$ for the simulation snapshots is calculated by averaging its value over a time span of $0.1\tau_a$ before and after the snapshot time, e.g., $0.1-0.3\tau_a$ for the snapshot at $t = 0.2\tau_a$. The values of $\sin\phi_{1,\rm eq}$ is indicated by grey solid lines (contour) in Fig. 2.3 and 2.4. $\sin\phi_{1,\rm eq}$ increases as getting closer to the orange line, which is also expected by Eq. (2.25). The picture of resonance trapping/crossing over the entire parameter space of the migration time-scale and eccentricity damping time-scale has now been clarified. Migration plays a role in exciting the planet's eccentricity, while eccentricity damping reduces it. On one hand, if a planet pair is in resonance, the eccentricity damping balances its excitation and finally librates near the equilibrium value. If the migration speed is so fast that there is no steady state solution for the resonance angle $\phi_{1,\rm eq}$ (Eq. (2.26)), the resonance is crossed. Otherwise, resonance trapping is ensured. On the other hand, if eccentricity is excited to be high enough, planets can be captured into resonance, but only temporarily, because of the continuous increase of the resonance libration amplitude (over-

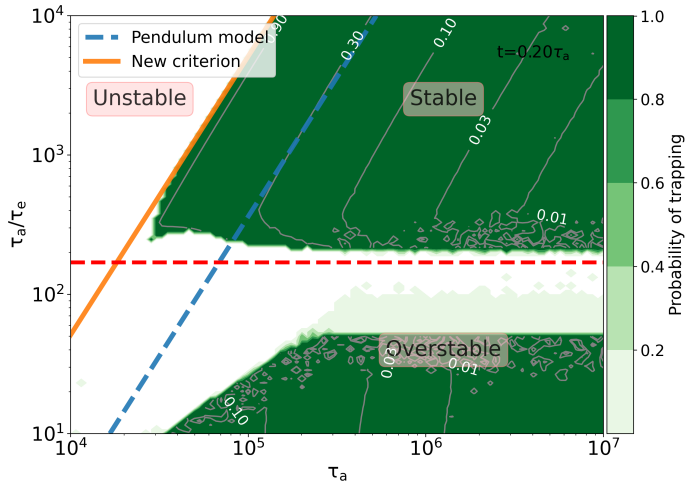


Figure 2.4. Same as Fig. 2.3, but for the 3:2 resonance. The video can be downloaded on Github: `https://raw.githubusercontent.com/shuohuangGIT/Infer-migration-history/main/q2.mp4`.

stability, cf. Goldreich & Schlichting 2014). Although not evident from the figures presented, all simulations located in the large green corner above the red dashed line exhibit permanent libration of $\sin\phi_1$, indicating that the planets are captured in resonance permanently. The amplitude of $\sin\phi_1$ during libration increases as the ratio τ_a/τ_e decreases, and approaches the red dashed line denoting overstability in Fig. 2.3 and 2.4. The green region situated below the red dashed line represents simulations in which planets are temporarily captured in resonance, with their amplitude of $\sin\phi_1$ increasing over time and circulating at the end of the simulation. In conclusion, both efficient eccentricity damping (τ_a/τ_e is high) and slow migration are required for permanent resonance trapping.

2.4 MCMC analysis

In this section, we first discuss how we select our sample in Sect. 2.4.1. Then we conduct an MCMC fitting to constrain the model parameters.

2.4.1 Sample selection

Our sample selection and all analysis are based on the NASA Exoplanet Archive. Our attention is drawn to planets detected through transits and TTV. As shown in Sect. 2.2.3, we need planets' masses to calculate the equilibrium eccentricities and period ratios in resonance. If only the radius is available, the M-R relationship described in Sect. 2.2.4 is used to calculate the masses of those transiting planets. Additionally, the semi-major axes and stellar masses are extracted.

We do not consider short-period planets in our sample. We take this simple step to reduce the effects of both photo-evaporation and stellar tides on the M-R relationship. First, photo-evaporation can alter the M-R relationship for planets with low-density atmospheres on time-scale of 1 Gyr (Fulton & Petigura 2018). It is believed to have triggered the so-called

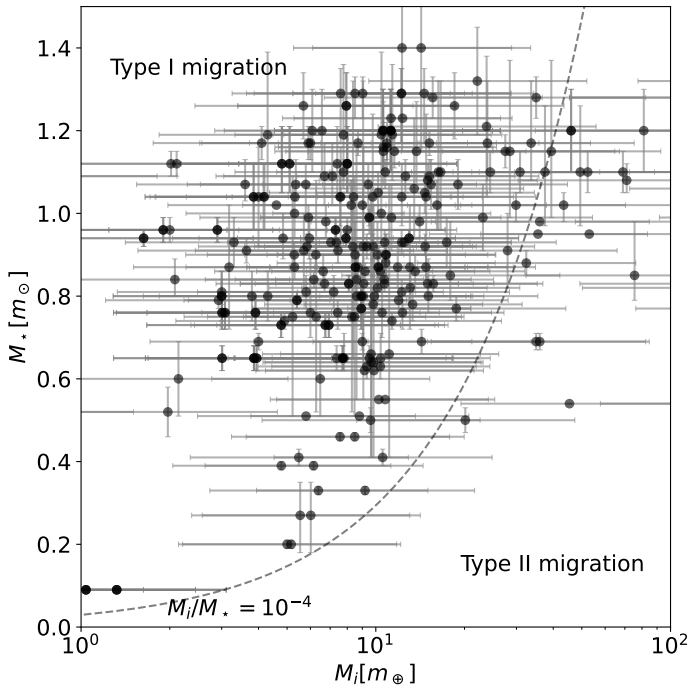


Figure 2.5. Planet mass versus stellar mass in the sample. Planet pairs with period ratios larger than $(j+1)/j$ and smaller than $(3j+2)/(3j-1)$ are chosen. We take j equal to 1, 2, 3 and 4. Planet masses and their host masses are indicated by black dots, with 1σ error bar. If the planet mass is inferred from its radius through the M-R relation, its uncertainty of the masses is assigned to be $\sigma_{\rm m} = 0.374$ dex. The grey dashed line indicates the position where the planet-to-star mass ratio equals $\mu = 10^{-4}$. We assume planets to the left of this line to follow Type I migration and otherwise Type II. Only Type I migrating planets are included in our analysis.

'radius gap' (Fulton et al. 2017). When planets get closer to their host stars, this effect is more obvious (Fulton & Petigura 2018). Second, stellar tides alter close-in planets' orbital properties (Lithwick & Wu 2012; Batygin & Morbidelli 2013; Charalambous et al. 2018; Papaloizou et al. 2018) and blur the information of the planets inherited from their protoplanet disc. Both mechanism are very sensitive to planets' semi-major axes. Excluding the planets with a cutoff period shorter than 5 days, though crude, can suppress the interference from stellar tides (Choksi & Chiang 2020) and photo-evaporation (Fulton & Petigura 2018) on our sample.

We display the planet mass versus their host mass in Fig. 2.5. The average planet mass is $10M_\oplus$ and the average stellar mass is $1\,M_\odot$. The planets' and stars' mass uncertainties are indicated by error bars. If the planet mass is inferred from the M-R relation, the log-normal standard deviation is then $\sigma_m = 0.374$ (Eq. (2.17)). The migration speed of low-mass planets in the proto-planetary disc scales linearly with planet mass, as dictated by the Type I migration limit. As planets become massive enough to perturb their surrounding disc, their migration gradually switches to Type II (Kanagawa et al. 2018; Pichierri et al. 2022). We set the boundary between two types of migration as $\mu_{\rm trans} = 10^{-4}$. Since our interests focus on Type I migration only planets with $\mu < \mu_{\rm trans}$ are included in our sample.

Finally, the sample size is reduced to 371 and the period ratios for all planet pairs are given

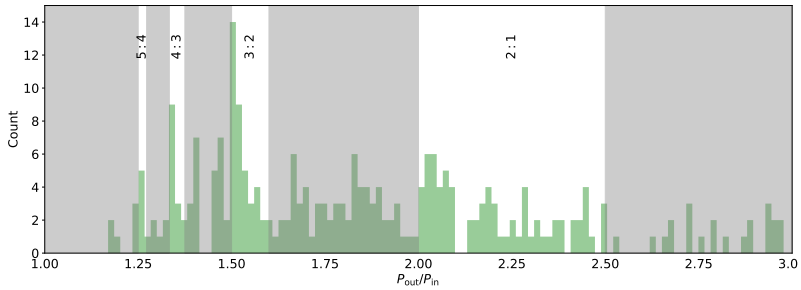


Figure 2.6. Distribution of the period ratio of all observed planet pairs in our sample (green histograms). We highlight the four windows in the vicinity of four different first-order resonances: 2:1, 3:2, 4:3 and 5:4. The left boundary of each window is $(j+1)/j$ and the right boundary is $(3j+2)/(3j-1)$. The total number of pairs is 371 in the green histogram and 128 in the windows.

by Fig. 2.6. The selected planets come from systems with two and more planets, including those with resonance chains.

To calculate the resonance offset, the resonance number j is required. There are excesses of systems ('peaks') just wide of the integer period ratios, which is suggestive of resonances. We only consider first-order resonances: 2:1, 3:2, 4:3, and 5:4. We assume that planets with period ratios slightly larger than the integer ratios are potentially in resonance until the period ratio "hits" the third-order resonance, because the resonant interaction is weaker as they become further from exact commensurability. Planet pairs with period ratios larger than $(j+1)/j$ but smaller than $(3j+2)/(3j-1)$ are possibly in $(j+1)/j$ resonance. Here, $(3j+2)/(3j-1)$ is the location of the closest third-order resonance. The selection of a period ratio limit for identifying planets in 2:1 resonance may seem arbitrary, given that the period ratio can extend up to 2.5, where planet pairs are unlikely to be in resonance. However, a slightly smaller window for the 2:1 resonance would not affect our conclusions. Nonetheless, this choice is useful for identifying planets in 3:2, 4:3, and higher j first-order resonances because planets located near these resonance locations are close to nearby higher-order resonances, and may therefore be more easily perturbed. The satisfied period ratio windows are highlighted in Fig. 2.10 (top panel) and the four lower panels zoom in on these four windows, for j =1, 2, 3, 4, where we instead show the distribution of the offset from resonance, Δ. Planets out of the windows may still be in first-order resonance, but their fraction must be very low and it is not covered by our analysis. We ignore other first-order resonances and all higher-order resonances.

2.4.2 Implication on planet-disc interaction from MCMC

We use `emcee` (Foreman-Mackey et al. 2013) to perform the MCMC analysis. We implement three different models:

1. General model. The disc structure is not specified and the MCMC is used to fit $\log_{10}(C_e h_{1au}^2)$, σ_Δ, s, q.

2. Irradiation model. Stellar irradiation is assumed to be the main heating source and the MCMC is used to fit $\log_{10} C_e$ and σ_Δ.

3. Viscous model. Viscosity-driven accretion is assumed to be the main heating source and the MCMC is used to fit $\log_{10}(C_e h_{1au}^2)$, σ_Δ.

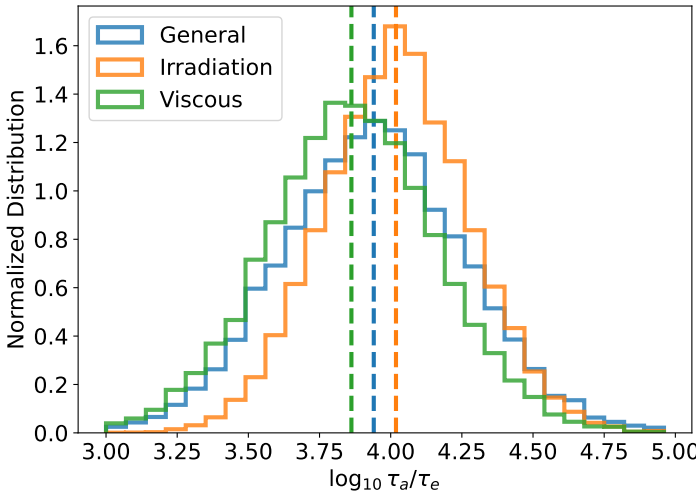


Figure 2.7. Distribution of $\log_{10}\tau_a/\tau_e$, the semi-major axis-to-eccentricity damping time-scale at the location of the inner planets averaged over all planet pairs, in General (blue), Irradiation (orange) and Viscous (green) model. We calculate this quantity based on the posterior distributions of the parameters in each model. Dashed lines indicate their median values.

The prior distribution of parameters $\log_{10}(C_e h_{1\mathrm{au}}^2)$, $\log_{10} C_e$, σ_Δ, s, q and the values we take for s, q and $h_{1\mathrm{au}}$ for the three different models are shown in Table 2.1. The convergence of MCMC chains are checked. We make use of the criterion that MCMC converges if the autocorrection time is shorter than 1/50 times its chain length. We checked that our results all satisfied the convergence criterion.

For the General model, we examine whether our method is capable to retrieve all the parameters in Appendix 2.B. It turns out that almost all parameters are degenerate. Therefore, the fitted values for $\{\log_{10}(C_e h_{1\mathrm{au}}^2), \sigma_\Delta, s, q\}$ may not be reliable (Appendix 2.B.1). The result of the General model is shown and analysed in Appendix 2.A. We also calculate the quantity $\log_{10}\tau_a/\tau_e$, the semi-major axis-to-eccentricity damping time-scale, at the location of the inner planets averaged over all planet pairs. This quantity, however, shows to be independent of the other parameters and can be reproduced within the 1σ error bar (Appendix 2.B.1).

We calculate $\log_{10}\tau_a/\tau_e$ in all three models, and their distributions are shown in Fig. 2.7. Two key points can be made. First, different disc structures result in nearly identical distributions. The parameter $\log_{10}\tau_a/\tau_e$ is not sensitive to the assumed disc structure. Second, the value of $\log_{10}\tau_a/\tau_e$ – peaking at 4 and almost always larger than 3 – is high. The high semi-major axis-to-eccentricity damping time-scale ratio indicates that temporary capture (overstable libration) did not operate for the planets in our sample, which would require $\tau_a/\tau_e \approx 170$ (Goldreich & Schlichting 2014) in Eq. (2.30).

By specifying the disc structure – the Irradiation or Viscous model – the parameters can be successfully retrieved within 1σ error bar (Appendix 2.B.2). We show the fit result of $\{\log_{10} C_e,\ \sigma_\Delta\}$ and $\{\log_{10}(C_e h_{1\mathrm{au}}^2),\ \sigma_\Delta\}$ for the Irradiation and Viscous model in Fig. 2.8 and Fig. 2.9, respectively. The python package `corner.py` (Foreman-Mackey 2016) is used to generate the plots of the posterior distributions.

The Irradiation model (Fig. 2.8) fits $\log_{10} C_e = 0.94^{+0.25}_{-0.25}$. For the viscous model, the disc aspect ratio is sensitive to the stellar accretion rate and disc opacity. Therefore, we fit the combination $C_e h_{1\mathrm{au}}^2$, and $\log_{10}(C_e h_{1\mathrm{au}}^2) = -4.60^{+0.30}_{-0.29}$ (Fig. 2.9). If we take $h_{1\mathrm{au}} = 0.0245$,

same value as the irradiation model, then $\log_{10} C_e = -1.38^{+0.30}_{-0.29}$. Increasing $h_{1\mathrm{au}}$ (or $L_\star$ in Eq. (2.5)) would result in a smaller value of C_e ($C_e \propto h_{1\mathrm{au}}^{-2}$). Theoretically, Tanaka et al. (2002) and Tanaka & Ward (2004) from the first principle calculate that $\log_{10} C_e = 0$ for locally isothermal discs. The fitting outcomes from both disk models suggest more efficient eccentricity damping than theories.

Additionally, the fitted values for σ_Δ are $0.65^{+0.10}_{-0.08}$ and $0.79^{+0.10}_{0.09}$ for the Irradiation and Viscous model, respectively. Their values are twice that of the mass dispersion. Indeed, we expect that the fitted σ_Δ is of the same magnitude as σ_m (Sect. 2.2.4). However, σ_Δ is fitted to be slightly larger than our expectation. This could be an implication of turbulent discs (Rein & Papaloizou 2009; Goldberg & Batygin 2022) and/or post-disc perturbations (e.g. Lithwick & Wu 2012; Chatterjee & Tan 2014; Stock et al. 2020). We further run an MCMC fitting fixing σ_Δ to 0.374, the resulting posterior distribution of $\log_{10} C_e$ or $\log_{10}(C_e h_{1\mathrm{au}}^2)$ are not significantly different from what we present here. It gives $\log_{10}(C_e h_{1\mathrm{au}}^2) = -3.95^{+0.29}_{-0.27}$ for the Viscous model and $\log_{10} C_e = 0.44^{+0.19}_{-0.20}$ for the Irradiation model.

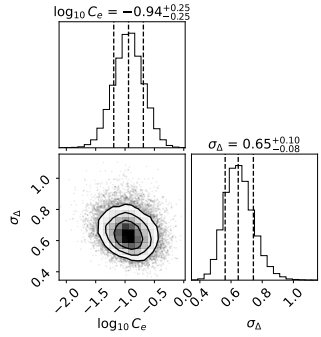


Figure 2.8. Corner plot of variables in the MCMC analysis ($\log_{10} C_e$ and σ_Δ) with 1σ, 2σ and 3σ confidence contours, for the Irradiation model, which fixes the surface density power law index $s = -15/14$ and the disc aspect ratio index $q = 2/7$. The 1σ uncertainty is labelled on the top of each column and indicated by left and right dashed lines. The middle dashed lines indicate their median values.

In summary, our MCMC model shows that eccentricity damping is effective ($\log_{10} \tau_a/\tau_e \approx 4$), making resonant over-stability unlikely. The observed period ratio excess of planets suggests more efficient eccentricity damping than the predictions by Tanaka et al. (2002) and Tanaka & Ward (2004) ($C_e \approx 1$), irrespective of whether the disk structure is dominated by irradiation or viscous heating. However, the aspect ratio of a viscous inner disc depends on the disc opacity and stellar accretion rate (e.g. Liu et al. 2019), which limits our ability to constrain C_e.

2.5 Implications for planet formation

In this section, we adopt the fit result from the Irradiation model and further study the implications of resulting resonant planets statistically. Ramos et al. (2017) and Charalambous et al. (2022) use similar prescription for their disc structure. The reason why we choose the Irradiation model is the following. Even though resonance trapping can happen much earlier, planets' period ratios (offsets) are more evolved at the end of the disc lifetime when the migration and eccentricity damping time-scales are longer than the disc dispersal time-scale.

The disc structure at this stage mostly determines what the corresponding mature planet system looks like. Because planet formation consumes solids and solids drift inward rapidly due to gas drag (Weidenschilling 1977; Andrews et al. 2012), the disc at this point becomes optically thin, rendering stellar irradiation the main heating source. The transition disc LkCa15 is arguably an example that low-mass planets can carve a large dust cavity (Leemker et al. 2022). Therefore, the Irradiation model is more applicable to transition discs.

The best-fitting resonance offset distribution is plotted in Fig. 2.10 (blue lines), with upper and lower 3σ uncertainty (blue shaded regions). We assume that the offset of non-resonant pairs follows a uniform distribution, which is also indicated in Fig. 2.10 (grey dashed lines). The MCMC fits the observed distribution better than the uniform-only model because it fits more planets with small Δ and fewer planets with large Δ, just as observed. The complete sample with 128 pairs are fitted simultaneously. However, we use four panels to display the four near-resonance planets because Δ depends on the resonance number j in a complex form. We cannot present one distribution of Δ to represent all 128 pairs while keeping the shape of log-normal profile.

For each planet pair, we calculate its probability of being in resonance ($P_{\mathrm{res},k}$, in Sect. 2.5.1). The total number of resonant pairs and planets' mean eccentricities in our sample is then obtained. The properties of their birthplace – the natal proto-planet disc – are then inferred, e.g., the upper limit of the surface density (Sect. 2.5.2) and the location of the migration barrier (Sect. 2.5.3).

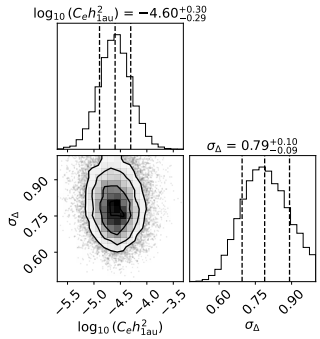


Figure 2.9. Similar to Fig. 2.8, but for the Viscous model. The surface density power law index is fixed at $s = -3/8$ and the disc aspect ratio index at $q = -1/16$.

2.5.1 Fraction of resonant pairs

Given the fitted value for C_e and σ_Δ, we can calculate the probability of each planet pair in resonance via two characteristic probability distribution functions (Eq. (2.19) and Eq. (2.20)): $P_{\mathrm{res},k} = p_{\mathrm{res}}(\Delta_{\mathrm{obs},k})/[p_{\mathrm{res}}(\Delta_{\mathrm{obs},k}) + p_{\mathrm{n-res}}(\Delta_{\mathrm{obs},k})]$. In Fig. 2.10, we plot the histogram of period ratio and resonance offset distribution of planet pairs weighted by $P_{\mathrm{res},k}$ (red hatches). It indicates the period ratio and resonance offset distribution of resonant pairs. The period ratio of resonant pairs peaks just wide of integer ratios, and, as the period ratio further increases, resonant pairs vanish. Not all pairs with period ratios close to integer ratio are in resonance.

The total number of resonant pairs is the summation of resonant probability over all

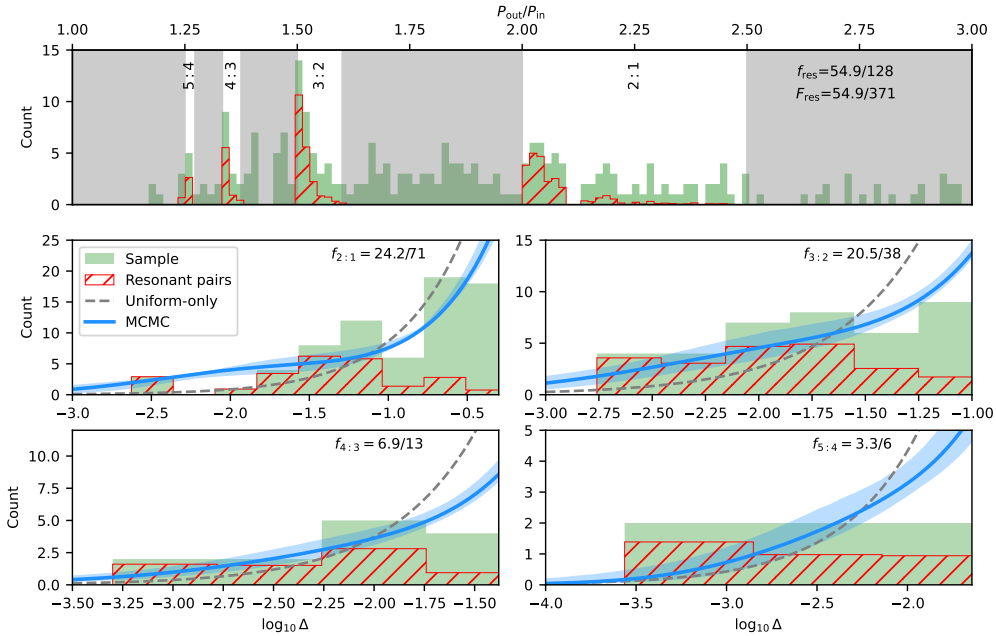


Figure 2.10. Distribution of period ratio (top panel, similar to Fig. 2.6) and resonance offset Δ (bottom panel) for the inferred resonant planet pairs (red hatches) versus all observed planet pairs in our sample (green histogram). The lower panels display the distribution of period ratio offset Δ within the highlighted four windows in the top panel. Grey dashed lines show the probability distribution of all planet pairs assuming they follow a uniform distribution (not in resonance). We compare it with the best MCMC fit result (blue curve, after bin size correction) assuming the Irradiated disc model. The shaded blue region indicates the 3σ uncertainty. We also label the fraction of inferred resonant planets, which is the ratio of the area between the red hatches and the green histograms (see Sect. 2.5.1 for details).

planet pairs:

$$N_{\rm res} = \sum_{k=1}^{N_{\rm pairs}} P_{{\rm res},k}. \tag{2.31}$$

We label the average fraction of resonant pairs, $f_{\rm res} = N_{\rm res}/N_{\rm pairs}$, on the top right of four lower panels in Fig. 2.10. $N_{\rm pairs}$ is the number of pairs in the narrow period ratio windows.

We also calculate the fraction of all resonant pairs among all pairs in our sample: $F_{\rm res} = N_{\rm res}/371 = 14.8^{+0.5}_{-0.7}\%$. The distribution is shown in Fig. 2.11 left panel. It is consistent with the crude estimation made by Wang & Ji (2014) (10%-20%). This number ignores higher-order resonances and first-order resonances with resonance numbers larger than 4 (5:4). The resonant fraction could therefore be higher.

We split the resonant planets into three groups, each group has a number of resonant pairs N_1, N_2, N_3, respectively, and $N_{\rm res} = N_1 + N_2 + N_3$ (see Sect. 2.2.5 for detail and Fig. 2.2 for a sketch). Three different resonant fractions are calculated:

- $f_{\rm res}({\rm Mig}|{\rm out}) = N_1/(N_1 + N_2 + N_5)$: fraction of `Migrating` pairs among the pairs where the inner planets migrate slower than the outer;

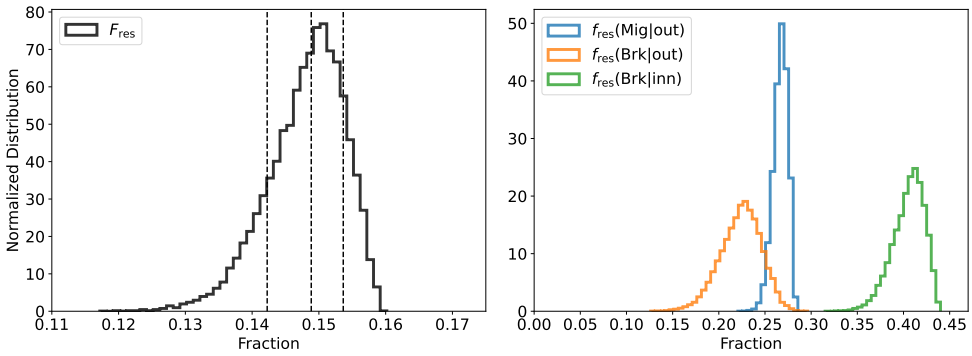


Figure 2.11. Resulting distribution of resonant fraction for all pairs in our sample (left) and detailed resonant distribution for pairs with period ratio within the near integer ratio windows (right). Here $f_{\rm res}$(Mig|out) is the fraction of planets that enter resonance during migration with the outer planet migrating faster. $f_{\rm res}$(Brk|out) is the fraction of resonant planets stopping at the disc inner edge with the outer planet migrating faster. $f_{\rm res}$(Brk|inn) is the fraction of resonant planets stopping at the disc inner edge with the inner planet migrating faster.

- $f_{\rm res}$(Brk|out) $= N_2/(N_1 + N_2 + N_5)$: fraction of `Braking` pairs among the pairs where the inner planets migrate slower than the outer;

- $f_{\rm res}$(Brk|inn) $= N_3/(N_3 + N_4)$: fraction of `Braking` pairs among the pairs where the inner planets migrate faster than the outer.

This classification allows us to compare the fraction of resonant pairs under different physical conditions. The distributions of the three fractions are shown in Fig. 2.11, right panel. It shows that $f_{\rm res}$(Mig|out) ≈ 0.27. This implies that in some pairs the ambient gas disc disperses before the pair reaches a migration barrier, i.e., either planet migration is slow or the disc disperses rapidly following planet migration and formation. The gas-poor formation scenario for sub-Neptunes (Dawson et al. 2015; Choksi & Chiang 2020) would be consistent with this picture. However, a still larger fraction of resonant pairs, $f_{\rm res}$(Brk|out) ≈ 0.23, and $f_{\rm res}$(Brk|inn) ≈ 0.41 reach their migration barriers. It implies that gas-poor formation applies to some of the observed systems, but not all of them. Interestingly, $f_{\rm res}$(Brk|out) is smaller than $f_{\rm res}$(Brk|inn), i.e., the inner planets tend to be more massive than the outers. A possible explanation would be that the inner edge of the disc – the location of the pressure maximum – would also be the place where pebbles accumulate. Pebble accretion at such locations can be very efficient (Chatterjee & Tan 2014; Jiang & Ormel 2023).

We also plot the eccentricity distribution for the planets in resonant pairs, weighted by their probability of being in resonance ($P_{{\rm res},k}$), in Fig. 2.12. Generally, the outer planets have smaller eccentricities consistent with Eq. (2.11). Their values mostly fall between 10^{-3} and 10^{-2}. It suggests that if we observe a sub-Neptune planet pair with relatively high eccentricities ($e \sim 0.1$), they are not likely to be in first-order resonance irrespective of their near-resonance period ratio. Post-disc perturbations (Choksi & Chiang 2022) could, however, excite eccentricities and change resonant pairs from apsidal anti-alignment to alignment (Laune et al. 2022). These apsidally aligned systems would have slightly larger eccentricities than what Fig. 2.12 predicts.

2.5.2 Upper limit on the disc surface density at resonance trapping

The constraints the MCMC model provides cannot be used to determine the absolute value of the natal disc surface density, as it cancels in the τ_a/τ_e expression. An upper limit for the natal disc surface density of resonant planets can, however, be deduced from the resonance trapping criterion. We use Eq. (2.26) in order to break the degeneracy and to find an upper limit for the disc surface density at the trapping location. It is assumed in the derivation of Eq. (2.26) that the outer planet is on a fixed circular orbit. Such an assumption is valid because the outer planets on average have lower eccentricities than their inner siblings (Fig. 2.12). From Sect. 2.4.2, we already found that $\tau_a/\tau_e > 10^3$ for observed transiting planets, that is, overstability is not likely to occur. In this regime, Eq. (2.26) alone gives the resonance trapping condition. Therefore, we can get the critical migration time-scale, below which the resonance would be crossed. In the Type I migration regime, planet migration speed is proportional to gas disc surface density. We are therefore able to obtain the upper limit of the disc gas surface density.

The upper limit is reached by combining Eq. (2.7), Eq. (2.9), Eq. (2.16) and Eq. (2.26):

$$\Sigma_{\max}(r_2) = 1.6|f_1|h^3(r_2)\left[(j+1)C_e\gamma_I\frac{\tau_{e_1}}{\tau_{e_2}}\right]^{\frac{1}{2}}\left(\frac{r_2M_1}{r_1M_2}\right)^{\frac{5}{4}}\frac{M_\star}{r_2^2} \tag{2.32}$$

inserting a disc model and extrapolating to 1 au, we obtain:

$$\begin{aligned}\Sigma_{\mathrm{1au,max}} =& 1.6|f_1|h_{\mathrm{1au}}^3\left[(j+1)C_e\gamma_I\right]^{1/2}\left(\frac{M_1}{M_2}\right)^{3/4}\\ &\times\left(\frac{r_1}{r_2}\right)^{2q-s/2-1.5}\left(\frac{r_2}{1\,au}\right)^{3q-s}\frac{M_\star}{r_2^2}.\end{aligned} \tag{2.33}$$

The expression $\Sigma_{\mathrm{1au,max}} \propto h_{\mathrm{1au}}^3$ is consistent with what Kajtazi et al. (2022) found in their simulations. In Fig. 2.13, we plot the $\Sigma_{\mathrm{1au,max}}$ for each planet pair that is possible in resonance, versus their host mass. The deeper the colour, the more likely it is that the pair is in resonance. The size of the symbol indicates the resonance index j. The figure shows that high-j resonances tend to be associated with high surface densities. This result is in line with Type-I migration theory. Massive discs result in faster migration, which allows the planets to cross the relatively strong resonance. In addition, Fig. 2.13 shows that $\Sigma_{\max}$ increases with stellar mass. That is because the migration speeds in the Type I limit depend on the star-to-disc mass ratio. Higher surface density is required to migrate faster. We indicate the surface density of the Minimum mass solar nebula (i.e., MMSN, Hayashi 1981) and the Minimum mass extra-solar nebula (i.e., MMEN, Chiang & Laughlin 2013) in Fig. 2.13. The upper limits of nearly all disc surface densities are below that of the MMEN, while the inferred disc surface densities are centred around the MMSN value.

We conclude this discussion with two final points. First, the value for $\Sigma_{\max}$ we obtained refers to the time when the planets were locked into resonance, not the upper limit over the entire disc lifetime. Second, planets in higher j resonances tend to provide higher upper limits on the disc surface density. However, they might alternatively have formed in close proximity to each other, avoiding crossing of lower-j resonances. In that case, the true value of Σ_{1au} is likely to be less than $\Sigma_{\mathrm{1au,max}}$.

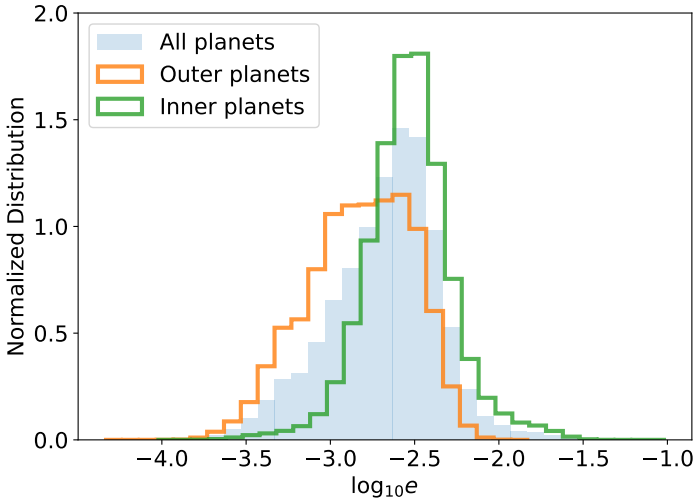


Figure 2.12. Eccentricity distribution of planet pairs that are in resonance, weighted by the probability of being in resonance. We compare the eccentricity distribution of the outer planets in all planet pairs with their inner planets.

2.5.3 Migration barrier reflects the disc inner rim

Planets can migrate in the disc, but their migration is believed to be halted somewhere as otherwise all planets would be consumed by the host star. However, the location and mechanism of the migration barrier are under debate. There are two main explanations for the barriers: dust sublimation (Kama et al. 2009; Flock et al. 2019) and the stellar magnetosphere (Königl et al. 2011; Hartmann et al. 2016).

If we assume a mass-luminosity relation for main sequence stars (Duric 2004), the dust sublimation radius becomes:

$$r_{\rm subl} = r_{\rm sub,0} \left(\frac{M_\star}{M_\odot} \right)^2, \tag{2.34}$$

where $r_{\rm sub,0}$ is the silicate dust sublimation radius for solar mass stars:

$$r_{\rm sub,0} = 0.13 \left(\frac{C_{\rm bw}}{1} \right)^{1/2} \left(\frac{0.1}{\epsilon} \right)^{1/2} \left(\frac{1400{\rm K}}{T_{\rm d}} \right)^2 {\rm au}, \tag{2.35}$$

where $C_{\rm bw}$ is the back-warming factor, ϵ is dust cooling efficiency and $T_{\rm d}$ is the dust sublimation temperature (Kama et al. 2009).

The magnetospheric infall radius tends to expand and converge to the stellar corotation radius due to angular momentum locking (Long et al. 2005). The stellar corotation radius is expressed as:

$$r_{\rm co} = 0.057 \left(\frac{P_\star}{5\,{\rm d}} \right)^{\frac{2}{3}} \left(\frac{M_\star}{M_\odot} \right)^{\frac{1}{3}} {\rm au} \tag{2.36}$$

The rotation periods of T Tauri stars (e.g. Bouvier et al. 2007; Lee & Chiang 2017) and young star associations (e.g.,Upper Sco and NGC 2264 Roquette et al. 2021) are several days (1-10 days).

The MCMC model is capable to identify (in a probabilistic sense) whether or not the planets have reached a migration barrier. We plot the location of the inner planet of those

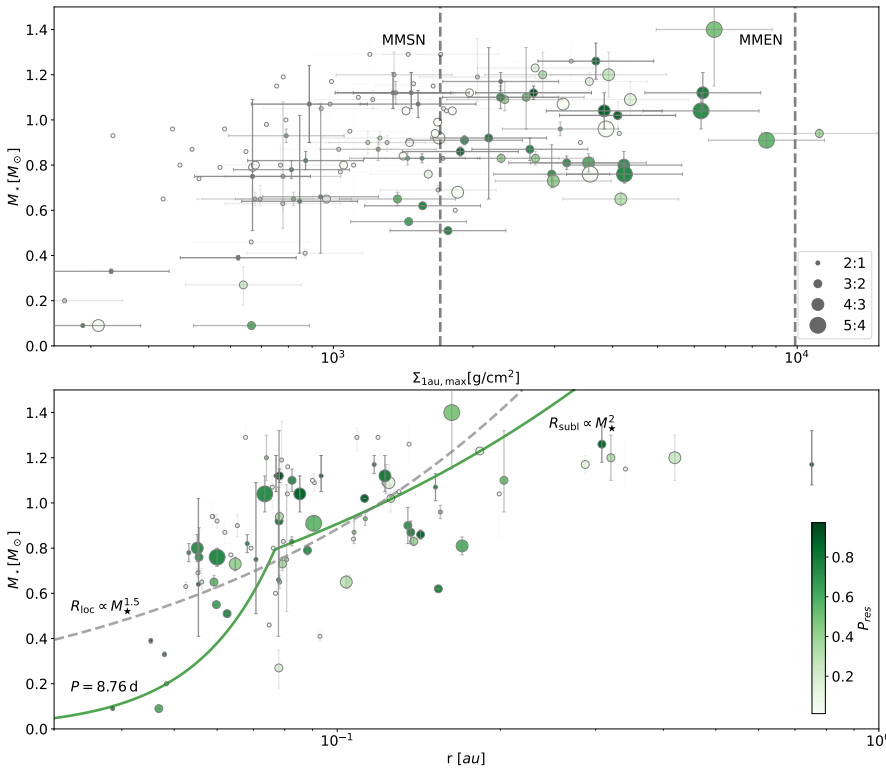


Figure 2.13. Inferred maximum surface density at 1 au for the resonant planets (top panel) and location of the migration barrier (bottom panel) versus the host stellar mass, for the 128 planet pairs in the four windows in Fig. 2.10. Different sizes of the circles indicate different resonance index j. The colour of the symbols indicates the probability of planets in resonance ($P_{\mathrm{res},k}$). In the top panel, error bars indicate the 1σ uncertainties in the stellar mass and $\Sigma_{\mathrm{1au,max}}$ – the latter follows from the uncertainty in C_e. The left and right grey dashed lines indicate the surface density of the MMSN and MMEN, respectively. In the bottom panel, grey and green lines give the best-fitting location of the migration barrier (the location of the inner planet in resonant pairs) fitted by a single power law and a broken power law, respectively.

pairs – the presumed location of the migration barrier – in Fig. 2.13. The symbol size again represents the resonance index j and the colour indicates how likely they are in resonance. From the plot, it can be seen that as the stellar mass increases the location of the migration barrier moves further away from the star. Motivated by the two theories about the migration barrier and aiming to figure out which radius is more consistent with observation, we fit the location of a migration barrier using the single power law expression:

$$r_{\mathrm{bar},k} = r_0 \left(\frac{M_{\star,k}}{M_\odot} \right)^l , \tag{2.37}$$

where r_0 is the location of the migration barrier for solar-mass stars. The Gaussian likelihood we construct is weighted by the resonance probability $P_{\mathrm{res},k}$:

$$\ln \mathcal{L} = \sum_{k=1}^{N_{\mathrm{pairs}}} \ln \left[\mathcal{N}(r_{\mathrm{bar},k} - r_k, \sigma_r^2) \cdot P_{\mathrm{res},k} \right] , \tag{2.38}$$

where $r_{\mathrm{bar},k}$, r_k and σ_r are the model predicted migration barrier location for the k-th pair (Eq. (2.37)), and the presumed location of the migration barrier and the standard deviation of the fitted migration barrier radius, respectively. If one pair has a larger $P_{\mathrm{res},k}$, it is more likely that the planets are formed in the protoplanet disc and undergo disc migration. The MLE fits $r_0 = 0.13$, $l = 1.49$ and σ_r is 0.079 au. The location of the migration barrier fitted by single power law relation is, however, shallower than the corresponding index of the dust sublimation radius but steeper than that of the magnetospheric radius. It may imply that there are two planet populations whose migration barriers are carved by either dust sublimation radius or magnetospheric radius. For this reason, we also fit a broken power law:

$$r_{\mathrm{bar},k} = \begin{cases} r_1 \left(\frac{M_{\star,k}}{M_\odot}\right)^{1/3} & \text{if } M_{\star,k} \le M_{\mathrm{crit}} \\ r_2 \left(\frac{M_{\star,k}}{M_\odot}\right)^{2} & \text{if } M_{\star,k} > M_{\mathrm{crit}}, \end{cases} \tag{2.39}$$

where $M_{\mathrm{crit}} = (r_1/r_2)^{3/5} M_\odot$ is the transition mass between the two different power laws. Similar to the single power law, we use MLE to fit the two parameters $r_1 = 0.08$ au and $r_2 = 0.12$ au and the transition mass M_{crit} is $0.79 M_\odot$ (see Fig. 2.13). The low mass fit corresponds to a corotation period of $P_\star = 8.76$ days, which is consistent with the observed rotation period for young stars (Bouvier et al. 2007; Lee & Chiang 2017; Roquette et al. 2021). The value of r_2 agrees with Eq. (2.35). Around these high-mass stars, planets are trapped at the dust sublimation location as it exceeds r_{co}. However, the uncertainty $\sigma_r = 0.078$ au is only slightly smaller than the value given by the single power law, suggesting that the broken power law model is only marginally better. A larger sample will make for a more reliable analysis.

2.6 Discussion

In this work, we have constructed a model that connects the planet migration history to the observed values of the offset from integer period ratios (Δ). If the resulting planet pair is in resonance, Δ follows a log-normal distribution. On the other hand, if it is non-resonant, the corresponding Δ is assumed to follow a uniform distribution. Based on this, we have developed a statistical model that constrains the migration histories of the observed planets by conducting a Markov Chain Monte Carlo method (MCMC) analysis. We examine our MCMC method using self-generated mock data Sect. 2.B and prove that it can indeed reproduce certain features.

Our model for resonance trapping is designed for two-planet systems and first-order resonances, but we also include observed systems with planets in a resonance chain. Kajtazi et al. (2022) have shown that the averaged properties of the resonance chain (involving three or more planets) still reflect the properties of the system as if there is only one resonant pair. Therefore, multi-planet systems do not significantly contaminate the results. In addition, we have not considered higher-order resonances. A more general model that applies to both first-order and higher-order resonances needs to be considered in the future. Finally, it is possible that the inner planets migrate across the inner disc edge and enter the disc cavity (Huang & Ormel 2022; Fitzmaurice et al. 2022), where our model would not be applicable. But those planets are plausibly massive enough to open a deep gap (Ataiee & Kley 2021; Chrenko et al. 2022), which are excluded by our sample selection.

A key assumption in the model is that the uncertainties in the planet masses and the ensuing Δ follow a log-normal distribution. We can then fit the excess of period ratio just wide

of integer ratio with a log-normal profile, thus extracting pairs in resonance. If we would adopt different distributions for the mass, the resulting distributions for Δ would become far more complex and no longer allow us to express the corresponding likelihoods in closed form. However, certain post-disc dynamics, e.g., post-disc energy dissipation from planetesimal scattering (Chatterjee & Ford 2015; Ghosh & Chatterjee 2022), stellar tides (Lithwick & Wu 2012; Batygin & Morbidelli 2013) and stellar encounters (Cai et al. 2019; Stock et al. 2020), could slightly change the period ratios of planet pairs. Therefore, they may play roles in broadening, shifting, or even skewing the log-normal profile. What the resulting Δ distribution may look like needs to be investigated in future work. Once addressed, one may learn the post-disc perturbation histories the planets have experienced. However, this also requires a much larger sample size than what we have at present, as already in this work the MCMC is unable to break some model degeneracies.

Our model mainly applies to those small planets unable to open a gap (in Type I migration regime). Tanaka et al. (2002) and Tanaka & Ward (2004) showed that the semi-major axis damping time-scale (τ_a) and eccentricity damping time-scale (τ_e) have a relation for locally isothermal disc: $\tau_e = 1.28 C_e h^2 \tau_a / \gamma_I$ and $C_e = 1$. If the planet partially opens a gap, the migration speed decreases linearly with the gas surface density in the gap (Kanagawa et al. 2018). The same holds for eccentricity damping (Pichierri et al. 2022). Therefore, the ratio τ_a/τ_e is independent of surface density and the constraints we obtain on it still hold when the planet opens a partial gap. Neither assuming a specific disc nor migration model, we obtain that $\tau_a/\tau_e \approx 10^4$, which is the most robust result of this study. After adopting the irradiation disc model, we further obtain $C_e \approx 0.1$, which is consistent with one earlier statistics work Charalambous et al. (2022). We summarize three possible reasons for arriving at such a small C_e value in practice compared to locally isothermal migration theories (Tanaka et al. 2002; Tanaka & Ward 2004).

1. Mounting evidence increasingly suggests that Wind-driven accretion (Pascucci et al. 2023), plays a more prominent role as the primary mechanism of accretion, displacing the conventional notion of viscous accretion (Lynden-Bell & Pringle 1974). In scenarios where the disk's viscosity remains low Fedele et al. (2018), the predominant source of heating arises from stellar irradiation. Intriguingly, when the disk was optically thick, the disk aspect ratio could be lower ($h \lesssim 0.01$) than the irradiation model in our original paper where we assume an optically thin disk.

2. Post-disc dissipation mechanisms. Although we excluded planets with periods shorter than 5 days from our sample, tidal interactions (Lithwick et al. 2012; Batygin & Morbidelli 2013) may still be effective beyond this limit. Planetesimal scattering (Chatterjee & Ford 2015; Ghosh & Chatterjee 2022) and stellar encounters (Cai et al. 2019; Stock et al. 2020) are also important in shaping the final architecture of multi-planet systems. A more detailed evaluation of the mentioned interactions should be addressed in future studies.

3. Small γ_I ($\ll 1$). Non-isothermal prescription of γ_I was investigated in depth by Paardekooper et al. (2010, 2011). Very often at certain locations of the disc, planet migration can be effectively suppressed, i.e., $|\gamma_I| \ll 1$ (Baruteau et al. 2014; Benítez-Llambay et al. 2015). Planets can therefore stay at small eccentricities and large resonance offsets (Wang et al. 2021b).

Furthermore, by improving the analytical criterion for resonance trapping, we are able to constrain the upper limit on the natal disc surface density for those planets in resonance.

The resulting maximum surface density is similar to that of the Minimum Mass Solar Nebular (MMSN) but smaller than that of the Minimum Mass Extra-solar Nebula (MMEN).

Several other migration prescriptions have been proposed, including more sophisticated ones such as those by Paardekooper et al. (2010, 2011). These prescriptions demonstrate that planets within a certain mass range can be naturally trapped at a location where the (positive) corotation torque exerted on the planet exceeds the (negative) Lindblad torque (Bitsch et al. 2013, 2014; Baruteau et al. 2014). To first order, for small planets, the migration behavior would still be predominantly linear (with planet mass and disk mass) except near these trapping locations. In our model, such a scenario is naturally incorporated through the `Braking` pair. Regarding the dependence of the damping terms on planet eccentricity, non-linear correction terms have been proposed by e.g., Cresswell & Nelson (2006, 2008); Ida et al. (2020). However, at low eccentricity, these non-linear terms are irrelevant and we do not include these terms in our investigation. Finally, our findings on the ratio τ_a/τ_e are robust, irrespective of the specific disc migration prescriptions and non-linear terms. This is because this ratio has a one-to-one correspondence to the resonance offset Δ. Therefore, our conclusion regarding τ_a/τ_e remains valid even if we incorporate different migration models (disc structures) or non-linear terms.

The imprint resonant trapping leaves behind tentatively allow us to assess where and when planets form in the discs. The evaluation of the probability of planet pairs in MMR is crucial, and this step also informs us of the number of resonant pairs. Since we employ different models for how planets get trapped in resonance (Sect. 2.2.5), it is possible to distinguish gas-poor formation scenarios (pairs trapped in resonance when migrating) and gas-rich formation scenarios (pairs stopped by the migration barrier). The former could be identified with late formation, while the latter, which are more dominant, are connected to the early formation in gas-rich discs. The present orbits of these planets further hint at the location of migration barriers. However, due to our small sample, we cannot unambiguously identify the physical origin of the migration barrier; either the dust sublimation radius or the magnetospheric radius would fit the data. The situation is, however, expected to improve in the near future. The upcoming launch of the PLAnetary Transits and Oscillations of stars (PLATO) mission (e.g. Rauer et al. 2014) and The Earth 2.0 (ET) mission (Ge et al. 2022; Ye 2022) could drastically increase not only the number but also the precision of planet detections. It will provide us with a more precise analysis of the planet formation and migration histories reflected in the dynamical properties of resonant planets.

2.7 Conclusions

We manage to construct a statistical model connecting planet migration theory to observed quantities of Kepler planets. Based on the inferred masses and resonance offsets, we conduct an MCMC analysis to extract the history of planet-disc interaction from planet-planet dynamics. The statistical approach provides us with the following findings:

1. The semi-major axis-to-eccentricity damping time-scale ratio can be constrained at $\log_{10} \tau_a/\tau_e \approx 4$ with a dispersion of $\approx$0.3 dex, irrespective of the assumed disc model. The eccentricity damping is so efficient that overstable libration of resonances is unlikely to have occurred.

2. After assuming the isothermal irradiation disc, we obtain $\log_{10} C_e = -0.94^{+0.25}_{-0.25}$ which connects eccentricity damping and semimajor axis damping in the Type-I migration theory. This value is 10 times smaller than what was theoretically derived by Tanaka

et al. (2002) and Tanaka & Ward (2004) but in line with some recent analyses on individual multi-planet systems. The discrepancy could be attributed to our neglect of post-disk (tidal) damping effects or uncertainty in our understanding of disk migration.

3. From the MCMC posterior, the probability that a planet pair is in resonance follows. The fraction of transit planet pairs in first-order MMR amounts to $14.8^{+0.5}_{-0.7}\%$.

4. Most of the inferred resonant planets are consistent with the scenario that they reached a migration barrier, indicative of early migration in a gas-rich disc. The location of the migration barrier could be the dust sublimation radius for massive stars ($M_\star > 0.79 M_\odot$) and the magnetospheric radius for low mass stars ($M_\star < 0.79 M_\odot$).

5. By evaluating the resonance strength of those inferred resonant planets, the upper limit of the proto-disc surface density during the planet formation era is obtained. Most systems have their $\Sigma_{1\mathrm{au}}$ below that of the Minimum Mass Extra-solar Nebula (MMEN) and half of them below that of the Minimum Mass Solar Nebula (MMSN).

6. It is found that the classical MMR trapping/crossing criterion based on the pendulum model does not match numerical simulation. We provide and numerically verify an improved criterion (Eq. (2.26)) based on the equilibrium resonance angle, which together with the overstability condition of Goldreich & Schlichting (2014) (Eq. (2.30)) fully describes the problem.

Future work could feature a more complete model accounting for high-order resonances and resonance chains. Detection of more resonant planets and more precise measurements of planetary and stellar properties with upcoming missions will definitely improve the confidence of our analysis.

Appendix

2.A Results of the General disc model

The full MCMC fitting corner plot of the General model is shown in Fig. 2.14. The fitted values for all four parameters are $\log_{10}(C_e h_{1\mathrm{au}}^2) = -3.55^{+0.71}_{-0.89}$, $s = 1.58^{+0.58}_{-1.05}$, $q = 0.31^{+0.37}_{-0.47}$. However, these values do not necessarily refer to the real physical disc parameters, due to the degeneracy among them. Therefore, we generate mock planet period ratio data (with the same size as our sample used here) and examine this MCMC model without specifying the disc structure in Sect. 2.B.1. Those tests indeed suggest that s and q are not able to be retrieved.

Fig. 2.14 reveals the degeneracy: s negatively correlates with $\log_{10}(C_e h_{1\mathrm{au}}^2)$, q correlates positively with $\log_{10}(C_e h_{1\mathrm{au}}^2)$ and q positively with s. We found that such correlations are well represented by:

$$4q - s = C_2, \tag{2.40}$$

from Eq. (2.13) and

$$\log_{10}(C_e h_{1\mathrm{au}}^2) + 2q \log_{10} \frac{r_2}{1\,au} - \log_{10}(0.78\gamma_I) + (4q - s) \log \frac{r_1}{r_2} = C_1, \tag{2.41}$$

from Eq. (2.15), Eq. (2.14) and Eq. (2.16). C_1 and C_2 are two constants. Eq. (2.41) and Eq. (2.40) are indicated in Fig. 2.14 (green dashed lines), and they match the correlation. The fitted

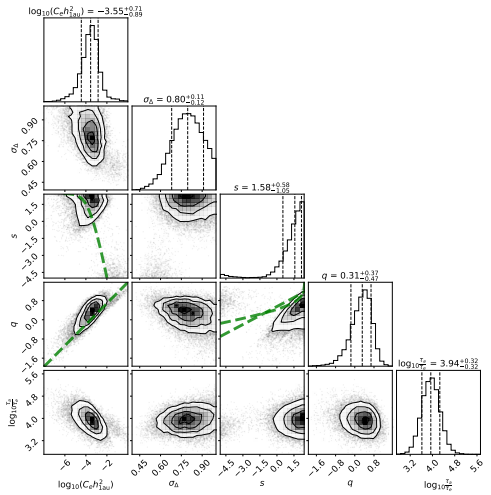


Figure 2.14. Corner plot of variables in the MCMC analysis ($\log_{10} C_e$, σ_Δ, s, and q) with 1σ, 2σ and 3σ confidence contours, w/o assuming the disc structure. We also calculate $\log_{10}(\tau_a/\tau_e)$ accordingly and add this variable into the corner plot. The 1σ uncertainty is labelled on the top of each column and indicated by left and right dashed lines. The middle dashed lines indicate their median values. Green lines indicate the correlation between different variables, which is Eq. (2.41) and Eq. (2.40).

log-normal dispersion σ_Δ, however, does not have any correlation with other parameters. It makes sense because our model does not depend on σ_Δ. We introduce another parameter:

$$\log_{10} \frac{\tau_a}{\tau_e} = \frac{C_e h(\bar{r}_1)^2}{0.78\gamma_I} \tag{2.42}$$

and it can be calculated given $\{\log_{10}(C_e h^2_{1\mathrm{au}}), \sigma_\Delta, s, q\}$. Here, $\bar{r}_1$ is the observed semi-major axis of inner planet average over all planet pairs. This parameter is calculated and put in the corner plot. It shows that $\log_{10} \tau_a/\tau_e$ is a quantity independent of s and q, but slightly depends on $\log_{10}(C_e h^2_{1\mathrm{au}})$.

2.B MCMC performance examination

As described in Sect. 2.4.1, we make use of planet masses, period ratios, semi-major axes and host masses from the NASA exoplanet database. Given these data as well as disc structure, we can then calculate the exact period ratios if planets are in resonance, and compare them to the observations. In this section, to examine the performance of the MCMC, we generate mock samples by replacing the actual period ratios with those assuming they are in or out of resonance. We randomly select a fraction of planet pairs to be in resonance and the fraction is f_{res}. If they are not in resonance, the resulting period ratio follows a uniform distribution. If they are in resonance, the resulting period ratio is calculated via Eq. (2.12). We finally add log-normal noise to the planet masses with σ_m, which enables us to compare it to the resulting σ_Δ. In this way, the mock sample is generated, with known disc parameters. We then run the MCMC model to check whether we can reproduce the input parameters. The mock sample has the same size as the real sample we used in Sect. 2.4.

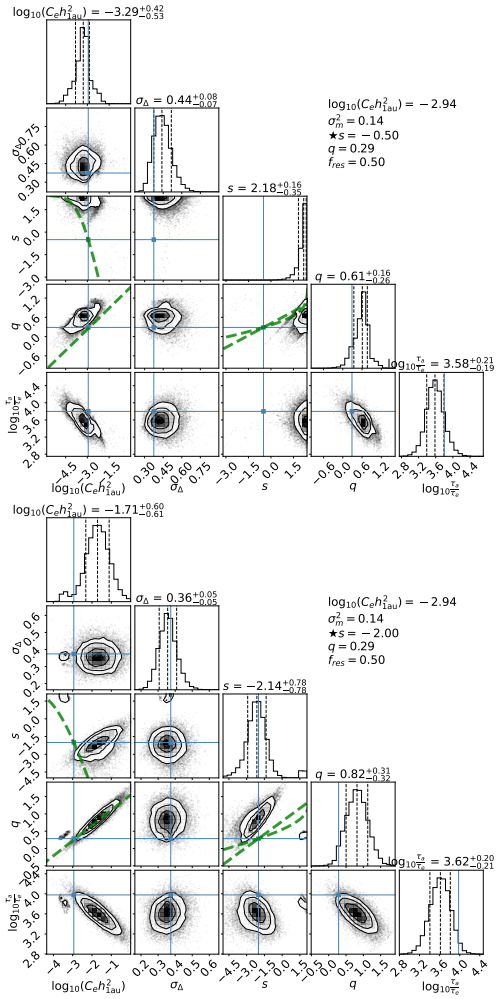


Figure 2.15. Similar to Fig. 2.14. Examination of MCMC model performance, without specifying the disc structure. In each panel, all parameters used are labelled in the upper right corner. We change the parameter s (labelled after ★) in different panels to examine the performance of MCMC model and we change s from -0.5 and -2. In each corner plot, blue lines show the true values. The 1σ uncertainty is labelled on the top of each column and indicated by left and right dashed lines. The middle dashed lines indicate their median values.

2.B.1 Tests without assuming a disc structure

We first examine whether the MCMC can reproduce $\log_{10}(C_e h^2_{\rm 1au})$, s and q, and whether the fitted σ_Δ is comparable to (the input) σ_m. Several sets of parameters are used for generating samples and model examination. The default parameters for generating the mock sample are $\log_{10}(C_e h^2_{\rm 1au}) = -2.94$, $\sigma_m = 0.374$, $s = -15/14$, $q = 2/7$ and $f_{\rm res} = 0.5$. We then test different values of s, q, and $f_{\rm res}$. The resulting corner plots are shown in Fig. 2.15, Fig. 2.16 and Fig. 2.17. The true value of parameters for generating mock samples is labelled at the top right of each panel and indicated by blue lines.

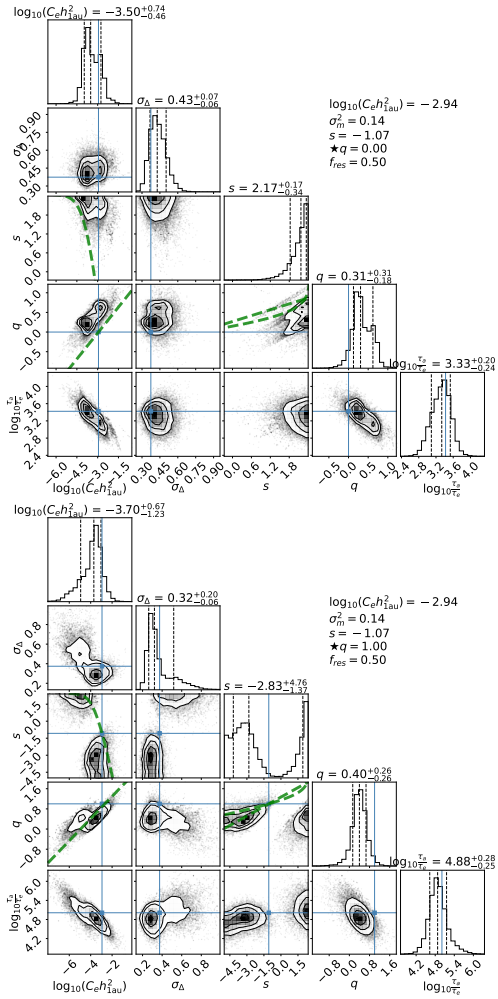


Figure 2.16. Similar to Fig. 2.15, but with different q. We change q from 0 and 1.

Unfortunately, the true values of $\log_{10}(C_e h^2_{1au})$, s and q are not properly retrieved. The posterior distribution gives the expected values for $\log_{10}(C_e h^2_{1au})$, s and q, but they are not consistent with the true values. However, the correlation between the parameters is revealed. The corner plot shows that s negatively correlates with $\log_{10}(C_e h^2_{1au})$, q is positively correlated to $\log_{10}(C_e h^2_{1au})$ and q is positively correlated to s. Their correlation is consistent with Eq. (2.41) and Eq. (2.40), indicated by green dashed lines.

Similar to Fig. 2.14, we also plot the posterior distribution of $\log_{10}(\tau_a/\tau_e)$ (Eq. (2.42)), which is a rather independent variable. The examination result suggests that $\log_{10}(\tau_a/\tau_e)$ can be fitted within 1.5σ error bar in all cases. The fitted σ_Δ is always very close to the log-normal error σ_m we impose for planet mass. It proves that the distribution of resonance offset Δ resulting from log-normal distributed planet masses also follows a log-normal distribution, when they are in resonance.

We therefore conclude that our MCMC model is useful for fitting $\log_{10}(\tau_a/\tau_e)$ but not $\log_{10}(C_e h^2_{1au})$, s and q if a disc structure has not been specified.

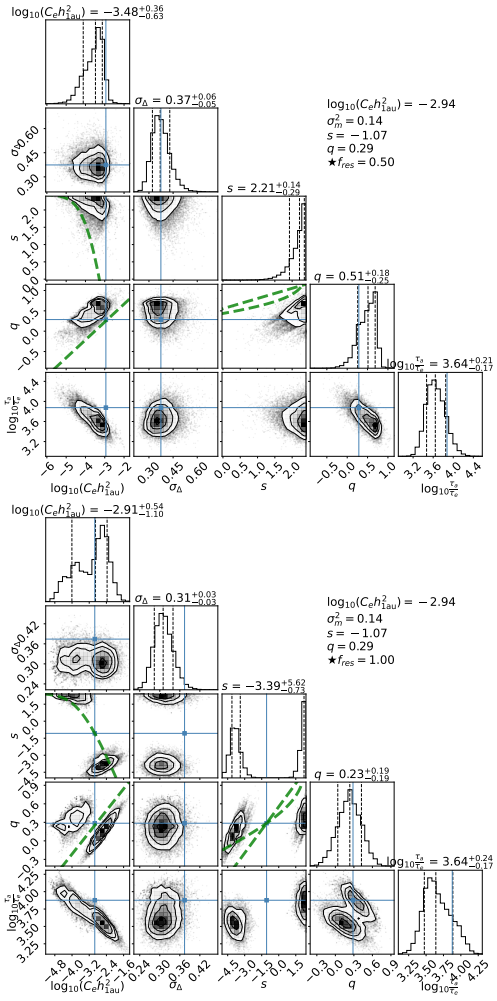


Figure 2.17. Similar to Fig. 2.15, but with different $f_{\rm res}$. We change fraction of pairs in resonance ($f_{\rm res}$) from 50% to 100%.

2.B.2 Tests assuming a disc structure

We here examine whether the MCMC can reproduce $\log_{10} C_e$, given a disc structure, and whether the fitted σ_Δ is still comparable to σ_m. We test several sets of parameters. The default parameter set is $\log_{10} C_e = 0.28$, $\sigma_m = 0.374$, $s = -15/14$, $q = 2/7$ and $f_{\rm res} = 0.5$. We then change each parameter to two other values, while keeping the other parameters the same.

The MCMC results are shown in Fig. 2.18. Different panels show the fit result for the mock sample generated from different parameter sets, and the true values of the parameters are labelled on the top right and indicated by blue lines. The true value of $\log_{10} C_e$ can always be reproduced within 1.5σ when $f_{\rm res} > 0.5$. The fitted σ_Δ is always consistent with σ_m as well. However, if we decrease the fraction of planets in resonance $f_{\rm res}$ to 0.1, the $\log_{10} C_e$ can no longer be retrieved and therefore the MCMC is no longer valid. However, when fitting

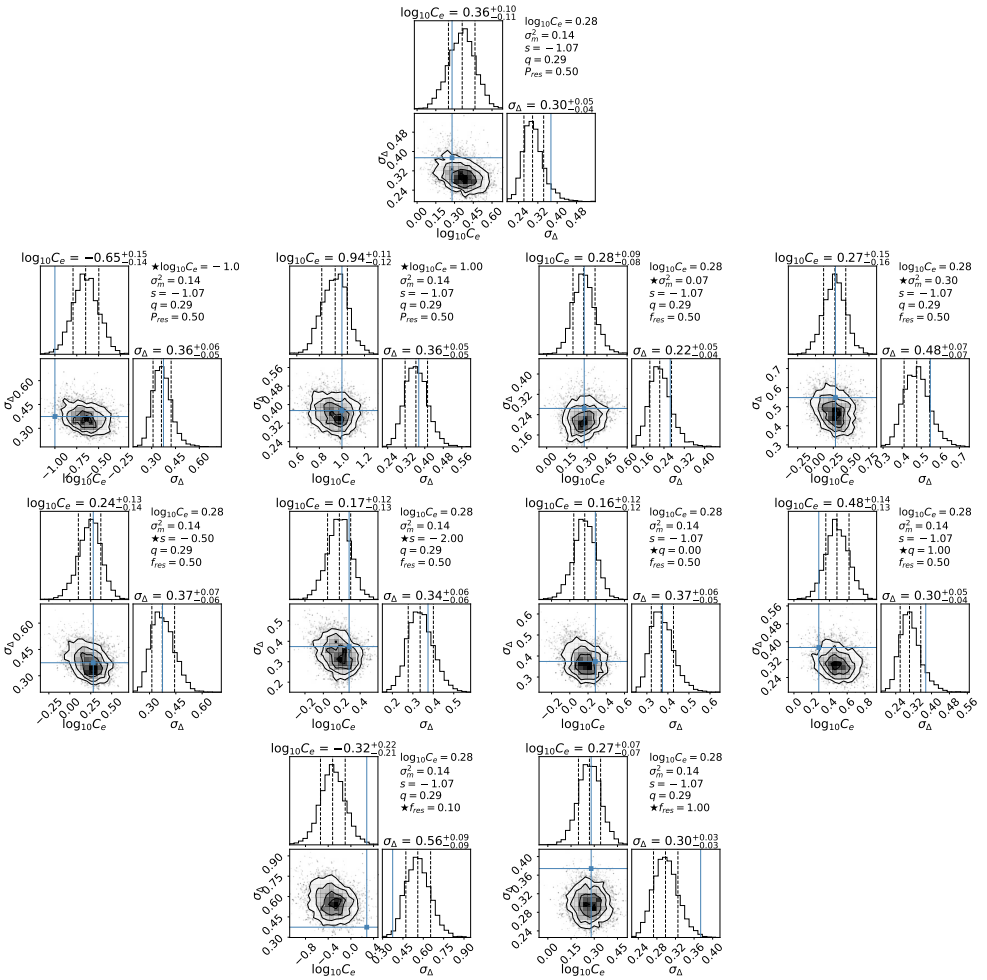


Figure 2.18. Examination of MCMC model performance, fixing the disc structure (the values of s and q). The top panel shows the fiducial model parameters. In each panel, all parameters used are labelled in the upper right corner. We then change every single parameter separately (labelled after ★) in each panel in the lower half of the figure. We change $\log_{10} C_e$ to -1, σ_m^2 to 0.07 and 0.3, s to -0.5 and -2, q to 0 and 1 and $f_{\rm res}$ to 10% and 100%. In each corner plot, blue lines show the true value of $\log_{10} C_e$ and $\sigma_{\rm m}$. The 1σ uncertainty is labelled on the top of each column and indicated by left and right dashed lines. The middle dashed lines indicate their median values.

the observed data, we have $f_{\rm res} \approx 0.5$ in most cases (Fig. 2.11 right panel). Therefore the MCMC results for the observed data are reliable.

3

The dynamics of the special resonance chain systems and their formation: TRAPPIST-1

TRAPPIST-1 is an 0.09 $M_\odot$ star, which harbours a system of seven Earth-sized planets. Two main features stand out: (i) all planets have similar radii, masses, and compositions; and (ii) all planets are in resonance. Previous works have outlined a pebble-driven formation scenario where planets of similar composition form sequentially at the H_2O snowline (~0.1 au for this low-mass star). It was hypothesized that the subsequent formation and migration led to the current resonant configuration. Here, we investigate whether the sequential planet formation model is indeed capable to produce the present-day resonant configuration, characterized by its two-body and three-body mean motion resonances structure. We carry out N-body simulations, accounting for type-I migration, stellar tidal damping, disc eccentricity-damping, and featuring a migration barrier located at the disc's inner edge. Due to the sequential migration, planets naturally form a chain of first-order resonances. But to explain the period ratios of the b/c/d-system, which are presently in higher-order resonances, we find that planets b and c must have marched across the migration barrier, into the gas-free cavity, before the disc has dispersed. We investigate both an early and late cavity infall scenario and find that the early infall model best matches the constraints, as well as being more probable. After the dispersal of the gaseous disc, stellar tidal torque also contributes towards a modest separation of the inner system. We outline how the insights obtained in this work can be applied to aid the understanding of other compact resonant planet systems.

S. Huang, C. W. Ormel★ (2022) The dynamics of the TRAPPIST-1 system in the context of its formation. MNRAS, 511, 3814

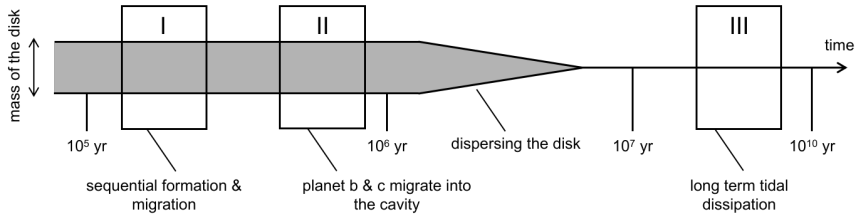


Figure 3.1. Schematic of the different stages in the dynamical evolution of the TRAPPIST-1 planet system. Time is oriented from left to right with the mass of the disc indicated by the vertical width of the line. Different boxes indicate different events (stages) that occur over specific time intervals. In the Early Cavity Infall model, Stage I and II are contemporaneous.

3.1 Introduction

TRAPPIST-1 is the first M8-dwarf star found to harbour seven transiting planets (Gillon et al. 2016, 2017). While the orbits are located within 0.1 au from the star in a compact (resonant) configuration, TRAPPIST-1's low luminosity renders planets d, e, and f to reside at equilibrium temperatures similar to Earth (Luger et al. 2017). Therefore, the system is at the forefronts of characterization efforts and habitability studies (Lincowski et al. 2018) and a prime target of the James Webb Space Telescope (Gillon et al. 2020; Meadows et al. 2021; Lim et al. 2021; Lin et al. 2021b). A particular intriguing question is whether planet systems like TRAPPIST-1 are common. Lying within the 1,000 closest stars from the Sun, it is natural to conjecture that planet systems like TRAPPIST-1 must be common in the galaxy. However, Sestovic & Demory (2020) and Sagear et al. (2020) argue that the seven planet TRAPPIST-1 discovery has been serendipitous, based on a study of over 500 low mass targets observed by the K2 spacecraft. Still, due to the challenging nature of detecting small planets around low-mass stars, the occurrence of TRAPPIST-1-like multi-planet systems is poorly constrained.

To characterize the planets of the TRAPPIST-1 system, Delrez et al. (2018) and Grimm et al. (2018) evaluate the planetary radii and masses via transit depths and Transit Timing Variation (TTV) from Spitzer data. Recently, Ducrot et al. (2020) present all transits records for TRAPPIST-1 from Spitzer. Agol et al. (2021) combine Spitzer observations (Delrez et al. 2018; Ducrot et al. 2020), ground-based observations (Gillon et al. 2016, 2017; Ducrot et al. 2018; Burdanov et al. 2019) and other space (K2 and HST) observations (Luger et al. 2017; Grimm et al. 2018), and refine the physical and dynamical properties of the TRAPPIST-1 planets. From these studies it follows that all seven planets in the TRAPPIST-1 system have roughly the same densities (Dorn et al. 2018; Agol et al. 2021), and similar low eccentricities ($e \lesssim 0.01$) and inclinations ($i \lesssim 0.01$) (Agol et al. 2021). The resonant configuration is one of the most astonishing features in the TRAPPIST-1 system. From inner-to-outer, the period ratio of every adjacent planet pair is near 8:5, 5:3, 3:2, 3:2, 4:3, 3:2. The observed near-integer period ratios likely reflect corresponding Mean Motion Resonances (MMRs). In addition, every adjacent planet triplet is connected by various three-body resonances (3BRs) (Luger et al. 2017).

The similarity among the TRAPPIST-1 planets may reflect a similar formation origin. Because of its compact nature, it is natural that the TRAPPIST-1 planets (or their building blocks) experienced significant radial migration. Planetesimals could originate within the snowline driven by the traffic jam effect of sublimated icy particles (Drążkowska et al. 2016; Ida & Guillot 2016; Schoonenberg et al. 2018). On the other hand, re-condensation from out-

ward diffusion of water vapour enhances the dust-to-gas ratio exterior the snowline, thus triggering streaming instability to form planetesimals (Schoonenberg & Ormel 2017; Ormel et al. 2017; Hyodo et al. 2019). In both scenarios, planets are formed at the same location, which explains the common composition. Population synthesis models – where planets are initialized at random locations – also claim to reproduce the TRAPPIST-1-like properties (Burn et al. 2021). After reaching a certain mass, planets migrate inwards, explaining the similar size of the planets, independent of whether growth is driven by planetesimal accretion or pebble accretion (Schoonenberg et al. 2019; Coleman et al. 2019; Burn et al. 2021; Zawadzki et al. 2021). An intriguing question is how much water these planets were born with and how much still remains. According to Agol et al. (2021) the present-day water mass fraction are much lower than prediction by Ormel et al. (2017) and Schoonenberg et al. (2019). However, ^{26}Al isotropic heating can desiccate terrestrial planets (Lichtenberg et al. 2019). In addition, Raymond et al. (2021) recently constrains that any water that (had been) present on the TRAPPIST-1 planets is likely to be accreted in the protoplanet disc phase.

Most of the above formation models did not address the dynamical evolution of the formed planets. In the TRAPPIST-1 system, 3BRs bind planets together to render the planets long-term dynamically stable (Tamayo et al. 2017). At the same time, Mah (2018) and Brasser et al. (2019) find that the libration centre of the 3BR angles may jump to different values after tens of thousand years. Until now, only several planetary systems are known to harbour 3BRs: GJ 876 (Rivera et al. 2010), Kepler-60 (Goździewski et al. 2016), Kepler-80 (Xie 2013; MacDonald et al. 2016, 2021), Kepler-223 (Mills et al. 2016), K2-138 (Christiansen et al. 2018; Lopez et al. 2019), HD-158259 (Hara et al. 2020), and TOI-178 (Leleu et al. 2021). Recently, one 3BR is confirmed in Kepler-221 (Goldberg & Batygin 2021) seven years after its discovery (Rowe et al. 2014). As hypothesized in this work, these resonances are fossils of the formation and evolution of planetary systems, which we can use to our advantage to reconstruct the planet formation history.

The convergent migration of planets in quasi-circular orbits generally results in first-order MMRs (Lee & Peale 2002; Correia et al. 2018). However, in the TRAPPIST-1 system, the innermost two planet pairs are near second or even third order MMRs. Conceivably, the innermost two planet pairs were near 3:2 MMR just after planet formation because it is the first order MMR closest to the current period ratio, whereafter the inner three planets separated from each other. Lin et al. (2021a) presented an analytical model in which Earth-mass planets in discs around low mass stars end up in first order MMRs chain. However, they did not investigate the deviation from first order MMRs for the inner three planets. Coleman et al. (2019), using a population synthesis approach where planets form at arbitrary locations, observe several cases that have separated inner planets after planet formation and disc dispersal. However, the corresponding 3BRs are inconsistent with the observation. It is likely that a more specific, subtle mechanism operated to shape the dynamical structure of the inner planets.

There are several ways to separate planets away from first-order MMR. In two-planets systems, divergent migration in the disc can drive planets away from MMRs, e.g., by magnetospheric rebound (Liu et al. 2017) or by adjusting the zero net torque location using a migration map approach (Wang et al. 2021b). In the absence of a gaseous disc, stellar tidal dissipation can reduce the eccentricities of planets, and divergently migrate planets away from exact MMR (Lithwick & Wu 2012; Batygin & Morbidelli 2013). In multi-planet systems connected by 3BR, divergent migration, as well as tidal dissipation, can separate planets with each other maintaining 3BR relationships (Charalambous et al. 2018; Papaloizou et al. 2018). In particular, Papaloizou et al. (2018) obtain the observed configuration of TRAPPIST-

1 planets purely using stellar tidal dissipation. However, their initial conditions arbitrarily lie close to the present state, raising the question of how their initial state did materialize. Teyssandier et al. (2021) find that the observed high order resonances can be reproduced only with a smooth inner disc edge, but even then it is a rare simulation outcome.

The goal of this paper is to connect the present long-term dynamical behaviour of the TRAPPIST-1 planets to their formation in the planet-forming disc. Our model consists of two steps. In the first step, a chain of first-order MMRs is set up in the proto-planet disc. Planets sequentially form and migrate inward one after the other. Migration ceases at the disc's inner edge. The second step involves the separation of the inner b/c/d subsystem until the observed period ratios are reached. For this stage, we distinghuish between late infall, where planets b and c fall in the cavity after the first step has completed, and early infall, in which planets b and c cross the disc edge upon their arrival. After the disc disappears, long-term tidal dissipation further expands the planet system modestly, helping to finally achieve the observed resonant configuration.

Using N-body simulations, we first examine several simple models that fail to establish a more separated inner subsystem. We conclude that planets b and c had to migrate interior to the disc truncation radius, which allowed them to separate already during the disc phase. Finally, accounting for long-term stellar tidal damping, we manage to reproduce the dynamical configuration of TRAPPIST-1 planets including their period ratios, eccentricities, and 3BRs.

This paper is structured as follows. In Sect. 3.2, we describe the terminologies and our physical method. We then present the results from simple models and assess the conditions for meeting Objective I in Sect. 3.3. Turning to Objective II, we carry out a parameter study to search for the conditions that can successfully reproduce our objectives (in Sect. 3.4). We then examine the Early Infall model in Sect. 3.5. Analytical support for our findings is given in Sect. 3.6. Finally, we assess our models and the significance of our findings in Sect. 3.7 and conclude in Sect. 3.8.

3.2 Model

3.2.1 Preliminaries and Terminology

Simulation stages

We conduct N-body simulations to integrate the planets equation of motion. In this work we follow the dynamical evolution of planets in three stages as shown in Fig. 3.1:

(I) the stage after their formation, where planets migrates inwards in the gas disc and end up in a chain of first-order resonances;

(II) the stage where planets b and c enter the gas-free cavity;

(III) the post-disc stage where stellar tides operate on ~Gyr time-scales.

A key simplification is to simulate each of these phases separately, instead of running one simulation that contains all these stages. Not every model contains each of these three stages. Usually Stage I, II and III occur in chronological order, but in the Early Infall model in Sect. 3.5, Stage I and Stage II happen simultanously.

Table 3.1. Radii, masses, semi-major axes and eccentricities of the TRAPPIST-1 planets. The values listed in the first three rows are used in the simulations. We compare the eccentricities in our simulation results to the eccentricities listed here from Agol et al. (2021). We also list the observed value of the 3BR angles in the TRAPPIST-1 system (Luger et al. 2017).

Planet:	b	c	d	e	f	g	h
$R[R_\oplus]$	1.116	1.097	0.788	0.920	1.045	1.129	0.755
$M[M_\oplus]$	1.374	1.308	0.388	0.692	1.039	1.321	0.326
$a[10^{-2}\,\mathrm{au}]$	1.154	1.580	2.227	2.925	3.849	4.683	6.189
e	0.004±0.003[a]	0.002±0.003	0.006±0.002	0.0065±0.0015	0.009±0.0015	0.004±0.0015	0.0035±0.0015
3BR		$\Phi^{2,5,3}_{\mathrm{b,c,d}} \approx 177^\circ$	$\Phi^{1,3,2}_{\mathrm{c,d,e}} \approx 49^\circ$	$\Phi^{2,5,3}_{\mathrm{d,e,f}} \approx -148^\circ$	$\Phi^{1,3,2}_{\mathrm{e,f,g}} \approx -76^\circ$	$\Phi^{1,2,1}_{\mathrm{f,g,h}} \approx 177^\circ$	

[a] The error bars are estimated from Fig. 21 in Agol et al. (2021).

Table 3.2. Definition of quantities, symbols and units. The last five parameters separated by horizontal line are the free parameters of the simulations.

	Description	Value	Reference
h	aspect ratio	0.03	Sect. 3.2.3
$\dot{M}_{\rm g}$	star accretion rate	$10^{-10} M_\odot {\rm yr}^{-1}$	Sect. 3.2.3
$M_\star$	stellar mass	$0.09 M_\odot$	Sect. 3.2.3
γ_I	in type-I migration rate	2	Eqs. (3.6,3.8)
$\tau_{\rm d}$	disc dissipation time-scale	10^5 yr	Sect. 3.2.2
Δ	migration threshold width	$2hr_{\rm c}$	Eqs. (3.9,3.11)
$Q_{\rm sim}$	tidal dissipation parameter	100(0.1 in Stage III)	Eq. (3.13)
$\tau_{a,\oplus}$	nominal semi-major axis damping timescale	$[1-40\,{\rm kyr}]$	Eq. (3.8)
C_e	eccentricity-damping prefactor	$[0.1-1]$	Eq. (3.7)
$r_{\rm c}$	truncation radius	$[0.013-0.030\,{\rm au}]$	Eqs. (3.9,3.11)
A_a	migration threshold height	50, 100, 150	Eq. (3.9)
A_e	enhancement of disc eccentricity-damping	$[1-40]$	Eq. (3.11)

Parameters

All masses, semi-major axes and radii of the TRAPPIST-1 planets are adopted from Agol et al. (2021) and are listed in Table 3.1. The values of the default parameters and the range of free parameters appearing in the equations of this paper are listed in Table 3.2.

Resonance angles

For two planets i and $i+1$, a two-body $j-o_i{:}j$ MMR angle can be defined

$$\phi_{i,i+1;i+X} = (j-o_i)\lambda_i - j\lambda_{i+1} + o_i\varpi_{i+X} \tag{3.1}$$

where o_i is the order of the resonance, λ_i and λ_{i+1} are the mean longitudes of planets i and $i+1$, and ϖ_{i+X} is either the longitude of periapsis of planet i ($X=0$) or $i+1$ ($X=1$). A similar MMR angle can be defined for the $(k-o_{i+1}){:}k$ MMR of planets $i+1$ and $i+2$. Then we can define the 3BR angle such that it does not involve the longitudes of pericentre:

$$\Phi^{p,p+q,q}_{i,i+1,i+2} = p\lambda_i - (p+q)\lambda_{i+1} + q\lambda_{i+2} \tag{3.2}$$

where $p = o_{i+1}(j-o_i)$ and $q = o_i k$. Observationally, it is hard to constrain the longitudes of pericentre when, as is typical, the eccentricity is low. The three-body angles can however be constrained more easily. TRAPPIST-1's c/d/e planets are currently near 3:5 and 2:3 MMRs, corresponding to $p=3$ and $q=6$, and the 3BR angle $\Phi^{3,9,6}_{\rm c,d,e} = 3\Phi^{1,3,2}_{\rm c,d,e}$. We list the five main 3BR angles of the TRAPPIST-1 system in Table 3.1.

3.2.2 Numerical integration

Every planet obeys the equation of motion which includes the two body forces from the star and other planets, the angular momentum loss and orbital circularization induced by the gas disc and damping from tides with the star:

$$\boldsymbol{F}_{\rm i} = \sum_{j\neq i}^{N} \frac{Gm_j}{\left|\boldsymbol{r}_{ji}\right|^3}\boldsymbol{r}_{\rm ji} + \boldsymbol{F}_{{\rm disc},i} + \boldsymbol{F}_{{\rm star},i}. \tag{3.3}$$

In Eq. (3.3) the first term on the right-hand side is the standard gravitational interaction N-body force, where $\boldsymbol{r}_{ji} = \boldsymbol{r}_j - \boldsymbol{r}_i$ and the index j represent the planets other than planet i. The term $\boldsymbol{F}_{\mathrm{disc},i}$ indicates the gas disc tidal force and $\boldsymbol{F}_{\mathrm{star},i}$ indicates the stellar tidal damping force acting on planet i.

Simulations were conducted using the `WHFast` integration method in REBOUND (Rein & Liu 2012) and our additional forces were implemented via REBOUNDx (Tamayo et al. 2020). In Eq. (3.3), only the $\boldsymbol{F}_{\mathrm{disc}}$ term is proportional to the disc gas density. During the disc dispersing, we add an exponential decay factor $\exp[-(t-t_0)/\tau_{\mathrm{d}}]$ to $\boldsymbol{F}_{\mathrm{disc}}$. In addition, the disc dispersal time-scale τ_{d} is taken to be 10^5 years. We ignore the disc torque term in the post-disc environment of stage III. The time-step during the simulations is less than 5% of the orbital period of the innermost planet.

3.2.3 Planet-disc interaction

The planet-disc interaction can cause planet migration (Goldreich & Tremaine 1980; Ward 1997) and eccentricity-damping (Ward 1988; Artymowicz 1993; Tanaka & Ward 2004). Following Papaloizou & Larwood (2000) we write the disc tidal force as:

$$\boldsymbol{F}_{\mathrm{disc},i} = -\frac{\boldsymbol{v}_{\mathrm{i}}}{2\tau_{\mathrm{a},i}} - \frac{2(\boldsymbol{v}_{\mathrm{i}} \cdot \boldsymbol{r}_{\mathrm{i}})\boldsymbol{r}_{\mathrm{i}}}{|r_i|^2\, \tau^{\mathrm{d}}_{\mathrm{e},i}} \tag{3.4}$$

where $\tau_{\mathrm{a},i}$ and $\tau^{\mathrm{d}}_{\mathrm{e},i}$ indicate the semi-major axis and eccentricity-damping time-scales of planet i due to migration.

We assume the gas disc is truncated at a radius r_{c} by the magnetic field from the star (Pringle & Rees 1972; D'Angelo & Spruit 2010). We assume the inner disc is viscously relaxed (Shakura & Sunyaev 1973; Lynden-Bell & Pringle 1974) within the snowline $r_{\mathrm{ice}} \sim 0.1\,\mathrm{au}$ (Schoonenberg et al. 2019; Lin et al. 2021a), implying constant $\dot{M}_g = 3\pi\nu\Sigma$ where ν is the viscosity and $\dot{M}_g$ is taken to be $10^{-10} M_\odot \mathrm{yr}^{-1}$ (Manara et al. 2015). The aspect ratio is fixed at $h = 0.03$ following Ormel et al. (2017), whose value is motivated by viscous heating and lamp-post heating (Rafikov & De Colle 2006) and the spectral energy distribution fitting (Mulders & Dominik 2012). In an alpha-disc model, $\nu = \alpha h^2 \Omega r^2$ with constant α parameter (Shakura & Sunyaev 1973), the disc surface density is therefore:

$$\Sigma_{\mathrm{g}} = \Sigma_0 \left(\frac{r}{r_0}\right)^{-0.5} \tag{3.5}$$

where Σ_0 is the disc surface density at distance r_0 ($< r_{\mathrm{ice}}$). Planets' semi-major axes and eccentricities are damped on time-scales:

$$\tau_{\mathrm{a},i} = \frac{h^2/f_{\mathrm{a}}}{2\gamma_I q_i q_{\mathrm{gas}} \Omega_{\mathrm{K}}} = \tau_{\mathrm{a},\oplus} \left(\frac{q_i}{q_\oplus}\right)^{-1} \left(\frac{1}{f_{\mathrm{a}}}\right) \tag{3.6}$$

$$\tau_{\mathrm{e},i} = C_e h^2 \tau_{\mathrm{a},i} \frac{f_{\mathrm{a}}}{f_{\mathrm{e}}}, \tag{3.7}$$

where γ_I is the prefactor in the type I migration torque expression and $q_i = m_i/M_\star$ (Tanaka et al. 2002; Kley & Nelson 2012). The semi-major axis damping time-scale is half of the angular momentum damping time-scale (Teyssandier & Terquem 2014). $\tau_{\mathrm{a},\oplus}$ is the nominal Type I semi-major axis damping time-scale:

$$\tau_{\mathrm{a},\oplus} = \frac{h^2}{2\gamma_I q_\oplus q_{\mathrm{gas}} \Omega_{\mathrm{K}}} = 1.2 \times 10^4 \left(\frac{\gamma_I}{2}\right)^{-1} \left(\frac{\dot{M}_g}{10^{-10} M_\odot \mathrm{yr}^{-1}}\right) \left(\frac{\alpha}{10^{-3}}\right) \mathrm{yr}, \tag{3.8}$$

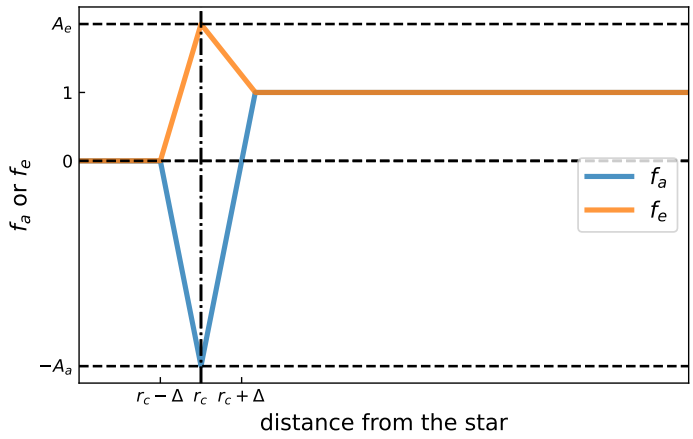


Figure 3.2. Sketch of $f_{\rm a}$ and $f_{\rm e}$. The x-axis denotes the distance measured from $r_{\rm c}$, the y-axis the value of $f_{\rm a}$ or $f_{\rm e}$. The horizontal black-dashed lines indicate A_a and A_e. The vertical dashed dotted line represents the location of $r_{\rm c}$.

where $q_\oplus$ stand for the mass ratio of an Earth mass planet over the stellar mass and $q_{\rm gas} = \Sigma_{\rm g} r^2/M_\star$. Therefore $\tau_{a,\oplus}$ and C_e are the parameters that control the damping of the planets in the N-body simulations.

In Eq. (3.7), C_e expresses the rate of eccentricity-damping mechanism over semi-major axis damping. In the linear theory its value is 1.28 (Tanaka & Ward 2004), which is consistent with the 3D hydro-dynamical simulations (Cresswell & Nelson 2008). However, Cresswell & Nelson (2006) suggest that $C_e \sim 0.1$ is sometimes needed to fit their hydro-dynamical simulations while generally this parameter encapsulates the uncertainty in (and variety of) disc migration mechanisms, which amount to considerable uncertainty in the type-I migration prefactor γ_I (Paardekooper et al. 2011; Baruteau et al. 2014; Benítez-Llambay et al. 2015; McNally et al. 2017). When the disc surface density gradient ($-{\rm d}\ln\Sigma_g/{\rm d}\ln r$) and temperature gradient ($-{\rm d}\ln T/{\rm d}\ln r$) become small, Type I migration slows down (γ_I decreases) and C_e goes down. In this study we take an agnostic view and examine C_e values in the range of 0.05 to 1.

The parameters $f_{\rm a}$ and $f_{\rm e}$ determine the behaviour of semi-major axis and eccentricity-damping near the disc inner edge. When the location of one planet $r \gg r_{\rm c}$, $f_{\rm a} = 1$. If the planet reaches the disc's inner edge, only Lindblad torques from the exterior disc remain. Similarly, only the upper horseshoe motion and associated co-orbital torque is present. In other words, the torques have become one-sided. For low-mass planets, the (positive) one-sided co-rotation torque will win out over the (negative) Lindblad torques, halting migration (Lin & Papaloizou 1979, 1993; Paardekooper & Papaloizou 2009; Liu et al. 2017). Therefore, $f_{\rm a}$ must change sign (become negative) at the disc's inner edge. We adopt an expression for $f_{\rm a}$ in Eq. (3.6) as:

$$f_{\rm a} = \begin{cases} 0 & (r < r_{\rm c} - \Delta) \\ A_a \frac{r_{\rm c}-\Delta-r}{\Delta} & (r_{\rm c} - \Delta < r < r_{\rm c}) \\ A_a \frac{r-r_{\rm c}-\Delta}{\Delta} & (r_{\rm c} < r < r_{\rm c} + \Delta + 1/A_a) \\ 1 & (r > r_{\rm c} + \Delta + 1/A_a) \end{cases} \tag{3.9}$$

where Δ and A_a determine the width and strength of the trap. If sharply truncated at the disc's inner edge, Δ is comparable to the half-width of the horseshoe region so $\Delta \sim H_{\rm c}$. For

Table 3.3. Summary of our model designs.

Model suite	Properties [a]			Stages included[b]			Objective[c]		Assessment
	r_c [au]	Formation imprint	Disc repulsion	I	II	III	I	II	
bC	0.013	-	N	✓	×	✓	×	×	cannot achieve all first order resonances
bCcgI	0.013	c & g	N	✓	×	✓	✓	×	period ratio outer planets expand too much
dCcgI	0.023	c & g	N	✓	✓	✓	✓	×	stellar tidal force alone cannot break 3BR of planet c
dCcgIcT	0.023	c & g	Y	✓	✓	✓	✓	✓	success with inward torque on c and high e-damping on d
dCcgIcL	0.023	c & g	Y	✓	✓	✓	✓	✓	success with early infall of b and c in cavity; more likely

[a] Listed are the cavity radius (location of disc inner edge) r_c, which planets are considered as the planet formation imprint, and the presence of disc repulsion on planets in the cavity.
[b] Stages with ✓ are included in a model while ones with × are excluded. Different stages are introduced in Fig. 3.1.
[c] The model that meets the objective is marked by ✓, if not we place × instead. The two objectives are introduced at the beginning of Sect. 3.3.

simplicity, we take $\Delta = 2H_c$, where H_c is the scale height of gas disc at truncation radius. According to Liu et al. (2017), A_a follows as the ratio of the (positive) one-side corotation torque (eq. 11 in Liu et al. 2017) over the Type I migration torque (two times the reciprocal of Eq. (3.6) times angular momentum)

$$A_a = \frac{\Gamma_{c,1s}}{\Gamma_I} = \frac{C_{hs}}{\gamma_I h}\left(\frac{q_p}{h^3}\right)^{-1/2} = \frac{135}{\gamma_I}\left(\frac{q_p}{10^{-5}}\right)^{-1/2}\left(\frac{h}{0.03}\right)^{1/2} \tag{3.10}$$

where $C_{hs} = 2.46$. For a planet-to-star mass ratio of $q = 10^{-5}$ and $h = 0.03$ this gives $A_a = 68$. Therefore we take A_a around this value. Equation (3.9) is similar in shape to the "deep drop" model Ataiee & Kley (2021) adopt in their N-body simulations.

In our simulations, we find that it is sometimes advantageous to enhance the eccentricity damping of planets at the disc edge ($f_e > 1$). Eccentricity damping of planets could be more efficient near the disc's inner edge for the following reasons:

- Material may pile up significantly near r_c if r_c is larger than the corotation radius of the star (D'Angelo & Spruit 2010);
- The absence of inner Lindblad resonances (they lie in the cavity), which would excite planets' eccentricity (Ward 1988);
- hydro-dynamical simulation indicate that eccentrities for planets at the disc inner edge are more strongly damped (see Fig.15 of Ataiee & Kley 2021).

Therefore we express f_e in Eq. (3.4) with a similar expression as f_a:

$$f_e = \begin{cases} 0 & (r < r_c - \Delta) \\ A_e \frac{r - r_c + \Delta}{\Delta} & (r_c - \Delta < r < r_c) \\ (A_e - 1)\frac{r_c + \Delta + 1/A_a - r}{\Delta + 1/A_a} + 1 & (r_c < r < r_c + \Delta + 1/A_a) \\ 1 & (r > r_c + \Delta + 1/A_a) \end{cases} \tag{3.11}$$

where A_e is the enhancement of the eccentricity-damping near the truncation radius. Not every simulations feature this anomalous eccentricity damping at the disc edge.

We plot f_a and f_e in Fig. 3.2. Near the truncation radius, f_a decreases sharply and becomes negative, thus pushing planets in this region outward. The outward torque peaks at r_c. Within r_c, the outward migration torque decreases to zero because there is no gas in the disc cavity (See Sect. 3.5.1, however, for the effects of a distant disc torque on planets inside the cavity).

3.2.4 Tidal dissipation

For a compact planet system in which planets are close to their host star, such as in TRAPPIST-1, tidal dissipation can be significant. The stellar tidal damping force term in Eq. (3.3) is:

$$\boldsymbol{F}_{\mathrm{star},i} = -\frac{2(\boldsymbol{v}_i \cdot \boldsymbol{r}_i)\boldsymbol{r}_i}{|r_i|^2 \tau^s_{e,i}}, \tag{3.12}$$

where $\tau^s_{e,i}$ refers to the eccentricity-damping time-scale induced by tidal interaction with the host star:

$$\tau^s_{e,i} = 7.6 \times 10^5 Q_{\mathrm{sim}} \left(\frac{m_i}{m_\oplus}\right)\left(\frac{M_\odot}{M_\star}\right)^{1.5}\left(\frac{R_\oplus}{R_i}\right)^5\left(\frac{a_i}{0.05\,\mathrm{au}}\right)^{6.5}\ \mathrm{yr}, \tag{3.13}$$

where $Q_{\rm sim} = 3Q/(2k_2)$, Q is the tidal dissipation function and k_2 is the Love number (Goldreich & Soter 1966; Papaloizou et al. 2018). For solar system planets in the terrestrial mass range, $Q_{\rm sim}$ is estimated between 50–2500. In this paper we take $Q_{\rm sim} = 100$ in most cases, similar to the terrestrial planets in our solar system. In Stage III, following Papaloizou et al. (2018), we take $Q_{\rm sim} = 0.1$ to accelerate the simulation by a factor 1,000.

3.3 Preliminary simulations

In this section, we summarize our model design and the principal outcomes. This work concentrates on the dynamic evolution after the planet formation process. We insert planets sequentially at the beginning of the simulation with fixed masses following Table 3.1. Ormel et al. (2017), Schoonenberg et al. (2019) and Lin et al. (2021a) hypothesize that the TRAPPIST-1 planets are formed at the snowline (≈0.1 au) and quickly accreted material, while Coleman et al. (2019) and Burn et al. (2021) initialize many planetary embryos in the disc to grow them to TRAPPIST-1 planets. In the context of this work planets could also have formed further out; but we simply fix the mass of every planets during the simulation.

Due to type I migration (Tanaka et al. 2002), planets migrate towards the host star when they grow massive enough and stop at the disc truncation radius. The migration speed is so fast that planets tend to be trapped in first order MMR while avoiding the higher-order MMR. Therefore, we initialize every new planet just beyond the 2:1 MMR location of the outermost planet by default. Still, by virtue of the short formation time (Lin et al. 2021a) planets may be born near 3:2 and 4:3 period ratios with the inner planet. Therefore, it is possible that planets are born at locations within the 3:2 MMR. We investigate whether this imprint of planet formation is needed to reproduce the orbital configuration.

Therefore, our first step is to park all planets in a chain of first order MMR, i.e., 3:2, 3:2, 3:2, 3:2, 4:3, 3:2 (hereafter referred to as Objective I). However, this contrasts the present-day dynamical state where the period ratio of planets c/b and d/c are 8/5 and 5/3, respectively, i.e., close to higher-order MMRs. Our second step is to evolve the first order MMR chain to the 8:5, 5:3, 3:2, 3:2, 4:3, 3:2 period ratios chain (hereafter Objective II). We separate the simulation into three stages as introduced in Fig. 3.1.

The set of our models is listed in Table 3.3. Different columns express model characteristics. In bC model, we set the cavity radius at $r_{\rm c} = 0.013$ au, which coincides with the observed location of planet b. In the bCcgI model, we insert planet g interior to the 3:2 MMR location. In the dCcgI model, we set $r_{\rm c} = 0.023$ au, which coincides with the observed location of planet d, and insert planet g interior to 3:2. In the dCcgIcT model, we additionally switch on the one-sided repulsive torque from the gas disc on planet c in the cavity, while in dCcgIcL we use a particular choice for this repulsive force. The first three models will be discussed in this section. Model dCcgIcT and dCcgIcL will be discussed in Sect. 3.4 and Sect. 3.5, respectively.

3.3.1 Planet b at the cavity edge (bC)

Objective I – the parking of planets in a chain of first order MMRs close to the observed period ratios – can most straightforwardly be achieved by the planet's sequential migration and pileup near r_c. Therefore, we let $r_{\rm c}$ coincide with the location of planet b. We vary $\tau_{\rm a,\oplus}$ and C_e, and run a set of Stage I simulations; A_e is taken to be unity. In the simulations, we insert a new planet every ∼10 kyr (long enough for the inner planets to stabilize). For

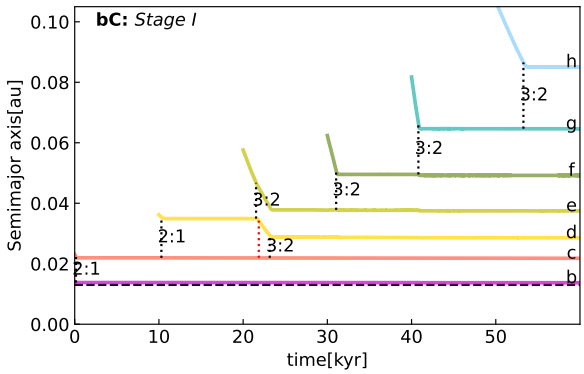


Figure 3.3. One-by-one migration of the TRAPPIST-1 planets after their sequential formation in the proto-planetary disc for a nominal migration time of $\tau_{a,\oplus} = 5 \times 10^3$ yr and $C_e = 0.1$. The eccentricity enhancement at the disc inner edge is $A_e = 1$. Solid lines with different colours indicate the semi-major axes of different planets. The horizontal black dashed line indicates the position of the migration barrier r_c. Vertical black and red dashed segments between every two planets trajectories indicate the moment planets converge to and depart from 2:1 and 3:2 period ratios.

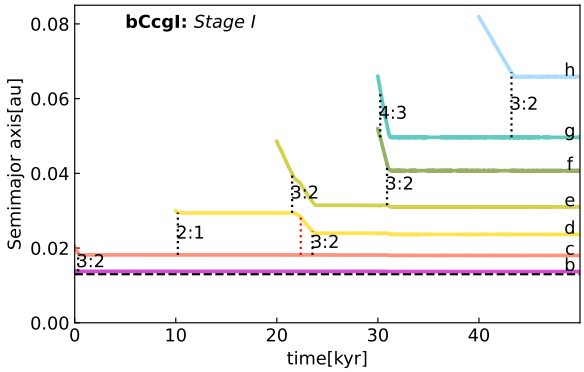


Figure 3.4. Similar to Fig. 3.3, but with planet c starting out inside the 2:1 period ratio and planet g initially inside the 3:2 period ratio. We take $\tau_{a,\oplus} = 5 \times 10^3$ yr, $C_e = 0.1$ and $A_e = 1$.

simplicity, We initialize planet b near r_c, and then the other planets outside the 2:1 period ratio.

One of our typical outcomes is shown in Fig. 3.3. We adopt $\tau_{a,\oplus} = 5 \times 10^3$ yr and $C_e = 0.1$. Planet c gets trapped by the 2:1 MMR with planet b. Similarly, planet d gets trapped by the 2:1 MMR with planet c. Planet e directly crosses the 2:1 MMR because planets d & e are less massive and further from the star than planet b, c, and d. Therefore, the Type-I migration can overcome the resonant repulsion and it gets trapped by the 3:2 MMR with planet d. At the same time, planet d crosses the 2:1 MMR because of the pushing from resonant interaction with planet e. Afterwards, the later planets are trapped by the 3:2 MMR with their former peers. The truncation radius acts to prevent planets migrating into the cavity. At the end of this simulation, the period ratios of every two adjacent planets are about 3:2, except planets b & c, which is about 2:1. However, Objective I requires planets b & c to park in 3:2 and planets f & g in 4:3.

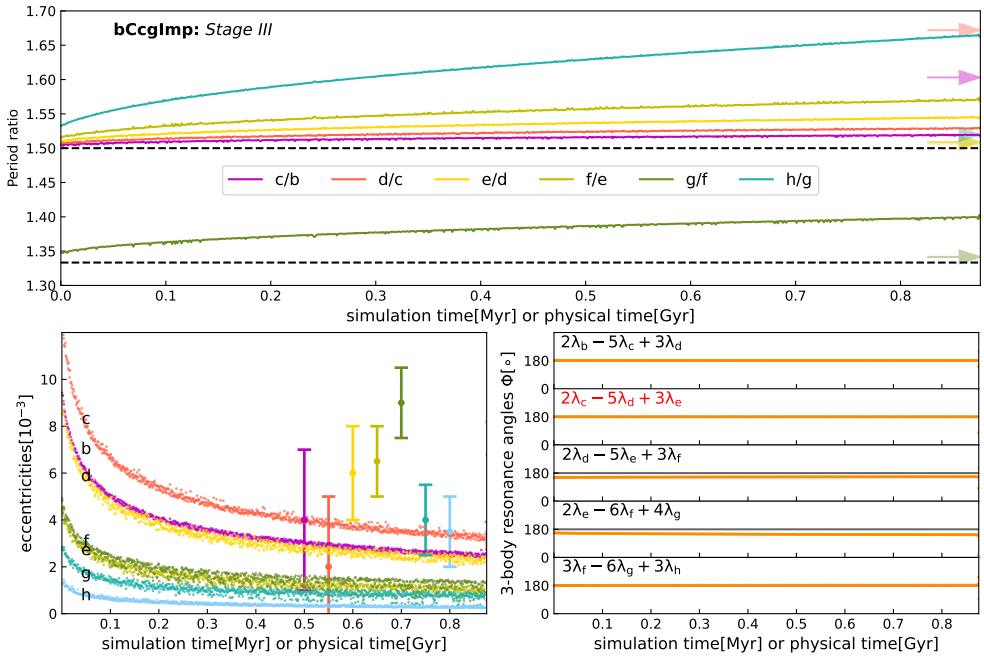


Figure 3.5. Period ratios (top panel), eccentricities (bottom-left panel) and 3BR angles (bottom-right panel) during tidal dissipation (with $Q_{\rm sim} = 0.1$). In the period ratios plot, dashed lines indicate the 3:2 and 4:3 period ratios. Arrows indicate the observed value of the period ratios. In the eccentricity plot, we label the name of each planets on the left and indicate the present-day eccentricities by error bars with different colours (the x-coordinate of the error bars does not have meaning). In the 3BR angles plots, we label the expression of each angle on the upper left of each panel. The angle labelled in red does not librate at present.

Naively, closer-spaced MMR can be obtained with a faster migration rate (lower $\tau_{a,\oplus}$). However, if we take $\tau_{a,\oplus} < 5{\times}10^3$ yr to migrate planets more rapidly, it results in the breaking of the 3:2 MMR of planet d & e. Therefore, the value of the nominal migration time-scale $\tau_{a,\oplus}$ must exceed 5×10^3 yr when the cavity radius is fixed at $r_c = 0.013$ au. Consequently, either b/c and f/g end up in too wide MMR or d/e ends up in a too close MMR, thus failing to accomplish Objective I.

3.3.2 Formation imprints for planet c and g (bCcgI)

Instead of accelerating planet migration, the closer MMR of planet b & c and planet f & g can be obtained by reducing the time/space span between their formation – a condition that we refer to an imprint of planet formation. In the bCcgI model, the parameters in the simulation are the same as in the bC model. We make the additional assumption that planets c and g are born within 2:1 and 3:2 period ratios in Stage I. One of our typical outcomes is shown in Fig. 3.4. Planet c gets trapped in the 3:2 MMR with planet b from the outset. Because planets f & g are inserted simultaneously and more massive planet migrate faster Eq. (3.6), planet g catches up with planet f and gets trapped in the 4:3 MMR. At the end of this simulation, the period ratios of every adjacent two planets are in 3:2 except planet f & g (4:3), fulfilling the requirement of Objective I.

Objective II is to separate the b/c/d subsystem from the 3:2 and 3:2 period ratios to 8:5 and 5:3 period ratios. As a first attempt, we disperse the disc to see if we are able to evolve the planet system naturally. During disc dispersal, the semi-major axis damping and eccentricity-damping forces decrease along with the profile of the disc exponentially on a time-scale $\tau_{\rm d} = 10^5$ yr. After $20\tau_{\rm d}$ we run the post-disc simulation (Stage III) where only the stellar tidal force operates on the planets.

Figure 3.5 shows the post-disc simulation. The eccentricities of the planets decrease with time because of tidal dissipation during the simulation, while the 3BR angles keep librating around values near π. The libration centres of the 3BR phase angles of the last adjacent planet triplets lie around 150° due to the perturbation from non-adjacent resonances (Siegel & Fabrycky 2021). Due to tidal dissipation, the gravitational potential energy of this system is decreasing while angular momentum is conserved. Therefore, angular momentum transfers outwards, from inner planets to outer planets and the period ratios of every adjacent planet pair increase together (Batygin & Morbidelli 2013; Papaloizou et al. 2018; Goldberg & Batygin 2021).

However, the simulation does not result in the observed TRAPPIST-1 planetary orbital configuration. The 3BRs that connect the planets are inconsistent with the observation, i.e., the angle $\Phi^{2,5,3}_{\rm c,d,e}$ (see the notation in Sect. 3.2) does not librate in the observation. Stellar tides increase the period ratios especially those of the outer planet pairs. Additionally, this simulation outcome results in eccentricities of planet b & c too high compared to the other planets, which is inconsistent with TTV analysis (Agol et al. 2021).

To sum up, bCcgI model succeeds in Objective I but fails in Objective II. Rather than separating the entire planet system, only the separation of the b/c/d subsystem after Stage I is required. Specifically, this requires that $\Phi^{2,5,3}_{\rm c,d,e}$ needs to be broken before the disc disappears because stellar tidal torques alone cannot. Since disc migration alone rarely reproduces the resonant chain in the TRAPPIST-1 system (Teyssandier et al. 2021), there must be special events that drive the expansion of the b/c/d subsystem before disc dispersal.

3.3.3 Planet d at the cavity edge (dCcgI)

Ormel et al. (2017) discussed one scenario to decouple the innermost two planets with the disc as the disc truncation radius moves outward due to magnetospheric rebound (Liu et al. 2017), allowing the 3:2 MMR of the inner two planet pairs to break. Here, we aim to obtain the same result by migrating planet b & c across the cavity radius during disc dispersal, motivated by that planet b and c are three times more massive than planet d (Table 3.1), therefore are easier to open a gap in the disc. Then, stellar tides might increase the period ratios of c/b and d/c Papaloizou et al. (2018). Therefore, $r_{\rm c}$ is set to be 0.023 au, coinciding with the observed location of planet d.

One of our typical results for Stage I is shown in Fig. 3.6. Similar to bCcgI model in Fig. 3.4, all seven planets park themselves at the desired first order MMRs. To obtain the configuration that planets b and c are in the cavity while the outer planets are in the disc, we switch off the disc torque term (in Eq. (3.3)) on the planet at the disc inner edge, ignoring for simplicity the details of how the disc profile evolves (Stage II). Figure 3.7 shows the simulation results for Stage II. At the beginning of this simulation, all planets are beyond the truncation radius $r_{\rm c}$. After first switching off the disc torque on planet b, the outer planets push planet b further into the cavity until planet c has reached the cavity radius. Because its mass is small, planet h migrates slowest and is left behind the other planets. Therefore, the period ratio of planet h/g increases until the migration of planet g is stopped by the resonant interaction

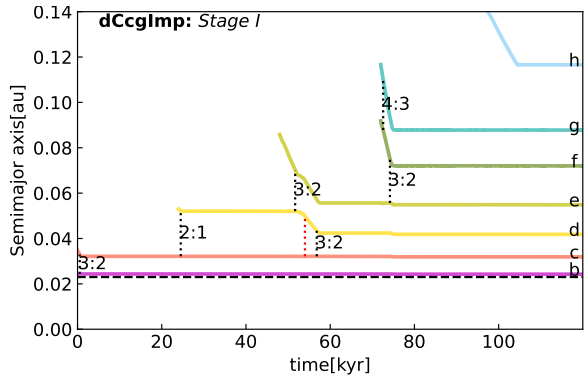


Figure 3.6. Similar to Fig. 3.4, but with $r_c = 0.023$ au. We take $\tau_{a,\oplus} = 1.4 \times 10^4$ yr, $C_e = 0.1$ and $A_e = 1$.

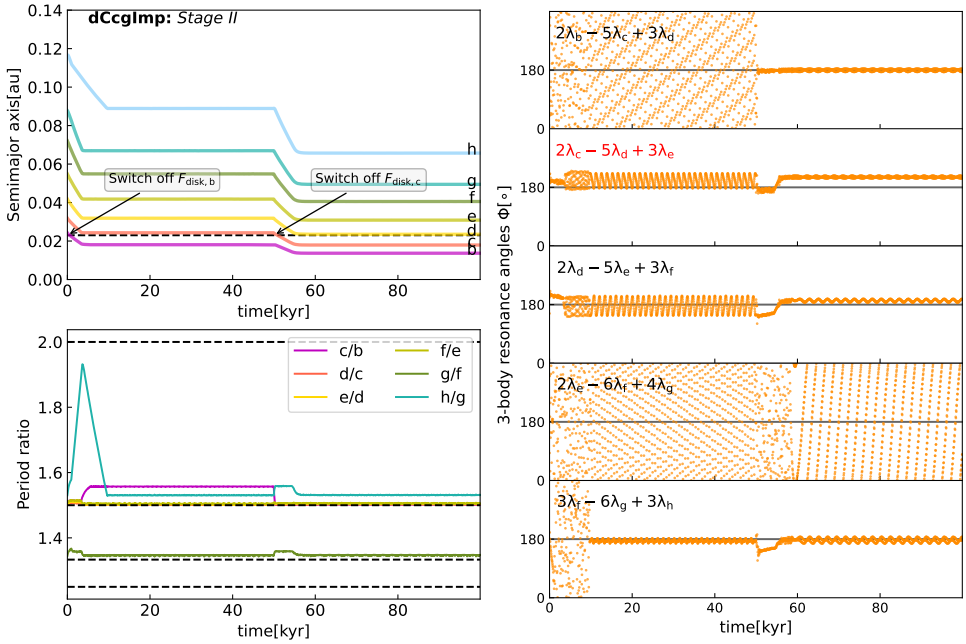


Figure 3.7. Stage II of model dCcgI. In the semi-major axis plot, arrows refer to the time that we switch off the disc force on the corresponding planet. In the 3BR angle plots, we label the expression of each angle in the upper left of each panel. The label in red means that the 3-body angle does not presently librate.

with the other planets in the disc. Then planet h catches up with its inner planets and the 3:2 MMR reforms. Meanwhile, stellar tides separate planet b in the cavity from exact 3:2 resonance and the period ratio of planet c/b increases to ≈1.56. Next, we switch off the disc torque on planet c, after which, the period ratio of planet h/g does not increase so much and the 3-body resonance angle $\Phi^{3,6,3}_{f,g,h} = 3\lambda_f - 6\lambda_g + 3\lambda_h$ librates.

However, after planet d stops migrating at the truncation radius, stellar tides are unable to sufficiently expand the b/c/d subsystem, i.e. to increase the period ratios of planet c/b and d/c to their observed values. As can be seen from Fig. 3.7, the 3BR angle $\Phi^{2,5,3}_{c,d,e} = 2\lambda_c -$

$5\lambda_d + 3\lambda_e$ still librates, preventing planet c from moving further inward. Therefore, we need an additional mechanisms to break the 3BRs, specifically $\Phi_{c,d,e}$, such that the planet b/c/d subsystem is allowed to expand until the observed period ratios (Objective II). This breaking of the 3-body resonance must occur before the disc disappears as otherwise *all* planets would undergo separation by stellar tides, similar to what is going on in Fig. 3.5. Therefore, a more sophisticated model is required to expand the b/c/d subsystem.

3.3.4 Parameter variation for Objective I (dCcgI)

To assess the likelihood of fulfilling Objective I, we conduct a sensitivity study of the model parameters during Stage I of the dCcgI model, assuming planets all start migrating outside the 2:1 MMRs of their inner planets, except for planet g, which starts just inside 3:2. The goal is to investigate whether (and which) additional planets feature such formation imprints, i.e., whether it is necessary to initialize planets inside 3:2 MMR or 2:1 MMR.

We run a set of Stage I simulations, varying three parameters: the migration time-scale $\tau_{a,\oplus}$, the eccentricity-damping prefactor C_e and the eccentricity-damping enhancement at the truncation radius A_e. The parameter C_e is taken in the range of [0.1, 1], $\tau_{a,\oplus}$ in the range of [5, 20] kyr and A_e within [1, 40]. We always initialize planet g inside the 3:2 MMR of planet f and other planets wide of the 2:1 MMR of their inner planets.

The simulation results are shown in Fig. 3.8. We divide the simulation outcomes into four groups according to:

1. the final orbital configuration of planet b & c: circles indicate that planet b & c are connected by 3:2 MMR and triangles indicate that planet b & c are connected by 2:1 MMR.

2. the final configuration of the outer planets other than planet b & c: green symbols indicate that all outer planet pairs are consistent with Objective I and blue symbols that at least one planet pair is connected by a wider MMR than envisioned by Objective I (and no pair in closer MMRs).

3. red crosses indicate that there is at least one planet pair connected by a closer MMR than stipulated in Objective I.

In panel (a), more green and blue triangles are present at higher $\tau_{a,\oplus}$ since planets are easier trapped into wider MMRs – i.e., the 2:1 – under conditions of slower migration. As C_e increases, the green and blue triangles move to the left. Higher C_e results in higher planet eccentricities, decreasing the critical time-scale to cross the resonance (consistent with the analysis in Sect. 3.6.1). Other panels show similar patterns but the higher the A_e, the easier for planet c to cross the 2:1 MMR with planet b. Therefore, more circles appear at high $\tau_{a,\oplus}$ as A_e increases. The analytical explanation can be found in Sect. 3.6.1. All green circles satisfy the requirement of Objective I. For runs labelled by blue markers, it is mostly planet h that fails to cross the 2:1 MMR. Therefore, we conclude that a formation imprint may be necessary for planets c, g and h for Objective I to be fulfilled – its outcome is surely not universal but does also not require extremely tuned conditions.

Since one of our assumptions is that the disc is viscously relaxed (as described in Sect. 3.2), the α-viscosity parameter can be constrained using Eq. (3.8). In Fig. 3.8, green circles are centred near $\tau_{a,\oplus} = 12$ kyr, corresponding to a value of $\alpha \sim 10^{-3}$. $\alpha \sim 10^{-3}$ is a typical value seen in observational studies, e.g., on the disc gas radii (Trapman et al. 2020) and stellar accretion rates (Hartmann et al. 2016), as well as theoretical studies, e.g. on modelling the

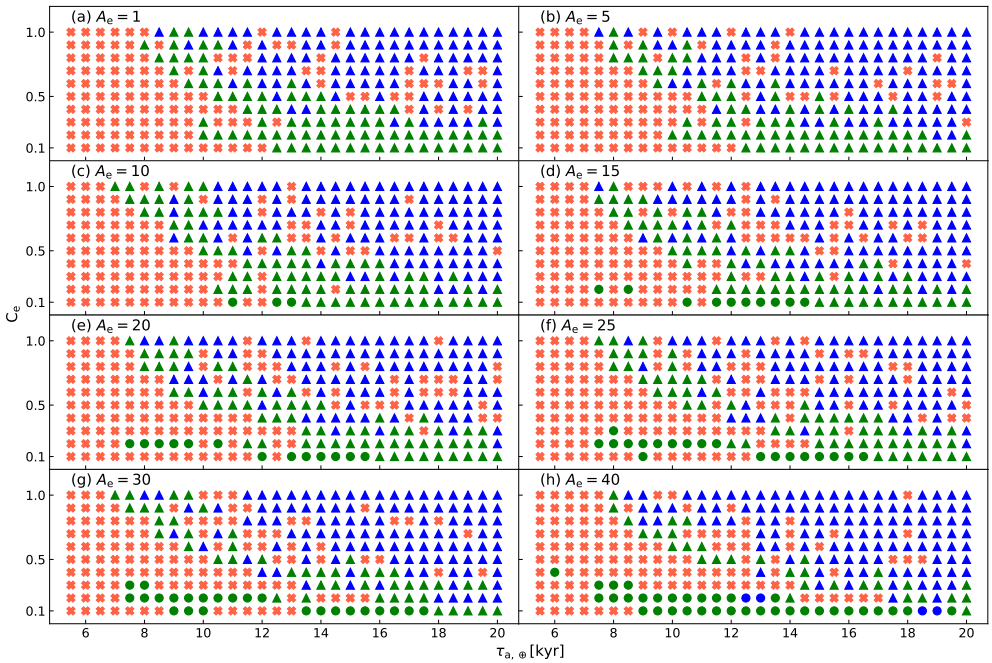


Figure 3.8. Sensitivity study of the dCcgI model. In all five panels the x-axis denotes the migration time-scale $\tau_{a,\oplus}$ and the y-axis the eccentricity-damping C_e, but in each panel the eccentricity-damping enhancement at the truncation radius parameter, A_e, differs. We label the value of A_e at the top of each panel. Different symbols represent different final orbital configuration in the simulation. Circles represent that planet b & c are connected by 3:2 MMR and triangles represent that planet b & c are in 2:1 MMR. Red crosses indicate there is at least one planet pair in a closer MMR than the desired configuration of Objective I, green indicates that all outer planet pairs are consistent with Objective I and blue indicates that at least one planet pair is in an MMR wider than the desired resonance chain.

dust size distribution (Birnstiel et al. 2018). A higher value $10^{-2} - 10^{-3}$ is suggested in the close-in region in the disc (Gammie 1996; Carr et al. 2004). Note that our modelling constrains the migration time-scale parameter $\tau_{a,\oplus}$; when converting to the disc proprieties (like α) additional uncertainty arises from other model-dependent parameters, i.e., $\dot{M}_\star$, γ_I.

3.4 Trapping and escape of planets in 3BRs

This section examines how the TRAPPIST-1 planets evolve from Objective I to Objective II, in which the inner three planets attain their final period ratios. We postulate that this is achieved after planets b and c enter the cavity and experience a phase of inward migration. Specifically, we envision that planet c is being pushed inwards, from an initial period ratios of 3:2 (with planet d) to the final ratio of 5:3. The rationale behind this scenario is that if the $\Phi^{2,5,3}_{\rm b,c,d}$ 3BR is maintained during this process, the inner planets will naturally end up near their observed period ratios.

However, while (gently) pushing planet c inwards, it needs to overcome other 3BR with the outer planets. We list four 3BRs that may halt the inward migration of planet c and therefore the expansion of the b/c/d subsystem. In order of increasing period ratio $P_{\rm d}/P_{\rm c}$, as

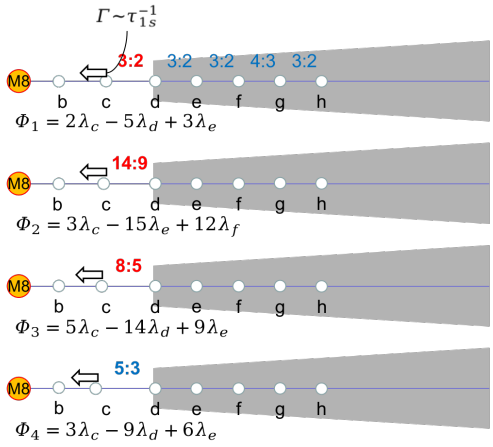


Figure 3.9. Four 3BR angles in which planet c could be trapped when it migrates from its 3:2 (top) period ratio to its observed value of 5:3 (bottom). The period ratios in blue are consistent with the present observation while those in red are inconsistent. Several three-body resonances need to be passed. Γ_{1s} (or its corresponding time-scale τ_{1s}) represents the torque from the exterior remnant disc.

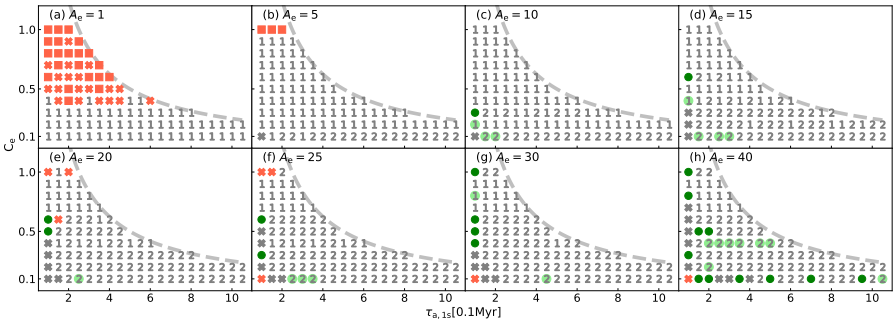


Figure 3.10. Results of the Late Infall model parameter study, featuring a one-sided torque Γ_{1s} (here expressed in terms of a time-scale τ_{1s}) acting on planet c. Different panels refer to different values of the cavity eccentricity enhancement factor A_e. In each panel, the x-axis denotes the semi-major axis damping time-scale acting on planet c in the cavity. The y-axis denotes the eccentricity-damping efficiency (Eq. (3.7)). The nominal migration time $\tau_{a,\oplus}$ is taken to be 16 kyr. The grey dashed line is $\tau_{1s} \times C_e = 2.5 \times 10^5$ yr. Different markers represent different final configurations. The markers '1', '2', '3' and the green dot represent respectively the Φ_1, Φ_2, Φ_3 and Φ_4 end stages, as shown in the four panels in Fig. 3.9. Furthermore, grey crosses mean that planet c crosses Φ_4, red crosses that at least one of outer planet pair breaks the desired MMRs, i.e., Objective I is not yet achieved, and red squares mean that planet d crosses the disc inner edge. Finally, light-green dots indicate at least one configuration ends up in Φ_4 in simulations with larger $\tau_{a,\oplus}$.

illustrated in Fig. 3.9:

- $\Phi_1 \equiv \Phi_{c,d,e}^{2,5,3}$ with period ratio $P_d/P_c = 1.5$;
- $\Phi_2 \equiv \Phi_{c,e,f}^{3,15,12}$ (non-adjacent) with period ratio $P_d/P_c = 1.556$;
- $\Phi_3 \equiv \Phi_{c,d,e}^{5,14,9}$ with period ratio $P_d/P_c = 1.6$;

- $\Phi_4 \equiv \Phi^{3,9,6}_{\rm c,d,e}$ with period ratio $P_{\rm d}/P_{\rm c} = 1.667$.

The last 3BR is the observed period ratio while the first three need to be crossed. We therefore search for parameter combinations that can break the first three 3BRs but not Φ_4. As a comprehensive (analytical) investigation of 3BR is beyond the scope of this work (but see some comments in Sect. 3.6), we instead solve the problem numerically in Sect. 3.4.1.That is, we vary the torque on planet c, as well as the disc parameters, to assess the conditions for which planet c crosses Φ_1, Φ_2 and Φ_3 but stays in Φ_4. Based on these findings, in Sect. 3.4.2, we implement a complete scenario for the emergence of the TRAPPIST-1 dynamical configuration. In Sect. 3.5.1, we comment on the nature of the inward torque that planet c experiences.

3.4.1 Crossing and trapping of the three-body resonances (dCcgIcT)

We conduct a parameter study to assess the conditions necessary for the above described scenario, varying the torque on planet c $\tau_{\rm 1s}^{-1}$, the nominal migration time $\tau_{a,\oplus}$ (see Eq. (3.6)), the eccentricity-to-semi-major axis damping parameter C_e (see Eq. (3.7)), and the eccentricity-damping boost at the disc inner edge (A_e; see Eq. (3.11)). The numerical simulations are conducted with all seven planets: five in the disc (d, e, f, g, and h) and two (b and c) in the cavity. All planets are initialized with a configuration that is consistent with Objective I. Next, we employ a negative torque on planet c in the cavity to break the 3BRs. We record the outcome of the simulation (see below). We conduct a parameter study varying $\tau_{\rm 1s}$ in the range $[10^5, 10^6]$yr, $\tau_{\rm a,\oplus}$ in the $[12, 36]$ kyr range, $1 \leq A_e \leq 40$ and $0.1 \leq C_e \leq 1$. Each simulation is integrated for $\approx\tau_{\rm 1s}/3$, such that it is long enough for $P_{\rm d}/P_{\rm c}$ to increase from 1.5 to 1.667 if planet c is not trapped.

Escape from 3BR is qualitatively different than escape from two-body MMR. In the two-body case, under the divergent situation described above, planet c will always move away from planet d; we have verified that the critical torque is smaller than 10^{-7} yr^{-1}. However, the presence of a third resonant body (here planet e or f) qualitatively changes the picture. Even though the torque acting on planet c is divergent, it does not necessarily break the resonance. For example, planet c, d, and e are connected by the 3BR Φ_1, corresponding to the 3:2 resonance locations of both planet c & d and d & e. Therefore, an increase in the period ratio $P_{\rm d}/P_{\rm c}$, due to a negative (divergent) torque acting on planet c, will likewise result in an increase of $P_{\rm e}/P_{\rm d}$, if Φ_1 does not break. In the scenario that planet d and e are in the disc, Type I (convergent) migration, however, prevents the $P_{\rm e}/P_{\rm d}$ expansion. Therefore, $P_{\rm d}/P_{\rm c}$ tends to stay near 1.5.

The results of our parameter study are displayed in Fig. 3.10. We present the final configurations from the simulations in which $\tau_{\rm a,\oplus} = 16$ kyr, and vary A_e (panels), $\tau_{\rm 1s}$ (x-axis) and C_e (y-axis). Empirically, as C_e increases from 0.1 to 1.0, Φ_2 becomes stronger and is more capable to trap planet c in the cavity (MMRs hold similar characteristics, which is analyzed in Sect. 3.6.1). It is found that planet c will always strand in either Φ_1 or Φ_2 when the combination $\tau_{\rm 1s} \times C_e = \tau_{\rm c}$ exceeds a certain value. Therefore, we limit $\tau_{\rm c} = 2.5 \times 10^5$ yr, which is indicated by the grey dashed line in Fig. 3.10.

Different markers represent different final configurations in the simulations. At the end of each simulation, we first check whether the outer planets are still in the desired MMRs; if not we mark them by red crosses. Second, we check whether planet d enters the disc cavity; if so we mark them by red squares. In both scenarios, Objective I has failed to materialize. Most red crosses and red squares are in the panel where $A_e = 1$ and C_e is relatively high, because the eccentricity of planet d is not sufficiently damped. Then, planet d will cross the disc inner edge when its eccentricity becomes as large as the migration barrier width

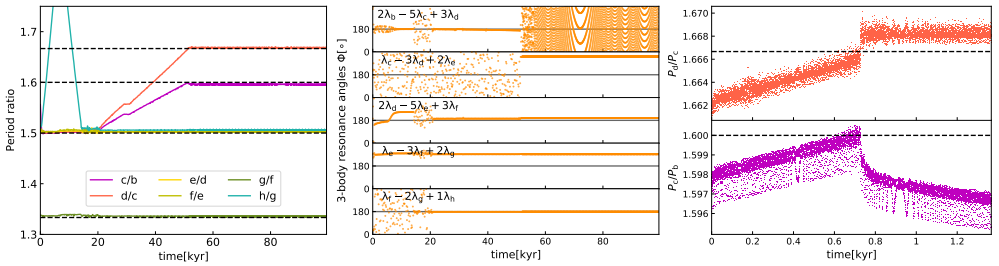


Figure 3.11. The period ratio and 3BR angles evolution in one of the systems drawn from Fig. 3.10, where $A_e = 15$, $C_e = 0.6$ and $\tau_{1s} = 0.1$ Myr. In the left panel, the period ratios 1.66, 1.60, 1.5, 1.33 are indicated by the four dashed horizontal lines from the upper to the bottom. In the middle panel, we label the expression of each 3BR angle. In the right panel, we zoom in on the period ratios P_c/P_b and P_d/P_c around the time where the b/c/d 3BR breaks.

($e \gtrsim \Delta$), or planet e crosses the 3:2 MMR due to perturbation from eccentric planet d. If planet c is trapped by Φ_1, Φ_2, Φ_3 or Φ_4, we mark the corresponding simulations with '1', '2', '3' or a green dot respectively. Otherwise, if planet c crosses all four 3BR listed here, we mark the outcome by a grey cross.

Figure 3.10 provides some insights into the physical properties of 3BRs. In each panel, planet c tends to be trapped in Φ_1 (marker '1') at high C_e. As C_e decrease down to 0.1, Φ_2 (marker '2') replaces it in most simulations. It indicates that Φ_1 becomes weaker if more efficient eccentricity damping is adopted. When increasing the one-side torque on planet c in the cavity, planet c breaks through Φ_2 and gets trapped in Φ_4 (green dots) in several simulations. These simulations reveal two points. First, the boundary between trapping in Φ_2 and Φ_4 is not so clear, hinting that the trapping process of planet c is stochastic. Second, planet c is either trapped by Φ_4 or just crosses Φ_4 after Φ_2, rather than be trapped by Φ_3. It implies that Φ_3 is much weaker than Φ_2 and Φ_4. Furthermore, Φ_2 and Φ_4 may have comparable strengths to trap planet c . Otherwise, more green dots would have popped up at the locations now occupied by grey crosses.

We give one possible reason for the stochastic nature of 3BR trapping/escaping. Apart from Φ_1, Φ_2, Φ_3 and Φ_4, there are 9×4 other 3BRs involving the outer five planets that could trap planet c at the four period ratios 1.5, 1.556, 1.6, 1.667. For instance, $\Phi^{3,6,3}_{c,d,g}$ is able to trap planet c at $P_d/P_c = 1.667$. Some of these 3BRs feature several different libration centers when differing the initial conditions slightly (Tamayo et al. 2017). All these different 3BRs or the same 3BR with different libration centers may have distinct strengths to trap planet c in the cavity. If the initial condition is different, planets may end up in a different configuration, thus contributing to the stochastic behavior.

At the beginning of all of these simulations, P_c/P_b increases in sync with P_d/P_c because 3BR 'bind' planet b/c/d together. However, in most of the simulations where planet c is trapped by Φ_4 as a final state, P_c/P_b is slightly smaller than 8/5. We present an example in Fig. 3.11. It shows that when P_d/P_c is about to arrive at 5/3, planet c undergoes an inward resonant repulsion (Lithwick & Wu 2012) which breaks the b/c/d resonance. Thereafter, P_c/P_b decreases to 1.595 as shown on the right panel in Fig. 3.11. This intermediate configuration is a natural output from our model, which is regarded as an initial configuration by Papaloizou et al. (2018). Long term tidal dissipation then expand P_c/P_b back to $\approx 8/5$ (Sect. 3.4.2, cf. Papaloizou et al. 2018), which is consistent with the current observation.

Disc evolution may also help to move the TRAPPIST-1 planets into their observed con-

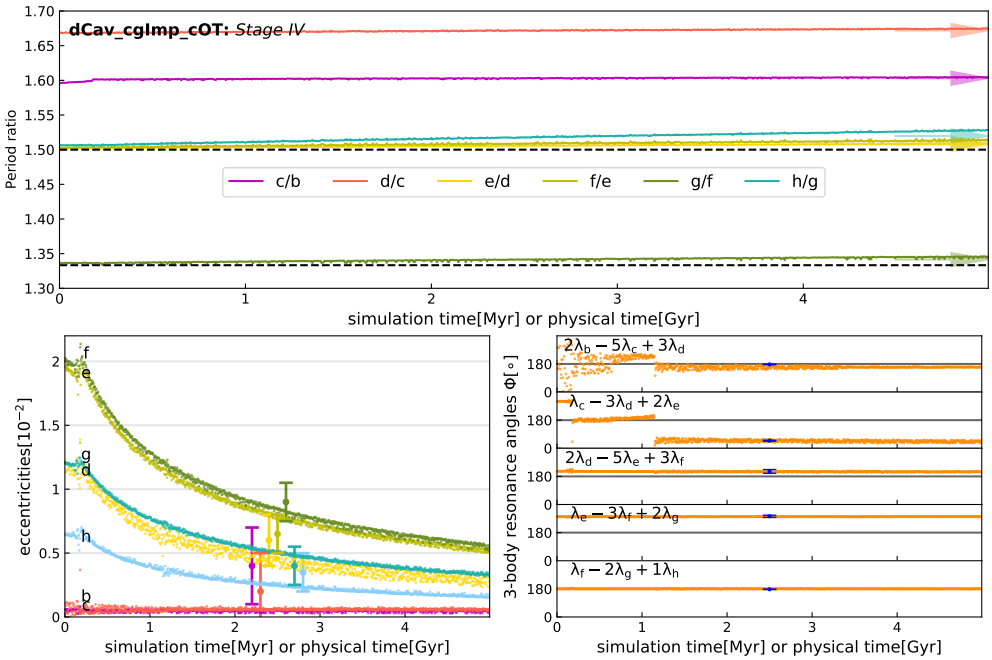


Figure 3.12. Long-term tidal damping simulations of the post-disc phase, illustrating how, after the completion of Objective II, the system evolves towards its present configuration. We present period ratios (top panel), eccentricities (bottom-left) and 3BR angles (bottom-right) during tidal dissipation (with $Q_{\rm sim} = 0.1$), after dispersing the gas disc of the system in Fig. 3.11. The figure style is the same as Fig. 3.5. We label the observed range of 3BR angles (Luger et al. 2017) on the lower right panel with blue error bars. Tidal damping reforms the $\Phi^{2,5,3}_{\rm b,c,d}$ 3BR and damps the eccentricities towards the observationally-inferred values.

figuration. We run five sets of simulations similar to Fig. 3.10, but with $\tau_{\rm a,\oplus}$ equal to 20 kyr, 24 kyr, 28 kyr, 32 kyr and 36 kyr (not shown). In several of these simulations with higher $\tau_{\rm a,\oplus}$ planet c becomes trapped by Φ_4 and we mark them by light-green dots in Fig. 3.10 together. Therefore, if disc evolution operates during the migration planet c may avoid trapping in Φ_1 and Φ_2 to end up in Φ_4.

In this model, we have successfully reproduced the orbital configuration of TRAPPIST-1 planets as well as their resonant relationship. However, most of the green dots feature low C_e (< 0.7) and extremely high A_e ($\gtrsim 10$). Besides, the one-sided torque on planet c in the cavity also needs to be tuned. Considering all these caveats, the probability of TRAPPIST-1 analogs produced by this scenario is not very compelling.

3.4.2 Long term tidal dissipation (dCcgIcT)

The breaking of 3BR of planets b, c, and d is a natural outcome in dCcgIcT model, as described in Fig. 3.11. The 3BR of the innermost three planets is believed to librate (Luger et al. 2017; Agol et al. 2021; Teyssandier et al. 2021). To reform this 3BR, long-term tidal dissipation is needed.

We therefore run a long-term simulation, similar to Fig. 3.5 for one particular parameter set (the same as the one in Fig. 3.11). We first disperse its disc on a e-folding time-scale

of 10^5yr and run the simulation for $20\tau_d$. Using the final snapshot from the disc dispersing simulation as an initial condition, we start long term tidal dissipation process. We take $Q_{sim} = 0.1$ for all planets to accelerate the simulation by 10^3 times (Papaloizou et al. 2018).

Since the disc dispersal does not modify the orbital properties of the planets in this system, we only present the evolution of the planets after removing the disc in Fig. 3.12. The period ratio P_c/P_b increases with time due to tidal damping during the first ≈ 0.2 Myr simulation time (≈ 0.2 Gyr physical time). After that, the period ratio P_c/P_b reaches 1.6 and $\Phi^{2,5,3}_{b,c,d}$ reforms. Then, the period ratio increase of the inner planets slows down because all planets are linked by a chain of 3BRs. At $t \approx 2.5$ Myr simulation time ($t \approx 2.5$ Gyr physical time), the eccentricities and period ratios of all planets are consistent with the inferred values by Agol et al. (2021) indicated by the $1\,\sigma$ error bars in Fig. 3.12. The libration centre of all five adjacent 3BRs lie within the observationally-inferred values as well.

Our simulation results can constrain the tidal quality factor of TRAPPIST-1 b. The estimated age of TRAPPIST-1 is 7.6 Gyr (Burgasser & Mamajek 2017), suggesting that the simulation in Fig. 3.12 evolves ≈3 times faster than the real TRAPPIST-1 system. We also run Stage III simulations that apply tidal torques on (i) only planet b; (ii) only planet b and c. The results are consistent with the simulation that applied the tidal torque on all seven planets. The tidally induced expansion is therefore dominated by the tidal dissipation of planet b (cf. Papaloizou et al. 2018). Since $Q_{sim} = 3Q/(2k_2)$, the chosen simulation constrains the tidal quality factor of planet b as $Q_b \approx 200k_2$. This value falls within the upper limit of $5,000k_2$ calculated by Brasser et al. (2019). Note that the bulk planetary eccentricities just after removing the surrounding disc are proportional to $\sqrt{C_e}$ (Goldreich & Schlichting 2014; Teyssandier & Terquem 2014; Terquem & Papaloizou 2019). The time one system spends in the tidal dissipation simulation to fit the observed TRAPPIST-1 system is positively correlated with the initial bulk eccentricities. Our model features that $C_e \lesssim 0.6$, and therefore the corresponding constraint on the tidal quality factor is $Q_b \gtrsim 200k_2$.

In Fig. 3.12, long term stellar tidal damping does not alter the period ratios very much compared to Fig. 3.5. Since the initial eccentricities of planets b and c are ten times smaller than in Fig. 3.5, stellar tidal forces on planets b and c are also smaller (Eq. (3.12)) hence dissipating the energy of the system on a longer time-scale. Therefore, the departures from exact commensurability increase more slowly in Fig. 3.12.

3.5 Early cavity infall (dCcgIcL)

In the preceding, we have assumed that planets b and c crossed the cavity only after the emergence of a first order resonance chain, separating Objective I and II. Objective II is the most challenging to meet, as this requires planet c to cross the Φ_1–Φ_3 3BRs but not to overshoot Φ_4. However, in reality these stages may be intertwined, such that planets b and c may enter the cavity before the outer resonance chain has established, that is, before (some of the) Φ_i even exist. For this scenario, we hypothesize that planet b and c, being larger, were able to open partial gaps in the disc that caused them to be disconnected from the disc (Ataiee & Kley 2021), whereas planet d, being smaller, did not suffer this fate and stayed at the cavity edge. While in the cavity we assume, as before, that planet c experiences an inward migration torque, which causes it to drift away slowly from planet d.

We only concentrate on how likely it is to evolve to Objective II from Objective I, because our analysis in Sect. 3.3.4 (see Fig. 3.8) is still roughly applicable. The model is illustrated in Fig. 3.13. At $t = 0$, we assume that planets b and c and d are initially in 3:2 MMR with d at the cavity edge. Subsequently, planets e, f, g, and h enter the resonant chain one after

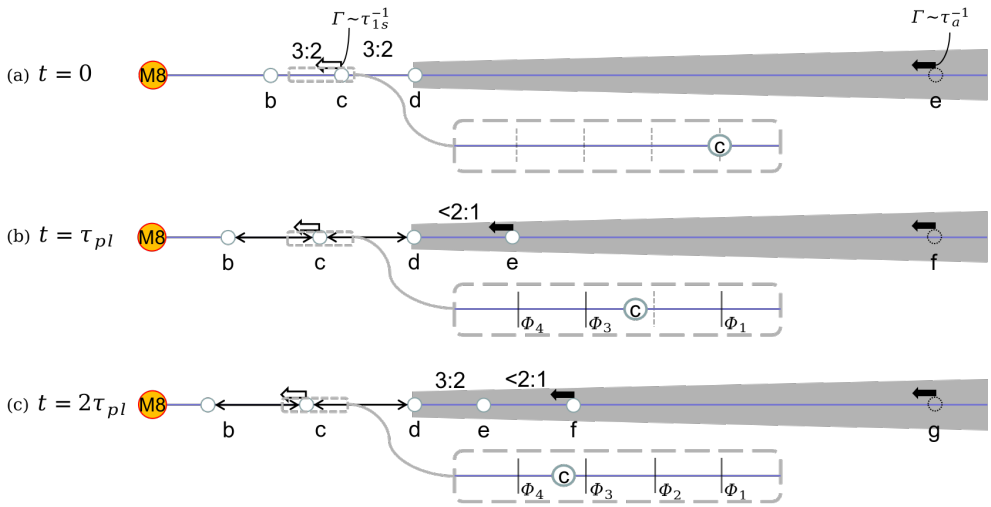


Figure 3.13. Schematic of the Early Cavity Infall model (dCcgIcL). At $t = 0$ (upper panel), planets b and c have already entered the cavity and planet d has migrated to the inner disc edge. Planet b, c, and d are in 3:2 MMRs. Planet e is still forming or migrating (on time-scale τ_a) far out in the disc. Planet c is pushed by the external disc inward on time-scale τ_{1s}. At $t = \tau_{pl}$ (middle panel; τ_{pl} is the planet formation interval time) planet e enters the resonant chain and is inserted inside the 2:1 MMR of planet d. At this point, planet f is forming or migrating in the outer disc. At $t = 2\tau_{pl}$ (bottom panel), planet f ends up inside the 2:1 MMR of planet e. Similarly, planet g and h are inserted after every τ_{pl}, inside 3:2 MMR and 2:1 MMR respectively. In each panel, we zoom in on the region around planet c and indicate the four 3BRs introduced in Sect. 3.4 that can trap planet c by solid vertical lines. At early times some of the Φ_i may not yet exist (dashed vertical lines; unlabelled), allowing planet c to cross these locations.

another, each separated by an interval time τ_{pl} – the planet formation time. Meanwhile planet c experiences a negative torque, expressed in terms of a migration time-scale τ_{1s}. We now introduce a specific model for the nature of this "one-sided" torque (Sect. 3.5.1), linking it to the the scaling of nominal Type I semi-major axis damping time-scale $\tau_{a,\oplus}$, i.e., τ_{1s} is no longer a free parameter. Furthermore, we no longer vary the eccentricity-damping enhancement parameter at the cavity edge, $A_e = 1$, leaving us to explore C_e, A_a, $\tau_{a,\oplus}$, and τ_{pl} in Sect. 3.5.2.

3.5.1 Disc repulsion on planets in the cavity

The Lindblad torque is capable to drive planets in the cavity inward. It arises due to gravitational exchange at the Lindblad resonance locations in the disc (Ward 1997). In the case that the planet is located in the inner disc cavity, only those outermost Lindblad resonances, which still lie in the disc will contribute. Because the nominal migration rate (for an 1 Earth mass planet) and the distant migration rate both scale with disc mass, the rates are linked through:

$$\tau_{1s,\oplus}^{-1} = \tau_{a,\oplus}^{-1} \sum_{m \text{ in disc}} f_m = 0.0054 \tau_{a,\oplus}^{-1} \tag{3.14}$$

where f_m is the torque, arising from the mth order Lindblad resonance, normalized to the nominal Type I migration torque ($L/2\tau_{a,\oplus}$, where L is the angular momentum of the planet), and the last expression assumes only $m = 1$ contributes (see below). The Lindblad resonance

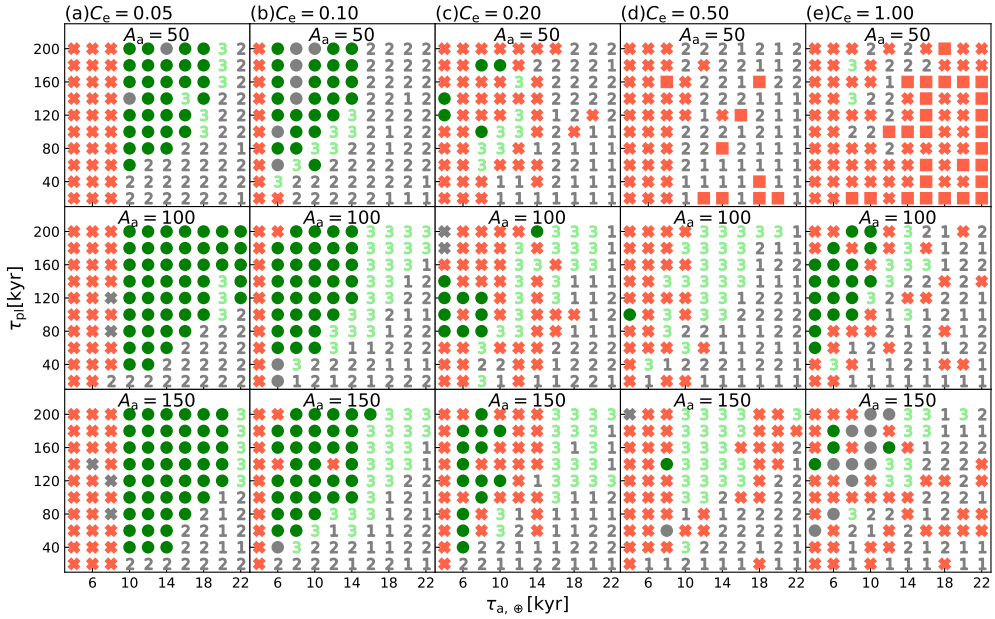


Figure 3.14. Final orbital configurations produced by the Early Cavity Infall model (dCcgIcL). Different columns and different rows refer to different eccentricity-damping parameter C_e and migration threshold height A_a. In each panel, the x-axis denotes the Type I semi-major axis damping time-scale $\tau_{a,\oplus}$, the y-axis denotes the planet formation span $\tau_{\rm pl}$. Different markers represent different final configurations, following the same style as Fig. 3.10. We additionally mark the configurations in which planet c stays in Φ_4 with $P_c/P_b < 1.53$ or $P_c/P_b > 1.63$ by grey dots.

condition for an orbit of mth order torque reads:

$$m[\Omega(r) - \Omega_p] = \pm\kappa\sqrt{1 + m^2h^2}, \tag{3.15}$$

where $\Omega(r)$ is the Keplerian velocity at distance r, Ω_p is the Keplerian velocity on the planet orbit and κ is the epicycle frequency. We follow the calculation by Ward (1997) and plot the value of f_m for m from 1 to 50 in Appendix 3.A.

In the case of the TRAPPIST-1 planets, after planets b and c have entered the cavity, planet d resides near the cavity radius location. As the period ratios of planets d and b are larger than 2:1, there is no one-sided Lindblad torque from the outer disc on planet b. On the other hand, the period ratio of planets c and d exceeds 1.5 but is less than 2. Therefore, only the outer 2:1 Lindblad resonance of planet c falls in the disc and the relevant order is $m = 1$. The value of f_1 for the outer Lindblad resonance is 0.0054. For instance, for $\tau_a = 10\,$kyr we arrive at $\tau_{1s} = 1.85\,$Myr. Although τ_{1s} is long, the time to cross a distance from −say− the 3:2 to the 5:3 resonance location is lower by about a factor ∼10. Therefore τ_{1s} may compete with the planet formation interval time-scale $\tau_{\rm pl}$.

3.5.2 Parameter study (dCcgIcL)

We conduct a parameter study to assess the conditions needed to obtain the desired resonance configuration. Apart from varying the interval time $\tau_{\rm pl}$ from 20 to 200 kyr, we also vary the eccentricity-to-migration damping parameter C_e from 0.05 to 1, the migration

threshold barrier parameter A_a from 50 to 150, and the nominal planet migration parameter $\tau_{a,\oplus}$ from 4 kyr to 22 kyr. We let the system evolve until $\sim\tau_{1s}$ (Eq. (3.14)). The results are shown in Fig. 3.14. We mark the final configurations following the same style as Fig. 3.10. We also mark the configurations where planet c stays in Φ_4 but where the period ratio has deviated by some amount from 8:5 ($P_c/P_b < 1.53$ or $P_c/P_b > 1.63$) with grey dots.

In this Early Cavity Infall model the new parameter τ_{pl} sensitively determines the resonant structure. Although we assume τ_{pl} is the same for all outer planets, what matters chiefly is the arrival time of planets e and f. If τ_{pl} is too long, planet c would migrate so far such that $P_d/P_c > 5/3$ before planet e enters the resonant chain. Our study does not cover such long τ_{pl}. In contrast, if τ_{pl} is too short, planet c would not migrate very far with $P_d/P_c < 14/9$ after the arrival of planet f, which bring about the existence of Φ_2. Then it is unlikely for planet c to overcome Φ_2. We are hence searching for the sweet spot where planet c finally stays at Φ_4.

Starting from the bottom-right corner of each panel in Fig. 3.14, the one-side torque is relatively weak and τ_{pl} is short. Planet c mostly stays in Φ_1 or Φ_2. With increasing τ_{pl} and decreasing $\tau_{a,\oplus}$, planet c can migrate over larger distances in the cavity before the outer planets appear. Hence, planet c increasingly ends in Φ_3 and Φ_4. Interestingly, in the left two columns green dots are more frequent than marker '3' and there is usually a clear boundary between the two markers. The corresponding one-sided torque at the boundary therefore represents the strength of Φ_3. It implies that Φ_4 is sturdier than Φ_3, which provides a wide range of parameter space to overcome Φ_3 but stay in Φ_4. For this reason, we colour '3' light green – if (for some reason) planet c manages to escape Φ_3, it is still likely to end up in Φ_4.

When $\tau_{a,\oplus}$ becomes too small, some planets in the disc will break their desired MMRs. As shown in Fig. 3.14 when $C_e < 0.2$, there are some red crosses on the left and a clear boundary between red crosses and green dots. The corresponding disc migration torque at the boundary indicates the critical torque, above which the desired configuration of outer planets (d, e, f, g, and h) will break. As C_e increases from 0.05 to 0.1, the desired configuration of outer planets becomes more stable (the boundary between red crosses and green dots moves to lower t_a). This trend is consistent with Fig. 3.8, and is analysed in Sect. 3.6.1.

However, when increasing C_e to higher values, the boundary between red crosses and green dots becomes less sharp and the appearance of red crosses becomes stochastic. The reason is that with higher C_e planet eccentricities are higher, which renders phenomena like resonance crossing more stochastic (Ogihara & Kobayashi 2013). Therefore, we see more and more red crosses distributed in the right columns of Fig. 3.14 (higher C_e).

We test the influence of the migration threshold barrier A_a by three different values, 50, 100, 150 in Fig. 3.14. If A_a is small, it shows more red squares, where planet d enters the cavity, when C_e is high. When increasing A_a, the results of $A_a = 100$ is largely similar to $A_a = 150$, signifying a threshold above which planet d stays at the disc edge.

We finally comment on the meaning of the grey dots in Fig. 3.14. As a rule of thumb we see that, similar to Fig. 3.11, when planet c reaches Φ_4 the 3BR $\Phi^{2,5,3}_{b,c,d}$ breaks, whereafter it will reform due to long term tidal dissipation (Fig. 3.12). However, it is found that in some of the simulations, the 3BR $\Phi^{2,5,3}_{b,c,d}$ already breaks early. Two physically different mechanisms result in grey dots: (a) If τ_{pl} is so long that Φ_4 is reached before planets f and g appear, the outer planets f and g will further push planet c slightly inward. This case applies to the top left two panels in Fig. 3.14, where τ_{pl} is long and A_a is small. (b) The 3BR $\Phi^{2,5,3}_{b,c,d}$ breaks early when Φ_3 is crossed or when a new planet enter the resonant chain. Since planet c is still repulsed inward by the Lindblad torque, P_c/P_b decreases towards $\approx$1.5. We have run long-term tidal dissipation simulation starting with the analog satisfying $P_c/P_b \approx 1.53$, but found that it fails

to reform the 3BR $\Phi_{\rm b,c,d}^{2,5,3}$.

When adopting low C_e ($\lesssim 0.20$) the low eccentricities of the outer planets render the system more stable, preventing resonance crossing. Interestingly, there is another green dots island on the panel where $C_e = 1$ and $A_a = 100$. We do not have a clear explanation for the occurrence of so many green dots in this panel. Possibly, the strength of Φ_3 is non-linearly dependent on C_e, such that it is strongest at $C_e \approx 0.5$ and breaks again when $C_e = 1$.

To achieve the observed TRAPPIST-1 configuration, the early cavity infall model compares favourably to the late infall model of Sect. 3.4.1. The early cavity infall model requires less parameter tuning – we fix $A_e = 1$ and link τ_{1s} to $\tau_{a,\oplus}$ – and the values for the A_a and τ_{1s} parameters are natural or in line with formation models (see Sect. 3.7.1). In particular for low C_e, the likelihood of a successful outcome is quite high.

3.6 Analysis

3.6.1 Trapping under convergent migration in MMRs

Through numerical simulations, we find that more efficient eccentricity-damping promotes resonance crossing (see Fig. 3.8). The trend can be understood using the pendulum model (Murray & Dermott 1999) for internal MMRs. Assuming small deviations from the equilibrium value for the resonance angle, the libration width of a $j{:}j-1$ MMR can be written as:

$$\Delta_a = \left(\frac{16|C_j|e}{2n}\right)^{1/2} a, \tag{3.16}$$

where n, e and a are the mean motion, eccentricity and semi-major axis of the inner planet, respectively. The constant C_j arises from the resonant part of the disturbing function (Murray & Dermott 1999):

$$C_j = \frac{m'}{M_\star} n \alpha_j f_j \tag{3.17}$$

which is proportional to the inner planet mass m'. In Eq. (3.17), α_j and f_j are the inner-to-outer planet semi-major axis ratio and the direct term in the expansion of the disturbing function. The value of the most commonly used f_j can be seen on page 334 in (Murray & Dermott 1999). The libration time-scale is:

$$\tau_{\rm lib} = \left(\frac{2\pi}{3|C_j|ne}\right)^{1/2}. \tag{3.18}$$

Following Ogihara & Kobayashi (2013), we write the critical migration time-scale $\tau_{\rm a,crit}$ as:

$$\tau_{\rm a,crit} = \frac{\tau_{\rm lib} a}{\Delta_a} = \left(\frac{2\pi}{16 C_j^2 e^2}\right)^{1/2}, \tag{3.19}$$

below which the corresponding MMR will break. In the case of convergent migration of two planets, the equilibrium eccentricities of planets balancing eccentricity-damping from the disc and excitation by resonant interaction reads:

$$e^2 \sim \frac{\tau_{\rm e}}{\tau_{\rm a}} \tag{3.20}$$

(Goldreich & Schlichting 2014; Teyssandier & Terquem 2014; Terquem & Papaloizou 2019). Combining Eq. (3.19) and Eq. (3.20) we obtain:

$$\tau_{\rm a,crit} \sim \frac{2\pi}{16 C_j^2 \tau_{\rm e}}. \tag{3.21}$$

This expression implies that we can either employ efficient eccentricity-damping (low $\tau_{\rm e}$) or use smaller planet mass (low C_j), in order to enlarge $\tau_{\rm a,crit}$ and cross the MMR. Note that although the above expressions are derived for an internal MMRs (where the outer planet is fixed), those for the external MMRs are almost the same (Murray & Dermott 1999).

The above analytic results is consistent with Fig. 3.8. The value of $\tau_{a,\oplus}$ at the boundary between triangles and circles indicate the critical migration time-scale $\tau_{a,\oplus}$ of the 2:1 MMR of planet b & c. As C_e decreases or A_e increases, the boundary moves to the right, implying longer $\tau_{a,\oplus}$.

3.6.2 Eccentricity-period relation in 3BRs

In a three-planet system connected by one 3BR with each of the adjacent two planets connected by $j-1{:}j$ and $k-1{:}k$ MMRs, the eccentricities and period ratios are related to each other. We define the distance to exact commensurability of planet i and $i+1$ as:

$$\delta_{i,i+1} = \frac{(j-1)P_{i+1}}{jP_i} - 1, \tag{3.22}$$

where P_i is the orbital period of planet i. The MMR angles in a planet pair near $j-1{:}j$ MMR are:

$$\phi_{i,i+1;i+X} = (j-1)\lambda_i - j\lambda_{i+1} + \varpi_{i+X}. \tag{3.23}$$

where $X = 0$ or $X = 1$. The time derivatives $\dot{\phi}_{i,i+1;i+X}$ average to zero if $\phi_{i,i+1;i+X}$ is librating. Taking the time derivative of Eq. (3.23) and combining it with Eq. (3.22), we have:

$$\delta_{i,i+1} = -\dot{\varpi}_{i+X}\frac{P_{i+1}}{2\pi j}. \tag{3.24}$$

A similar relation holds for planet $i+1\,\&\,i+2$. Without external perturbation the three planets are locked in common apsidal precession, $\dot{\varpi}_i = \dot{\varpi}_{i+1} = \dot{\varpi}_{i+2}$. Then, the ratio of the distance to exact commensurability of two planet pairs is:

$$\frac{\delta_{i+1,i+2}}{\delta_{i,i+1}} = \frac{jP_{i+2}}{kP_{i+1}} \approx \frac{j}{k-1}. \tag{3.25}$$

In Laplace resonances where $j = k$, the right hand term of Eq. (3.25) is larger than unity. Ramos et al. (2017) and Teyssandier & Libert (2020) insert Lagrange's planetary equation, $\dot{\varpi} = C_j \cos\phi/e$, into Eq. (3.24) and get:

$$\delta_{i,i+1} = \frac{1}{j}\alpha_j^{-1/2} f_j \frac{m_{i+1}}{M_\star}\frac{1}{e_i} \tag{3.26}$$

Combining Eq. (3.25) and Eq. (3.26), we arrive at:

$$\frac{e_i}{e_{i+1}} = \frac{m_{i+1}f_j}{m_{i+2}f_k}\left(\frac{\alpha_k}{\alpha_j}\right)^{1/2}\frac{P_{i+2}}{P_{i+1}} \approx \frac{m_{i+1}f_j}{m_{i+2}f_k}\left[\frac{k(j-1)}{j(k-1)}\right]^{1/3}\frac{k}{k-1}. \tag{3.27}$$

In Laplace resonances, the right hand term of Eq. (3.27) is larger than unity when planets have nearly the same mass. Therefore, outer planets tend to further depart from exact commensurability (Eq. (3.25)) and have smaller eccentricities (Eq. (3.27)). The eccentricities and the period ratios relationships of model bC, in which planets stay in first-order MMR, is revealed by Fig. 3.5. The deviations from exact commensurability increase and the eccentricities decrease from planet b to planet h. In the final stage of dCcgIcT (Stage III in Fig. 3.12, planet b & c and c & d are near MMRs of order higher than one. Because the analysis above only holds for first-order resonances, the relationship between the eccentricity and period ratios can be seen for outer planets but not for planet b/c/d.

3.7 Discussion

3.7.1 Model Assessment

In this work, we have aimed to connect the present-day dynamical properties of the TRAPPIST-1 planets to their formation. We have assumed that the planets are formed at locations further away from their present orbits, were subject to inward (Type I) migration, which was halted at the disc inner edge. Subsequently, the planets formed a chain of first-order MMRs, predominantly of 3:2 commensurability, and a plethora of three-body resonances (Stage I). In the next Stage II, which is either separated in time from Stage I (Sect. 3.4) or occurs contemporaneously with Stage I (Sect. 3.5), the two inner-most planets fell into the cavity, allowing their period ratios to expand due to the (weak and distant) torque from the disc. Finally, stellar tidal interactions after the demise of the gas disc (Stage III) provided the final act in moving the planets into a configuration consistent with their present-day orbital periods, period ratios, eccentricities, and three-body resonance angles.

The first successful model matching the observed TRAPPIST-1 configuration has Stage I, II, and III occurring separately (Sect. 3.4). However, the model has several drawbacks: (i) The probability of a successful case is low. (ii) It requires rather high additional eccentricity-damping on the planet at the disc inner edge ($A_e \gg 10$). Intriguingly, such enhanced eccentricity-damping at the disc edge has recently been observed (but not quite understood) in hydrodynamical simulations of planet-disc interaction (Ataiee & Kley 2021). Magnetospheric effects may also contribute towards a pileup of material near the cavity radius (D'Angelo & Spruit 2010), which would be the most natural explanation for the enhanced damping. Therefore, this model demands a very high surface density at the edge of the disc or some unknown mechanisms that would give rise to the anomalous efficient eccentricity-damping around the truncation radius. (iii) The physical origin of the one-sided negative torque on the planet in the disc cavity is not motivated. The torque required is usually ~10 times stronger than the Lindblad torque calculated in Sect. 3.5.1. Hence, for this scenario to work, the surface density of the gas needs to be boosted by a factor ~10 near the cavity region. Even then, the probability of an outcome consistent with the TRAPPIST-1 system remains low.

Finally, we have investigated the Early Cavity Infall model (Sect. 3.5) which features planets b and c entering the cavity before the outer planets park in resonance near the inner disc, combining Stage I and Stage II. In this scenario, we adopt a value for the Lindblad torque acting on planet c consistent with the disc mass. The key drawback of this model is that it introduces another parameter – the time interval between planet formation ($\tau_{\rm pl}$) – which needs to be tuned such that it is at least one-tenth of the time-scale over which planet c is

being pushed in.[1] Only then can planet c migrate sufficiently far inwards to cross the locations of the 3BRs before their appearance. In addition, success is more likely for low values of the eccentricity damping parameter C_e. Nevertheless, this scenario is attractive for the following reasons: (i) the planet formation interval time ($\tau_{\rm pl}$) of $\sim 10^5$ yr is in line with the pebble-driven growth scenario that we have previously explored (Ormel et al. 2017; Schoonenberg et al. 2019). (ii) Other parameters are also natural or in line with the constraints from Objective I. No anomalous eccentricity damping is present ($A_e = 1$), the value of A_a is in line with theory (Liu et al. 2017), and the values of $\tau_{a,\oplus}$ that are required are overall consistent with the Objective I results. Hence, we favour this scenario to explain the architecture of the the TRAPPIST-1 system.

In the Early Cavity Infall model (Fig. 3.14), efficient eccentricity-damping is preferred to prevent the outer planets, especially planet d, from crossing the desired resonances due to the stochastic nature of resonance trapping at high eccentricity. For the TRAPPIST-1 system, such high eccentricity-over-semi-major axis damping (low C_e) is also used in other literature studies, e.g., Teyssandier et al. (2021) and MacDonald et al. (2021). The most straightforward explanation is that Type I disc migration, being a complex phenomenon, operated less efficient in TRAPPIST-1, i.e., that γ_I is smaller than what linear theory prescribes. In addition, subdued Type-1 migration would also ensure A_a will be above the required threshold. A low C_e parameter is also required in the K2-24 planetary system to reproduce its observed TTV signals (Teyssandier & Libert 2020).

3.7.2 Resonances Establishing and Breaking

Three-body resonances play a crucial role in shaping these scenarios. A multi-planet resonant system as TRAPPIST-1 is characterized by many adjacent and non-adjacent three-body resonances, with some of the Φ_i librating, while others do not. This dynamical imprint strongly constrains the formation history of the TRAPPIST-1 system. In 3BRs, resonance locking limits the ability for period expansion. In the literature, certain mechanisms that have been invoked to separate two-planet systems by divergent migration, e.g., stellar tidal damping (Lithwick & Wu 2012; Batygin & Morbidelli 2013) or magnetospheric rebound (Liu et al. 2017). When, however, the planets are instead connected to other planets through three-body resonances, all planets participate in the expansion and the effects on –say– the inner two planets are potentially limited. Specifically, for TRAPPIST-1 the $\Phi^{2,5,3}_{\rm c,d,e}$ resonance, corresponding to the 3:2 and 3:2 MMR of planets c/d/e, naturally forms during the migration phase (Stage I), but greatly hinders the further period expansion of the inner planet system towards their observed period ratios. As this angle is currently not librating, we conclude that it must have been broken early, which would be achieved when planets b and c fell into the cavity and were repulsed by the gas disc. This allows the subsequent expansion of the inner planet system b/c/d towards their observed orbital period ratios.

This (temporary) decoupling of the inner planet system from the other TRAPPIST-1 planets was already employed in the study by Papaloizou et al. (2018), where initially two dynamically separate subsystems (b/c/d and e/f/g/h), each locked in their respective three-body resonances, dynamically converge into the present configuration under the action of stellar tidal forces only. As in that scenario stellar tides would primarily operate on the inner system, it naturally explains its expansion. However, Papaloizou et al. (2018) do not motivate the origin of the two subsystems, their initial separations and the initial period ratios within

[1] That is, $\tau_{1\rm s}/10 \lesssim \tau_a + \tau_{\rm pl}$. The factor 10 reflects the distance over which planet c migrates, which is about 1/10 of its semi-major axis. Also, $\tau_a \ll \tau_{\rm pl}$.

each system. Indeed, the initial setup of these simulations follows from the formation stage. We find that during the expansion, planets may well enter the wrong three-body resonance (especially $\Phi^{2,5,3}_{c,d,e}$, $\Phi^{3,15,12}_{c,e,f}$ and $\Phi^{5,14,9}_{c,d,e}$; see Fig. 3.9, Fig. 3.10 and Fig. 3.14), which stellar tides alone is too weak to break. This supports our scenario where the inner-most planets were pushed into the disc cavity.

To achieve a first-order resonant chain, we need to assume that planets c and g start in a 3:2 and 4:3 resonance (Fig. 3.8). Coleman et al. (2019) and Burn et al. (2021) also initialize planet embryos close to each other such to avoid trapping in wider MMR like 2:1 and 3:2. A natural explanation is that these planets formed rapidly one-after-another, which is conceivable in the pebble-driven formation model (Schoonenberg et al. 2019; Lin et al. 2021a).

In this work, we simplify the disc model without complicating disc-planets interactions via introducing, e.g., radial gravity (Nagasawa et al. 2003; Pan et al. 2020) and stochastic torque (Rein & Papaloizou 2009; Paardekooper et al. 2013) induced by the disc and raised on planets. How much difference those mechanisms can make to 3BR trapping and escaping need to be addressed in the future.

3.7.3 Application to other systems

In our model, the planet in the disc cavity can be repulsed inward slowly by Lindblad resonance from the external disc. Three-body resonance with two planets in the external disc can then halt the inward migration in the disc cavity. This mechanims therefore enables a configuration with the inner planets more separated from each other than the outer planets. Although three-body resonances are not ubiquitous in the Kepler data (Goldberg & Batygin 2021), we expect that configurations with separated inner planets near higer-order resonances may be connected by three-body resonances.

We give three examples. HD 158259 is a six planets system (Hara et al. 2020). The period ratios are $P_c/P_b = 1.57$, $P_c/P_b = 1.51$, $P_c/P_b = 1.53$, $P_c/P_b = 1.51$ and $P_c/P_b = 1.44$, where planet b and c are more separated than other adjacent plant pairs. Interestingly, planet c, d and e in HD 158259 are near 3:2 mean-motion resonance, similar to planet d, e and f in TRAPPIST-1. Based on our analysis in Sect. 3.4, we predict that the three-body resonance angle $\Phi_{b,d,e} = 3\lambda_b - 15\lambda_d + 12\lambda_e$ in HD 158259 system is librating. This angle is equivalent to Φ_2 in TRAPPIST-1 (Sect. 3.4 and Sect. 3.5).

Other systems, while not sharing the same period ratios configuration as TRAPPIST-1, do feature wider-spaced inner planets. Recently, Leleu et al. (2021) found that the five outermost planets of the six-planet TOI-178 system constitute a 2:4:6:9:12 chain of Laplace resonances. The period ratio of the second-to-innermost planet is 1.69. Since this period ratio is close to 5:3, it may indicate that planet b is connected by the outer planets through three-body resonance. In the Kepler-80 system, the period ratios of the six planets are 3.1, 1.511, 1.518, 1.35, and 1.538 from inner to outer respectively (Xie 2013; MacDonald et al. 2021). Although the period ratio of 3.1 cannot be explained by the Lindblad torque mechanism, it would still be worthwhile to investigate whether a 3BR trapping may occur at this location. To address what role 3BRs in these systems have played in shaping the configuration of these systems, the first step is to evaluate their strength by numerical simulations such as done in this work.

3.8 Conclusions

We conducted N-body simulations to reconstruct the origin of the dynamical structure of planets in the TRAPPIST-1 system. Our model covers the stages directly after planet forma-

tion ($\sim 10^5$ yr) in the proto-planet disc, until the present age. Two objectives were pursued: the formation of a chain of first-order MMR (Objective I) and the evolution of the inner-most planets towards their present dynamical configuration (Objective II). In the Late Infall Model planets b and c entered the disc cavity at some time after all planets entering the resonant chain, and were repulsed by the one-sided Lindblad torque exerted by the exterior disc. Together with stellar tidal damping, this provided for the expansion of the inner sub-system towards its present configuration. In the preferred Early Infall Model, planet b and c fall in the cavity before the outer planets entering the resonant chain. Then, planet c can migrate across the resonant locations in the cavity before their existence.

We list our main findings from this study:

1. The 4:3 MMR of planet f & g stands out as the closest resonance. In simple disc models planets f & g fail to cross the 3:2 resonance without preventing other planets from obtaining a more compact configuration. The 4:3 MMR could be explained as an imprint of rapid sequential planet formation, whereafter f and g migrated convergently.

2. Simple scenarios that feature only disc and stellar tidal damping fail to meet Objective II. Due to three-body resonance locking, the inner subsystem cannot expand independently from the rest of the system.

3. Objective II can be reached when planets b and c entered the disc cavity. The disc further repulsed the planets in the cavity by virtue of the order $m = 1$ outer Lindblad torque whose resonant location still resides in the disc. This repulsion is a crucial mechanism in aligning the inner system towards the observed 3BRs and period ratios.

4. Efficient eccentricity-damping ($C_e \sim 0.1$) and a strong disc inner barrier ($A_a \sim 100$) were found to be advantageous to obtain the desired resonance configuration. These imply a small value for the Type I migration prefactor γ_I.

5. In the Late Infall model, planet b and c enter the disc cavity after outer planets enter the resonant chain. To reproduce TRAPPIST-1, it is necessary to enhance the eccentricity damping of planet d at the cavity by large amounts ($A_e \gtrsim 10$).

6. In our preferred scenario, planet b and planet c enter the disc cavity early, before the outer planets have joined the resonance chain. To allow planet c to migrate across the barrier resonances, the planet formation interval time $\tau_{\rm pl}$ is about 10^5yr.

7. Tidal dissipation decreases the eccentricities and increases the period ratio among planets in a three-body resonance chain. After all planets have been connected by three-body resonances, it is the period ratio of the outermost planet pair (h and g) that increases most, while the rate of the expansion is determined by the tidal dissipation of the innermost planet b. For our model, we constrain the tidal quality factor of planet b $Q_b \gtrsim 200 k_2$.

8. Three-body resonances play an important role in shaping the dynamical structure of the TRAPPIST-1 planets. In contrast to two-body resonances, 3BRs do not necessarily break when exposed to a divergent force. In this study, a numerical approach was used to assess the strength of 3BR and we have highlighted the role of non-adjacent 3BR. Due to their significance in shaping scenarios containing divergent migration, a more comprehensive understanding of 3BR is in need.

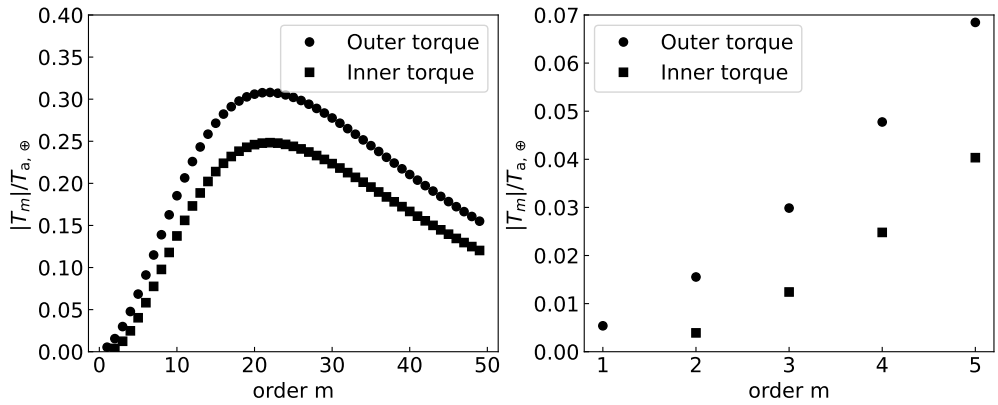


Figure 3.15. Torque magnitude as a function of order, m, normalized to the Type I migration time-scale for scale height $h = 0.03$ and disc surface density gradient $k = 0.5$. Left panel present the order m from 1 to 50. Right panel zoom in m from 1 to 5.

Appendix

3.A Lindblad torque

Following Ward (1997), we calculate the magnitude of the Lindblad torque at different order (m) of Lindblad resonance. We insert disc scale height $h = 0.03$, disc power-law surface density gradient $k = d\ln\Sigma_g/d\ln r = 0.5$ and disc temperature gradient $l = \mathrm{d}\ln T/\mathrm{d}\ln r = 1$. The left panel of Fig. 3.15 shows the Lindblad torque scale by Type I migration torque at the first 50 orders Lindblad resonance location and the right panel only shows the first five orders. For m=1 only an outer Lindblad torque is present, which is used in this work. Its value is 0.0054.

4

The dynamics of the broken resonance chain systems and their formation: the Solar System

In the past two decades, transit surveys have revealed a class of planets with thick atmospheres – sub-Neptunes – that must have completed their accretion in protoplanet disks. When planets form in the gaseous disk, the gravitational interaction with the disk gas drives their migration and results in the trapping of neighboring planets in mean motion resonances, though these resonances can later be broken when the damping effects of disk gas or planetesimals wane. It is widely accepted that the outer Solar System gas giant planets originally formed in a resonant chain, which was later disrupted by dynamical instabilities. Here, we explore whether the early formation of the terrestrial planets in a resonance chain (including Theia) can evolve to the present configuration. Using N-body simulations, we demonstrate that the giant planet instability would also have destabilized the terrestrial resonance chain, triggering moon-forming giant impacts in 20–50% of our simulated systems, dependent on the initial resonance architecture. After the instability, the eccentricity and inclination of the simulated planets match their present-day values. Under the proposed scenario, the current period ratio of 3.05 between Mars and Venus – devoid of any special significance in traditional late formation models – naturally arises as a relic of the former resonance chain.

S. Huang★, C. W. Ormel, S. Portegies Zwart, E. Kokubo, T. Yi (2025) A Resonant Beginning for the Solar System's Terrestrial Planets. ApJ, 988, 137

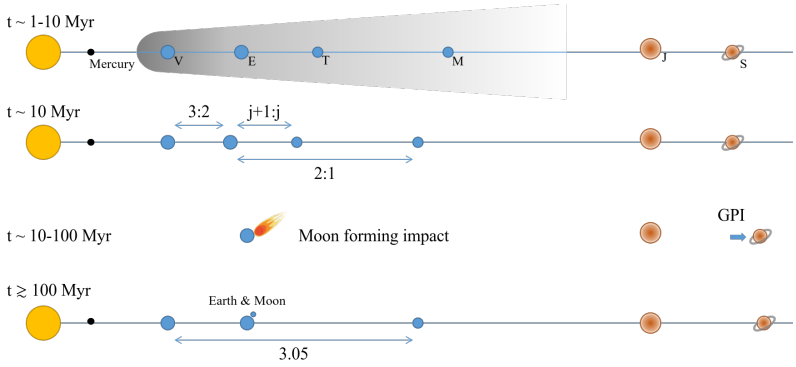


Figure 4.1. Sketch illustrating the dynamical evolution of the solar system planets during and after disk dissipation. The two-sided arrows represent the existence of mean motion resonances. Blue and brown scatters represent terrestrial bodies, including Venus (V), proto-Earth (E), Theia (T), and Mars (M), and gas giants including Jupiter (J) and Saturn (S). In the disk phase ($t \lesssim 1$ Myr), terrestrial planets form and migrate convergently. Theia and Earth are in $j+1:j$ resonance, where j is the resonance number. At $t \gtrsim 1$ Myr, i.e., just after disk dispersal, planets are still locked in a resonance chain. At $t \sim 10$ Myr, the outward migrating Saturn excites Jupiter, triggering the giant planet instability (GPI), which also destabilizes the resonance chain and triggers the moon-forming giant impact. After $t \sim 100$ Myr, the planets stabilize to the current architecture.

4.1 Introduction and motivation

If two planets are in a (first-order) orbital mean motion resonance, their period ratio stays close to an integer ratio, $j+1{:}j$. Because the conjunction point occurs close to the pericenter of the inner and apocenter of the outer planet, the mean motion resonance enhances the dynamical stability of planetary systems (Tamayo et al. 2017; Goldberg et al. 2022). Mathematically, the resonance angles, which express the point where in the orbit conjunctions take place, are said to librate for planets in resonance. Examples in our solar system are the 1:2:4 resonance among Galilean moons and the 3:2 resonance between Neptune and Pluto. Many exoplanet systems are discovered to be in resonance as well, e.g., TRAPPIST-1 (Gillon et al. 2017; Luger et al. 2017), TOI-178 (Leleu et al. 2021), TOI-1136 (Dai et al. 2022), HD110067 (Luque et al. 2023). Planets in resonances are expected to experience large-scale migration, which is naturally explained by the formation of planets early, in a gas-rich disk (Papaloizou & Szuszkiewicz 2005). Exoplanet formation is widely believed to occur within protoplanetary disks, as supported by both observations (Andrews et al. 2018; Keppler et al. 2019; Barber et al. 2024) and theoretical models (Drążkowska et al. 2023; Mordasini et al. 2015). Efficient Type I migration often traps planets into mean motion resonances, as evidenced by the observed period ratio distributions in exoplanet populations (Huang & Ormel 2023; Hamer & Schlaufman 2024), particularly in young systems (Dai et al. 2024). In contrast, non-resonant planets with circulating resonance angles located near integer period ratios are much less stable (Hu et al. 2025a).

Giant planets in our solar system are widely believed to start in a resonant configuration (Tsiganis et al. 2005). The resonance chain was then broken during giant planet instability (GPI, Liu et al. 2022; Griveaud et al. 2024; Brown et al. 2024). GPI is widely recognized as a turning point in the early evolution of our Solar System. In particular, such an event plays a key role in reproducing the observed orbital properties of the outer solar system bodies, such

Table 4.1. Orbital properties of Solar system planets (Murray & Dermott 1999). The planet mass, semimajor axis, orbital period, eccentricity, and inclination in the ecliptic and invariable planes are listed.

Name	m_p [$M_\oplus$]	a_p [au]	P [days]	e	Ecliptic i [deg]	Invariable i [deg]
Venus	0.82	0.72	224.7	0.0068	3.394	2.19
Earth	1.00	1.00	365.2	0.0167	0.000	1.57
Mars	0.11	1.52	687	0.0934	1.850	1.67
Jupiter	317.8	5.20	4331	0.0484	1.303	0.32
Saturn	95.2	9.57	10747	0.0541	2.485	0.93

as the eccentricities and inclinations of the giant planets (Tsiganis et al. 2005), distribution of the Kuiper Belt (Levison et al. 2008) and asteroid belt (O'Brien et al. 2007), Trojan asteroids of Jupiter and Neptune (Morbidelli et al. 2005), and irregular moons around giant planets (Nesvorný et al. 2014). However, the migration of giant planets during GPI not only affects their own orbits but also has profound consequences for any existing terrestrial planets. As Saturn migrates outward, it induces sweeping secular resonances that can perturb the orbits of inner planets, potentially triggering orbital crossing and collisions (Brasser et al. 2009; Kaib & Chambers 2016; Thommes et al. 2008).

Dynamical constraints indicate that the GPI occurred within 100 Myr after the formation of the Solar System (Nesvorný et al. 2018; de Sousa et al. 2020). This timing suggests that terrestrial planet formation was largely complete before the instability took place (Kobayashi & Dauphas 2013). Consequently, the terrestrial planets would have been in place when GPI perturbed their orbits, setting the stage for significant dynamical rearrangement and collisions. The most compelling evidence of such a collision in our inner Solar System must be the Moon-forming giant impact (Canup & Asphaug 2001). Cosmochemical studies constrain the Moon-forming event to have occurred between 40 and 120 Myr after Solar System formation (Barboni et al. 2017; Thiemens et al. 2019), which overlaps significantly with the estimated timing of the GPI. This temporal correlation has motivated studies suggesting that the dynamical disturbances associated with the GPI may have triggered the Moon-forming giant impact (Clement et al. 2023). Specifically, in their model terrestrial planets form after gas dispersal by collisional growth between Mars-sized embryos (Clement et al. 2019).

It is still under debate whether terrestrial planets largely complete their growth early in the protosolar nebulae, when gas was still present (Johansen et al. 2024; Morbidelli et al. 2024). Here we hypothesize that the terrestrial planets in our Solar System formed early in the protosolar nebulae—a scenario supported by both formation models (Johansen et al. 2021; Brož et al. 2021) and observational work on Mars isotopes (Kobayashi & Dauphas 2013) and Earth oxidation state (Young et al. 2023; Johansen et al. 2023). Naturally, planets can get trapped in resonance due to disk migration. However, it remains unclear whether the observed architecture of the terrestrial planets can be reproduced starting from an initial resonance chain. To investigate this hypothesis, this work initializes terrestrial planets in a resonance chain. Their long-term dynamical evolution is tracked and studied.

The paper is structured as follows. We detailed the methodology in Sect. 4.2. Our main results and their comparison to the present solar system are in Sect. 4.3. The implications of our findings are discussed in Sect. 4.4. Finally, we state our conclusions in Sect. 4.5.

4.2 Model

We illustrate the dynamical evolution of terrestrial planets in Fig. 4.1 over time. In our setup, we include four terrestrial planets—Venus, proto-Earth, Theia, and Mars—in resonance. We exclude Mercury from the resonance chain because of its potentially distinct formation history compared to the other terrestrial planets (e.g. Johansen & Dorn 2022; Morbidelli et al. 2022). Mercury is also very far from other terrestrial planets, interior to the 3:1 period ratio of Venus. Including it would not affect the current results due to the very low mass of Mercury (half that of Mars). Besides, Mercury seems to experience more complex dynamical interaction with the Sun, as evidenced by the 3:2 spin-orbit resonance (e.g. Wieczorek et al. 2012; Noyelles et al. 2014).

In addition, we include two gas giants, Jupiter and Saturn, initially arranged more compactly than observed today with a period ratio smaller than 2, and Saturn migrates outward to its present orbit (Morbidelli et al. 2007; Levison et al. 2011). During this migration phase (giant planet instability), Jupiter's eccentricity is excited at various resonance locations, and the terrestrial planets experience secular perturbations from the giant planets (Brasser et al. 2009; Kaib & Chambers 2016).

In our scenario, the terrestrial resonance chain is broken during Saturn's outward migration, leading to increased eccentricities among the terrestrial planets. The Moon-forming giant impact is then triggered once the orbits of proto-Earth and Theia overlap. Since Venus and Mars are relatively distant from their neighboring terrestrial planets, their orbits remain largely unchanged, thereby preserving the initial 3:1 period ratio between Mars and Venus, which is consistent with current observations.

We use the REBOUND (Rein & Liu 2012) package to conduct the N-body calculations. The migration and eccentricity damping forces are implemented using REBOUNDx (Tamayo et al. 2020) and the MERCURIUS integrator (Chambers 1999; Rein et al. 2019) is employed.

4.2.1 Initial conditions

The terrestrial planets are initially set in resonance in our N-body simulations. In our model, Venus reaches the migration barrier, possibly the disk inner edge, which promotes convergent migration and thus resonance trapping (see Fig. 4.1). To achieve these initial resonant conditions, we follow the approach of (Tamayo et al. 2017): we first position the planets slightly away from exact resonance and then allow convergent migration to capture them into resonance while damping their eccentricities. The acceleration term due to the gravitational interaction with the disk used in our N-body calculations is

$$\boldsymbol{F_i} = \frac{\boldsymbol{v_i}}{2\tau_{\mathrm{a},i}} + \frac{2(\boldsymbol{v_i}\cdot\boldsymbol{r_i})\boldsymbol{r_i}}{r_i^2\tau_{\mathrm{e},i}}, \tag{4.1}$$

where $\boldsymbol{v_i}$ and $\boldsymbol{r_i}$ denote the velocity and position vector of planet i, and $\tau_{\mathrm{a},i}$ and $\tau_{\mathrm{e},i}$ are the semimajor axis and eccentricity damping timescale. Venus migrates outward on a timescale τ_{a} of 10 Myr. Such a long timescale represents the end stage of the disk environment. Planet eccentricities are damped on a timescale of $\tau_{\mathrm{e}} = \tau_{\mathrm{a}}/K_{\mathrm{e}}$, where K_{e} is a free parameter ranging from 10^2 to 10^4. The parameter K_{e} controls the eccentricities of the terrestrial planets in the resonance chain (Tanaka & Ward 2004). Large K_{e} leads to smaller eccentricities.

The simple migration setup described above ensures convergent migration and, consequently, resonance trapping in a controlled manner. In reality, however, the process of resonance trapping is more complex. Convergent migration may occur, for instance, if Venus

halts its migration at the migration barrier of the protoplanet disk (Liu et al. 2022; Ogihara et al. 2024; Wu & Chen 2025). The detailed processes by which terrestrial planets form and migrate within the disk remain uncertain but do not matter for this study as long as the terrestrial planets end up in the resonance chain depicted in Fig. 4.1.

Jupiter and Saturn are also included in the simulation. Jupiter is initialized at its present-day orbital period with eccentricity $e_{\mathrm{J,ini}}$ ranging from 0 to 0.05, and an inclination of 0.5 degrees. Saturn is placed at an initial period ratio of 1.9 with Jupiter, i.e., closer to Jupiter than at present and within the 2:1 resonance location.

Most simulations succeed in forming a resonance chain, characterized by the libration of resonance angles among the terrestrial planets. We consider the point when Venus has migrated to 0.72 au (the current location of Venus) as the initial conditions for the post-disk dynamical evolution.

4.2.2 Giant planet instability

During the phase of giant planet instability, Saturn migrates outward. The driven process and the timescale of such migration are still under active debate (Liu et al. 2022; de Sousa et al. 2020; Agnor & Lin 2012). We therefore parameterize Saturn's migration with the additional acceleration term in the N-body calculation:

$$\boldsymbol{F} = \frac{1}{2}\frac{a_0 - a_f}{a}\frac{\boldsymbol{v}}{\tau_{\mathrm{S}}}e^{-t/\tau_{\mathrm{S}}}, \tag{4.2}$$

where a_0 and a_f are the initial and expected final positions of the body, a and $\boldsymbol{v}$ are the semi-major axis and velocity of the migrating body, and τ_{S} controls the timescale of the migration. It results in the semimajor axis changing in the form of $a(t) = a_f + (a_0 - a_f)e^{-t/\tau_{\mathrm{S}}}$ (Brasser et al. 2009; Kaib & Chambers 2016; Fang et al. 2025). Such exponential migration has been implemented in REBOUNDx by Ali-Dib et al. (2021). We run simulations varying the outward migration timescale of Saturn τ_{S} from 0.8 to 16 Myr. The solar system is integrated for 100 Myr. The parameter sensitivity is discussed in Appendix 4.B

4.2.3 Theia and proto-Earth mass-radius calculation

After Theia collides with proto-Earth, the resulting merger—the Earth-Moon system—is located at the center of mass of the two original bodies. Since Earth currently orbits at 1 au, we fix the center of mass at 1 au in our setup, meaning that different initial configurations for Earth and Theia yield different planet mass ratios.

Assuming a perfect merger and small eccentricities, angular momentum conservation gives:

$$m_{\mathrm{E}}\sqrt{a_{\mathrm{E}}} + m_{\mathrm{T}}\sqrt{a_{\mathrm{T}}} = (m_{\mathrm{E}} + m_{\mathrm{T}})\sqrt{a_{\oplus}}. \tag{4.3}$$

The "E" and "T" notations are for proto-Earth and proto-Theia, while $\oplus$ notation is for the present-day Earth. After inserting values, we find

$$m_{\mathrm{T}} = m_{\mathrm{E}}\frac{\sqrt[3]{\frac{2P_{\oplus}}{3P_{\mathrm{V}}}} - 1}{\sqrt[3]{\frac{j+1}{j}} - \sqrt[3]{\frac{2P_{\oplus}}{3P_{\mathrm{V}}}}} = m_{\mathrm{E}}\frac{0.0272}{\sqrt[3]{\frac{j+1}{j}} - 1.0272} \tag{4.4}$$

where j is the resonance number of proto-Earth and Theia. When $j = 4$, $m_{\mathrm{T}} = 0.54m_{\mathrm{E}}$. when $j = 3$, $m_{\mathrm{T}} = 0.37m_{\mathrm{E}}$. We assume $m_{\mathrm{E}} + m_{\mathrm{T}} = 1.05m_{\oplus}$ in all of our calculations. Venus and Mars

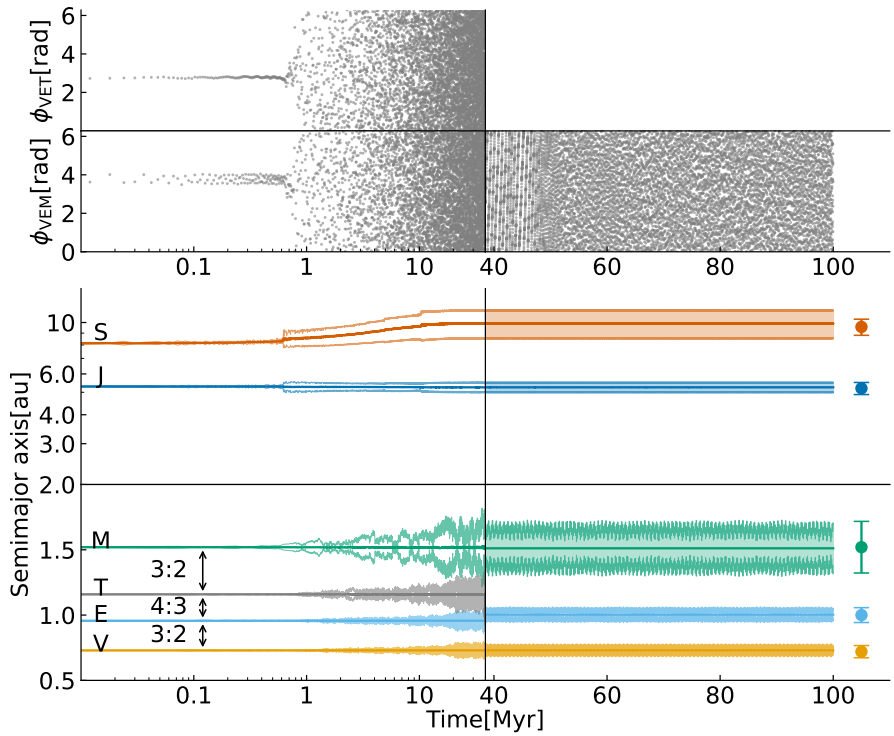


Figure 4.2. Dynamical evolution of planets during Saturn's outward migration and the post-Moon-forming impact phase. The top panel shows the evolution of 3-body resonance angles of Venus, Earth, and Theia (ϕ_{VET}) and Venus, Earth, and Mars (ϕ_{VEM}). The resonance angles are defined in Sect. 4.3. The bottom panel shows the changes of planet semimajor axis and eccentricity with time. The curves show the orbital evolution of each body, including its semi-major axis (thick), perihelion, and aphelion (thin). The terrestrial planets are initially in a resonance chain. The corresponding resonances are labeled by the double-headed arrows. The semimajor axis, aphelion, and perihelion of the current solar system planets are denoted by the error bars at the right. The adopted parameters are: $e_{J,ini} = 0.005$, $\tau_S = -4.7$ Myr and $K_e = 5.6 \times 10^3$. The crossing of the 2:1 resonance between Saturn and Jupiter (≈1 Myr) also destabilizes the inner solar system, breaking its resonances and resulting in the Moon-forming event (≈35 Myr).

do not experience giant impacts as suggested for Earth, and their mass does not change in our model.

Planets collide if their physical radii overlap. Planet radii are adopted from current measurements, except for proto-Earth and Theia, which no longer exist in the present Solar System. For bodies with masses below $1\,m_\oplus$, we use the mass-radius relationship

$$\frac{R}{1\,R_\oplus} = \left(\frac{m}{1\,m_\oplus}\right)^{0.29} \tag{4.5}$$

as given in (Seager et al. 2007), which employs a polytropic model to describe the internal structure of rocky planets. The adopted planet properties are summarized in Table 4.1.

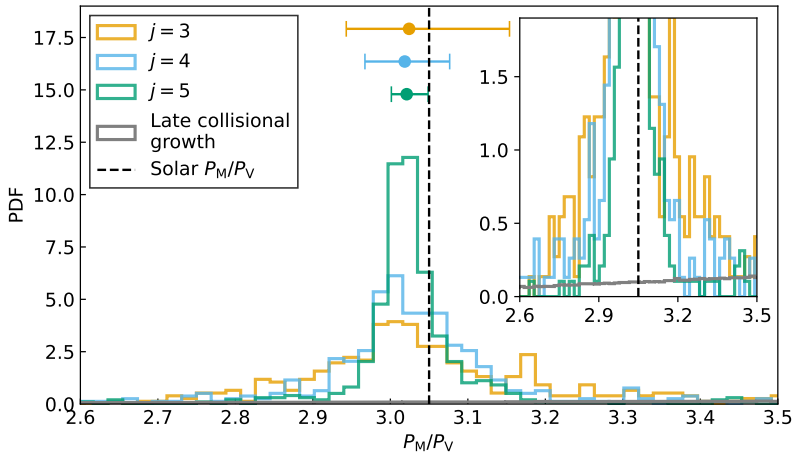


Figure 4.3. Mars-Venus period ratio probability distribution from different models. The current value is shown by the vertical dashed line. The colored histograms are the subgroup of simulated systems (defined in Fig. 4.7) of the early, resonant, formation models, with different colors representing the Theia and Earth resonances through the resonance number j. The corresponding median 50% ranges and the median values are indicated by the error bars and their center values. The grey histograms are the results of the post-nebulae collisional growth model, which does not feature an elevated probability near the 3:1 period ratio (see Appendix 4.C). The figure inset features a shorter range of the y-axis

.

4.3 Comparison with Solar system

Firstly, we hypothesize that the four terrestrial planets—Venus, Earth, Theia, and Mars—emerged from the gaseous disk in a 2:3:4:6 resonance chain. We find that this resonant architecture is a natural consequence regardless of whether planet formation proceeds via pebble accretion or planetesimal accretion (see Appendix 4.A). This resonance chain guarantees a 3:1 period ratio between Mars and Venus. Due to their close spacing, Theia and proto-Earth are prone to collide once the resonance is broken, giving rise to the Earth-Moon system at 1 au. Consequently, the mass ratio between Theia and proto-Earth is based on their initial positions; with Venus fixed at its current distance of 0.72 au, the mass ratio amounts to 0.37 (see Eq. (4.4)).

It was constrained that the giant planet instability occurred in the first $10 - 100$ Myr after the formation of Calcium-aluminum-rich Inclusions (CAIs) (Edwards et al. 2024). This instability may be triggered either by gas disk dissipation (Liu et al. 2022; Thommes et al. 2008), by self-driven dynamical processes (de Sousa et al. 2020; Griveaud et al. 2024), or even by stellar encounters (Portegies Zwart et al. 2021; Brown et al. 2024). In our simulations, we simply migrate Saturn outward, following approaches used in previous studies (Brasser et al. 2009; Kaib & Chambers 2016; Fang et al. 2025). The timescale of Saturn's outward migration, τ_S, is parameterized between 0.8 and 16 Myr (Liu et al. 2022; Griveaud et al. 2024). Although the dynamical instability of the giant planets has shaped many other features of the outer Solar System (e.g. Tsiganis et al. 2005; Morbidelli et al. 2005; Ormel & Huang 2025), here we focus on its effect on the architecture of the terrestrial planets.

Figure 4.2 illustrates a representative simulation in which the primordial resonance chain is broken by the migrating Saturn. Initially, both 3-body resonance angles, which are com-

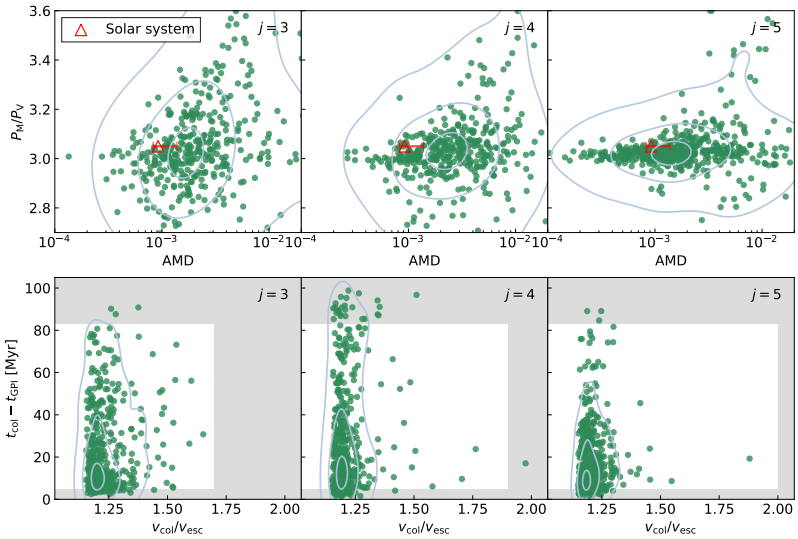


Figure 4.4. Planet properties for the simulated Solar-like systems in which Theia collides with Earth. The definition of Solar-like system is inFig. 4.7. Each simulation starts with a terrestrial resonance chain and two gas giants. Theia and Earth are initially in $j+1{:}j$ resonance, with the resonance number j=3, 4, or 5 labeled on the top right of each panel. The top panels show the Angular Momentum Deficit (x-axis) and Mars-Venus period ratio (y-axis). The present-day Solar System is marked by a triangle for comparison, while the error bar shows the range in secular evolution (Ito & Tanikawa 2002). The bottom panels show Theia's collision velocity with Earth in terms of the escape velocity (x-axis) and the collision time with respect to the GPI (y-axis). Permissible cosmochemical constraints on the timing (Barboni et al. 2017; Thiemens et al. 2019) of the GPI and SPH simulation constraints on the impact velocity of the Moon-forming event (Timpe et al. 2023) are indicated by the white window, in which the GPI is assumed to occur at 37 Myr after CAI (de Sousa et al. 2020).

posed of the mean longitudes of relevant planets ϕ_{VET} and ϕ_{VEM} librate, where $\phi_{\mathrm{VET}} = 2\lambda_{\mathrm{V}} - 6\lambda_{\mathrm{E}} + 4\lambda_{\mathrm{V}}$ and $\phi_{\mathrm{VEM}} = 2\lambda_{\mathrm{V}} - 4\lambda_{\mathrm{E}} + 2\lambda_{\mathrm{M}}$. In our model, Jupiter's eccentricity is excited to approximately $e_{\mathrm{J}} \approx 0.05$ as Saturn crosses the 2:1 resonance (Lithwick et al. 2012). Subsequently, the g_5 secular resonance (Brasser et al. 2009) sweeps through the terrestrial planets' orbits and the angular momentum deficit (AMD) – a measure of the dynamical excitation of the system (Laskar 1997) – diffuses (Kaib & Chambers 2016), disrupting their resonant configuration. With circulating resonance angles planets are no longer in resonance, but remain near integer period ratios. In addition to the secular perturbations from Jupiter, close encounters among near-resonant terrestrial planets further amplify planet eccentricities, leading to orbital overlap between Theia and Earth, culminating in their collision. Following the Moon-forming event, the terrestrial orbits stabilize as they are displaced away from both secular and mean-motion resonances. Although the semi-major axes remain essentially constant, the eccentricities continue to librate under Jupiter's secular influence (Murray & Dermott 1999). Overall, our simulation reproduces the orbital properties of the present-day terrestrial planets.

Perhaps the most direct quantity to compare the simulated systems with the current Solar System is the period ratio between Venus and Mars, which is observed to be $P_{\mathrm{M}}/P_{\mathrm{V}} = 3.057$. We compile the period ratios from our simulations across different parameter sets. The statistics of simulated systems, such as displayed in Fig. 4.3, include only those simulations

in which Jupiter's free and forced eccentricities match their present-day values. See appendix 4.B (Fig. 4.7) for discussion on how this selection was made. All other figures in the main text are also based on this conditional subset. The probability distribution of P_M/P_V peaks at approximately 3.01, consistent with the planets' pre-instability configuration—a value that arises from the balance between planet migration and eccentricity damping (Charalambous et al. 2022). Due to planet-planet scattering during the simulation, the distribution broadens from a δ-function, with the observed period ratio falling within the 25% range from the median. For comparison, we also overplot the period ratio distribution from the late formation model (see Fig. 4.11 in Appendix 4.C), in which terrestrial planets grow via mutual giant impacts between planet embryos. Compared to the late formation model, the early formation scenario yields a probability density higher by more than an order of magnitude of reproducing the observed Mars-Venus period ratio. The zoomed-in version of the period ratio distribution in the late formation scenario is also shown, in the subset.

We also run two additional sets of simulations, varying the resonant configurations of Theia and proto-Earth by initializing them in a 4:5 mean-motion resonance (MMR, j=4) and a 5:6 MMR (j=5), while preserving the 2:3:6 resonance chain among Venus, proto-Earth, and Mars to maintain the 3:1 period ratio between Mars and Venus. In each case, we recalculate the mass ratio of Theia-to-proto-Earth to ensure that their center of mass remains at 1 au. As the resonance index j increases, Theia's mass also increases. The resulting Mars-Venus period ratios are shown in Fig. 4.3 (blue and green lines). When Theia starts in a closer orbit to Earth (i.e., with a higher j value), the spread of the period ratio distribution narrows. This occurs because a more massive Theia is less susceptible to excitation and remains closer to Earth, making it more difficult to perturb Mars. Consequently, the simulated Mars-Venus period ratio exhibits a stronger peak around 3.01, although the observed value still falls within the quartile range of the distribution. Later dynamical processes could further adjust the planet positions. For example, the ≈0.05 wt% late veneer accreted by Mars (Brasser et al. 2016) may have slightly shifted its orbit outward.

Apart from the period ratio, we used another system-level indicator to test whether our simulated systems are consistent with the global properties of the Solar System – the Angular Momentum Deficit (AMD)

$$\mathrm{AMD} = \frac{\Sigma_j M_j \sqrt{a_j}(1 - \sqrt{1 - e_j^2}\cos i_j)}{\Sigma_j M_j \sqrt{a_j}}. \tag{4.6}$$

Our simulation results match the Solar System well. As shown in Fig. 4.4 (top panels), the solar system resides within the central 10% of the distribution derived from our simulations. The higher eccentricity of Jupiter (grey scatter) results in systems with larger terrestrial AMD. A more direct approach is to individually compare each planet's eccentricity and inclination. As demonstrated in Fig. 4.8, the terrestrial planets in our simulations exhibit eccentricities and inclinations similar to those observed in the present-day Solar System.

The simulated planet systems exhibit a wide range of dynamical outcomes. In our simulations, Theia does not always collide with Earth; it may instead impact Mars, or if the system becomes too dynamically excited, it may lead to multiple planet collisions. Conversely, in some simulations, the planets remain on their initial orbits with minimal excitation, or they become over-excited to high inclinations that no collisions occur at all. Figure 4.5 presents the statistical distribution of these outcomes. The desired scenario—Theia colliding with Earth—occurs in 20-50% of simulated systems, depending on the initial resonant configuration (j). Naturally, placing Theia in a mean-motion resonance (MMR) closer to Earth pro-

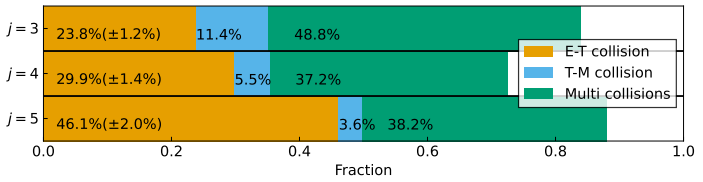


Figure 4.5. Statistical outcomes of simulated Solar-like systems, with final Jupiter eccentricities similar to the present day value (Fig. 4.7). The architecture of simulated systems is classified into four groups: Theia collides with Earth (orange); Theia collides with Mars (blue); There are multiple collisions (green); No collisions occur (white). The fractions of different types of simulated Solar systems are stated, where for the Earth-Theia collision case the Poisson error is also stated. Different j values (y-axis) represent different initial resonance configurations between Earth and Theia.

motes orbital overlap between the two bodies, while simultaneously reducing the probability of Theia impacting Mars.

It is commonly accepted that the Moon was formed through a giant impact (Canup et al. 2023). We record the time of the Theia-Earth impact in our simulations in Fig. 4.4. About 50% of our simulated systems have Theia and Earth colliding within 30 Myr. Since our simulations start with the onset of giant planet instability (GPI), the absolute time (w.r.t CAI formation) of the Theia-Earth collision needs to be corrected accordingly. Dynamical evidence of Kuiper belt objects in our solar system shows that the GPI occurs at 37-62 Myr after CAI (de Sousa et al. 2020). Assuming GPI occurs at 37 Myr, then the simulated Theia and Earth collide at $\approx$ 67 Myr w.r.t CAI formation. Such timing is consistent with the cosmochemical constraints that the Moon-forming giant impact is at 40-120 Myr (Barboni et al. 2017; Thiemens et al. 2019).

In the canonical model of the Moon-forming event, a Mars-sized body collides with proto-Earth, delivering the angular momentum required for the Earth-Moon system (Canup & Asphaug 2001). However, the isotopic similarities between the Earth and the Moon (Wiechert et al. 2001) suggest that either the impactor had nearly the same composition as Earth or, more naturally, that the collision was highly energetic. For this reason, a scenario with a more massive impactor has recently emerged as a promising alternative (Lock et al. 2018; Asphaug et al. 2021), which also guarantees a sufficiently massive proto-lunar disk (Timpe et al. 2023). In our model, the mass ratio γ between Theia and proto-Earth is 0.37, 0.54, and 0.76 for the initial 4:3, 5:4, and 6:5 Theia-Earth resonances, respectively. Given these mass ratios, the collision velocity is constrained to $\lesssim 1.5 v_{\rm esc}$, where $v_{\rm esc}$ is the mutual escape velocity of the target and impactor (Timpe et al. 2023; Asphaug et al. 2021). As shown in Fig. 4.4, our simulated systems exhibit relatively low impact velocities because the resonance configuration allows the planets to be closely spaced initially. These modest impact velocities are in line with the aforementioned constraints in the scenario of a more massive Theia than the canonical model.

4.4 Implications

The implication of our model is that proto-Earth formed early, which has been argued to be inconsistent with the observed Hf-W isotope system in bulk silicate Earth (BSE) (Morbidelli et al. 2024). This occurs because, during core formation, the lithophile parent element ^{182}Hf remains in the mantle, leading to an excess of its decay product ^{182}W relative to present-day

measurements (Olson et al. 2022). However, several factors could operate to decrease the relative abundance of ^{182}W in the Earth's mantle. For example, an effective equilibration between the iron core and the mantle after the Moon-forming event (Deguen et al. 2011), the late accretion of ∼10% planetesimals (Olson & Sharp 2023), or multiple collisions in a hit-and-run scenario (Asphaug et al. 2021), would reduce the concentration ^{182}W in the mantle. Because Venus never experienced violent impact events such as the Moon-forming giant impact in our model, we expect the Venus mantle to be largely primordial, with a much higher ^{182}W abundance than in Earth's mantle.

An early formation scenario, as proposed here, would resolve the challenges posed by the later formation model. These include: 1) The absence of a moon for Venus is puzzling (Asphaug et al. 2021; Malamud & Perets 2024), giving the prevalence of giant impacts in the late accretion model (Jacobson et al. 2014). 2) The need for post-impact damping mechanisms (Clement et al. 2023), such as by leftover planetesimals, to reduce the eccentricities to their observed values (Hansen 2009). Collisional growth also results in random orientation of the spin axis (Chambers 2001; Miguel & Brunini 2010), inconsistent with solar terrestrial planets. 3) The magma ocean may exist and prevent the formation of an early and stable crust due to the frequent collisions in the late collisional growth scenario, inconsistent with the early crust on Earth (Harrison 2009).

Mars grew up in the first 1-10 Myr (Dauphas & Pourmand 2011; Kobayashi & Dauphas 2013; Marchi et al. 2020; Woo et al. 2021), contemporaneous with the lifetime of the gaseous protoplanetary disk (Weiss et al. 2021). There are no fundamental reasons why growth for the other terrestrial planets would have been stalled at Mars size. Mature exoplanets are widely believed to be formed in the gas disk (Drążkowska et al. 2023; Mordasini et al. 2015), as evidenced by the detections of young planets (David et al. 2019; Keppler et al. 2019; Barber et al. 2024; Dai et al. 2024).

Yet >80% of those found by Transit (using Kepler and TESS) are not in resonance (Huang & Ormel 2023; Hamer & Schlaufman 2024). Various scenarios have been proposed to explain the overall observed non-resonant planetary architecture statistically, due to dynamical instability triggered by disk dispersal (Izidoro et al. 2021), and planet-planet scattering (Wu et al. 2024b; Li et al. 2024). Recently, radial velocity follow-up studies have revealed the existence of outer gas giant(s) to systems hosting inner planets with irregular architecture (He & Weiss 2023). This finding aligns with the scenario that an external perturber destroyed the inner resonance architecture. Scenario similar to the one proposed here for the Solar System could therefore have been common in the evolution of exoplanet systems (Yi et al. 2025b). Notably, no outer giant planet has yet been observed in evolved resonance chain systems (e.g., TRAPPIST-1 Boss et al. 2017).

4.5 Conclusions

We hypothesize that terrestrial planets (including Theia) in our Solar system formed early in the protosolar nebula. Naturally, they are trapped in a resonance chain. Starting with the resonant configuration, we use N-body simulations to study the destabilization of the resonance chain and long-term evolution. During the evolution, Theia commonly collided with proto-Earth (at a rate 20 ∼ 50%, depending on the initial resonance between Earth and Theia). A comparison with the properties of Solar System terrestrial planets shows that our model satisfies four key constraints:

1. The Mars-Venus period ratio of 3.05 is a relic of the former resonance chain. This value

arises naturally in the early formation scenario, with a probability density an order of magnitude higher than in the late formation model (Fig. 4.3).

2. The resulting planet eccentricities and mutual inclinations are moderate in the simulated systems. Their values are consistent with the current solar system (Fig. 4.4 upper panels and Fig. 4.8). No post-moon forming damping is required.

3. The impact velocity between Earth and Theia is always $\lesssim$1.5 of the escape velocity (Fig. 4.4 lower panels) in our simulated systems, consistent with the Moon-forming giant impact (Timpe et al. 2023).

4. The Earth-Theia giant impact follows the onset of giant planet instability, and occurs $\gtrsim$ 10 Myr afterwards (Fig. 4.4 lower panels). It is in line with cosmochemical dating.

Two immediate predictions follow from our investigation. First, a giant impact event with Venus is disfavored in our model. Therefore, its mantle composition stays largely primordial, and we expect its isotopic signature to reflect early formation. Future missions characterizing isotopic abundances on Venus would offer the opportunity to verify the early formation models for the Solar terrestrial planets in this work.

Second, most exoplanets are not in resonance. They may start in resonance but later get destabilized. We demonstrate that the outer massive companion can destroy the resonance chain. Our dynamical study hints that those exoplanet systems that harbor evolved long resonance chains are unlikely to host external gas giants.

Appendix

4.A Formation of a resonant chain in the pebble accretion and planetesimal accretion models

We employ simplified planet formation models to demonstrate that the initial resonant architecture of the terrestrial planets is feasible. In Fig. 4.6, we show that both pebble accretion and planetesimal accretion can produce a resonant configuration within a gaseous disk—the starting condition for our study. In the pebble accretion scenario, planet embryos are introduced sequentially at the water iceline, then grow and migrate inward one after another. In contrast, the planetesimal accretion scenario initializes embryos simultaneously at different orbital distances. Ultimately, these processes yield a 2:3:4:6 resonance chain corresponding to Venus, Earth, Theia, and Mars. Notably, the final resonant architecture depends on the time interval (for pebble accretion) or spatial separation (for planetesimal accretion) between adjacent planet pairs. To achieve a tighter resonance between Theia and Earth, the interval between the initial Earth and Theia embryos must be reduced.

In the following, we detail the models and the parameter choices used for planet formation. We fix the gas disk surface density distribution at:

$$\Sigma_{\rm g} = \Sigma_{\rm g,0} f_{\rm g} \left(\frac{r}{1\,{\rm au}}\right)^{\beta_0} \left(1 - \sqrt{\frac{r}{R_{\rm in}}}\right) e^{-\left(\frac{r}{R_{\rm out}}\right)^{2-\beta_0}}, \tag{4.7}$$

where $\Sigma_{\rm g,0} = 2\,400\,{\rm g/cm^2}$ is the surface density in the minimum-mass solar nebulae (MNSN), $f_{\rm g} = 5$ is the scaling factor of the initial gas surface density with respect to MNSN, $R_{\rm out} = 30\,{\rm au}$ is the disk outer radius, and $\beta_0 = -1.5$ is the surface density power law index. The

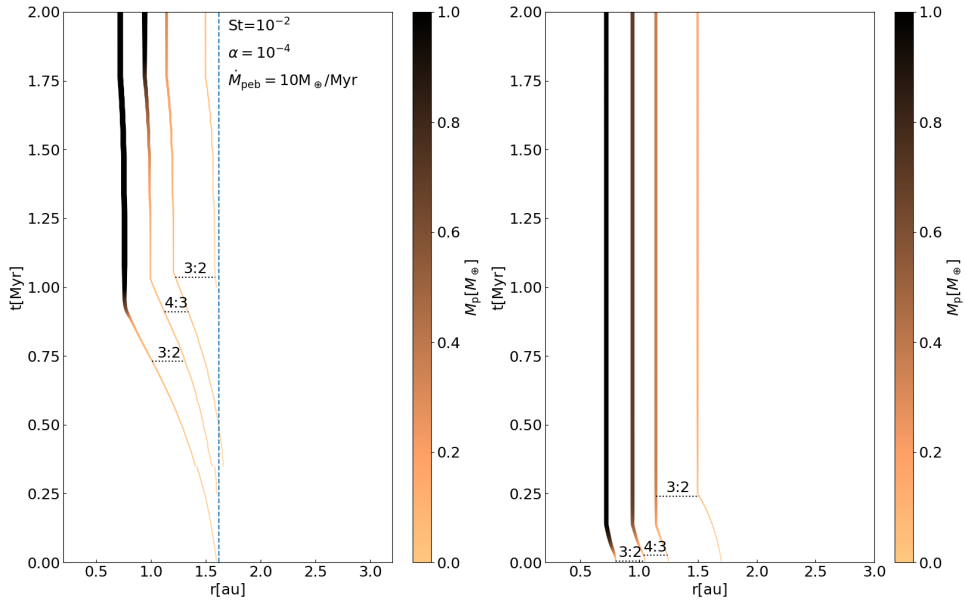


Figure 4.6. Simulations of planetary accretion and migration, illustrating the formation of resonant architectures. The left panel shows planets growing via pebble accretion, while the right panel depicts growth through planetesimal accretion, both occurring within a gaseous protoplanetary disk. In each panel, the trajectories represent the evolution of the semimajor axis (x-axis) and planetary mass (copper color) over time (y-axis). They denote, from left to right, Venus, Earth, Theia, and Mars. In the left panel, the vertical blue line marks the water snowline.

disk inner radius is set to be $R_{\rm in} = 0.6\,$au, which prevents Venus from migrating further inward. Such an effective inner disk edge (migration barrier) could be triggered by the wind-driven accretion increasing with time (Ogihara et al. 2024; Wu & Chen 2025). It ensures the convergent migration of terrestrial planets (Brož et al. 2021; Clement et al. 2021). The disk temperature profile is fixed at

$$T = T_0 \left(\frac{r}{1\,\mathrm{au}}\right)^{\xi_0}, \tag{4.8}$$

we take the temperature power law index $\xi_0 = -0.5$ and the temperature at 1 au $T_0 = 200\,$K.

For type-I migration, we use,

$$\dot{r} = -k_{\rm mig} \frac{m}{m_\star} \frac{\Sigma_{\rm g} r^2}{m_\star} h^{-2} v_{\rm K}, \tag{4.9}$$

where $\dot{r}$ is the shrinking rate of the planet's semimajor axis, h is the disk aspect ratio, and we take the mean molecular weight as 2.4. The prefactor $k_{\rm mig}$ depends on the disk properties. We adopt the fit from D'Angelo & Lubow (2010),

$$k_{\rm mig} = 2(1.36 - 0.62\beta - 0.43\xi), \tag{4.10}$$

where β and ξ are the local gradient indices of disk surface density and temperature. As the two adjacent planets convergently migrate to the resonance location, they get trapped with their periods near integer commensurability.

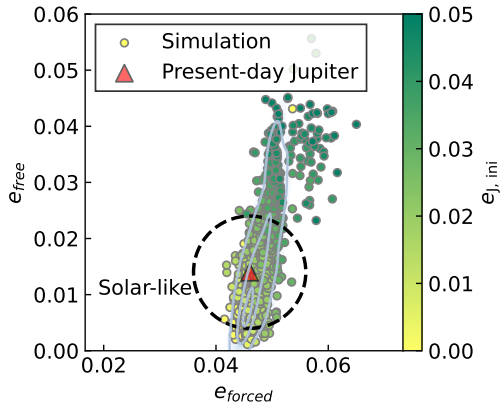


Figure 4.7. Jupiter's free and forced eccentricities obtained at the end of the simulations. The scatters with different colors are the results of the simulations starting with different initial Jupiter eccentricities. The solar system is marked as a triangle. The scatters in the circle (of radius 0.01) are indicated as the Solar-like systems in the simulation because they have similar Jupiter eccentricities as the present-day Jupiter.

If planets grow by pebble accretion (Fig. 4.6 left panel), we can get the accretion rates of the planet via

$$\dot{m} = \epsilon \dot{M}_{\rm solid}, \tag{4.11}$$

The 3D pebble accretion efficiency ϵ is calculated following Ormel & Liu (2018). It depends on the planet's eccentricity, the particle Stokes number St, the local gas pressure gradient η, the disk aspect ratio h, and the gas turbulent diffusion parameter $\alpha_{\rm t}$. The quantities h and η follow from the disk structure. We assume zero eccentricities, fix St=0.01 and $\alpha_{\rm t} = 10^{-4}$, and assume an incoming pebble mass flux of $\dot{M}_{\rm dust} = 10\, m_\oplus\, {\rm Myr}^{-1}$.

One of our simulation results is shown in Fig. 4.6 left panel. Similar to Johansen et al. (2021), we initialize four planet embryos at the iceline sequentially. They grow and migrate inward one by one. Venus stops its migration at 1 Myr because it reaches the migration barrier (Ogihara et al. 2024; Wu & Chen 2025). As the latter planets join, they form a 2:3:4:6 resonance chain. Their mass also increases after the formation of a resonance chain due to pebble drift in the disk. At the end of the simulation time (2 Myr), all four planets have their mass close to the present values.

Alternatively, if planets grow up from accreting planetesimals (Fig. 4.6 right panel), the planet oligarchic growth timescales follow from (Kokubo & Ida 2002)

$$\tau_{\rm p} = 1.2\times10^5\ {\rm yr} \left(\frac{\Sigma_{\rm plts}}{10\,{\rm g\,cm^{-2}}}\right)^{-1} \left(\frac{r}{1\,{\rm au}}\right)^{\frac{3}{5}} \left(\frac{m}{m_\oplus}\right)^{\frac{1}{3}} \left(\frac{\Sigma_{\rm g}}{2400\,{\rm g\,cm^{-2}}}\right)^{-\frac{2}{5}} \left(\frac{m_{\rm plts}}{10^{18}\,{\rm g}}\right)^{\frac{2}{15}}, \tag{4.12}$$

where m is planet mass, the mass of a planetesimal $m_{\rm plts}$ is fixed to be 10^{18} g, equivalent to a diameter of ≈6 km for an internal density of 1 g/cm^3. The initial planetesimal disk surface density distribution $\Sigma_{\rm plts}$ follows a similar shape as the gas disk in Eq. (4.7),

$$\Sigma_{\rm plts} = 90\,{\rm g/cm^2} \left(\frac{r}{1\,{\rm au}}\right)^{\beta_{\rm plts}} \left(1-\sqrt{\frac{r}{R_{\rm in}}}\right) \exp\left[-\left(\frac{r}{R_{\rm out}}\right)^{2-\beta_{\rm plts}}\right], \tag{4.13}$$

but with most of the planetesimal concentrated at $\sim$ 1 au by using a much steeper gradient value $\beta_{\rm plts} = -5.5$. Such a ring-like distribution of planetesimals is advantageous for forming

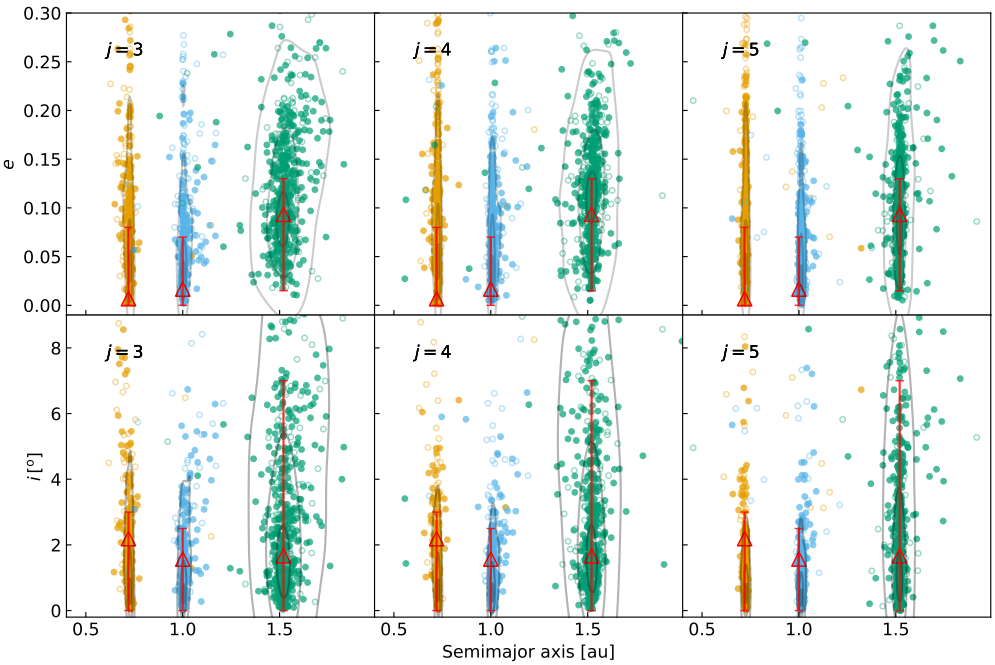


Figure 4.8. Dynamical properties for planet systems, in which Theia collides with Earth. The upper panels show the final eccentricities of Venus, Earth, and Mars, while the lower panels display their final inclinations relative to the invariable plane. Different scatter points are the results of the simulations that end up with Solar-like (solid dots) or other (open dots) systems (see Fig. 4.7 for definition). We overplot the median 10%, 50%, and 90% contours of the scatter. Each column corresponds to a different initial Venus-Mars resonance. For reference, we include the present-day eccentricities of the terrestrial planets and the inclinations (triangle) and the range of them on secular timescales (error bar) of the terrestrial planets (Ito & Tanikawa 2002).

a small Mars, aligning with the previous findings (Woo et al. 2024). Similar to Emsenhuber et al. (2021), we subtract the accreted planetesimal mass from the planetesimal surface density profile. The width of the feeding zone is 6 times the planet Hill radius centered at the planet orbit (Lissauer 1993).

The planet formation simulation via the above planetesimal accretion is shown on the right panel of Fig. 4.6. All four embryos are initialized at the start, but at different locations. The ring-like distribution of planetesimals is centered at 1 au, promoting the growth of Venus and Earth. Therefore, they gain more mass than Theia and Mars. Finally, they consume all the planetesimals in their feeding zones, reaching the planetesimal isolation mass. The planets are born inside the 2:1 resonance. With slight migration, they are trapped in the 2:3:4:6 resonance chain.

Despite simplifying processes such as disk evolution and planetesimal scattering, and lacking exhaustive parameter exploration, these simulations reveal that both planetesimal and pebble accretion models yield resonant configurations comparable to the initial conditions of our post-disk N-body framework.

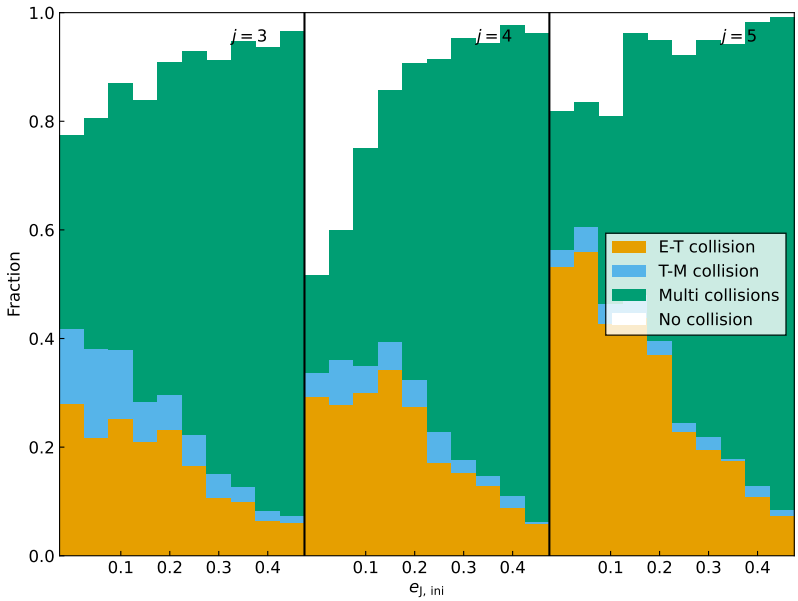


Figure 4.9. Statistical outcomes of the simulated Solar Systems and their dependence on initial conditions. The architecture of simulated systems is classified into four groups: 1) Theia collides with Earth (orange); 2) Theia collides with Mars (blue); 3) There are multiple collisions (green); 4) No collisions occurred within the end time of the simulation (white). The left, middle, and right panels display results for different initial resonances between Earth and Theia (the resonance number is shown at the top right of each panel). Within each panel, separate histograms represent simulation outcomes starting with different initial eccentricities for Jupiter.

4.B Parameter sensitivity

To assess how the properties of the simulated systems depend on the initial conditions, we systematically varied two key parameters: the initial eccentricity of Jupiter $e_{\mathrm{J,\,ini}}$, and the initial resonance configuration between Earth and Theia, characterized by the resonance number j. In contrast to these parameters, our experiments show that the results are nearly insensitive to variations in the eccentricity damping parameter in the disk K_{e} and Saturn's outward migration timescale τ_{S}. The timescale of Saturn's outward migration τ_{S} is parameterized between 0.8 to 16 Myr. The eccentricity damping factor K_{e} is changed logarithmically in a range of evenly-spaced grids from 10^2 to 10^4.

Naturally, varying the initial eccentricity of Jupiter affects its final eccentricity. In Fig. 4.7, we show the forced and free eccentricities from all our simulations. We change $e_{\mathrm{J,\,ini}}$ in the range of 0 to 0.05 (linear grid). As $e_{\mathrm{J,\,ini}}$ increases, both e_{forced} and e_{free} rise, with e_{free} exhibiting a more pronounced increase. For comparison, we also plot the observed value of Jupiter's eccentricity. Our results indicate that simulated systems align best with the Solar System when $e_{\mathrm{J,\,ini}} < 0.02$.

We select the simulated systems with their final Jupiter eccentricity close to the present-day Jupiter. Those systems are labeled as "Solar-like systems", as highlighted by the circle in Fig. 4.7. The radius of the circle is 0.01. Then, the dynamical properties of the planets in the Solar-like systems are compared with those in the real Solar system. We already studied the angular momentum deficit (AMD), period ratio, impact velocity, and the timing

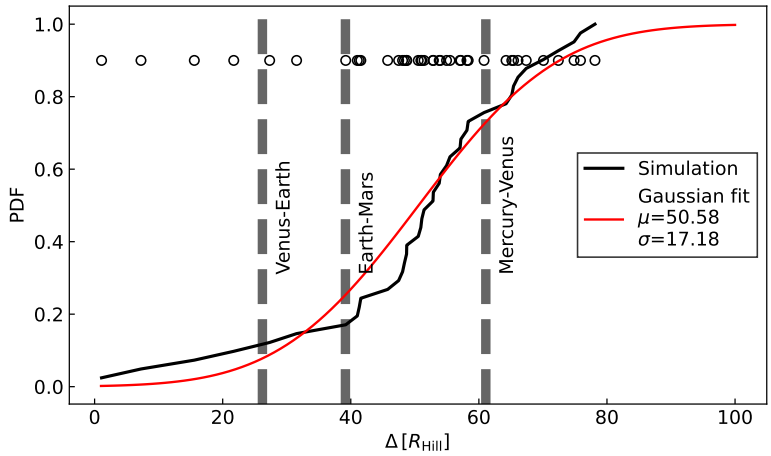


Figure 4.10. Cumulative distribution of the mutual separation (Δ) between each two adjacent terrestrial planets in the collisional growth scenario. The unit is the mutual Hill radius. The black curve shows the distribution of the simulation results. Each data point from the simulation is shown with the black circles. We use a Gaussian to fit the probability distribution, as shown in the red curve. The vertical dashed lines show the values from the terrestrial planets in the Solar system.

between Theia and Earth in the main text (Fig. 4.4). Here, the eccentricity and inclination of each terrestrial planet are shown in Fig. 4.8. The eccentricity and inclination values in our simulated systems are consistent with the secular evolution of the real Solar system. To give a full comparison, the information of those systems that are not Solar-like is also exhibited using open circles in Fig. 4.8. We also test three different initial architectures, corresponding to three different values of the resonance number $j = 3, 4, 5$ between Theia and Earth. As j increases, Theia stays in an orbit closer to the Earth. As a result, Mars experiences less close encounters with Theia and its semimajor axis is less dispersed.

Variations in the initial eccentricity of Jupiter, $e_{\mathrm{J,ini}}$, lead to markedly different system architectures (see Fig. 4.9). A higher $e_{\mathrm{J,ini}}$ more strongly perturbs the inner terrestrial planets via secular interaction, resulting in a higher frequency of multiple collision events. In contrast, when Jupiter starts on a nearly circular orbit, such violent interactions are less common. A higher fraction of systems only have one single collision or are even collision-free over the 100 Myr simulation period. In the systems that stayed collision-free, half have their resonance angles circulate. For those systems, we expect the planets to eventually collide. Otherwise, the terrestrial planets are still linked by the original resonance chain. As j increases, more and more simulated systems have Theia and Earth collisions (orange bars) while fewer have Theia colliding with Mars (blue bars). In Fig. 4.9, the number of collision-free systems increases when j increases from 3 to 4, due to the stronger resilience of the 5:4 resonance. As j increases to 5, the number of collision-free systems decreases again due to the instability triggered by too close orbits between Theia and Earth (Petit et al. 2020).

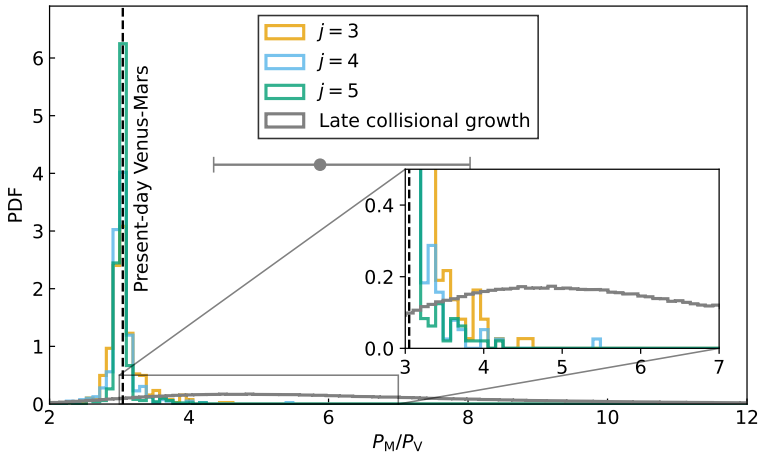


Figure 4.11. Mars-Venus period ratio probability distribution from different models. Similar to Fig. 4.3, here we zoom in to display the shape of the period ratio distribution resulting from the late formation scenario (grey histogram). The median 50% range and the median value of the late formation distribution are indicated by the error bar and its center value. We zoom in on the plot in the inset such that the peak of the period ratio distribution in the late formation scenario is visualized.

4.C Venus-Mars period ratio in the late collisional growth scenario

While exhibiting the properties of simulated systems in our early formation scenario, we also compare the Venus-Mars period ratio with that from the late formation scenario. In such a case, planets are formed by the collisional growth between planetesimals and Mars-sized embryos.

The simulation setups for the late collisional growth scenario are the same as those used in Kokubo et al. (2025). We give a brief description here. The simulations start with 15 protoplanets of equal mass, each with $m = 0.15\,m_\oplus$. Their semimajor axes are distributed between 0.5 and 1.5 au, with adjacent protoplanets separated by 10 times the mutual Hill radius. The initial eccentricities and inclinations follow Rayleigh distributions with dispersions of $\sigma_e = 0.01$ and $\sigma_I = 0.005$. Each body is assumed to have a mean bulk density of $3\,\mathrm{g\,cm^{-3}}$. In total, 20 independent simulations are performed.

The dynamical evolution of the system is computed using a modified Hermite integrator, as described by Kokubo et al. (2025), which efficiently resolves close encounters while ensuring accurate energy conservation in gravitational N-body simulations. To accelerate the simulation, a block timestep scheme has been adopted (Makino 1991). Perfect accretion is assumed when two planets collide, conserving both mass and momentum. Each simulation runs for 1.7×10^2 Myr.

We here calculate the separation between each pair of adjacent planets at the end of the 20 simulations, and the results are shown in Fig. 4.10. This figure shows the distribution of the post-giant impact semi-major axes difference among the planets in units of the mutual Hill radius (Δ). Systems with close-to-zero Δ are allowed (stable) due to their large mutual inclinations, $\sim 10^o$. The separations among the terrestrial planets in the Solar system are also indicated. The simulated distribution of separations closely matches the values observed in

the Solar system. We find that the probability distribution peaks around 50 Hill radii. To fit this distribution, we use a Gaussian profile. The best fit to the distribution in Δ is given by a mean value of $\mu = 50.58$ and a standard deviation $\sigma = 17.18$.

Using this separation distribution, we apply the Monte Carlo method to generate a distribution of the period ratio between Venus and Mars. We generate two sets of separation distances: one covering the Venus-Earth pair and the other for the Earth-Mars pair, assuming that $\Delta \sim \mathcal{N}(\mu, \sigma)$ for each of them. The set of synthetic Δ is then converted back into period ratios, and the resulting distribution is shown in Fig. 4.3. Figure 4.11 provides the same information, but with an extended period ratio. The peak of the period ratio distribution of the late formation scenario (≈ 4.9) is about twice that of the present-day value (3.05). Statistically, only the lower 10% percentile covers the real Mars-Venus period ratio of 3.05. More detailed analyses are presented in (Kokubo et al. 2025) in the context of dynamical stability criteria for Kepler planet systems.

5

Birth stellar cluster dynamics matters: planet population synthesis with external photo-evaporation

Current exoplanet formation studies tend to overlook the birth environment of stars in clustered environments. However, the effects of this environment on the planet formation process are important, especially in the earliest stage.
Aims: We investigate the differences in planet populations forming in star-cluster environments through pebble accretion and compare these results with planet formation around isolated stars. We strive to provide potential signatures of the young planetary systems to guide future observations.
Methods: We present a new planet population synthesis code designed for clustered environments. This planet formation model is based on pebble accretion and includes migration in the circumstellar disk. The disk's gas and dust have been evolved via 1D simulations, while considering the effects of photo-evaporation of the nearby stars.
Results: Planetary systems in a clustered environment are different than those born in isolation; the environmental effects are important for a wide range of observable parameters and the eventual architecture of the planetary systems. Planetary systems born in a clustered environment lack cold Jupiters, as compared to isolated planetary systems. This effect is more pronounced for low-mass stars ($\lesssim 0.2\ M_\odot$). On the other hand, planetary systems born in clusters show an excess of cold Neptunes around these low-mass stars.
Conclusions: In future observations, finding an excess of cold Neptunes and a lack of cold Jupiters could be used to constrain the birth environments of these planetary systems. Exploring the dependence of cold Jupiter's intrinsic occurrence rate on stellar mass offers insights into the birth environment of their proto-embryos.

S. Huang★, S. Portegies Zwart, M. J. C. Wilhelm (2024) Suppression of giant planet formation around low-mass stars in clustered environments. A&A, 689A, 338

5.1 Introduction

Since the first discovery of an exoplanet around a solar-type star (Mayor & Queloz 1995), the rapidly growing number of detected exoplanets continues to improve our understanding of planet formation. The abundance and diversity of known exoplanets offer the opportunity to take a statistical approach to planet formation theories (Zhu & Dong 2021).

Planets are expected to form in the circumstellar disks surrounding young stars. The Atacama Large Millimeter/submillimeter Array (ALMA) has provided unprecedented views into these planet-forming disks (e.g., Andrews et al. 2018; Long et al. 2018; Cieza et al. 2019; Öberg et al. 2021). ALMA continuum observations reveal the presence of (sub)millimeter-sized particles, commonly known as pebbles, within protoplanetary disks (e.g., Ansdell et al. 2017). These pebbles are the essential building blocks for planets and play a crucial role in the efficient accretion onto planet cores, facilitating their growth (so-called pebble accretion, Ormel & Klahr 2010; Lambrechts & Johansen 2012).

Pebble accretion is advantageous for the rapid growth of cold giants due to its short timescale (Johansen et al. 2019). Planetesimal accretion can also grow planets, particularly in short Keplerian orbits (Johansen & Bitsch 2019). As the core mass is massive enough, gas accretion commences and gas giants can be formed (via so-called core accretion Perri & Cameron 1974). Another way to form a gas giant is direct gravitational instability (GI, Toomre 1964; Boss 1997), however, it requires a cold and massive disk that goes on to fragment and collapse. Once planets grow massive enough, they perturb the gas disk and exchange angular momentum, triggering planet migration (Lin & Papaloizou 1979; Goldreich & Tremaine 1980). These simplified planet formation theories help improve our understanding of the observed exoplanet demographics. This objective has driven numerous planet population synthesis studies (e.g., Mordasini et al. 2009; Ida et al. 2018; Chambers 2018; Forgan et al. 2018; Johansen et al. 2019; Miguel et al. 2020; Emsenhuber et al. 2021; Johnston et al. 2024; Lau et al. 2024; Chakrabarty & Mulders 2024).

The effects of the star cluster environment on planet formation are not typically addressed in simplified planet formation models. The validity of such simplifications warrants examination from two perspectives: the importance and ubiquity of star clusters for the planet formation process. Firstly, its importance is evident during planet formation. Protoplanetary disks, where the building blocks of planets originate, can be influenced by the cluster environment. A compelling example is Proplyds, identified in the Orion Nebula Cluster (ONC; O'Dell et al. 1993; O'Dell & Wen 1994). These objects are observed to lose mass due to intense external photo-evaporation (EPE), highlighting the impact of the cluster environment on planetary systems. Various simulations are conducted addressing the EPE effect on protoplanet disks in the cluster. Secondly, the clustered nature of star formation is a common occurrence. Stars predominantly form within molecular clouds (Lada & Lada 2003), which are extensive structures spanning tens to hundreds of light-years. The regions within these clouds undergo gravitational collapse that ultimately leads to the formation of star clusters Portegies Zwart et al. (2010). Nevertheless, the relatively short disassociation timescale of clusters into the Galactic field ($\sim$ 100 Myr, Lamers et al. 2005; Portegies Zwart et al. 2010; Krumholz et al. 2019) may result in a much less clustered distribution than what is currently observed .

Star clusters exert various effects on protoplanetary disks, including external photoevaporation (e.g., Winter et al. 2022; Wilhelm et al. 2023; Qiao et al. 2023; Weder et al. 2023), external heating (Ndugu et al. 2018), and dynamical truncation (Portegies Zwart 2016; Ndugu et al. 2022). Recent planet population synthesis studies have incorporated close truncation

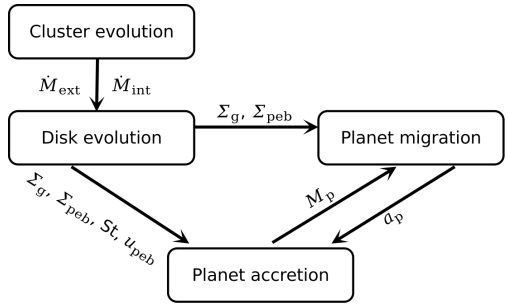


Figure 5.1. Sub-modules and most important exchanged quantities of our population synthesis model. The boxes indicate different physical modules. The arrows refer to the direction of data transported from one module to another.

and external heating to investigate the behavior of planet demographics post-formation using planet population synthesis models (Ndugu et al. 2018, 2022). The impact of external photoevaporation on the resulting planet population in clusters remains unclear. In this paper, we employ our newly developed code, namely, PACE using the AMUSE framework (Portegies Zwart et al. 2009, 2013b; Pelupessy et al. 2013), to synthesize and simulate planet formation in the perturbed environments.

The structure of the paper is outlined as follows. In Sect. 5.2, we detail the processes involved in planet formation. In Sect. 5.3, we describe our initial conditions and parameter selections. The results from planet population syntheses are analyzed in Sect. 5.4. Additionally, we present our simplified analytical criteria for forming cold Jupiters and its validation against simulation results in Sect. 5.5. Finally, our discussion is presented in Sect. 5.6, followed by our conclusion in Sect. 5.7.

5.2 Methods

Our model includes four main physical processes: cluster evolution, proto-planet disk evolution, planet accretion, and planet migration, as shown in Fig. 5.1. Different sub-modules are bridged via VENICE (Wilhelm & Portegies Zwart in prep.) using the AMUSE framework (Portegies Zwart et al. 2009, 2013b; Pelupessy et al. 2013). In the following subsections, we describe in detail how each sub-module works and interoperates, illustrating these details in Fig. 5.1.

5.2.1 Cluster evolution

We started by simulating star formation in the molecular cloud. From the spatial position of stars, we can calculate and apply external photoevaporation to each planetary system. The EPE mass-loss rates are derived from interpolation on the FRIED grid (Haworth et al. 2018). Only stars more massive than 7 $M_\odot$ exert extreme ultraviolet (EUV, $E_\gamma = 13.6 +$ eV) and far ultraviolet (FUV, $E_\gamma = 5.6 - 13.6$ eV) radiation to nearby stars. The dynamical truncation is ignored as its effect is small compared to EPE (Wilhelm et al. 2023).

We summarize the model used to evolve star formation and cluster evolution, following the approach outlined in Wilhelm et al. in prep (employing methods similar to those described in Wilhelm et al. 2023). We used TORCH (Wall et al. 2019, 2020) to simulate the

Table 5.1. Default disk and planet parameters used during the planet formation.

Description	Symbols	Value(s)
Metallicity	[Fe/H]	0.02
Disk-to-star mass ratio	$M_{\rm d,0}/M_\star$	0.1
Mean molecular weight	μ	2.3
Viscosity-α	$\alpha_{\rm t}$	10^{-4}
Accretion-α	$\alpha_{\rm acc}$	10^{-3}
Adiabatic index	γ	7/5
Dust fragmentation velocity [m/s]	$v_{\rm frag}$	10
Minimum dust size [cm]	a_0	0.001
Envelope opacity [$\rm m^2 kg^{-1}$]	κ	0.005

collapse of the molecular cloud. The dynamical interactions between stars and the gas are considered using BRIDGE (Fujii et al. 2007; Portegies Zwart et al. 2020) in the AMUSE framework (Portegies Zwart et al. 2009; Pelupessy et al. 2013).

Initially, the star-forming cloud has a mass of 10^4 $\rm M_\odot$, a radius of 7 pc, and an ambient temperature of 30 K. The cloud features a Gaussian density profile and a turbulent velocity field with a Kolmogorov spectrum. Notably, our realization of the turbulent velocity field differs from that in Wilhelm et al. (2023) and has an initial virial ratio of 1. The resulting stellar density in the cluster depends on the initial virial ratio. The cloud is embedded in a uniform background medium with a density of 1.25 hydrogen nuclei $\rm cm^{-3}$ and a temperature of 8000 K.

In Fig. 5.2, we present the cluster with its residual gas at an age of 2.43 Myr after the start of the collapse of the giant molecular cloud. At this stage in the evolution, the cluster is composed of two separated structures, which are expected to merge eventually. The cluster has 6,890 stars with a total mass of 4019 $\rm M_\odot$. The cluster is quite dense, with a 90% Lagrangian radius of 1.69 pc, a half-mass radius of 0.35 pc, and a central density of $\sim 1.1\times10^4$ stars/$\rm pc^3$.

We indicate the EPE of each disk in Fig. 5.2 in colors. Circumstellar disks close to the cluster density centers are more strongly affected by external photoevaporation than those further out, even though some of the most massive stars are orbiting the cluster periphery. Mass segregation has caused massive stars to sink toward the density center, and the core mass function is flat with an exponent of $\alpha \simeq 1.35$ compared to Salpeter ($\alpha = 2.35$). This flatter slope is consistent with the predicted core-mass function of a cluster in a state of core-collapse Fujii & Portegies Zwart (2011). Circum-stellar disks that were prevented from escaping the cluster center are strongly affected by FUV and EUV from the nearby massive stars. Strong radiation of nearby stars and the star formation process also drive a large cavity at the center of the molecular cloud. This reduces the effect of shielding the core population from FUV and EUV photons. The EPE of stars between 1.9 and 7 $M_\odot$ are not calculated in the FRIED grid; thus, they are not shown in Fig. 5.2.

The star-averaged EPE at each time and time-averaged EPE for each star are calculated in Fig. 5.3 (left and right panels, respectively). The initial EPE is low because the most massive stars have not yet formed. Generally, the majority of disks have been externally evaporated effectively, with the mass loss rate of $\sim 10^{-7}\,M_\odot \rm yr^{-1}$. Only 26 disks have an EPE smaller than $\sim 10^{-9}\,M_\odot \rm yr^{-1}$: these stars are nearly isolated from the massive stars in the cluster and we expect their circumstellar disks to disperse after $\gtrsim 10$ Myr (so-called Peter Pan disk), which is much longer than typical disks (Wilhelm & Portegies Zwart 2022).

5.2.2 Disk model

After a star forms, the conservation of angular momentum causes the nearby bound gaseous material to flatten and become a circumstellar disk. Stars with mass $< 1.9\,M_\odot$ are assumed to form circumstellar disks in our model with ~ 10 percent of the host mass. Further evolution of the disk is simulated following Wilhelm et al. (2023). The model includes the viscous evolution of the gas disk and the dust radial drift. Our adopted disk-evolution model is one-dimensional (1D) and does not account for asymmetric structures such as density spirals or warps.

Gas evolution

The evolution of the gas profile in the disk bases on VADER (Krumholz & Forbes 2015), which is a numerical integration of the α-disk model (Shakura & Sunyaev 1973; Lynden-Bell & Pringle 1974). The disk accretion for α-disk $\lesssim 10$ au is approximately

$$\dot{M}_\mathrm{g} = 3\pi\nu\Sigma_\mathrm{g}, \tag{5.1}$$

where $\upsilon = \alpha_\mathrm{acc} h^2 \Omega$ is the viscosity, Ω is the Keplerian orbital frequency, and $h = \sqrt{k_\mathrm{B}T/\mu m_H}$ is the disk scale height. As pointed out by Johansen et al. (2019), the α-disk model would not be valid if the disk accretion is driven by disk winds (Bai & Stone 2013). We therefore simply parameterize α_acc as a dimensionless representation of the disk accretion flux, instead of the turbulent viscosity parameter that is typically used.

External photoevaporation (EPE) causes the reduction of the disk mass from the outer disk edge inward. The amount of mass removed depends on the irradiation due to the other stars in the cluster (Sect. 5.2.1). The EPE mass loss rates are updated every 10 kyr. Given that the evolution of the cluster structure occurs on much longer timescales and is not affected by the planet formation processes, this approach does not compromise the validity of our conclusions.

The effect of internal photo-evaporation (IPE) depends on the X-ray luminosity from the central star. The X-ray luminosity-mass relation of stars is fitted by Flaccomio et al. (2012) using the Chandra observation on stars in the Orion Nebula Cluster:

$$L_\mathrm{X} = 10^{1.7\log_{10}(M_\star/M_\odot)+30}\,\mathrm{erg/s}. \tag{5.2}$$

The IPE rate is calculated via

$$\log_{10}\left(\frac{\dot{M}_\mathrm{IPE}}{1\,M_\odot \mathrm{yr}^{-1}}\right) = A_\mathrm{L}\exp\left[\frac{(\ln(\log_{10}(\frac{L_X}{1\,\mathrm{erg/s}})) - B_\mathrm{L})^2}{C_\mathrm{L}}\right] + D_\mathrm{L}, \tag{5.3}$$

where $A_\mathrm{L} = -2.7326$, $B_\mathrm{L} = 3.3307$, $C_\mathrm{L} = -2.9868$ and $D_\mathrm{L} = -7.2580$ (Picogna et al. 2019).

Dust evolution

We adopted the two-population model based on Birnstiel et al. (2012). It utilizes two characteristic dust populations with small-size and large-size grains of radius a_0 and $a_1(t)$, respectively. Initially, all dust consists of small grains with $a_1(t = 0) = a_0$. Over time, the small grain size a_0 remains fixed, while a_1 increases exponentially on the timescale of

$$\tau_\mathrm{grow} = \xi(Z_0\Omega_\mathrm{K})^{-1}. \tag{5.4}$$

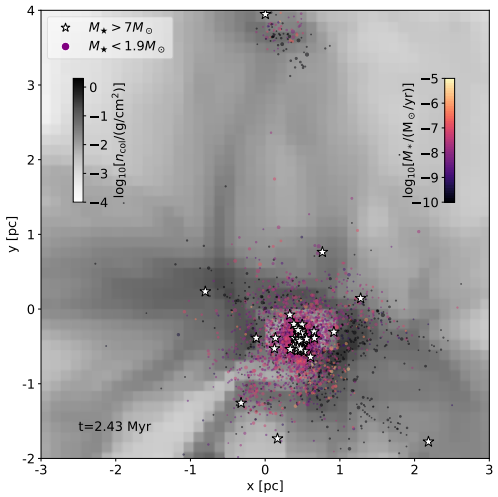


Figure 5.2. Spatial distribution of stars born in the collapsing molecular cloud in the final snapshot. The star symbol indicates the position of massive background stars ($> 7M_\odot$) that emit FUV and EUV radiation. Dots represent the relative low-mass stars ($< 1.9M_\odot$) that host disks. The size of the dot refers to the mass of the star, smaller dots are for smaller stars. The color of the dot indicates the external radiation strength and we convert it to the EPE of the disk, the magma color map is for the high EPE and the black is for the low EPE. The background gray color map of the grids represents the column density of the molecular cloud.

Here, Z_0 is the dust-to-gas ratio at orbital frequency $\Omega_{\rm K}$, with $\xi = 10$ (Krijt et al. 2016). The final grain size, a_1, is limited by radial drift, fragmentation, and drift-induced fragmentation. The mass fraction of the large dust population is

$$f_{\rm m} = \begin{cases} 0.97 & \text{if radial drift limits dust size,} \\ 0.75 & \text{otherwise.} \end{cases} \tag{5.5}$$

The two-population model allows for shorter computing times, which is advantageous in planet population synthesis studies. However, a more precise dust size evolution model, such as `Dustpy` (Stammler & Birnstiel 2022), is more costly in terms of computational time.

We incorporate the effect of EPE on the dust as well. Gas evaporates from the disk's midplane due to EPE. The gas flow carries small grains, while larger grains remain unaffected. The maximum grain size ($a_{\rm entr}$) that can be entrained with the EPE gas flow ranges from 0.1 μm to 1 mm (see Facchini et al. 2016, for detailed calculations). In this model, we assume a size distribution of the dust with power law $p = 3.5$. The fraction of dust smaller than $a_{\rm entr}$ is calculated and subtracted (Sellek et al. 2020).

5.2.3 Planet growth

Planet growth in this paper follows core accretion (Perri & Cameron 1974). The planet first forms the core, and it starts to accrete gas when it is massive enough.

Pebble accretion

Pebble accretion (Ormel & Klahr 2010; Lambrechts & Johansen 2012) is efficient in growing planets, especially for a Ceres- or Moon-sized planet embryo (Visser & Ormel 2016; Johansen

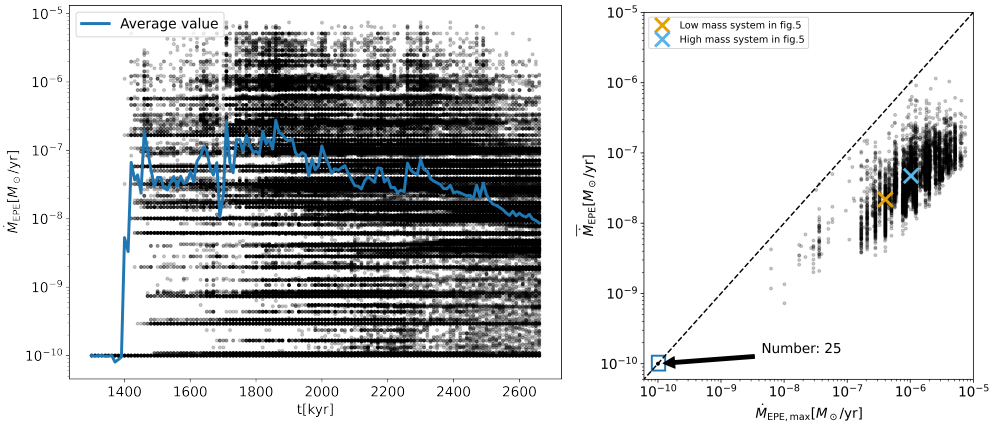


Figure 5.3. External photo-evaporation rate of disks in the cluster. The left panel shows the external photo-evaporation rate of each disk (black dots) and the averaged values over all disks (blue line) at different simulation times. The right panel shows the maximum external photo-evaporation rate versus the averaged value over the cluster lifetime of each disk. We also indicate the location and the number of isolated stars with their external photo-evaporation rates remaining at the lowest limit. In addition, the yellow and blue crosses display low- and high-mass systems, which are discussed further in Sect. 5.4.1.

& Lambrechts 2017). The embryo grows by accreting pebbles at a rate of

$$\dot{M}_{\rm peb} = \varepsilon 2\pi r u_{\rm peb} \Sigma_{\rm peb}. \tag{5.6}$$

Here, ε is the pebble accretion efficiency. We calculated the efficiency following Ormel & Liu (2018)[1]. The pebble-drift velocity is $u_{\rm peb}$. Both ε and $u_{\rm peb}$ depend on pebble Stokes number St. For self-consistency, we calculate the mass-weighted Stokes number as:

$$\mathrm{St} = (1 - f_{\rm m})\mathrm{St}_0 + f_{\rm m}\mathrm{St}_1, \tag{5.7}$$

as well as the mass-weighted drift velocity, $u_{\rm peb}$, as:

$$u_{\rm peb} = (1 - f_{\rm m})v_0 + f_{\rm m}v_1, \tag{5.8}$$

from the two-population dust model (Sect. 5.2.2) for the pebble flux. The stokes number and drift velocity for the small dust population are represented by St_0 and v_0, respectively, while St_1 and v_1 for large dust grains.

Once a planet grows sufficiently large to induce a pressure bump exterior to its orbit, it halts the incoming pebble flux and, as a consequence, pebble accretion terminates. We adopted the 3D pebble isolation mass from (Bitsch et al. 2018) as follows:

$$M_{\rm iso} = 25 M_\oplus \left(\frac{h}{0.05}\right)^3 \left[0.34\left(\frac{-3}{\log_{10}\alpha_t}\right)^4 + 0.66\right] \times \left[1 - \frac{\partial \ln P/\partial \ln r + 2.5}{6}\right] \frac{M_\star}{M_\odot}. \tag{5.9}$$

Here, $\partial P/\partial r$ is the local pressure gradient of the radial gas disk, and $\alpha_{\rm t}$ is the viscous alpha-parameter.

[1]The python script for calculating ε is available at: `https://github.com/chrisormel/astroscripts`

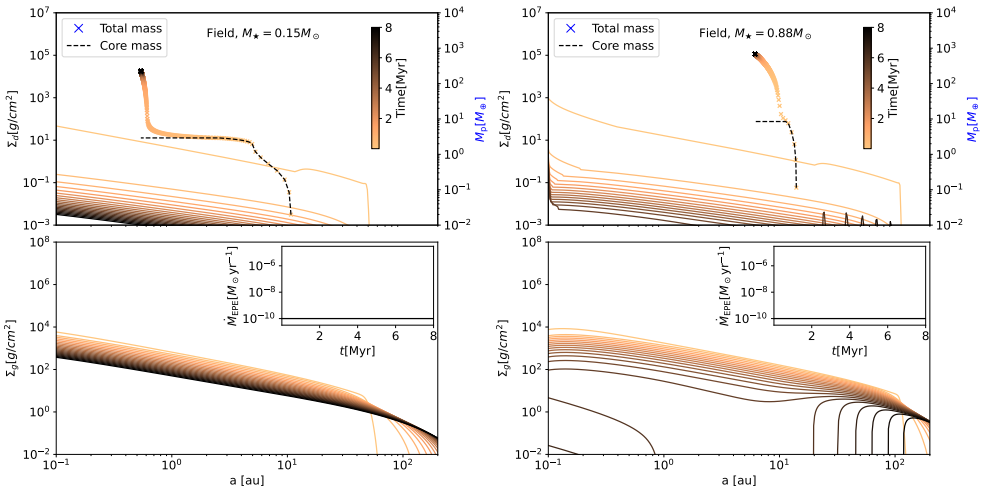


Figure 5.4. Comparison of disk evolution and planet growth tracks between a low-mass star ($0.15M_\odot$, left panels) and a relatively high-mass star ($0.88M_\odot$, right panels) in an isolated environment ($\dot{M}_{\rm EPE} = 10^{-10}M_\odot{\rm yr}^{-1}$).In the top panels, we display the evolution of dust surface density (left axis) alongside planet mass (right axis). The planet's total mass and core mass are tracked separately using cross dots and dashed lines, respectively. The bottom panels show the evolution of gas surface density. The inset in the top right corner illustrates the history of external photo-evaporation rates experienced by the system. Both the top and bottom panels in each column share the same color bar, indicating the age of the system.

Gas accretion

As pebble accretion stops when a planetary core reaches the pebble isolation mass, hydrodynamic pressure no longer supports the gas envelope around the core against planetary gravity (Lambrechts et al. 2014). If the supply of gas is sufficient, the gas accretion rate onto the gas giant is regulated by Kelvin–Helmholtz quasi-static contraction of the gas envelope (Ikoma et al. 2000):

$$\dot{M}_{\rm KH} = 10^{-5}\left(\frac{M_{\rm p}}{M_\oplus}\right)^4\left(\frac{\kappa}{0.1\,{\rm m^2kg^{-1}}}\right)^{-1} M_\oplus{\rm yr}^{-1}. \tag{5.10}$$

Here, κ is the opacity of the planet envelope. However, the gas accretion rate can later be limited by the amount of gas flowing into the Hill sphere at a rate of (Tanigawa & Tanaka 2016):

$$\dot{M}_{\rm Hill} = \frac{0.29}{3\pi h^4}\left(\frac{M_{\rm p}}{M_\star}\right)^{4/3}\frac{\dot{M}_{\rm g}}{\alpha_{\rm acc}}\frac{\Sigma_{\rm gap}}{\Sigma_{\rm g}}, \tag{5.11}$$

where $\Sigma_{\rm gap}/\Sigma_{\rm g} \cong (1+0.04K)^{-1}$ is the fitted depth of the gap that a massive planet creates in the gas disk. This estimate matches the results of hydrodynamic simulations from previous studies (e.g., Duffell & MacFadyen 2013; Kanagawa et al. 2015; Fung & Chiang 2016). The gap depth factor, K, is

$$K = \left(\frac{M_{\rm p}}{M_\star}\right)^2 h^{-5}\alpha_{\rm t}^{-1}. \tag{5.12}$$

One other limitation of the gas flow is the global disk-accretion rate $\dot{M}_{\rm g}$. We therefore set the gas accretion rate onto giant planets as the minimum value of all the above:

$$\dot{M}_{\rm GA} = \min\left[\dot{M}_{\rm KH}, \dot{M}_{\rm Hill}, \dot{M}_{\rm g}\right]. \tag{5.13}$$

This gas accretion methodology is the same as the one implemented in Ida et al. (2018) and Johansen et al. (2019).

The disk accretion rate, $\dot{M}_{\rm g}$, used in this study is an approximation (Eq. (5.1)), chosen for the simplicity of calculations. The exact disk accretion rate depends on the detailed processes of disk evaporation (e.g., IPE and EPE), and may differ from the rate we used.

5.2.4 Planet migration

When planets grow to moon-mass bodies, they begin to gravitationally interact with the gas disk, exchanging angular momentum and thereby experiencing natural migration within the disk. We adopt the locally isothermal type I migration prescription as outlined in Paardekooper et al. (2010, 2011). This migration model considers the total torque, which is the combined effect of Lindblad torque ($\Gamma_{\rm L}$) and corotation torque ($\Gamma_{\rm C}$), both of which scale with the gas surface density. We simply refer to the appendix of Izidoro et al. (2021) for a detailed summary of the migration prescription.

As planets grow in mass, their migration transitions into the type II regime. The planets begin to open gaps in the gas disk. Kanagawa et al. (2018) discovered that the torque exerted on these gap-opening planets is suppressed and it is dependent on the surface density at the bottom of the gap. Consequently, the migration timescale is generalized as:

$$\tau_a = -\frac{1 + 0.04K}{\gamma_{\rm L} + \gamma_{\rm C}\exp\left(-K/K_{\rm t}\right)}\tau_0(r_{\rm p}). \tag{5.14}$$

Here, $\gamma_{\rm L}$ and $\gamma_{\rm C}$ are the strengths of the Lindblad torque ($\gamma_{\rm L} = \Gamma_{\rm L}/\Gamma_0$) and corotation torque ($\gamma_{\rm C} = \Gamma_{\rm C}/\Gamma_0$) relative to the nominal torque $\Gamma_0 = (q/h)^2\Sigma_{\rm g} r_{\rm p}^4 \Omega_{\rm p}^2$. The nominal migration timescale is given by $\tau_0 = r_{\rm p}^2\Omega_{\rm p}M_{\rm p}/2\Gamma_0$. For low viscosity conditions ($\alpha_{\rm t} < 10^{-2}$), the corotation torque cutoff parameter $K_{\rm t}$ is fitted to a value of 20. We utilize Eq. (5.14) to compute the migration timescale for planets. When a planet is of low mass ($K \sim 0$), the migration timescale follows the type I prescription: $\tau_{\rm a,I} = (\gamma_{\rm L} + \gamma_{\rm C})^{-1}\tau_0$.

5.3 Initial conditions and parameter choices

The parameters utilized in our model are outlined in Table 5.1, with brief explanations provided below. For the gas disk, we adopted initial conditions and boundary conditions similar to those in Wilhelm & Portegies Zwart (2022). The gas disk's initial density profile follows a self-similar formulation (Lynden-Bell & Pringle 1974):

$$\Sigma_{\rm g}(t=0) = \frac{M_{\rm d}}{2\pi R_{\rm out}(1-e^{-1})}\frac{\exp(-r/R_{\rm out})}{r}, \tag{5.15}$$

where $M_{\rm d} = 0.1M_\star$ is the initial disk mass. However, our model diverges from self-similarity due to the inclusion of external photoevaporation (EPE) and internal photoevaporation (IPE). The outer disk radius $R_{\rm out}$ is determined by:

$$R_{\rm out} = 117\left(\frac{M_\star}{M_\odot}\right)^{0.45}\ {\rm au}, \tag{5.16}$$

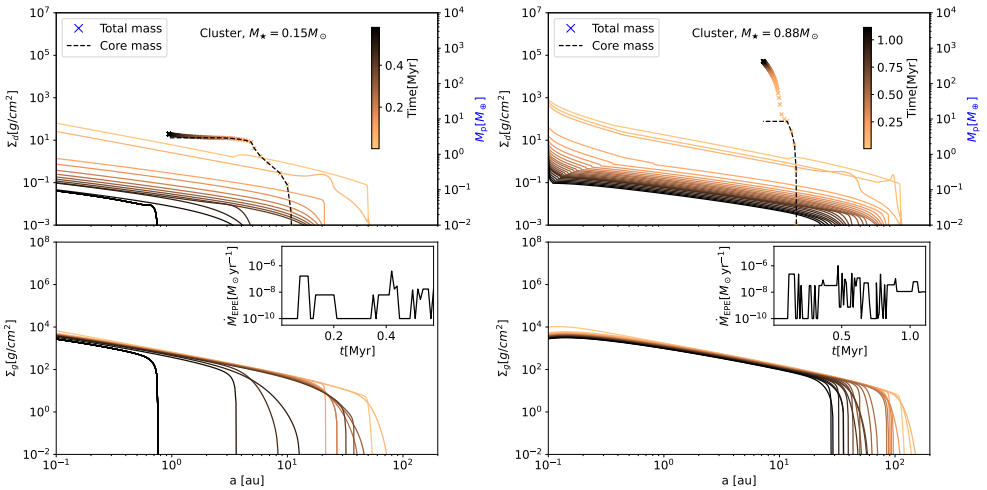


Figure 5.5. Same as Fig. 5.4, but in reference to the cluster. The star masses are $0.15 M_\odot$ (left) and $0.88 M_\odot$ (right). The insets on the top right of the bottom panels indicate the external photo-evaporation rate history the system experienced in the cluster.

which is used in Wilhelm et al. (2023).

The inner boundary of the disk is set by the inner disk radius, which is randomly distributed between 2 and 12 days following a normal distribution: $\log_{10}(P_{\rm in}/1, {\rm day}) \sim \mathcal{N}(\mu_{\rm in}, \sigma_{\rm in}^2)$, with $\mu_{\rm in} = \log_{10} 2$ and $\sigma_{\rm in} = 0.5$ (Batygin et al. 2023).

The disk temperature profile is assumed to be

$$T = 100 \left(\frac{M_\star}{M_\odot}\right)^{1/4} \left(\frac{r}{1\,{\rm au}}\right)^{-1/2} {\rm K}, \tag{5.17}$$

which has a similar radial power law as the radiation-dominated temperature case (the power-law is $-3/7$ in Chiang & Goldreich 1997). Such a low temperature is consistent with the cases in magnetically accreting laminar disks (Mori et al. 2021).

In our model, we set $\alpha_{\rm acc} = 10^{-3}$ and $\alpha_{\rm t} = 10^{-4}$, with $\alpha_{\rm acc}$ representing the gas angular momentum via a viscous gas evolution model and $\alpha_{\rm t}$ denoting viscous-α. The value of $\alpha_{\rm acc}$ is motivated by relatively high observed disk accretion rates (e.g., Rafikov 2017). A lower value of $\alpha_{\rm t}$ comes from low disk viscosity in some observed disks (e.g., Fedele et al. 2018; Flaherty et al. 2020; Portilla-Revelo et al. 2023). The adiabatic index of the disk is set to 7/5.

The initial and minimum dust grain size $a_1(t = 0)$ and a_0 are both 0.001 cm. The impact on the final results is negligible due to rapid dust growth timescales compared to orbital timescales. The dust fragmentation velocity is $v_{\rm frag} = 10\,{\rm m/s}$.

One planet seed per disk is initialized outside the iceline, with the semimajor axis following a uniform distribution $\log_{10}(a_{\rm p,0}/1\,{\rm au}) \sim \mathcal{U}(\log_{10}(R_{\rm ice}/1\,{\rm au}), (R_{\rm out}/1\,{\rm au}))$. The ice line is located at $R_{\rm ice} \approx 0.67\,(M_\star/M_\odot)^{0.5}$ au, where the disk temperature is 150 K. Each planet seed is of 0.01 $M_\oplus$, optimizing pebble-accretion efficiency over planetesimal accretion (Visser & Ormel 2016; Johansen & Lambrechts 2017).

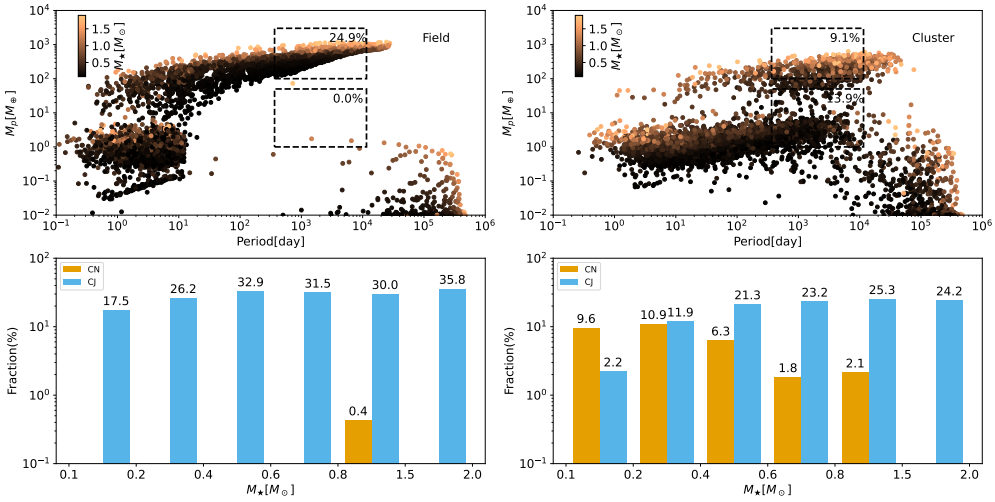


Figure 5.6. Planet population for isolated stars (left panels) and stars in the cluster (right panels). The initial condition is identical in the two scenarios, while proto-planet disks around stars in the cluster are more massively photo-evaporated during their evolution. In the upper panels, the position of the scatter represents the planetary orbital period and mass at the end of the simulation. The color denotes the host mass. The upper and lower black dashed boxes indicate the boundaries of Jupiter-like and Neptune-like planets, with the associated synthetic fraction labeled. In the lower panels, we separate the occurrence rate of cold Jupiter (blue bar) and cold Neptune (yellow bar) into different host mass ranges.

5.4 Results

5.4.1 Planet formation for two example stars

We first show the planet growth track and the disk evolution around a 0.15 $M_\odot$ star and a 0.88 $M_\odot$ star in isolation in Fig. 5.4, with $\dot{M}_{\rm EPE}$ fixed to $10^{-10} M_\odot {\rm yr}^{-1}$ for both calculations. Both systems are simulated for 8 Myr.

The evolution of gas and dust follows distinct pathways around low-mass and high-mass stars but also shows some common features. In the early stages, gas profiles evolve viscously, leading to an extended disk outer edge. By around 4 Myr, the high-mass star, with its stronger internal photoevaporation (IPE) rate, drives a gas gap out to about 10 au. This gap's size is determined by the balance of radiation intensity, gas density, and temperature profile. Such a gap does not appear in the disk of low-mass stars until later in the simulation. The stellar accretion rates are compared with the observed disks in (Wilhelm & Portegies Zwart 2022). In the initial snapshots of both systems, dips in dust surface density are observed at 10 and 20 au. These occur because small dust particles beyond these locations have insufficient time to grow larger due to longer growth timescales at greater distances from the star. The dust disk around the high-mass star shows peaks at about 50 au, attributed to a pressure maximum in the gas profile induced by IPE. Over time, the dust profile diminishes due to rapid radial drift.

The growth of planets around low-mass and high-mass stars exhibit notable differences. On the right axis of the upper panels in Fig. 5.4, planets initially build their cores efficiently through pebble accretion. Once they reach the pebble isolation mass, gas accretion com-

mences. The pebble isolation mass is relatively low in the low-mass system (left panel). Consequently, when gas accretion begins, the planet migrates inward because the gas accretion timescale is longer than the type I migration timescale. While the planet continues to grow, migration slows down due to its ability to gradually open a gap in the disk, thereby reducing migration (Kanagawa et al. 2018). In contrast, the planet in the high-mass system (right panel) has a higher pebble isolation mass, driving faster gas accretion (Eq. 5.10) and resulting in migration over a much shorter distance. Ultimately, planets in both low-mass and high-mass systems evolve into gas giants within 1 million years.

To examine the impact of external photoevaporation (EPE) on planet formation, we calculated the two stars in the cluster illustrated in Fig. 5.4. We carried out a simulation of planet formation using identical initial conditions to those displayed in Fig. 5.4, but in the context of a cluster environment. The results of this comparison are presented in Fig. 5.5. The simulation stops either when the disk is dispersed or at the end of the cluster simulation.

The insets in the lower panels of Fig. 5.5 illustrate the evolution of the external photoevaporation (EPE) induced by nearby massive stars in the cluster with a time resolution of 10 kyr. The $\dot{M}_{\rm EPE}$ evolution curves exhibit discrete feature for two main reasons: i) Clumps within the molecular cloud shift their relative position to the star, occasionally shielding the FUV and EUV luminosity from nearby massive stars. ii) Close encounters between stars are transient events, contributing to fluctuations in the radiation received. The latter effect matters particularly for low-mass stars, which tend to be further away from the cluster center than the more massive stars due to mass segregation.

The disk surrounding the low-mass star is strongly influenced by EPE. In the low-mass system, the $\dot{M}_{\rm EPE}$ peaks at $10^{-7} M_\odot {\rm yr}^{-1}$ between 0.1 and 0.2 Myr, causing truncation of both the dust and gas components. Between 0.2 and 0.3 Myr, the $\dot{M}_{\rm EPE}$ remains at the low value, enabling the viscous evolution of the gas disk and the subsequent expansion of the disk's outer edge. On the other hand, the disk around the high-mass star is more resilient against the EPE. The time-averaged EPE experienced by the low-mass and high-mass systems is indicated by the blue and red crosses in Fig. 5.3, respectively. The more massive system undergoes an average EPE approximately two times higher than that experienced by the less massive one. The gas disk around the $0.88\,M_\odot$ star shrinks to a lesser extent because the disk is more massive initially and the majority of the disk mass is in the outer regions.

Compared to the isolated systems, the growth of the planet before the pebble isolation mass is similar in both cases. The pebble-accretion timescale is short ($\gtrsim$ 10 kyr), during which the disks undergo minimal evolution.

The planet experiences gas accretion differently in the cluster compared to isolation. Gas accretion lasts for $\gtrsim$ 100 kyr. Figure 5.5 depicts the planet mass in the cluster at the final snapshot of the cluster simulation. By that time, the planet within the low-mass system gains little gas due to the strong EPE, which induces a short lifetime of the protoplanet disk. The planet in the high-mass system has evolved into a gas giant, and continues to accrete gas while the gas is available.

The clustered stellar environment leads to distinct planet outcomes compared to planetary systems born in isolation. Low-mass stars have shorter disk lifetimes in clusters, resulting in inefficient planet growth and migration, and therefore more distant rocky (gas-poor) planets. In contrast, high-mass stars have longer disk lifetimes and are more resistant to the environment. On the one hand, high-mass stars are born with more massive disks and, on the other hand, high-mass stars have higher stellar accretion rates, more materials are transported to the outer disk through viscous processes. These two aspects help the disk radius to shrink less. The resulting planet population in the cluster is similar to the one born in

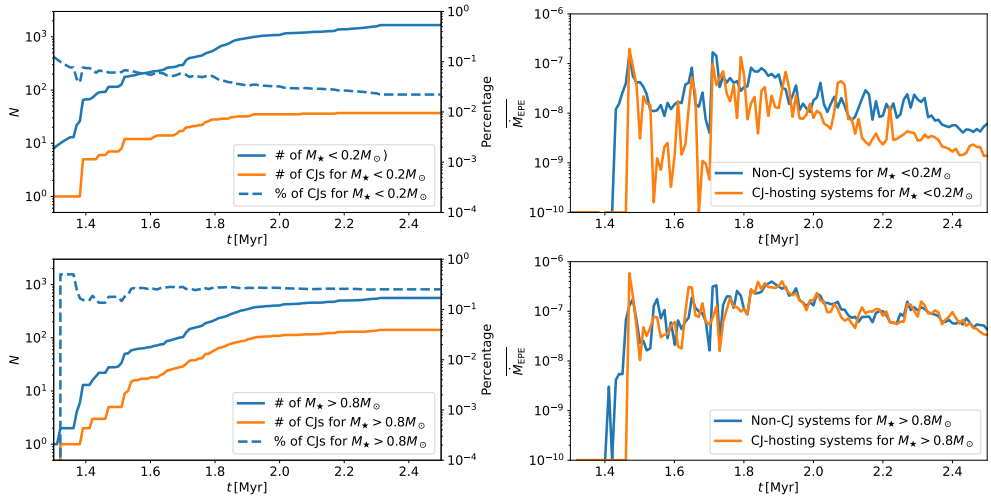


Figure 5.7. Time evolution of the planet population in the cluster. The top panels illustrate the evolutionary trends of CJ-hosting and non-CJ low-mass systems ($< 0.2M_\odot$), while the lower panels focus on high-mass systems ($> 0.8M_\odot$). The total number of low-mass ($< 0.2M_\odot$) and high-mass ($> 0.8M_\odot$) systems is depicted with blue solid lines in the left panels. Additionally, the left panels display the number of CJ-hosting systems (orange solid line) and the fraction of CJ-hosting systems (blue dashed line). In the right panels, we compare the system-averaged EPE experienced by non-CJ systems (blue line) and CJ-hosting systems (orange line) just before their CJs are formed.

isolation.

A recent observation with JWST aligns with our simulations. Berné et al. (2024) deduced the outward mass flux from the photodissociation regions of the d203-506 disk (a proplyd in the Orion Nebula), situated around an M-star with a mass <0.3$M_\odot$. The estimated mass loss rate is $\dot{M} = 1.4 \times 10^{-7} - 4.6 \times 10^{-6} M_\odot$, indicating a disk lifetime shorter than 0.13 Myr. The short disk lifetime limits the timeframe for gas accretion. The short lifetime of the observed disk is consistent with our simulation of the $0.15M_\odot$ system (left panel of Fig. 5.5).

5.4.2 Planet population: Isolated versus clustered

In the cluster, the EPE varies from star to star and from time to time. A population study is therefore necessary to delineate the statistical behavior of planets formed within the cluster. This section elucidates the distinct planet demographics resulting from isolated stars and those within the clustered environment.

In isolation (upper left panel in Fig. 5.6), most rocky (gas-poor) planets reach the disk's inner edge through type I migration. Gas giants, on the other hand, remain in wider orbits because they have much longer migration timescales than terrestrial planets due to the gap-opening process. In addition, most of the rocky planets accrete pebbles and reach a pebble isolation mass in the outer orbits, then migrate inward. Given that the pebble isolation mass is higher in the outer regions (see Eq. (5.9)), those rocky planets have their mass above the local pebble isolation mass.

Compared to isolated stars, there are fewer gas giants formed in the star cluster, especially around low-mass stars (upper-right panel in Fig. 5.6). In the star-cluster environment, the disk's lifespan is shortened due to intense FUV irradiation. The lower mass stars have lower

mass disks and, therefore have shorter disk lifetime. Consequently, some low-mass systems have a disk lifetime that is shorter than the gas giant formation timescale. Once the disk disperses, planets are unable to continue gas accretion and fewer gas giants form within the cluster. Furthermore, fewer planets reach a pebble isolation mass in the star cluster, due to there being less solid content present within the disks than in the isolated environments (cf. Qiao et al. 2023).

Planets originating in the cluster environment tend to remain further from the central star compared to those born in isolation. Migration within the disk occurs due to gravitational interactions between the disk and the planet. However, in the cluster environment, many disks evaporate early on. Consequently, once the ambient gas disk dissipates, planetary migration ceases as well. As a result, planets in the cluster are inclined to remain in wider orbits.

Given the difference between the demographic discrepancies between planets in isolation and the star cluster, we here define the cold Jupiter (CJ) and cold Neptune (CE) planets as:

- CJ: Planets with a period time between 1 to 31.6 years (equivalent to 1-10 au if they orbit around a solar mass star) and planet-to-star mass ratio between 0.03% to 1% (equivalent to 0.3 to 10 Jovian masses if their hosts' mass is one solar mass).
- CN: Planets with period time between 1 to 31.6 years (equivalent to 1-10 au if they orbit around a solar mass star) and planet mass between 1 to 50 Earth masses.

The motivation of such a definition is elaborated in Sect. 5.6.2. In the planet demographic plot (Fig. 5.6 upper panels), we denote CJ and CN planets with upper and lower boxes, respectively, with their occurrence rates labeled. Such a definition of planet populations is advantageous because of their distinct occurrence within and out of the cluster environment. Overall, CJ planets are rare, while CN planets are more abundant in the cluster than in the isolated environment. However, the occurrence rates vary notably across different host masses.

We studied the stellar dependency of the planet population by segmenting the stellar population into different mass categories and calculating the corresponding occurrence rates of CJ and CN. The outcomes are illustrated in the lower panels of Fig. 5.6. We note a more obvious decline in the occurrence rate of CJ as the host mass decreases. For stars smaller than 0.2 $M_\odot$, the CJ occurrence rate plummets by nearly an order of magnitude. Within the range of 0.2 to 0.4 $M_\odot$ stars, the CJ occurrence rate experiences a twofold decrease. Conversely, CN planets are notably more abundant around low-mass stars within the cluster, with occurrence rates declining as the host mass increases. These CN-harboring systems resemble those depicted in the left panel of Fig. 5.5. If these systems were to form in an isolated environment, they have more opportunities to accrete gas and evolve into gas giants.

Overall, almost no CNs are formed around isolated stars. Planets there grow and migrate more efficiently than those in the cluster due to longer disk lifetime (especially for M stars). A more detailed comparison between planets in the cluster and isolation is put in Sect. 5.A.

Finally we remark that the simulated planet population exhibits features consistent with observed exoplanet populations. Our simulation produces hot, warm, and cold Jupiters, as well as hot, warm, and cold super-Earths (sub-Neptunes). However, making direct comparisons with observations is not appropriate for two reasons: 1) theoretically, our disk model is simplified and does not account for factors such as viscous heating and disk substructures and 2) observationally, the cold planet population, especially super-Earths, is poorly constrained. Our goal is to study the effect of star clusters on planet formation, and we leave more detailed comparisons for future work.

5.4.3 Co-evolution between CJ formation and the cluster

The young star-forming cluster is a dynamic environment, with its properties constantly changing. The intensity of FUV irradiation experienced by different stars varies strongly across different stages of cluster evolution. Thus, in this section, we analyze planet populations at different times in the cluster evolution.

In Fig. 5.7, we focus on two groups of planetary systems: those with stellar masses $< 0.2M_{\odot}$ and those $> 0.8M_{\odot}$. The total number of these systems at different moments in time is represented by the blue solid lines. The shapes of the blue lines in the upper and lower left panels exhibit similar patterns, reflecting the consistent star formation dictated by the same initial mass function (IMF) within the cluster. Overall, star formation decelerates around 1.9 Myr and ceases around 2.3 Myr.

We compare the EPE experienced by CJ-hosting and non-CJ systems around both low and high-mass stars in the right panels of Figure 5.7. Low-mass systems experience (on average) lower FUV flux than high-mass systems in the simulation. This is due to the effect of mass segregation. Low-mass stars are more prone to scattering toward larger distances from the cluster center, while their more massive counterparts tend to hardly migrate. As they are farther from both the cluster center and the FUV sources, low-mass systems receive lower FUV flux.

Furthermore, for low-mass systems, CJ-hosting systems exhibit lower EPE than non-CJ systems in nearly all the simulation time. In contrast, minimal differences are observed between CJ-hosting and non-CJ systems around high-mass stars. These findings directly highlight the resilience of high-mass systems to EPE irradiation compared to their low-mass counterparts.

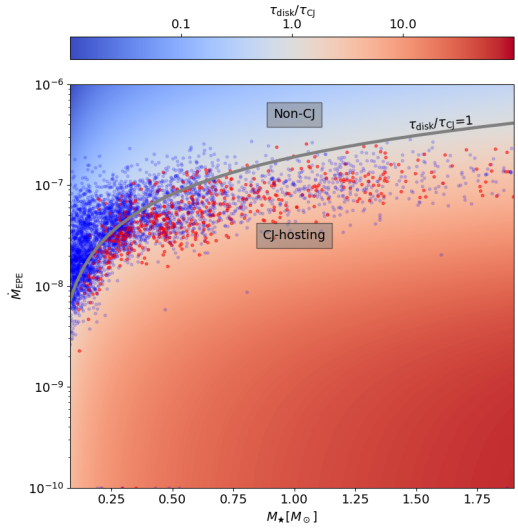


Figure 5.8. Disk lifetime over CJ growth time with varying host mass $M_{\star}$ and $\dot{M}_{\rm EPE}$. The color represents the values of $\tau_{\rm disk}/\tau_{\rm CJ}$. The contour line shows where the disk lifetime equals the CJ growth time. CJ-hosting systems are expected to lie below this line, while non-CJ systems lie above it. Our simulation results (Sect. 5.4) are over-plotted, with non-CJ systems shown as blue dots and CJ-hosting systems as red dots.

5.5 Analytical criteria for CJ formation in the cluster

Gas giants can form if the planet's formation timescale is longer than the disk lifetime. In this section we analytically approximate a planet formation timescale at a $P = 31.6$ yr orbit. Such an orbit is (by definition) where our outermost CJ is located. The disk lifetime is calculated under different FUV environments. The analytical comparison between the two timescales is then used to validate the simulation outcomes.

The disk lifetime is determined by both self-accretion and external photo-evaporation processes. In the cluster, the disk mass loss is dominated by the external photo-evaporation rate ($\dot{M}_{\rm EPE}$). We can simplify this by assuming both rates remain constant over time with $\dot{M}_{\rm g} = 3\pi\nu\Sigma_{\rm g}(t=0)$. The disk's lifetime can then be estimated using the formula:

$$\tau_{\rm disk} = \frac{M_{\rm d}}{\dot{M}_{\rm g} + \dot{M}_{\rm EPE}}, \tag{5.18}$$

with the disk mass, $M_{\rm d}$, proportional to the host mass. It reveals that lower-mass stars have shorter disk lifetimes than higher-mass stars if they are in the same dense cluster environment.

To become a gas giant, a planetesimal first needs to reach pebble isolation mass, then continue to accrete gas. Planet migration complicates this process, but it is ignored in the approximation. With this simplified model, we can then calculate the timescale for one planet to grow from 0.01 to $100M_{\oplus}$.

The pebble accretion rate in the 2D Hill regime (Ormel & Klahr 2010; Lambrechts & Johansen 2012) is used for the analytical calculation:

$$\dot{M}_{\rm peb} = 2\left(\frac{\rm St}{0.1}\right)^{2/3} \Omega R_{\rm H}^2 \Sigma_{\rm p}. \tag{5.19}$$

Here, $\dot{M}_{\rm peb}$ relies on the dust Stokes number and surface density. We set ${\rm St} = 10^{-3}$. Radial drift causes the dust surface density evolves over time. We adopt an approximate analytical form of the dust surface density from Gurrutxaga et al. (2024), which accounts for radial drift and dust growth:

$$\Sigma_{\rm p} = Z_0 T^{-\frac{1}{2-\gamma_{\rm t}}\frac{\chi {\rm St}}{3\alpha_{\rm acc}}} \Sigma_{\rm g}, \tag{5.20}$$

where Z_0 is the initial dust-to-gas ratio, $\gamma_{\rm t}$ represents the viscosity index, and χ corresponds to the negative disk pressure gradient (approximately constant). These values align with the simulation setup outlined in Sect. 5.3. We integrate Eq. (5.19) and calculate the time, $\tau_{\rm core}$, needed for one planet to grow its core from 0.01 to $M_{\rm iso}$. At this point, gas accretion commences. At the early stage of gas accretion, Kelvin-Helmholz contraction (Eq. 5.10) dominates. We therefore calculate the time for gas accretion $\tau_{\rm gas}$ from $M_{\rm iso}$ to $100M_{\oplus}$ via integrating Eq. (5.10). Finally, the CJ growth timescale is:

$$\tau_{\rm CJ} = \tau_{\rm core} + \tau_{\rm gas}. \tag{5.21}$$

This allows us to compare $\tau_{\rm CJ}$ to $\tau_{\rm disk}$. If $\tau_{\rm disk} > \tau_{\rm CJ}$, CJs can form. In contrast, if $\tau_{\rm disk}$ is shorter, the planet cannot grow efficiently into a CJ.

We varied the host mass, $M_{\star}$, and $\dot{M}_{\rm EPE}$, then calculated the ratio $\tau_{\rm disk}/\tau_{\rm CJ}$. The results are shown in Fig. 5.8. Generally, $\tau_{\rm disk}/\tau_{\rm CJ}$ is smaller in the upper left corner and larger in the lower right corner. Low-mass stars, which have initially low-mass disks, exhibit shorter disk lifetimes under the same external conditions. Moreover, the pebble isolation mass is

smaller around low-mass stars because their disks are cooler. Consequently, the growth of an embryo into a gas giant takes longer, as the Kelvin-Helmholtz (KH) contraction timescale (Eq. 5.10) is sensitive to the planet's initial mass. Therefore, low-mass stars need more time to form gas giants. Our simulation results align with this pattern. In the regime of low-mass stars, namely, between 0.08 and 0.25 $M_\odot$, the power law of $\tau_{\rm disk}/\tau_{\rm CJ} = 1$ line exceeds unity. That is because $\tau_{\rm CJ}$ negatively correlated with stellar mass and it decreases by a factor of two.

In the star clustering environment, CJ planets can form if the disk lifetime is sufficiently long. As shown in Fig. 5.8, most simulated CJ-hosting systems have $\tau_{\rm disk} > \tau_{\rm CJ}$ and relatively low $\dot{M}_{\rm EPE}$ compared to non-CJ systems. In the figure, we include the curve for $\tau_{\rm disk}/\tau_{\rm CJ} = 1$. Above this line, the disk evaporates before the gas giant can form, preventing CJ formation. Below the line, CJ formation is possible if the initial planetesimal forms near $P = 31.6$ year.

As a planet grows to Jupiter mass, it begins to open a deep gap in the gas disk, which restricts the amount of material that can enter its Hill sphere (Eq. (5.11)). In this approximated calculation, we only consider KH contraction.

Our simulation outcomes are over-plotted in Fig. 5.8, with CJ-hosting systems shown as red dots and non-CJ systems as blue dots. The simulation aligns with the analytical results. CJ-hosting systems stay in the lower part with low EPE. The transition from CJ-hosting to non-CJ systems matches $\tau_{\rm disk}/\tau_{\rm CJ} = 1$. For massive stars ($M_\star \gtrsim 1 M_\odot$), disk lifetimes exceed the CJ formation timescale. Not all stars successfully cook the CJs because the planets either migrate to the inner hot region of the disk or remain in wider orbits, depending on the initial position of the planet embryos.

In our particular cluster, planet formation around high-mass stars is resistant to the stellar environment, this may change in a denser cluster. Because a denser cluster makes the planet-forming disks closer to the FUV sources (with $F_{\rm EPE} \sim \rho_{\rm OB}^{2/3}$). For example, in the cluster Westerlund 1, with its mean density of $\sim 3.4 \times 10^4$ stars/pc^3 (about three times larger compared to the low-density environment simulated in this paper), we expect that fewer CJs have thus formed. As the disks are in a more irradiative environment. In Fig. 5.8, these stars would be located further up toward the "non-CJ" region than our simulated cluster.

5.6 Discussion

5.6.1 Model assessment

We introduce the planet population synthesis code PACE to study planet formation in a complex, perturbed environments such as that of dense stellar clusters. While planets grow within the protoplanetary disks, these disks evaporate due to external photoevaporation from nearby stars in the cluster.

We updated the EPE of all disks every 10 kyr using simulation results from Wilhelm et al. in prep (same methodology as Wilhelm et al. 2023). We note that the pebble accretion timescale is $\gtrsim$ 10 kyr. While our findings on the planet population generated in the cluster remain qualitatively robust, increasing the time resolution may enhance the precision of planet formation calculations within individual systems.

The initial disk radius (Eq. (5.16)) and mass (10% of the host mass) are fixed for a given stellar mass. Although Wilhelm et al. (2023) found consistency when comparing the disk radii and mass during the simulation with those of disks observed in dynamic encounters, this simple initialization may introduce some bias to the simulation results. Future studies

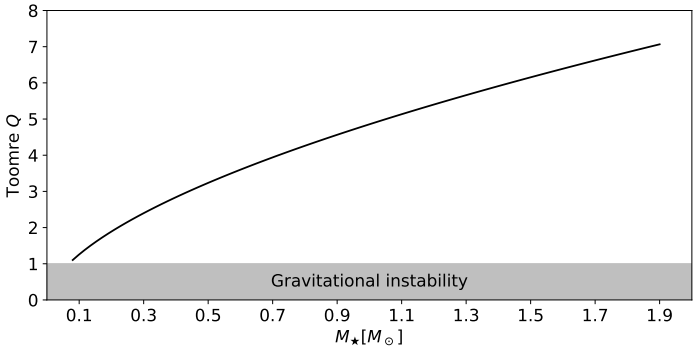


Figure 5.9. Toomre Q values of initial disks at the outer boundary orbit of our cold planet definition (P = 31.6 yr) for different stellar masses. The lower gray area indicates the region of $Q < 1$ where gravitational instability can occur.

should use more observationally motivated initial conditions to better explain the observed exoplanet populations.

The gas disks we initialize here are relatively massive, making up 10% of the host mass. To evaluate whether the gas disk is gravitationally stable, we calculate the Toomre-Q parameter via

$$Q = \frac{C_s \Omega}{\pi G \Sigma_g}, \tag{5.22}$$

where C_s is the sound speed. The Toomre-Q values are assessed at P = 31.6 yr orbits, corresponding to the outermost orbit of our interest for different stars. The results, illustrated in Fig. 5.9, reveal Toomre-Q values exceeding unity across all samples. This indicates that core accretion is the prevailing pathway for forming gas giants in our simulated systems. We remark that out of P = 31.6 yr orbit, the disk is gravitationally unstable (especially around low-mass stars) and may form giant planets directly.

This work uses a simplified model for disk evolution, whereby we neglected the dynamical truncation of a protoplanetary disk resulting from stellar flybys. In most cases, external photoevaporation dominates the disk mass loss over dynamical truncation (Wilhelm et al. 2023). However, dynamical truncation (e.g., Portegies Zwart 2016, and references therein) becomes more important in denser clusters with fewer massive stars (i.e., fewer FUV sources). For instance, less massive stars are formed due to the strong magnetic fields in the nuclear molecular clouds of NGC 1097 (Tabatabaei et al. 2018). The clouds likely fragment, giving rise to numerous low-mass stars. Dynamical truncation then needs to be considered. Additionally, our model overlooks disk orientation, which may result in different evolution pathways for disks even in cases where the FUV and EUV environment is exactly the same.

Nearby massive stars can elevate the outer disk temperature beyond our assumed stellar radiation-dominated disk temperature (Haworth 2021). This temperature increase results in a puffier disk with a larger aspect ratio, which raises the pebble isolation mass Eq. (5.9) and reduces the efficiency of pebble accretion. Consequently, the runaway gas accretion phase of the proto-planets may be prolonged.

The formation timescale of cold Jupiters is a critical factor in this study. Recent research suggests that gas accretion begins earlier during the core growth phase (Gurrutxaga et al. 2024), potentially shortening the planet's formation timescale. On the other hand, atmospheric recycling could introduce complexity, thereby prolonging the gas accretion process

(e.g., Ormel et al. 2015; Moldenhauer et al. 2021). However, the effectiveness of this process in delaying gas accretion in distant orbits remains uncertain (Wang et al. 2023; Bailey & Zhu 2023). Furthermore, the atmosphere's opacity is also important in the gas accretion phase but uncertain.

The rapid formation of planetesimals is one key assumption in our model. We assume that when the most massive planetesimal reaches moon mass, the surrounding disk retains the same mass as our initial disk conditions. The optimal initial planetesimal mass is still under debate (Schäfer et al. 2017; Abod et al. 2019; Rowther et al. 2024). However, if a planetesimal attains moon mass later in the process (intuitively, later for planetesimals in the outer orbits), there may not be sufficient accretion material available as pebbles rapidly drift inward (Lau et al. 2024). As a result, the planet's accretion and formation timescales are significantly extended. This makes planet formation more susceptible to external photoevaporation. If disk substructures exist, they may extend the radial drift of pebbles and therefore facilitate planet accretion (Morbidelli 2020; Chambers 2021; Jiang & Ormel 2023; Gárate et al. 2024).

5.6.2 Cold Jupiter and Neptune in observation

Our definition of cold planets pertains to those located between 1 and 10 au. Pebble accretion is particularly effective in this range, where both planetesimal accretion (Johansen & Bitsch 2019; Emsenhuber et al. 2021) and gravitational instability (GI; Forgan et al. 2018) are less effective.

Our simulations of planet formation on relatively wide orbits in star clusters reveal intriguing systematics that are qualitatively alignd with observational findings, as follows:

1. Low-mass stars are born with low-mass disks, therefore generating fewer (by less than a factor of two) giant planets than around high-mass stars in isolation. However, the early truncation of gas supply by external photo-evaporation in the star clustering environment leads to even fewer (by an order of magnitude) cold giants around low-mass stars than high-mass stars Fig. 5.6. This is in alignment with the observation that M-stars are less likely to host Jupiters, compared to FGK stars (Gan et al. 2023b).

2. In contrast to planet formation around stars in isolation, our simulated planet population in star clusters exhibits a higher abundance of cold super-Earths and Neptunes. Planets on wide orbits are difficult to detect. Microlensing observations have suggested that cold Neptunes are prevalent (Suzuki et al. 2016; Zang et al. 2023) and, potentially, these planets could be formed in the star clustering environment.

3. Gan et al. (2023a) has observed that the occurrence rate of cold Jupiters around M-stars shows a weak dependence on metallicity, in contrast to closer-in planets (Lu et al. 2020). It is necessary to establish a process that is independent of metallicity and favors wide orbits to explain this statistical trend. External photoevaporation (investigated in this work), stellar close encounters (Ndugu et al. 2022), and extra heating (Ndugu et al. 2018) on protoplanet disks in the young cluster together emerge as plausible explanations given their independence with respect to disk metallicity and the existence of planets in outer radii.

The observational statistics mentioned above rely on a limited number of radial velocity and microlensing detections. Future missions, designed to explore wide-orbit planets, such

as PLAnetary Transits and Oscillations of stars (PLATO, Rauer et al. 2014), Telescope for Habitable Exoplanets and Interstellar/Intergalactic Astronomy (THEIA, Spergel et al. 2009), and ET2.0 (Ge et al. 2022), or the upcoming event Gaia Data Release 4, jointly offer the promise of providing a more extensive dataset. These missions enable a more accurate characterization of the occurrence rates of cold Jupiters and Neptunes across diverse stellar populations and help validate our findings.

5.7 Conclusions

We designed and built a planet population synthesis code to investigate the impact of an Orion-like star cluster on the planet formation process. With nearby massive stars as FUV sources, the planet-forming disks are prone to external photoevaporation. We studied the resulting planet population and compare it to the population born in isolation.

The key result of our study is that fewer cold Jupiters are formed overall, whereas cold Neptunes are more common around M dwarfs in the dense cluster environment. Neptune-sized planets born in isolation always migrate to the disk's inner edge, while planet formation around high-mass stars is less affected by the star cluster. The main reason is that low-mass stars are born with less massive disks and end up losing mass more rapidly than those around high-mass stars, due to external photoevaporation in the star cluster environment. Consequently, these planets rarely undergo accretion or migration. In contrast, high-mass disks are more resilient to the cluster environment and gas giants can form.

We also derived the critical FUV environment necessary for forming cold Jupiters, which is aligned with our population synthesis simulation results.

Appendix

5.A Planet population in isolated stars and a star cluster

We compare isolated planets with those in a cluster in Fig. 5.10. The left panels display the masses and orbital periods of planets born around isolated stars. The right panels show the same for planets born in a cluster. Each planet in the cluster has a corresponding planet in isolation with the same initial conditions. We calculate the mass and period ratios between each planet in isolation and its cluster counterpart (or vice versa), starting from the same initial embryo.

In isolation, planets are always more massive or at least as massive as those formed in the cluster. In both scenarios, rocky (gas-poor) planets near the disk's inner edge have similar masses. The most massive gas giants also have similar masses in both scenarios, as they form around massive stars and are more resistant to external environments, as seen in Fig. 5.6.

In the isolation case, there is a small group of planets around $\sim 0.1\ M_\oplus$ with orbits of 1-10 days. These embryos originate from much wider orbits, between $10^4 - 10^5$ days. They slowly accrete pebbles until all pebbles drift away, then gradually migrate to the inner edge of the disk. At this location, some pebbles are trapped due to the pressure bump. The embryos then accrete more pebbles and reach the local pebble isolation mass.

As for the embryos starting $\gtrsim\ 10^5$ days, the pebbles outside the embryos' orbits are insufficient to grow them up to $\sim$ Earth mass. Additionally, their migration timescales are too long. Therefore, they remain close to the initial positions, both in terms of isolation and the cluster.

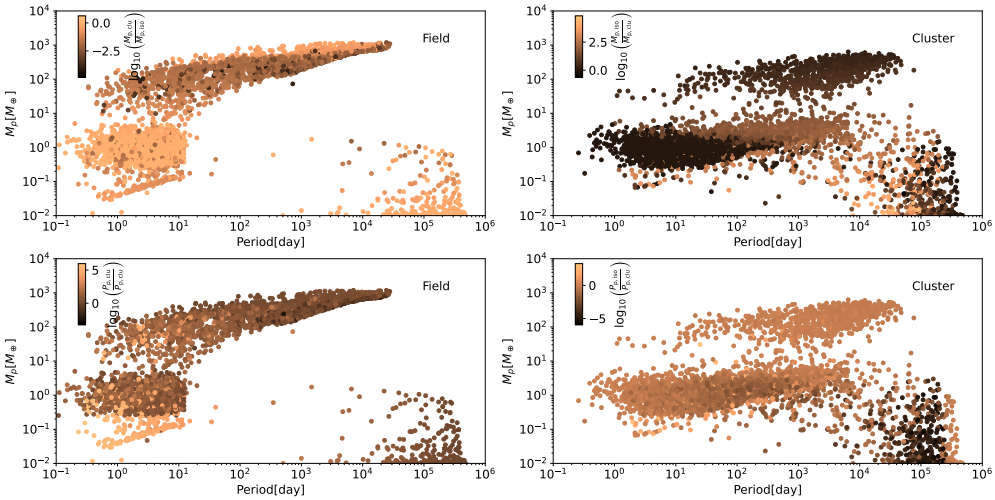


Figure 5.10. Similar to the upper panels of Fig. 5.6, but with colors indicating different properties. In the upper left panel, the color shows the logarithmic value of the mass ratio of planets in the cluster to those in isolation. In the upper right panel, it shows the opposite: the mass ratio of planets in isolation to those in the cluster. In the lower panels, the colors represent the logarithmic value of the period ratio of planets. The lower left shows the period ratio of planets in isolation to those in the cluster, while the lower right shows the period ratio of planets in the cluster to those in isolation.

6

ALMA signature of closely-spaced pebble-accreting protoplanets in Transition disks

Protoplanetary disks surrounding young stars are the birth places of planets. Among them, transition disks with inner dust cavities of tens of au are sometimes suggested to host massive companions. Yet, such companions are often not detected.
Aims: Some transition disks exhibit a large amount of gas inside the dust cavity and relatively high stellar accretion rates, which contradicts typical models of gas-giant-hosting systems. Therefore, we investigate whether a sequence of low-mass planets can create the appearance of cavities in the dust disk.
Methods: We evolve the disks with low-mass growing embryos in combination with 1D dust transport and 3D pebble accretion, to investigate the reduction of the pebble flux at the embryos' orbits. We vary the planet and disk properties to understand the resulting dust profile.
Results: We find that multiple pebble-accreting planets can efficiently decrease the dust surface density, resulting in dust cavities consistent with transition disks. The number of low-mass planets necessary to sweep up all pebbles decreases with decreasing turbulent strength and is preferred when the dust Stokes number is $10^{-2} - 10^{-4}$. Compared to dust rings caused by pressure bumps, those by efficient pebble accretion exhibit more extended outer edges. We also highlight the observational reflections: the transition disks with rings featuring extended outer edges tend to have a large gas content in the dust cavities and rather high stellar accretion rates.
Conclusions: We propose that planet-hosting transition disks consist of two groups. In Group A disks, planets have evolved into gas giants, opening deep gaps in the gas disk. Pebbles concentrate in pressure maxima, forming dust rings. In Group B, multiple Neptunes (unable to open deep gas gaps) accrete incoming pebbles, causing the appearance of inner dust cavities and distinct ring-like structures near planet orbits. The morphological discrepancy of these rings may aid in distinguishing between the two groups using high-resolution ALMA observations.

S. Huang★, N. van der Marel, S. Portegies Zwart (2024) Origin of transition disk cavities: Pebble-accreting protoplanets vs super-Jupiters. A&A, 691A, 155

6.1 Introduction

Since the discovery of the first exoplanet around a solar-type star (Mayor & Queloz 1995), thousands of mature exoplanets have been confirmed, which keep challenging our understanding of planet formation. Planets are expected to form in protoplanetary disks. Thanks to the Atacama Large Millimeter/submillimeter Array (ALMA), hundreds of planet-forming disks have been imaged and studied (e.g., Andrews et al. 2018; Long et al. 2018).

A group of disks of particular interest is classified as "transition disks," featuring large cavities in the dust continuum (e.g. Kenyon & Hartmann 1995; van der Marel 2023, and references therein). Such large cavities in dust disks can indicate the existence of planets. These cavities are potentially cleared by super Jovian planets, as they are able to perturb the gas disk and create pressure bumps (Lin & Papaloizou 1979; Goldreich & Tremaine 1980), leading to the convergence of dust and the formation of distinct ring-like structures within the disks.

Some transition disks, including PDS 70, have much lower stellar accretion rates than typical full disks with similar stellar mass as well as a deep inner gas cavity, as demonstrated by spatially resolved ^{12}CO and ^{13}CO images (Muley et al. 2019; Facchini et al. 2021). Disks with giant planets (such as PDS 70) may have already evolve to the rather later stage of giant planet formation. Other transition disks have more typical accretion rates, indicating material transport across the gap. Possibly, their planet's masses are not so high that only shallow gas gaps are opened (Dodson-Robinson & Salyk 2011; Leemker et al. 2022).

It remains a question whether there are super-Jovian planets in most of the transition disks. The confirmation of proto-planets through direct imaging within the circumstellar disks was achieved only in three disks: PDS 70 (Keppler et al. 2018; Haffert et al. 2019), AB Aur (Currie et al. 2022; Zhou et al. 2022), and HD 169142 (Hammond et al. 2023), whereas most other targets do not show significant planet signals (Asensio-Torres et al. 2021).

Considering the lack of direct confirmation of massive companions in the disk gaps and cavities as well as the difficulty of explaining giant planet formation on wide orbits, various other mechanisms have been proposed to explain gaps and cavities. With pressure bumps, these mechanisms include disk dispersal through magnetohydrodynamic (MHD)-driven winds (Takahashi & Muto 2018) or photoevaporative flows (Ercolano & Pascucci 2017), zonal flows in MHD disks (Johansen et al. 2009), mass pile-up at the boundary between magnetically active and dead zones (Flock et al. 2015), and spontaneous ring formation due to reduced accretion by concentrated dust (Dullemond & Penzlin 2018; Hu et al. 2019). Moreover, rings can form even without the presence of pressure maxima due to the condensation fronts at icelines (Zhang et al. 2015), temperature dips (Zhang et al. 2021c), traffic jam effect (Jiang & Ormel 2021), and grain growth processes (Ohashi et al. 2021).

Recent studies have revisited the possibility that most, if not all cavities are caused by planets. On one hand, pebble accretion has been shown to efficiently grow planets even in orbits wider than 10 au (Johansen & Bitsch 2019; Jiang & Ormel 2023; Gurrutxaga et al. 2024; Huang et al. 2024). Also, the occurrence rate of giant planets exhibits a similar dependence on stellar mass as the occurrence rate of structured protoplanetary disks (van der Marel & Mulders 2021). This suggests that the disk substructures could be primarily caused by planets.

Low-mass planets are not often considered as the initiator of disk substructures, since they cannot generate pressure bumps. However, they may still alter the dust transport. In disks hosting low-mass planets, dust tends to drift inward. When the inward pebble flux intersects with a planet's orbit, some of it can be accreted onto the planet's surface — a

process known as pebble accretion (Ormel & Klahr 2010; Lambrechts & Johansen 2012). Consequently, the planet acts as a filter, reducing the inward pebble flux. In this paper, we investigate whether multiple planets, from Neptunian up to Saturnian mass, can lead to the formation of dust gaps and cavities due to pebble accretion only, without the aid of gas pressure bumps.

The paper is structured as follows: We present the dust transport model and simulation initial conditions in Sect. 6.2. In Sect. 6.3, we investigate and analyze dust transport and its dependence on planet and disk properties. Following this, in Sect. 6.4, we compare the morphology differences between the rings induced by Neptunian- and (super-)Jupiter-mass planets and find observational consistencies with our theoretical understanding. We discuss and summarize the results in Sect. 6.5 and Sect. 6.6, respectively.

6.2 Methods

6.2.1 Dust transport including pebble accretion

The dust surface density during its transport is modeled through the 1D advection-diffusion equation (e.g. Birnstiel et al. 2012):

$$\frac{\partial \Sigma_{\rm d}}{\partial t} + \frac{1}{r}\frac{\partial}{\partial r}(r v_{\rm drift}\Sigma_{\rm d}) - \frac{1}{r}\frac{\partial}{\partial r}\left[rD\frac{\Sigma_{\rm g}}{\Sigma_{\rm d}}\frac{\partial}{\partial r}\left(\frac{\Sigma_{\rm d}}{\Sigma_{\rm g}}\right)\Sigma_{\rm d}\right] = 0, \tag{6.1}$$

where $\Sigma_{\rm d}$ and $\Sigma_{\rm g}$ are the dust and gas surface densities, respectively, and D is the dust diffusivity. The dust loses angular momentum and drifts inward, due to the friction between the gas in the sub-Keplerian rotation and the dust in the Keplerian rotation. The dust radially drifts (Nakagawa et al. 1986) at the speed of:

$$v_{\rm drift} = -\frac{2{\rm St}}{1+{\rm St}^2}\eta v_{\rm K}, \tag{6.2}$$

where St and $v_{\rm K}$ represent dust Stokes number and local Keplerian velocity, respectively. The mid-plane gas pressure gradient η is expressed as:

$$\eta = -\frac{1}{2}\frac{\partial \log P}{\partial \log r}\left(\frac{H_{\rm g}}{r}\right)^2, \tag{6.3}$$

and $H_{\rm g} = c_s r/v_{\rm K}$ is the gas scale height, $c_s = \sqrt{k_{\rm B}T/\mu m_H}$ is the sound speed at the mid-plane. The gas mean molecular weight is taken to be 2.3.

We subtract the accreted pebble flux to account for pebble accretion during dust transport. The numerical treatment is given in Sect. 6.A. We calculate the 3D pebble accretion efficiency following Ormel & Liu (2018). This calculation depends on the planet's eccentricity, the dust Stokes number St, the local gas pressure gradient η, the gas scale height $H_{\rm g}$, and the vertical viscosity. The radial diffusion of the dust particles is ignored.

The diffusion process is ignored when including pebble accretion (Sect. 6.3 and Sect. 6.4.1). The steep pebble profile driven by pebble-accreting planets induces unrealistic leaks of pebbles near planet orbits in the numerical simulation ($D\frac{\Sigma_{\rm g}}{\Sigma_{\rm d}}\frac{\partial}{\partial r}\left(\frac{\Sigma_{\rm d}}{\Sigma_{\rm g}}\right) \gg -v_{\rm drift}$ in Eq. 6.1). The consequence of such simplification is discussed in Sect. 6.5.1. We also assess that dust radial diffusion can be negligible in the process of pebble accretion in Sect. 6.B, as the distance dust particles diffuse is smaller than the planet's Hill radius over one synodical timescale.

6.2.2 Initial conditions

Since the dust radial drift timescale is much shorter than the disk typical disk lifetime, the gas profile is fixed over time. We set up a protoplanetary disk with the usual power law plus cutoff shape (Lynden-Bell & Pringle 1974),

$$\Sigma_{\rm g}(r) = \frac{M_{\rm d}}{2\pi R_{\rm out}(1-e^{-1})}\frac{\exp(-r/R_{\rm out})}{r}, \tag{6.4}$$

where $M_{\rm d} = 0.1M_\star$ is the disk mass and $R_{\rm out}$ is the disk characteristic radius. The initial dust surface density distribution is set after assuming an initially constant dust-to-gas ratio:

$$\Sigma_{\rm d}(t=0,r) = Z\Sigma_{\rm g}(r), \tag{6.5}$$

where Z stands for the metallicity. Then the dust can be transported in the fixed background of gas.

The gas temperature profile is

$$T(r) = 200K\left(\frac{r}{1\,{\rm au}}\right)^{-0.5}, \tag{6.6}$$

which also sets the gas scale height, as well as the dust scale height through:

$$H_{\rm d} = \left(1+\frac{\rm St}{\alpha}\frac{1+2{\rm St}}{1+{\rm St}}\right)^{-1/2}H_{\rm g} \tag{6.7}$$

(Youdin & Lithwick 2007), where α is the gas viscosity parameter and St is the dust Stokes number. The St is defined by ${\rm St} = \pi s\rho_{\rm s}/2\Sigma_{\rm g}$, where s and $\rho_{\rm s}$ are the dust grain size and internal density. The choices of different temperature profiles hardly affect our calculations, which is discussed further in Sect. 6.5.1.

6.3 Pebble flux reduction

In this section, we studied how much the Neptunian- to Saturnian-mass planets (which are too small to open gas gaps $\gtrsim 10$ au at our disk conditions) reduce the pebble flux via pebble accretion around a solar-type star without making pressure bumps. The simulations are conducted using AMUSE (Portegies Zwart et al. 2009, 2013a; Pelupessy et al. 2013).

6.3.1 Pebble accretion efficiency

Once a planet grows sufficiently large to induce a pressure bump exterior to its orbit, it halts the incoming pebble flux and, as a consequence, pebble accretion stops. The maximum mass that one planet can reach before opening a gap is the pebble isolation mass, which is fitted from 3D-hydrodynamical calculation (Bitsch et al. 2018):

$$m_{\rm iso} = 25M_\oplus\left(\frac{h}{0.05}\right)^3\left[0.34\left(\frac{-3}{\log_{10}\alpha}\right)^4+0.66\right]\times\left[1-\frac{\partial\ln P/\partial\ln r+2.5}{6}\right]\frac{M_\star}{M_\odot}. \tag{6.8}$$

Here $\partial P/\partial r$ is the local pressure gradient of the radial gas disk. Planets at pebble isolation mass can decrease the ambient gas density by 10-20% (Bitsch et al. 2018). The pebble isolation

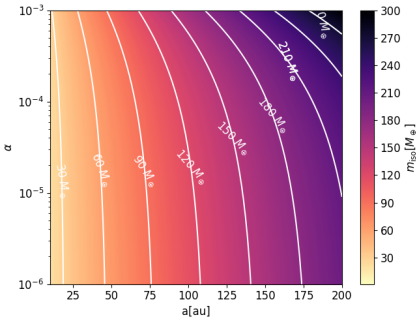


Figure 6.1. Pebble isolation mass around a solar-type star, with varying viscosity-α (y-axis) at different orbits (x-axis). The color bar indicates the pebble isolation mass calculated following Bitsch et al. (2018).

Table 6.1. Definition of quantities, symbols, and units.

Parameters	Value(s)	Description
α	10^{-6}, 10^{-5}, 10^{-4}	Viscosity parameter
St	$10^{-3.5}$, 10^{-3}, $10^{-2.5}$	Stokes number of dust
$m_{\rm p}/m_{\rm iso}$	0, 0.5, 0.75, 1.0	Planet mass normalized by local pebble isolation mass
Z	0.0134	Disk metallicity
$M_{\rm d}$	$0.1M_\star$	Disk mass
$R_{\rm out}$	200 au	Disk characteristic radius
μ	2.3	Gas mean molecular weight
$M_\star$	$M_\odot$	Star mass

Notes. The first three parameters separated from the rest by a horizontal line are the free parameters of the simulations.

mass at different distances with different viscosities is shown in Fig. 6.1. The pebble isolation mass increases toward high α and longer distance.

We calculated the pebble accretion efficiency $\epsilon_{\rm PA}$, assuming planets are in circular orbits. Remarkably, eccentric orbits (10^{-2}-10^{-1}) can enhance the pebble accretion efficiency by a factor of up to 3-5 (Liu & Ormel 2018). The planet mass is fixed at the local pebble isolation mass.

Our calculation in Fig. 6.2 shows the same results as Ormel & Liu (2018) found. When α increases, the pebble accretion efficiency decreases. That is because higher α stirs up more pebbles, especially with low St. This lowers $\epsilon_{\rm PA}$ as 3D pebble accretion becomes more common. Efficiency increases and then decreases as St grow from 10^{-5} to 10^{-1}. The accretion efficiency peaks when the pebble accretion cross section matches the pebble height, signaling the switch from 2D to 3D pebble accretion. As α drops, the peak shifts down because the dust height decreases. Bigger pebbles (higher St) lose efficiency since they drift too fast, missing the planet. Smaller pebbles (lower St) have a better chance of being captured because they spread out more.

As α drops below 10^{-4}, the peak $\epsilon_{\rm PA}$ reaches 0.5. This sweet spot expands as α decreases. At $\alpha = 10^{-5}$, $\epsilon_{\rm PA}$ exceeds 0.9 around St $= 10^{-3}$ beyond 50 au. With $\alpha = 10^{-6}$, $\epsilon_{\rm PA}$ hits unity if St falls between 6×10^{-5} and 2×10^{-3} at nearly all distances in the disk. The accretion sweet spot (with high $\epsilon_{\rm PA}$) area expands even more if lower α is used.

Pebble accretion is very efficient, with an efficiency always over 0.1, even at $\alpha = 10^{-3}$. This is because the planet mass we used is the maximum mass that the planet can reach before opening a deep gas gap. The pebble accretion efficiency for smaller planets can be roughly

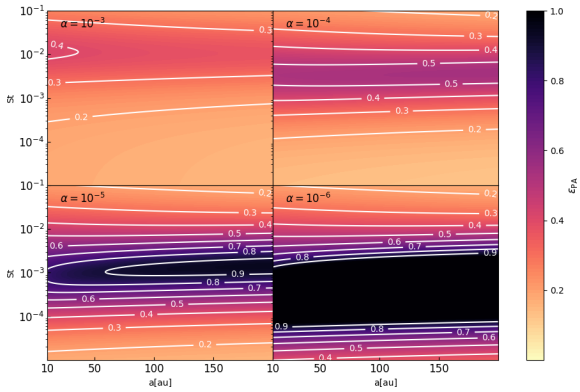


Figure 6.2. Efficiency map illustrating pebble accretion onto a planet in a circular orbit. We manipulated the planet's semimajor axis (x-axis) and the dust Stokes number (y-axis). The planet's mass corresponds to the pebble isolation mass within its local disk. Variations in viscosity (α) are indicated across four panels. Contours and the color display the values of the pebble accretion efficiency.

estimated. It shows a positive correlation with planet mass, following a power law ranging from 0.5 to 1.0 (in the 2D and 3D regime, respectively Ormel & Liu 2018). For example, a planet with half the pebble isolation mass exhibits roughly half the accretion efficiency depicted in Fig. 6.2.

6.3.2 Dust cavity and ring structure

Efficient pebble accretion can shape the dust continuum profile noticeably due to planets. This effect is expected to be more apparent in closely packed multi-planet systems. In this section, we focus on understanding the geometry of the resulting dust substructures and how they relate to disk and planet parameters.

Due to the angular momentum exchange between the gas disk and planets, planets can migrate in the disk (Lin & Papaloizou 1979; Goldreich & Tremaine 1980). Mean Motion Resonance (MMR) is a natural outcome of planet migration (Terquem & Papaloizou 2007; Raymond et al. 2008). This is consistent with exoplanet observations as we already found many multi-planet systems in resonance chains. For instance, the two (possibly three Christiaens et al. 2024) planets in PDS 70 are in MMR(s) (Wang et al. 2021a). The four directly imaged planets in HR 8799 are in MMRs (Zurlo et al. 2022). There are more planets in MMRs in the Kepler field (10-20%, Huang & Ormel 2023; Hamer & Schlaufman 2024).

Therefore, we begin with five planets arranged in a 3:2 resonance pattern, with their orbital periods close to integer ratios. The innermost planet is positioned at 28 au, with subsequent planets at 36.7, 48.1, 63.0, and 82.6 au. The mutual dynamical interactions are not modeled, instead, we assumed they are stable at their orbits and then study the disk evolution using the 1D model. Simulations run until $t_{\rm end} = 0.5(0.01/{\rm St})$ Myr, allowing sufficient drift of dust particles with varying St. Extending the simulation duration does not alter the normalized density distribution's shape, only decreasing its absolute values.

We varied three parameters: planet mass, disk viscosity (α), and the dust Stokes number St. All the planets have the same mass ratio $m_{\rm p}/m_{\rm iso}$, reflecting the ratio of the planet's mass to the local pebble isolation mass. The parameter values and ranges are shown in Table 6.1. The ranges of α and St are further assessed in Sect. 6.5.2.

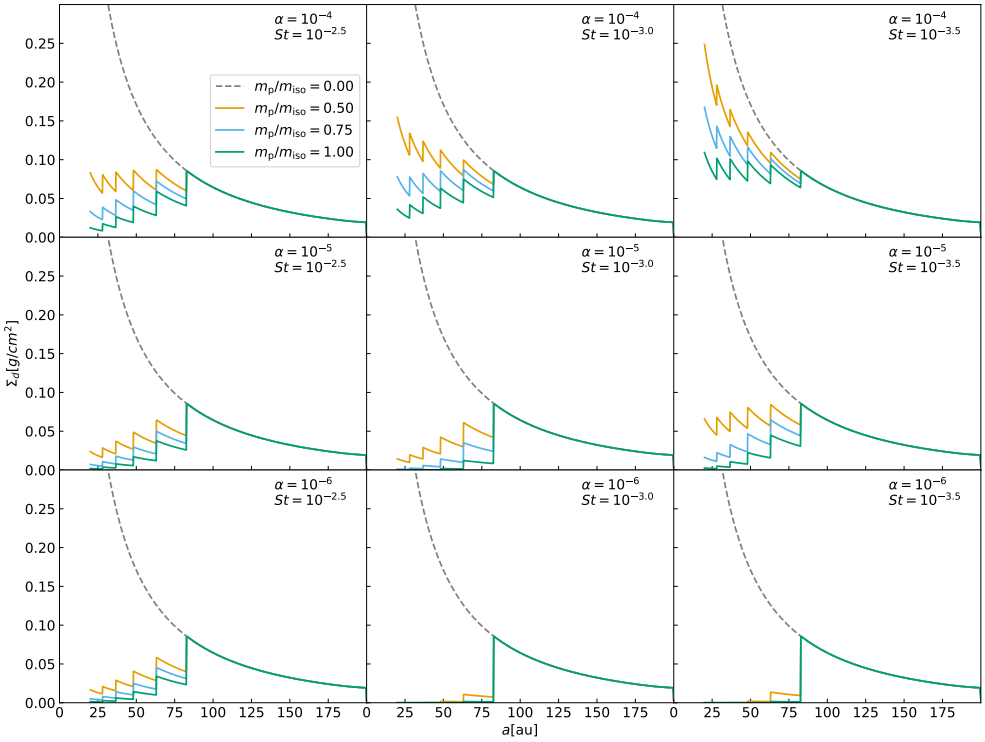


Figure 6.3. Equilibrium dust surface density profiles across various planet masses, viscosities, and Stokes numbers at different planetary orbits. There are five planets in a 3:2 MMR chain and dust surface density drops at planets' orbits due to pebble accretion. Each row corresponds to a different α value, while each column represents a different Stokes number (St). The color distinguishes between dust profiles associated with different planet masses, with the grey dashed line denoting the no-planet case.

The resulting dust profile is shown in Fig. 6.3. Reductions in dust surface density appear at all planetary orbits due to pebble accretion. Overall, the inward pebble flux decreases at each of the planet locations, resulting in lower surface densities compared to scenarios without planets. Notably, most disks in the simulations with planets show inner cavity features, with their dust surface density peaking at ≈ 80 au, far from the disk's inner edge.

Our simulations are consistent with the efficiency map of pebble accretion discussed in Sect. 6.3.1. The depth of the cavity increases as α decreases, corresponding to the rise in $\epsilon_{\rm PA}$. Furthermore, when α is fixed, the deepest cavity shifts toward smaller St values, mirroring the movement of the high-efficiency sweet spot indicated by the deep-colored regions in Fig. 6.2.

When the mass ratio $m_{\rm p}/m_{\rm iso} = 1.0$, the simulation with $\alpha = 10^{-4}$ and $\mathrm{St} = 10^{-3.5}$ is particularly interesting. The simulation does not exhibit the cavity feature. Instead, the peak dust surface density is near the disk's inner edge. This occurs because of the combination of small dust particles and high viscosity, resulting in a dust scale height much greater than the planet's accretion cross-section. Consequently, the efficiency of pure 3D pebble accretion is insufficient to create a cavity-like feature in the dust profile with five planets.

The fraction of disks with a cavity is low in the simulations when the planets are rela-

tively small $m_p/m_{peb} = 0.5$. Essentially, the cross-section between the pebbles and planets is proportional to the planet Hill radius (Ormel & Liu 2018), hence smaller planets induce a lower net probability of pebble accretion and shallow cavity. In theory, a larger number of planets in the system could still result in the formation of a cavity, with the depth of the cavity increasing as the number of planets rises.

If the viscosity is at its minimum in our parameter space ($\alpha = 10^{-6}$), the deep cavity persists. The cavity radius reaches ≈ 80 au, at the orbit of the outermost planet when St $= 10^{-3}$ and $10^{-3.5}$, because the efficiency of planet pebble accretion approaches unity with low turbulence. In such cases, the outermost one or two planets can accrete the entire incoming pebble flux, leading to the formation of the inner cavity. Lower viscosity facilitates the creation of deep cavities even in systems with fewer planets.

As the disk evolves and approaches the stage where the dust disk becomes optically thin, the continuum intensity becomes proportional to the dust surface density. Consequently, density drops at the orbits of planets manifesting as ring-like structures. These rings exhibit a distinctive feature: the inner part of the ring appears sharp due to efficient pebble accretion, while the outer part of the ring appears much smoother, as outer pebbles gradually and smoothly drift inward. This special feature can be used to distinguish pebble accretion-induced rings from others in observations, especially when the disk substructures can be resolved to spatial scales of $\lesssim 10$ au with ALMA at high angular resolution.

Table 6.2. Source properties and information of the used ALMA observation.

Source	Inc[°]	PA1[a] [°]	Distance[pc]	FWHM[mas]	PA2[b] [°]	Band
GM Aur	53.21	57.17	159	45×25	2.2	6
PDS 70	51.7	156.7	112.4	74×57	63	7

Notes. [(a)] Position angle between the major axis of the disk to the North.
[(b)] Position angle between the major axis of the beam to the North.

References. (1) Huang et al. (2020), (2) Keppler et al. (2018)

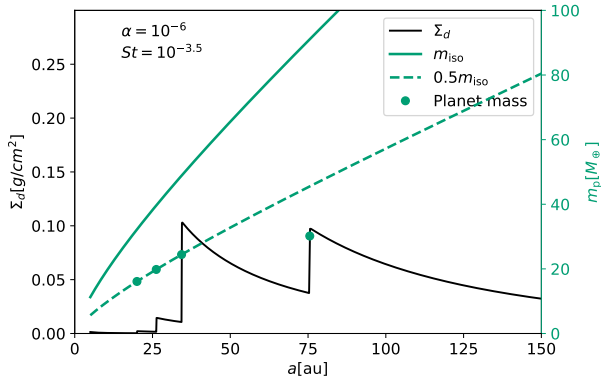


Figure 6.4. Dust profile and the planet mass in the simulated GM Aur disk. The disk parameters used are labeled on the top left. The solid line is the dust surface density profile and the values are shown on the left y-axis. The black dashed line represents the pebble isolation mass at different locations (x-axis), while the grey dashed line represents half of the pebble isolation mass. Black dots indicate the location and the mass of the planets. The right y-axis shows the values of planet mass.

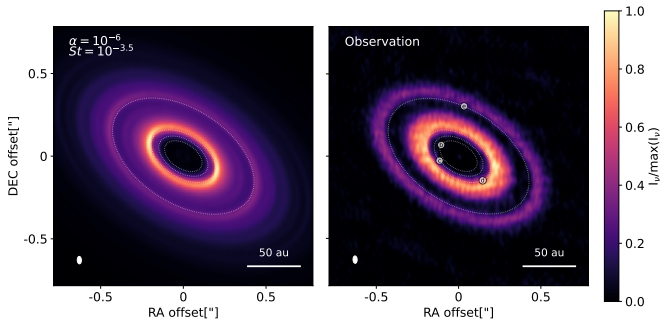


Figure 6.5. Comparison between the dust continuum in the simulation (left panel) and observation (right panel) for GM Aur disk from Huang et al. (2020), both of them are at 1.3 mm, in ALMA Band 6. The intensities are normalized to the maximum values. We indicated the synthesized beam (lower left corner) and the physical scale of the disk (lower right corner). The simulated dust continuum uses the same dust surface density distribution as in Fig. 6.4, with the used disk parameters labeled on the top left in the panel. The thin white dashed lines indicate the orbit of the imposed planets in the simulation. We overplotted the orbits of the hypothesized four planets on top of the observed continuum.

6.4 Two groups of planet-hosting transition disks

In the previous section, we showed that pebble accretion is able to create the appearance of an inner dust cavity without pressure bumps. Our scenario is consistent with the disks with deep dust cavities but no apparent deep gas cavities, such as GM Aur (Huang et al. 2020). This contrasts with disks hosting giant planets, such as PDS 70 (Keppler et al. 2018), where a gas giant opens up a deep gap in the gas disk, trapping dust in the pressure maximum outside the gas gap.

We propose that there are two groups of **planet-hosting** transition disks based on the planet's mass:

- Above pebble isolation mass: In this group, the planet(s) within the disk exceeds the local pebble isolation mass. The presence of gas giant(s) disrupts the gas disk, leading to pressure bumps that affect the dust profile.

- Below pebble isolation mass: Here, the planet(s) within the disk is below the local pebble isolation mass. The gas disk remains undisturbed by the planet(s), while the pebble flux is reduced at planet orbit(s) due to pebble accretion.

We selected two example sources, representing the two groups respectively, and compare the simulated continuum with observations. The sources are GM Aur and PDS 70. The source properties and the information of the used observational data are shown in Table 6.2.

The continuum image is generated using RADMC3D (Dullemond et al. 2012). We input 3D dust volume density distribution into RADMC3D. In the vertical direction, the dust density is assumed to follow Gaussian distribution with the scale height calculated via Eq. (6.7). The 1D dust surface density distribution can then be projected to 3D volume density distribution. The DSHARP dust opacity (Birnstiel et al. 2018) is used and is calculated via `optool` (Dominik et al. 2021). The dust follows the default power law distribution with a minimum size of 0.05 μm, a maximum size of 3 mm, and a power law slope of 3.5.

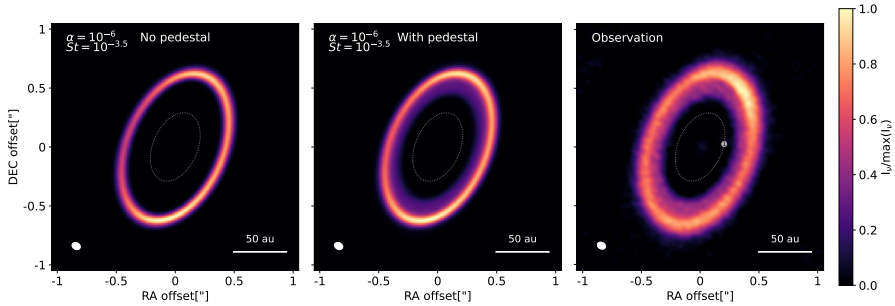


Figure 6.6. Similar to Fig. 6.5. Comparison between the dust continuum in the simulation (left and middle panels) and observation (right panel) for PDS 70 disk from Keppler et al. (2018), all of them are at 0.9 mm, in ALMA Band 7. In the left panel, the dust profile is from the dust evolution simulation. In the middle panel, we added a small dust population onto the simulated dust profile, to simulate the inner pedestal inside the ring.

6.4.1 Below pebble isolation mass: GM Aur

GM Aur is of particular interest for this paper as it is a transition disk with distinctive features in its continuum. It exhibits two rings, with the inner ring displaying an outer "shoulder" around $R \approx 40$ au. Notably, the inner part of this ring appears steeper than the outer part. This characteristic draws our interest because rings induced by pebble accretion often exhibit similar features – sharp inner edge but smooth outer edge. In addition, Zhang et al. (2021a) ruled out a deep gas cavity in GM Aur using ALMA observations of CO isotopologues.

For these reasons, we tailored the planet and disk properties in the feasible range following Table 6.1, to show the physical consistency between GM Aur and our proposed pebble accretion scenario. Finally, we included four planets, with the inner three planets in a 3:2 resonance chain while the outermost planet does not join. The location of the outermost planet is set to match the position of the observed outer ring in GM Aur. The planets are at 20.0, 26.2, 34.3, 75.5 au orbits, respectively. The planet masses are no more massive than half of the local pebble isolation mass, they are 16.1, 19.8, 24.4, 30.2 $M_\oplus$, respectively. The viscosity α is chosen to be 10^{-6} and St is $10^{-3.5}$.

The resulting dust surface density profile is shown in Fig. 6.4. At each planet's orbit, the dust profile shows a cliff-like feature. The inner three planets are half of the local pebble isolation mass. They are responsible for the inner dust cavity, as they accrete the drifting dust efficiently. The efficient accretion is consistent with Fig. 6.3. The fourth planet is about 1/3 of the local pebble isolation mass. The mass of planet e is chosen such that the inner ring is as bright as in the ALMA continuum image (Huang et al. 2020).

In addition, we find that the planet orbits always coincide with the inner edge of the rings. This is because the inner edge of the rings is the location where the dust surface density drops, which is caused by pebble-accreting planets in our scenario. This is different from the gap opening scenario, where the planets are usually located at the center of the gap (see e.g. Kanagawa et al. 2017).

The corresponding continuum image for the simulated dust profile is displayed in Fig. 6.5, in comparison with the observed image of GM Aur (Huang et al. 2020). The orbits of the imposed planet are indicated by the dashed lines and overplotted on top of the observed continuum image. The longitudes of the planets on their orbits are consistent with the scenario that they are connected by a Laplace resonance chain.

After convolving the image with the beam, the two rings are still observed in the simulated continuum which is consistent with the observation. As expected, the inner ring in the simulated GM Aur continuum has an extended outer edge than the inner, which is consistent with the observations. ALMA also shows that there is an extended outer dust disk of the second ring (Huang et al. 2020), indicating the ongoing dust drifting process.

The gap between the two rings is not as pronounced as observed. One possible explanation is that planet e has grown beyond the gap-opening mass. The pressure bump created by planet e prevents the inward drift of small pebbles, which could account for the deeper gap between the two rings seen in observations. If this is the case, planet e must have reached this size within the last few $\sim$ kyr; otherwise, most of the dust would have been trapped in the outer ring, making the inner ring significantly fainter due to dust radial drift.

The inner edge of the simulated ring is not extremely sharp because a small percentage of the pebble flux bypasses the orbit of planet d without being accreted. Observations show a similar feature, though with a shallower gradient. Increasing the mass or the eccentricity of planet d would result in a sharper inner edge that is more consistent with observation.

We included three planets within the cavity to ensure that most of the dust pebble flux is accreted. In Sect. 6.C, we also explored the scenario where planet b is removed, but find that the resulting cavity is not as deep as observed. Enhancing the accretion efficiency of pebble flux and clearing the cavity can be achieved by increasing the number of planets, increasing planet mass, and putting planets on eccentric orbits (Liu & Ormel 2018).

We managed to explain the clear inner cavity along with dust drifting outer disk in GM Aur by a sequence of pebble-accreting planets. A detailed fitting going through a larger parameter space could still improve the match to the observed continuum image in the future, and potentially give a firmer prediction of the properties of planet candidates.

6.4.2 Above pebble isolation mass: PDS 70

PDS 70 is known to host two directly observed giant planets that create a large gap in both the gas and dust disks (Haffert et al. 2019). This system provides valuable insights into disk structures with massive giant planets. Therefore, we selected PDS 70 as a representative disk hosting giant planets with masses above the pebble isolation mass.

To simulate the outer ring in PDS 70, we imposed a 10 $M_{\rm J}$ mass planet at 34.3 au. We adopted the analytical shape of the gas gap opened by the planet following Kanagawa et al. (2017) and Pichierri et al. (2024). The detail is illustrated in Sect. 6.D. The dust diffusion and radial drift are considered during its transport. The dust ring structure does not sensitively depend on the disk parameter we choose. As an example, we used $\alpha = 10^{-6}$ and $\mathrm{St} = 10^{-3.5}$, which is same as the values taken in Sect. 6.4.1.

The simulated dust profile is used to generate a continuum image through RADMC3D and presented in the left panel in Fig. 6.6. The dust drifts inward and accumulates at the pressure maximum outside the gap opened by the gas giant. The observed Band 7 high-resolution continuum image (Keppler et al. 2018) is shown in the right-hand panel. The simulated dust ring is located at the separation similar to the observation.

An apparent discrepancy between observation and simulation is that the observed continuum shows a pedestal at the inner edge of the dust ring while the simulated dust ring is radially symmetric. We note that including small grains might be able to explain the pedestal (Pinilla et al. 2024). We think that there are a couple of possible scenarios to explain the pedestal. The pedestal may be composed of i) small dust grains following the gas gap profile as they are too small to get trapped in the pressure bump; ii) small dust entrained by

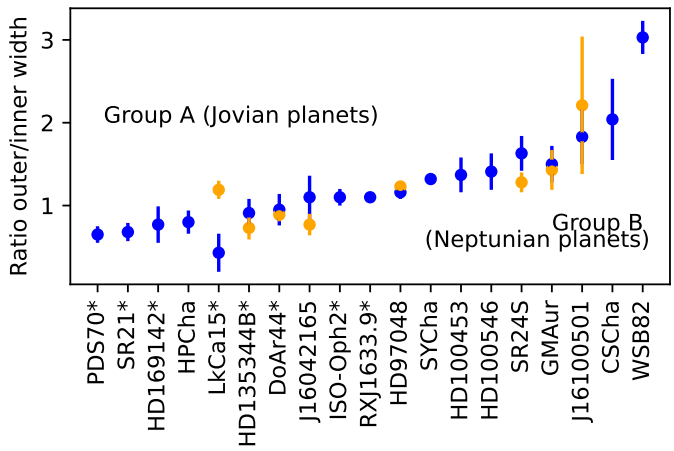


Figure 6.7. Ratio between outer and inner width of the dust rings in a sample of transition disks, as derived in Sect. 6.E. The blue symbols correspond to the inner ring, and the orange symbols to the outer ring, if present. Disks with an inner pedestal have been marked with a star. The targets are sorted by the average value of the ratio. Lower values $\lesssim 1$ are thought to correspond to Group A (Jovian protoplanets with a dust trap), and higher values $\gtrsim 1$ are thought to correspond to Group B (Neptunian protoplanets which are creating an apparent cavity by pebble accretion.

the accretion flow onto the planet (Toci et al. 2020); iii) small dust entrained by the irradiated flow from the inner gas wall (Franz et al. 2022).

While explaining the pedestal is out of the scope of this work, we here simply assumed there is a population of small dust grains that are well-coupled with gas. The dust distributes in the outer slope in the gas gap with a surface density of one percent of the gas:

$$\Sigma_{\rm d,sm}(r) = \begin{cases} 0.01\Sigma_{\rm g}(r) & \text{for } \Delta r_1 < (r - r_{\rm p}) < \Delta r_2, \\ 0\,{\rm g/cm^2} & \text{otherwise.} \end{cases} \tag{6.9}$$

The planet's orbit is $r_{\rm p}$, Δr_1 is the gap bottom radius and Δr_2 is the gap edge radius. The simulated dust continuum image after adding the small dust population is shown in Fig. 6.6 middle panel. By construction, we now observe the inner pedestal within the main ring in the generated continuum. Whether the protoplanetary disks with gas giants always exhibit rings with pedestals outside the planets' orbits needs to be examined in the future, when more proto-giant planets are confirmed.

Regardless of the pedestal, the dust ring morphology outside a massive planet is distinct from a dust ring outside a sequence of pebble-accreting planets. Compared to the dust rings induced by pebble-accreting low-mass planets (e.g., in GM Aur), the dust rings trapped in the pressure maximum caused by gap-opening planets have more radially symmetric rings (maybe show even smoother inner edges in observation e.g., in PDS 70). This difference arises from the physics involved: in PDS 70, the diffusion of the dust near the gas pressure maximum results in a symmetric ring. Conversely, in GM Aur, the sharp cutoff of pebble flux by the planet's pebble accretion creates a cliff-like feature at the ring's inner edge.

6.4.3 A sample of transition disks

Whether the planet in the disk is below or above the local pebble isolation mass results in different radial ring morphologies. Motivated by the apparent morphologies of PDS70 and

Table 6.3. Sample of transition disks with dust ring ratios, CO properties, and stellar properties.

Target	R_1	R_2	Ped.[a]	CO analysis	^{12}CO gap?	^{13}CO gap?	Ref.	Class	d (pc)	M_* ($M_\odot$)	log M_{acc} ($M_\odot$ yr^{-1})
PDS70	0.7±0.1	-	Y	deep	Y	Y	1,2	A	113	0.8	-10.2
SR21	0.7±0.1	-	M	deep	Y	Y	3,4	A	138	2.0	-7.9
HD169142	0.8±0.2	-	Y	deep	Y	Y	5	A	114	2.0	-8.7
HPCha	0.8±0.1	-	N	-	-	-	-	A	160	1.4	-9.0
LkCa15	0.4±0.2	1.2±0.1	Y	moderate	M	M	5	A/B?	158	0.8	-8.4
HD135344B	0.9±0.2	0.7±0.1	Y	deep	Y	Y	3,6	A	136	1.6	-7.4
DoAr44	1.0±0.2	0.9±0.1	Y	deep	-	Y	3	A	146	1.0	-8.2
J16042165	1.1±0.3	0.8±0.1	N	deep	Y	Y	7,8	A	150	1.2	-10.5
ISO-Oph2	1.1±0.1	-	M	-	N	-	9	A/B?	144	0.5	-8.5
RXJ1633.9	1.1±0.1	-	M	-	Y	-	9	A/B?	141	0.8	-10.0
HD97048	1.2±0.1	1.2±0.1	N	-	Y	Y	10,11	A	185	2.4	-8.2
SYCha	1.3±0.0	-	N	-	N	-	12	B	183	0.8	-9.4
HD100453	1.4±0.2	-	N	-	N	-	13	B	104	1.5	<-8.3
HD100546	1.4±0.2	-	N	deep	Y	Y	14	A/B?	110	2.2	-7.0
SR24S	1.6±0.2	1.3±0.1	N	-	N	N	9,15	B	114	1.5	-7.2
GMAur	1.5±0.2	1.4±0.2	N	moderate	N	M	16	B	160	1.0	-8.3
J16100501	1.8±0.3	2.2±0.8	N	-	-	-	-	B	145	0.6	-8.6
CSCha	2.0±0.5	-	N	-	Y	-	17	B	176	1.5	-8.3
WSB82	3.0±0.2	-	N	-	N	-	9	B	156	-	-

Notes. [(a)] Presence of a pedestal: Y=Yes, N=No, M=Maybe.

References. (1) Muley et al. (2019), (2) Facchini et al. (2021); (3) van der Marel et al. (2016); (4) Yang et al. (2023); (5) Leemker et al. (2022); (6) Casassus et al. (2021); (7) Dong et al. (2017b); (8) Stadler et al. (2023); (9) Antilen et al. (2023); (10) Pinte et al. (2019); (11) Wölfer et al. (2023); (12) Orihara et al. (2023); (13) Rosotti et al. (2020); (14) Leemker et al. (2024); (15) Pinilla et al. (2017); (16) Zhang et al. (2021b); (17) Kurtovic et al. (2022);

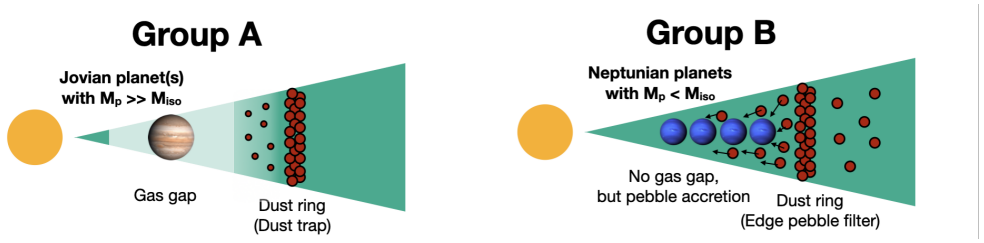


Figure 6.8. Cartoon demonstrating the two proposed mechanisms responsible for the transition disk cavity appearance. For disks classified as Group A it is thought that one or more Jupiter-like planets with a mass well above the pebble isolation mass have carved a gas gap, trapping the millimeter dust in a narrow ring outside its orbit, whereas for disks classified as Group B a number of Neptunian planets with a mass below pebble isolation mass are still actively accreting pebbles, thereby creating the appearance of a dust cavity as the inner edge of the dust ring is acting as a 'filter' where pebbles are accreted, and the pebbles in the dust ring are not trapped, but follow a smooth dust density pattern.

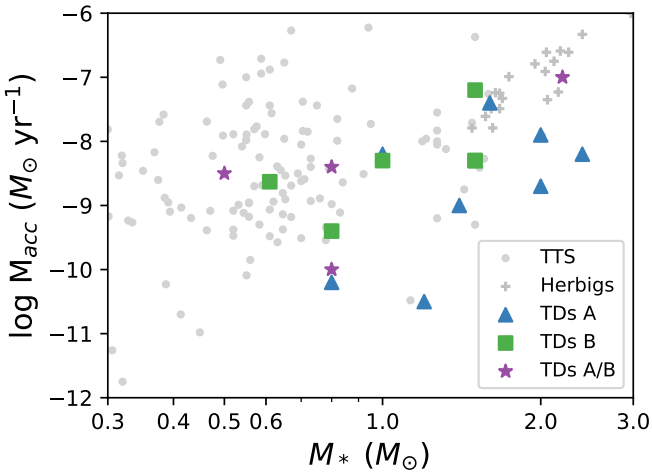


Figure 6.9. Accretion rates of the transition disks in our sample (colored symbols) compared with those of the larger disk population, taken from Manara et al. (2023); Wichittanakom et al. (2020). Group A transition disks appear to have very low accretion rates compared to the general disk population, whereas Group B transition disk accretion rates are more typical. For the Group A/B transition disks the classification from dust and CO observations is still unclear.

GM Aur, we calculated the ratio of the outer to inner width of dust rings ($R = \sigma_{\rm outer}/\sigma_{\rm inner}$) in the radial profiles of a larger sample of ∼20 transition disks (see Sect. 6.E). The results are shown in Fig. 6.7. If two rings are present, both ring ratios are shown. We tentatively classify the transition disks into two groups according to the dust ring structure:

- Group A: The width ratio of the ring is $\lesssim 1$ and a pedestal may be present.
- Group B: The width ratio of the ring is $\gtrsim 1$ and no pedestal is present.

Group A is consistent with giant planet disks with the planet mass above the pebble isolation mass. Group B is consistent with the disks with the planet mass below the pebble isolation mass. The difference is illustrated in Fig. 6.8.

Furthermore, we searched the literature for information about the gas inside the cavity through spatially resolved CO 3-2 or 2-1 isotopologue ALMA images. This helps distinguish between cavities with a protoplanet massive enough to carve a deep gas gap (Group A) and cavities with less massive protoplanets that cannot carve such a gap, like GM Aur (Group B). Only CO data with sufficient spatial resolution to fully resolve the dust cavity by at least three beams are considered. For half of our sample, physical-chemical modeling has been used to derive the gas cavity depth (e.g. van der Marel et al. 2016), which is often found to be at least two orders of magnitude depleted in density ('deep'), but sometimes just a factor of a few ('moderate'). Deep gas cavities usually show a deficit of ^{12}CO emission in the center of the disk, as even the ^{12}CO emission becomes optically thin. For transition disks without physical-chemical analysis, it is still possible to assess the possibility of a deep gas cavity considering the presence of a ^{12}CO and/or ^{13}CO deficit. Table 6.3 summarizes the results for all targets in our sample for both the dust ring ratios and the CO properties as well as its stellar properties (taken from van der Marel 2023). Based on CO and dust ring properties, each disk is then classified as either A-type or B-type. Some disks have inconsistencies when considering the dust profile and the CO properties, or are on the borderline: these are marked as A/B.

Using the classifications derived in Table 6.3, we finally explored the accretion rates of the two groups. Figure 6.9 shows the accretion rates of the transition disks in our sample compared with the accretion rates of all nearby T Tauri stars, using the stellar data from Manara et al. (2023) as well as the accretion rates of all nearby Herbig stars, using the stellar data from Wichittanakom et al. (2020).

When comparing the accretion rates of the two groups, Group A transition disks appear to have very low accretion rates compared to the general disk population, whereas Group B transition disk accretion rates are 1-2 orders of magnitude higher and more similar to typical accretion rates. This is consistent with a scenario where the protoplanets in Group A transition disks are almost finished accreting gas, as they have already grown to (super-)Jupiter sizes and cleared a gap in their gas distribution, whereas Group B transition disks contain protoplanets that have not started runaway gas accretion yet, which is expected for planets well below pebble isolation mass with high pebble accretion rates (Brouwers et al. 2021; Ormel et al. 2021).

6.5 Discussion

6.5.1 Model assessment

We have simulated dust transport, accounting for the reduction of pebble flux due to pebble accretion. This approach enables us to analyze the resulting dust surface density profile

across various disks hosting low-mass planets (below pebble isolation mass). The planets are assumed to have zero eccentricities, while eccentric planets can increase the pebble accretion efficiency by 3-5 (Liu & Ormel 2018).

We neglected the perturbation that the planet exerts on the gas disk. When a planet approaches the pebble isolation mass, it can still create shallow gaps. Bitsch et al. (2018) suggest that a planet at this mass can generate a gap with a depth of about 10-20%. Dust may accumulate at such shallow pressure maxima. Additionally, gas polar inflow and radial outflow induced by the planet's gravity can inhibit pebble drift (Kuwahara et al. 2022; Bi & Lin 2024, and references therein), and possibly decrease pebble accretion efficiency (Kuwahara & Kurokawa 2020; Okamura & Kobayashi 2021).

This work focuses on capturing the changes in pebble flux and surface density profiles due to pebble accretion. Arguably, our model applies even to the planets with their mass slightly above the pebble isolation mass because the timescale for gap opening correlates with the viscous timescale. Therefore, when a planet doubles its mass, the gap-opening process may not be complete (Bergez-Casalou et al. 2020), allowing dust to drift inward while the pressure bump is forming.

The model is not very sensitive to the gas temperature profile. The dust scale height and pebble isolation mass increase with the temperature increase. Increasing scale height decreases the probability for the pebbles to hit one planet, which is lower in the 3D limit. In contrast, larger pebble isolation mass makes the planets more difficult to open the gap, which enhances pebble accretion efficiency because of the increase of the cross-section between the larger planet and the pebbles.

We did not account for the radial diffusion of dust when studying the resulting dust profile after pebble accretion. The inclusion of radial diffusion may have two main differences: On one hand, dust diffusion could slow down the dust radial drift speed (Gerosa et al. 2024). The random motion of dust particles could increase their chances of close encounters with the planet and potentially enhance the pebble accretion rate. On the other hand, if the dust is too diffusive, the dust may bypass the planet's orbit rather than being accreted. We assess that dust diffusion during pebble accretion is not important in Sect. 6.B, where we show that the distance dust particles diffuse is smaller than the planet's Hill radius. However, we acknowledge that the full impact of radial dust diffusion on pebble accretion requires a more detailed investigation.

6.5.2 Feasibility of the "sweet spot" on the accretion map

Low viscosity ($\alpha = 10^{-5} - 10^{-6}$) is justified both theoretically and observationally. High stellar accretion rates observed in protoplanetary disks have been interpreted as evidence for $\alpha = 10^{-3} - 10^{-2}$ in the classic viscous disk model (Lynden-Bell & Kalnajs 1972), where viscosity may arise from magneto-rotational instability (Balbus & Hawley 1991). However, in regions with low ionization and weak coupling between gas and magnetic fields, hydrodynamic or non-ideal MHD effects could dominate angular momentum transfer, resulting in stellar accretion rates matching observations (Bai & Stone 2013; Flock et al. 2020). In such scenarios, turbulent parameters can be as low as $\alpha = 10^{-4} - 10^{-6}$, as preferred in our study. Observations of inclined protoplanetary disks, such as HL Tau and Oph 163131, reveal settled dust profiles in the midplane, indicating low turbulence with $\alpha \lesssim 10^{-5}$ (Pinte et al. 2016; Villenave et al. 2022). From line broadening, Flaherty et al. (2020) suggests weak turbulence for MWC 480 and V4046 Sgr.

Recent simulations of dust size evolution suggest a near-monodisperse distribution cen-

tered around St $\sim 10^{-3}$ (Dominik & Dullemond 2024). The maximum size of dust particles is constrained by fragmentation, radial drift, and bouncing (Kelling et al. 2014; Kruss et al. 2016), limiting the dust Stokes number to $\sim 10^{-3}$ (Dominik & Dullemond 2024). In low α disks, the bouncing barrier primarily restricts the upper limit of the dust size distribution, resulting in near-monodisperse size distributions in simulations. Notably, the Stokes number depends on the gas surface density, St $\sim s/\Sigma_{\rm g}$. Our Group B disks are likely in an early phase with relatively massive gas disks, so the corresponding grain Stokes number (with the same size s) could be relatively small compared to other more evolved disks.

6.5.3 Emerging the planet formation story in transition disks

Since the direct detection of proto-giant planets in the PDS 70 disk, (super-)Jovian-mass planets have been favored for explaining transition disks. Their substantial mass allows them to strongly perturb the disk and create cavities or gaps (e.g., Dong et al. 2015, 2017a; Li et al. 2019; Garrido-Deutelmoser et al. 2023b; Wu et al. 2023, and references therein). In this study, we proposed that a chain of planets below the pebble isolation mass could also account for transition disks, named Group B disks. Group A disks are those hosting (super-)Jupiters.

Group A transition disk may evolve from B transition disks. If Jovian-mass planets form through core accretion (e.g., Perri & Cameron 1974), they must first pass through a stage where they are of Neptunian size. Our study shows that dust cavities begin to appear even when planets are still low-mass and the gas disk remains largely unperturbed. As planets grow, while pressure bumps form gradually, dust continues to drift and accumulate at these pressure bumps. Over time, we expect the dust ring morphology to become more radially symmetric (possibly even developing an inner pedestal, as seen in PDS 70, Sect. 6.4.2) and the Group B disk to gradually transition into a Group A disk. However, Jovian-mass planets may also form directly via Gravitational Instability (GI, Boss 1997). In such cases, the period of maintaining Neptunian mass may be too short for dust to drift. Potentially, the Group B stage is skipped in the case of GI and the two groups do not necessarily represent evolutionary stages. It is worth noting that GI may also form super-Earth to Neptune mass planets (Kubli et al. 2023), but this still needs further investigation.

Group B disks also do not necessarily evolve into Group A from the perspective of gas accretion. The growth of Neptunian-mass planets via pebble accretion (Ormel & Liu 2018; Johansen & Bitsch 2019) and subsequent gas accretion (Ida et al. 2018) can lead to Jovian-mass planets. Gas accretion is a complex process. It is initially governed by Kelvin-Helmholtz contraction but then limited by the amount of gas entering the Hill-sphere of the planet (Tanigawa & Tanaka 2016). The envelope contraction speed depends on the cooling timescale. If the atmosphere opacity is high, or the atmospheric recycling is efficient (e.g. Ormel et al. 2015), the gas accretion can be prolonged. If the gas disk disperses before the runaway gas accretion on the planet can happen, the Group B transition disk can never evolve to A.

In a Group B transition disk, the creation of a large dust cavity in the protoplanetary disk necessitates a multi-planet system, typically comprising three or more planets. Such large planet multiplicity aligns with observations of certain systems. For instance, the four gas giants in the HR 8799 system (Goździewski & Migaszewski 2020) may grow from a sequence of low-mass planets. Similarly, the PDS 70 system has two confirmed planets and possibly a third one (Christiaens et al. 2024). However, it's noteworthy that the observed multiplicity of planets at wide orbits (beyond $\gtrsim$10 au) might be lower than expected. Several factors contribute to this trend. 1) The innermost planet may not have yet encountered the migration barrier. Planets migrate inward to the region $<$ 10 au in Type I or II regime (Paardekooper

et al. 2010; Kanagawa et al. 2018). 2) Planets may undergo inefficient growth, and the disk may dissipate before they enter the runaway growth phase, analogous to the giant planets in our solar system (Gurrutxaga et al. 2024). Small planets on wide orbits are challenging to detect. 3) As the number of planets in a system increases, the dynamical stability of the system tends to decrease (Pichierri & Morbidelli 2020). Consequently, some planets may become inclined or unbound from their host stars following the onset of instability, so a multi-Neptunian protoplanet system may end up with a smaller number of bound Jovian planets.

6.5.4 Consequence for planet detection

The planets in Group B disks are often Neptune-sized and located at the inner edge of the dust rings. Current instruments are not sensitive enough to detect protoplanets below a few Jupiter masses (Asensio-Torres et al. 2021; Choksi & Chiang 2024). Even with more sensitive instruments in the future, detecting Neptunian protoplanets would still be extremely challenging due to their spatial proximity to the dust ring. Selecting the right targets (with a Group A morphology) would thus be the best strategy for future direct imaging campaigns.

6.6 Conclusions

We used dust transport models to study the dust surface density profiles in pebble-accreting multi-planet systems, in order to understand how the dust profile in protoplanetary disk changes with planet mass, disk viscosity, and dust size. We then compared the dust substructure morphology induced by pebble-accreting planets with those caused by pressure bumps. These are our main findings:

1. Multi-Neptunian planets (below the local pebble isolation mass) can sculpt deep cavities in the dust disk, potentially contributing to the appearance of some observed transition disks.

2. Planet-hosting transition disks may consist of two sub-groups. In Group A disks, gas giants open deep gas gaps and truncate the disk. In Group B disks, a sequence of Neptune-mass planets accrete all the inward pebble flux, leaving the gas disk unperturbed.

3. Rings formed by pebble-accreting planets often feature sharp inner edges and smooth outer shoulders (Group B disks), unlike the more symmetric rings induced by pressure bumps exterior to the gas gaps carved by massive gas giants (Group A disks).

4. In Group B disks, planets harbor near the inner edge of the induced rings, whereas in Group A disks the giant planets are located at the center of gaps or cavities.

5. Our classification of transition disks (Group A and B disks) is supported by observations. Transition disks with rings featuring extended outer but sharp inner edges coincide with higher stellar accretion rates and lack deep gas cavities inside the dust cavity, likely hosting pebble-accreting planets. The other disks, characterized by smooth rings, have lower accretion rates and deep gas cavities, likely hosting super-Jupiters.

Pebble accretion alters the dust profile in planet-forming disks, especially in low-turbulence environments. Although Neptunian-size planets at tens of au orbits remain beyond current

observational capabilities, they may yield dust rings with unique morphology in the continuum. Future high-resolution ALMA observations hold promise for expanding the sample size and corroborating our findings with enhanced statistical confidence.

Appendix

6.A Numerical treatment of pebble flux reduction

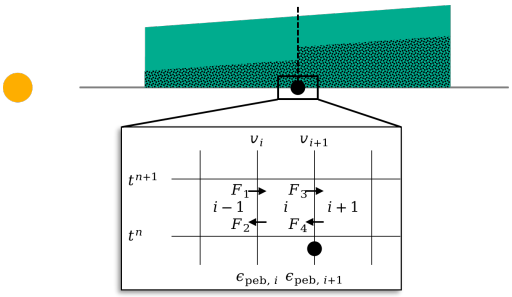


Figure 6.10. Sketch of the dust transport calculation on the disk grid i, from the time t^n to the time t^{n+1}, including pebble accretion. The disk is segmented into N grids. We focus on the region surrounding disk cell i in the zoomed-in view. Arrows depict the direction of various pebble fluxes. The flux going through the planet's orbit r_i is reduced by a factor $\epsilon_{\mathrm{peb},i}$, which is the planet's pebble accretion efficiency.

To solve for dust transport, we considered a grid of N cells valued by the dust surface density at their centers. An example of calculating the dust surface density in cell i from time n to $n+1$ is a sketch provided in Fig. 6.10. the adopted differential form of the advection term is

$$(\Sigma_{\mathrm{d},i}^{n+1} - \Sigma_{\mathrm{d},i}^{n})\frac{\Delta r}{\Delta t} = F_1 + F_2 + F_3 + F_4, \tag{6.10}$$

where $\Sigma_{\mathrm{d},i}^{n}$ is the dust surface density in cell i at time n, and F_1, F_2, F_3, and F_4 are expressed as:

$$F_1 = (1 - \epsilon_{\mathrm{pebb},\,i}) \cdot \max[v_i \Sigma_{\mathrm{d},i-1}, 0], \tag{6.11}$$

$$F_2 = \min[-v_{i+1}\Sigma_{\mathrm{d},i}, 0], \tag{6.12}$$

$$F_3 = \min[v_i \Sigma_{\mathrm{d},i}, 0], \tag{6.13}$$

$$F_4 = (1 - \epsilon_{\mathrm{pebb},\,i+1}) \cdot \max[-v_{i+1}\Sigma_{\mathrm{d},i+1}, 0], \tag{6.14}$$

respectively. They represent the pebble flux from cell $i-1$ to i (outward), from cell i to $i-1$ (inward), from cell i to $i+1$ (outward) and from cell $i+1$ to i, respectively. The dust velocities at the edges between cells $i-1$, i and i, $i+1$ are v_i and v_{i+1}. To simulate the pebble accretion effect on the dust, we reduced the incoming flux F_1 (Eq. 6.11) and F_4 (Eq. 6.14) by factors of $\epsilon_{\mathrm{pebb},\,i}$ and $\epsilon_{\mathrm{pebb},\,i+1}$, which stand for the 3D pebble accretion efficiency on the planets at the two edges. If no planet is included, the corresponding efficiency is set to zero. For example, in Fig. 6.10, a planet is located at the inner boundary of cell $i+1$ but not at i, so $\epsilon_{\mathrm{pebb,\,i+1}}$ is calculated, while $\epsilon_{\mathrm{pebb,\,i}}$ remains zero. In this case, only F_4 is reduced when determining the dust surface density in cell i.

6.B Evaluating dust diffusion during pebble accretion

We evaluated the feasibility of neglecting dust diffusion in our simulations. If dust diffusion is strong, dust particles may travel across the planet's orbit without being accreted. To assess

this, we calculated the distance over which dust diffuses during a synodical timescale with the nearby planet and compare it to the planet's Hill radius.

The synodical timescale between the planet and dust just outside the planet's Hill radius is given by:

$$t_{\rm syn} = \frac{4\pi}{3\Omega_{\rm K}} \frac{r}{R_{\rm Hill}}, \tag{6.15}$$

where $R_{\rm Hill}$ is the planet Hill radius and $\Omega_{\rm K}$ is the Keplerian frequency at planet's orbit. The diffusivity of small dust particles can be approximated by the gas diffusivity:

$$D = \alpha H_{\rm g}^2 \Omega_{\rm K}. \tag{6.16}$$

Thus, the distance dust diffuses over the synodical period is:

$$\Delta r_{\rm diff} = \sqrt{D t_{\rm syn}}. \tag{6.17}$$

If $\Delta r_{\rm diff}$ exceeds the planet's Hill radius, the dust is less likely to be accreted due to strong diffusion. Conversely, if $\Delta r_{\rm diff}$ is small, the dust can still be accreted. We define the dimensionless quantity C as:

$$C = \frac{\Delta r_{\rm diff}}{2R_{\rm Hill}} = 0.1 \left(\frac{T}{100\,{\rm K}} \frac{r}{10\,{\rm au}} \frac{\alpha}{q_{\rm p}} \frac{M_\star}{M_\odot} \right)^{0.5}, \tag{6.18}$$

where $q_{\rm p}$ is the planet-to-star mass ratio. The dust hardly diffuses across planet orbit if C is smaller than unity. Dust diffusion can be considered negligible if C is smaller than unity. In our simulations, with α ranging from 10^{-4} to 10^{-6} and the planet about Neptune mass, the value of C remains below unity. The dust diffusion can reasonably be ignored in our pebble accretion simulations.

6.C Simulated continuum of GM Aur with three planets

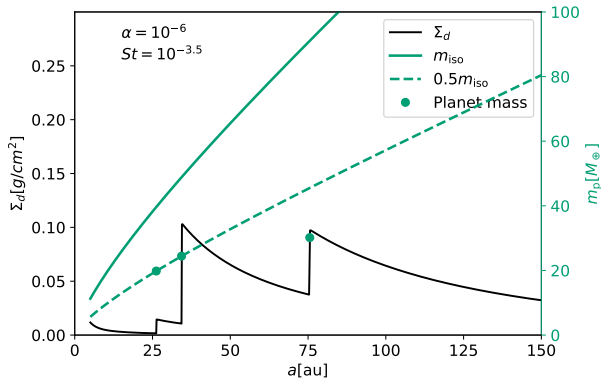


Figure 6.11. Similar to Fig. 6.4 but with three planets.

Similar to Sect. 6.4.1, we adopted three planets in the simulation by removing the innermost planet in Sect. 6.4.1. The planets are at 26.2, 34.3, 75.5 au orbits, respectively. The planet masses are no more massive than half of the local pebble isolation mass, they are 19.8, 24.4, 30.2 $M_\oplus$, respectively. The viscosity α is chosen to be 10^{-6} and St is $10^{-3.5}$.

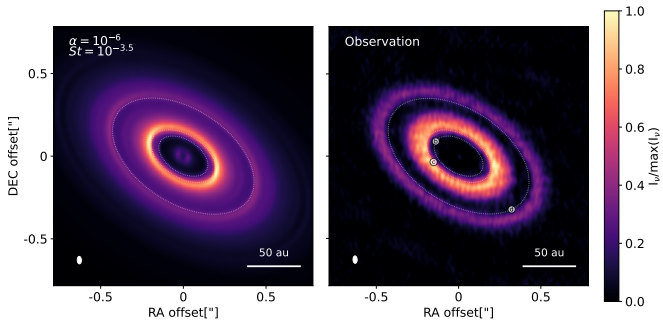


Figure 6.12. Similar to Fig. 6.5 but with three planets.

The resulting dust surface density profile is shown in Fig. 6.4. The corresponding continuum image for the simulated dust profile is displayed in Fig. 6.5, in comparison with the observed image of GM Aur (Huang et al. 2020). The orbits of the imposed planet are indicated by the dashed lines and overplotted on top of the observed continuum image.

The inward pebble flux is not fully accreted by the planets. The dust surface density grows as the semimajor axis decreases with conserving flux ($\Sigma_\mathrm{d} \sim F/rv_\mathrm{drift}$). Consequently, the simulated GM Aur has an inner disk, which is inconsistent with observation.

6.D Profile of the gap opened by planet

The gap shape is similar to the one shown in Kanagawa et al. (2017). The radial profile of the surface density in the vicinity of the gap is:

$$\Sigma_\mathrm{g}(r) = \begin{cases} \Sigma_\mathrm{min} & \text{for } |r - r_\mathrm{p}| < \Delta r_1, \\ \Sigma_\mathrm{gap}(r) & \text{for } \Delta r_1 < |r - r_\mathrm{p}| < \Delta r_2, \\ \Sigma_0 & \text{for } |r - r_\mathrm{p}| > \Delta r_1. \end{cases} \tag{6.19}$$

The gas surface density at the bottom of the gap is:

$$\Sigma_\mathrm{min} = \frac{\Sigma_0}{1 + 0.04 K_\mathrm{3D}}, \tag{6.20}$$

where Σ_0 is the initial gas surface density before the gap opening, and K_3D is the gap depth factor fitted by 3-D hydrodynamical simulations by Pichierri et al. (2024):

$$K_\mathrm{3D} = 28 q^{2.3} h^{-5.4} \alpha^{-0.72}. \tag{6.21}$$

The surface density at the edge of the gap smoothly transitions to Σ_0 in the form

$$\frac{\Sigma_\mathrm{gap}(r)}{\Sigma_0} = \frac{4}{\sqrt[4]{K'_\mathrm{3D}}} \frac{|r - r_\mathrm{p}|}{r_\mathrm{p}} - 0.32, \tag{6.22}$$

where we scale $K'_\mathrm{3D} = h^2 K_\mathrm{3D}$. The width of the gap excluding and including the transition slop are

$$\Delta r_1 = \left(\frac{\Sigma_\mathrm{min}}{4\Sigma_0} + 0.08 \right) r_\mathrm{p}, \tag{6.23}$$

and

$$\Delta r_2 = 0.33\sqrt[4]{K'_{3D}}r_p, \tag{6.24}$$

with respectively.

6.E Quantify the morphology of dust rings

For the sample study of transition disks, we selected all known transition disks from van der Marel (2023) at <200 pc with published high-resolution ALMA continuum observations with a spatial resolution of 0.05" or better (<10 au resolution), so that the radial profile is sufficiently resolved. Disks with strong asymmetries, high inclinations (>70° inclination) or cavity size <30 au are excluded. This results in 19 targets, listed in Table 6.4, including their beam size and reference to the origin of the data, as well as the parameters of our best fit. Radial intensity profiles are extracted using azimuthal averaging of the images following the original reference, and normalized to the peak.

The radial profiles of each target are fit using a 1D asymmetric Gaussian, or in case of two rings the sum of two 1D asymmetric Gaussians with different peak values. Such a Gaussian is described mathematically as follows:

$$I(r) = \begin{cases} I_0 \exp\left(-\frac{(r-r_{\rm peak})^2}{2\sigma^2_{\rm left}}\right) & \text{for } r < r_{\rm peak}, \\ I_0 \exp\left(-\frac{(r-r_{\rm peak})^2}{2\sigma^2_{\rm right}}\right) & \text{for } r > r_{\rm peak}. \end{cases} \tag{6.25}$$

The parameter of interest is the ratio between the outer width and inner width:

$$R = \frac{\sigma_{\rm right}}{\sigma_{\rm left}} \tag{6.26}$$

which can distinguish between profiles with a smooth, extended outer profile (like GM Aur) and profiles with a sharp, narrow ring (like PDS 70). When calculating the ratio, we considered an error on the radial width based on the convolution with the beam size, normalized by the number of beams along the dust ring, i.e. $R_{\rm err} = R_{\rm beam}/\sqrt{N_{\rm beams}}$. Although this is a rather simple approach, it is sufficient for our purposes.

The best fits are determined using the `curvefit` procedure in `scipy.optimize`, which is a non-linear least-squares fitting tool. Figure 6.13 shows the best fits and Table 6.4 includes the best-fit parameters as well as the resulting width ratios. The table also lists whether an inner pedestal appears to be present. For HD100453 and HD100546 an inner Gaussian was included in the fit to match the strong centrally peaked emission which is thought to originate from free-free emission from the star (Rota et al. 2024).

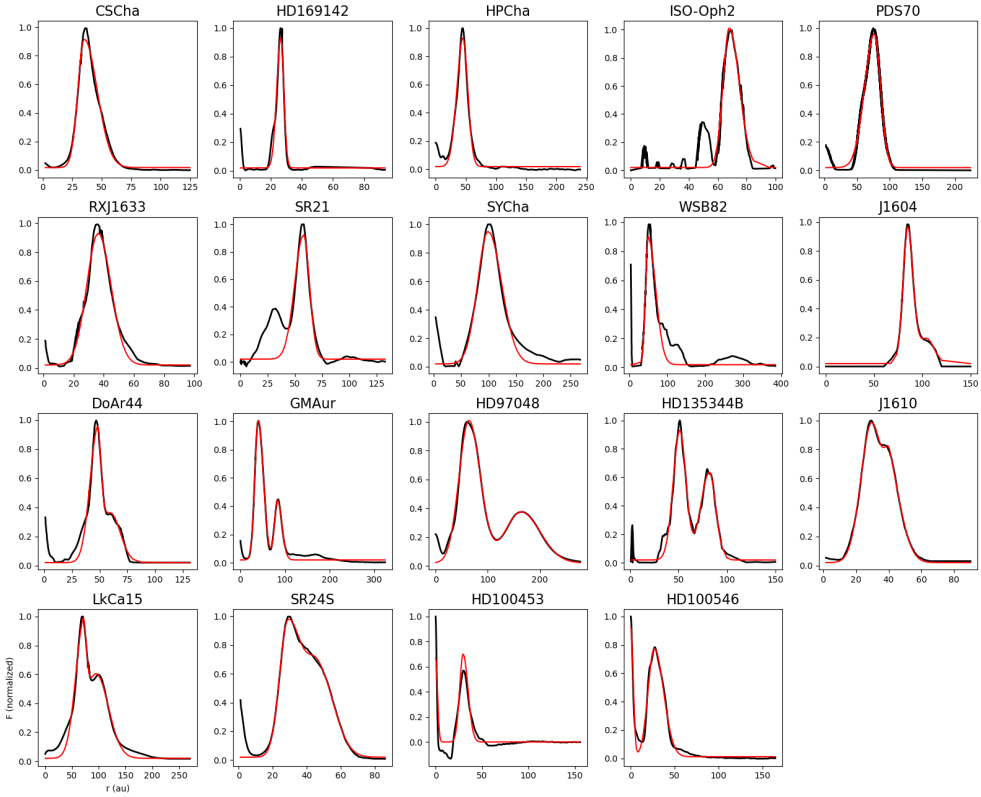


Figure 6.13. Radial profiles of the selected sample of transition disks. Data are shown in black, best fits in red. The first 9 disks are fit with a single Gaussian, the next two disks with a single Gaussian as well as a central peak, and the final 8 disks with two Gaussians, to match both rings. The best-fit parameters of interest are given in Table 6.4.

Table 6.4. Gaussian fits of the radial profiles of the sample of transition disks considered in this study.

Target	Gaussian 1				Gaussian 2				Ped?[a]	Origin	
	$r_{peak,1}$ (au)	$\sigma_{left,1}$ (au)	$\sigma_{right,1}$ (au)	R_1	$r_{peak,2}$ (au)	$\sigma_{left,2}$ (au)	$\sigma_{right,2}$ (au)	R_2		beam (")	Ref.
CSCha	35	5.4	11	2.0 ± 0.5	-	-	-	-	N	0.05x0.03	1
HD169142	26	2.6	2	0.8 ± 0.2	-	-	-	-	Y	0.03x0.02	2
HPCha	45	10	8	0.8 ± 0.1	-	-	-	-	N	0.05x0.03	3
ISO-Oph2	68	4.3	6.9	1.1 ± 0.1	-	-	-	-	M	0.03x0.02	4
PDS70	76	15	9.7	0.7 ± 0.1	-	-	-	-	Y	0.07x0.05	5
RXJ1633.9-2442	36	7.7	8.5	1.1 ± 0.1	-	-	-	-	M	0.02x0.02	4
SR21	58	8.1	5.5	0.7 ± 0.1	-	-	-	-	M	0.04x0.03	6
SYCha	99	19	25	1.3 ± 0.0	-	-	-	-	N	0.04x0.02	7
WSB82	48	6.6	20	3.0 ± 0.2	-	-	-	-	N	0.03x0.02	4
HD100453	30	3.8	5.2	1.4 ± 0.2	-	-	-	-	N	0.04x0.03	3
HD100546	27	7.1	10	1.4 ± 0.2	-	-	-	-	N	0.06x0.05	3
J16042165	85	4.9	5.4	1.1 ± 0.3	104	10	7.7	0.8 ± 0.1	N	0.06x0.04	8
DoAr44	47	4	3.8	1.0 ± 0.2	60	10	8.9	0.9 ± 0.1	Y	0.03x0.03	4
GMAur	40	7.6	11.4	1.5 ± 0.2	84	6.8	9.7	1.4 ± 0.2	N	0.05x0.03	9
HD97048	63	19	22	1.2 ± 0.1	167	30.1	36.9	1.2 ± 0.1	N	0.06x0.03	3
HD135344B	51	6.9	6.3	0.9 ± 0.2	82	9.1	6.6	0.7 ± 0.1	Y	0.05x0.04	10
J16100501	30	7.1	13	1.8 ± 0.3	41	3.3	7.3	2.2 ± 0.8	N	0.05x0.04	11
LkCa15	70	15	6.4	0.4 ± 0.2	95	19.5	23.15	1.2 ± 0.1	Y	0.07x0.05	11
SR24S	29	4.9	8	1.6 ± 0.2	47	7.1	9.1	1.3 ± 0.1	N	0.04x0.03	4

[a] Presence of a pedestal: Y=Yes, N=No, M=Maybe.

Refs: 1) Kurtovic et al. (2022), 2) Pérez et al. (2019), 3) Francis & van der Marel (2020), 4) Cieza et al. (2021), 5) Facchini et al. (2021), 6) Yang et al. (2023), 7) Orihara et al. (2023), 8) Stadler et al. (2023), 9) Huang et al. (2020), 10) Casassus et al. (2021), 11) Facchini et al. (2020)

Bibliography

Abod, C. P., Simon, J. B., Li, R., et al. 2019, ApJ, 883, 192

Agnor, C. B. & Lin, D. N. C. 2012, ApJ, 745, 143

Agol, E., Dorn, C., Grimm, S. L., et al. 2021, The Planetary Science Journal, 2, 1

Agol, E., Steffen, J., Sari, R., & Clarkson, W. 2005, MNRAS, 359, 567

Ali-Dib, M., Marsset, M., Wong, W.-C., & Dbouk, R. 2021, AJ, 162, 19

Andrews, S. M., Huang, J., Pérez, L. M., et al. 2018, ApJ, 869, L41

Andrews, S. M., Wilner, D. J., Hughes, A. M., et al. 2012, ApJ, 744, 162

Ansdell, M., Williams, J. P., Manara, C. F., et al. 2017, AJ, 153, 240

Antilen, J., Casassus, S., Cieza, L. A., & González-Ruilova, C. 2023, MNRAS, 522, 2611

Artymowicz, P. 1993, ApJ, 419, 166

Asensio-Torres, R., Henning, T., Cantalloube, F., et al. 2021, A&A, 652, A101

Asphaug, E., Emsenhuber, A., Cambioni, S., Gabriel, T. S. J., & Schwartz, S. R. 2021, PSJ, 2, 200

Ataiee, S. & Kley, W. 2021, arXiv e-prints, arXiv:2102.08612

Bae, J., Zhu, Z., Baruteau, C., et al. 2019, ApJ, 884, L41

Bai, X.-N. & Stone, J. M. 2013, ApJ, 769, 76

Bailey, A. & Zhu, Z. 2023, arXiv e-prints, arXiv:2310.03117

Balbus, S. A. & Hawley, J. F. 1991, ApJ, 376, 214

Barber, M. G., Mann, A. W., Vanderburg, A., et al. 2024, Nature, 635, 574

Barboni, M., Boehnke, P., Keller, B., et al. 2017, Science Advances, 3, e1602365

Baruteau, C., Crida, A., Paardekooper, S. J., et al. 2014, in Protostars and Planets VI, ed. H. Beuther, R. S. Klessen, C. P. Dullemond, & T. Henning, 667

Batygin, K. 2015, MNRAS, 451, 2589

Batygin, K., Adams, F. C., & Becker, J. 2023, ApJ, 951, L19

Batygin, K. & Morbidelli, A. 2013, AJ, 145, 1

Batygin, K. & Petit, A. C. 2023a, ApJ, 946, L11

Batygin, K. & Petit, A. C. 2023b, arXiv e-prints, arXiv:2303.02766

Benisty, M., Bae, J., Facchini, S., et al. 2021, ApJ, 916, L2

Benítez-Llambay, P., Masset, F., Koenigsberger, G., & Szulágyi, J. 2015, Nature, 520, 63

Bergez-Casalou, C., Bitsch, B., Pierens, A., Crida, A., & Raymond, S. N. 2020, A&A, 643, A133

Berné, O., Habart, E., Peeters, E., et al. 2024, Science, 383, 988

Bi, J. & Lin, M.-K. 2024, ApJ, 971, 76

Biersteker, J. B. & Schlichting, H. E. 2021, MNRAS, 501, 587

Birnstiel, T., Dullemond, C. P., Zhu, Z., et al. 2018, ApJ, 869, L45

Birnstiel, T., Klahr, H., & Ercolano, B. 2012, A&A, 539, A148

Bitsch, B., Crida, A., Morbidelli, A., Kley, W., & Dobbs-Dixon, I. 2013, A&A, 549, A124

Bitsch, B., Morbidelli, A., Johansen, A., et al. 2018, A&A, 612, A30

Bitsch, B., Morbidelli, A., Lega, E., Kretke, K., & Crida, A. 2014, A&A, 570, A75

Boss, A. P. 1997, Science, 276, 1836

Boss, A. P., Weinberger, A. J., Keiser, S. A., et al. 2017, AJ, 154, 103

Bouvier, J., Alencar, S. H. P., Boutelier, T., et al. 2007, A&A, 463, 1017

Brasser, R., Barr, A. C., & Dobos, V. 2019, MNRAS, 487, 34

Brasser, R., Mojzsis, S. J., Werner, S. C., Matsumura, S., & Ida, S. 2016, Earth and Planetary Science Letters, 455, 85

Brasser, R., Morbidelli, A., Gomes, R., Tsiganis, K., & Levison, H. F. 2009, A&A, 507, 1053

Brouwers, M. G., Ormel, C. W., Bonsor, A., & Vazan, A. 2021, A&A, 653, A103

Brož, M., Chrenko, O., Nesvorný, D., & Dauphas, N. 2021, Nature Astronomy, 5, 898

Brown, G., Malhotra, R., & Rein, H. 2024, arXiv e-prints, arXiv:2412.04583

Burdanov, A. Y., Lederer, S. M., Gillon, M., et al. 2019, MNRAS, 487, 1634

Burgasser, A. J. & Mamajek, E. E. 2017, ApJ, 845, 110

Burn, R., Schlecker, M., Mordasini, C., et al. 2021, arXiv e-prints, arXiv:2105.04596

Cai, M. X., Portegies Zwart, S., Kouwenhoven, M. B. N., & Spurzem, R. 2019, MNRAS, 489, 4311

Calcino, J., Price, D. J., & Ormel, C. W. 2025, arXiv e-prints, arXiv:2510.05601

Cambioni, S., Weiss, B. P., Asphaug, E., et al. 2025, A&A, 696, A174

Canup, R. M. & Asphaug, E. 2001, Nature, 412, 708

Canup, R. M., Righter, K., Dauphas, N., et al. 2023, Reviews in Mineralogy and Geochemistry, 89, 53

Carr, J. S., Tokunaga, A. T., & Najita, J. 2004, ApJ, 603, 213

Casassus, S., Christiaens, V., Cárcamo, M., et al. 2021, MNRAS, 507, 3789

Chakrabarty, A. & Mulders, G. D. 2024, ApJ, 966, 185

Chambers, J. 2018, ApJ, 865, 30

Chambers, J. 2021, ApJ, 914, 102

Chambers, J. E. 1999, MNRAS, 304, 793

Chambers, J. E. 2001, ICARUS, 152, 205

Charalambous, C., Martí, J. G., Beaugé, C., & Ramos, X. S. 2018, MNRAS, 477, 1414

Charalambous, C., Teyssandier, J., & Libert, A. S. 2022, MNRAS, 514, 3844

Chatterjee, S. & Ford, E. B. 2015, ApJ, 803, 33

Chatterjee, S. & Tan, J. C. 2014, ApJ, 780, 53

Chiang, E. & Laughlin, G. 2013, MNRAS, 431, 3444

Chiang, E. I. & Goldreich, P. 1997, ApJ, 490, 368

Choksi, N. & Chiang, E. 2020, MNRAS, 495, 4192

Choksi, N. & Chiang, E. 2022, arXiv e-prints, arXiv:2211.15701

Choksi, N. & Chiang, E. 2024, arXiv e-prints, arXiv:2403.10057

Chrenko, O., Chametla, R. O., Masset, F. S., Baruteau, C., & Brož, M. 2024, A&A, 690, A41

Chrenko, O., Chametla, R. O., Nesvorný, D., & Flock, M. 2022, arXiv e-prints, arXiv:2208.10257

Christiaens, V., Samland, M., Henning, T., et al. 2024, A&A, 685, L1

Christiansen, J. L., Crossfield, I. J. M., Barentsen, G., et al. 2018, AJ, 155, 57

Cieza, L. A., González-Ruilova, C., Hales, A. S., et al. 2021, MNRAS, 501, 2934

Cieza, L. A., Ruíz-Rodríguez, D., Hales, A., et al. 2019, MNRAS, 482, 698

Clement, M. S., Deienno, R., & Izidoro, A. 2023, ICARUS, 389, 115260

Clement, M. S., Kaib, N. A., Raymond, S. N., Chambers, J. E., & Walsh, K. J. 2019, ICARUS, 321, 778

Clement, M. S., Quintana, E. V., & Stevenson, K. B. 2025, AJ, 169, 16

Clement, M. S., Raymond, S. N., & Chambers, J. E. 2021, ApJ, 923, L16

Coleman, G. A. L., Leleu, A., Alibert, Y., & Benz, W. 2019, A&A, 631, A7

Correia, A. C. M., Delisle, J.-B., & Laskar, J. 2018, in Handbook of Exoplanets, ed. H. J. Deeg & J. A. Belmonte (Springer), 12

Cresswell, P. & Nelson, R. P. 2006, A&A, 450, 833

Cresswell, P. & Nelson, R. P. 2008, A&A, 482, 677

Currie, T., Lawson, K., Schneider, G., et al. 2022, Nature Astronomy, 6, 751

Dai, F., Goldberg, M., Batygin, K., et al. 2024, AJ, 168, 239

Dai, F., Masuda, K., Beard, C., et al. 2022, arXiv e-prints, arXiv:2210.09283

D'Angelo, C. R. & Spruit, H. C. 2010, MNRAS, 406, 1208

D'Angelo, G. & Lubow, S. H. 2010, ApJ, 724, 730

Dauphas, N. & Pourmand, A. 2011, Nature, 473, 489

David, T. J., Petigura, E. A., Luger, R., et al. 2019, ApJ, 885, L12

Dawson, R. I., Chiang, E., & Lee, E. J. 2015, MNRAS, 453, 1471

de Sousa, R. R., Morbidelli, A., Raymond, S. N., et al. 2020, ICARUS, 339, 113605

Deguen, R., Olson, P., & Cardin, P. 2011, Earth and Planetary Science Letters, 310, 303

Delisle, J. B. & Laskar, J. 2014, A&A, 570, L7

Delrez, L., Gillon, M., Triaud, A. H. M. J., et al. 2018, MNRAS, 475, 3577

Dodson-Robinson, S. E. & Salyk, C. 2011, ApJ, 738, 131

Dominik, C. & Dullemond, C. P. 2024, A&A, 682, A144

Dominik, C., Min, M., & Tazaki, R. 2021, OpTool: Command-line Driven Tool for Creating Complex Dust Opacities, Astrophysics Source Code Library, record ascl:2104.010, ascl:2104.010

Dong, R., Li, S., Chiang, E., & Li, H. 2017a, ApJ, 843, 127

Dong, R., van der Marel, N., Hashimoto, J., et al. 2017b, ApJ, 836, 201

Dong, R., Zhu, Z., & Whitney, B. 2015, ApJ, 809, 93

Dorn, C., Mosegaard, K., Grimm, S. L., & Alibert, Y. 2018, ApJ, 865, 20

Dou, J., Carter, P. J., & Leinhardt, Z. M. 2024, MNRAS, 529, 2577

Drążkowska, J., Alibert, Y., & Moore, B. 2016, A&A, 594, A105

Drążkowska, J., Bitsch, B., Lambrechts, M., et al. 2023, in Astronomical Society of the Pacific Conference Series, Vol. 534, Protostars and Planets VII, ed. S. Inutsuka, Y. Aikawa, T. Muto, K. Tomida, & M. Tamura, 717

Ducrot, E., Gillon, M., Delrez, L., et al. 2020, A&A, 640, A112

Ducrot, E., Sestovic, M., Morris, B. M., et al. 2018, AJ, 156, 218

Duffell, P. C. & MacFadyen, A. I. 2013, ApJ, 769, 41

Dullemond, C. P., Juhasz, A., Pohl, A., et al. 2012, RADMC-3D: A multi-purpose radiative transfer tool, Astrophysics Source Code Library, record ascl:1202.015

Dullemond, C. P. & Penzlin, A. B. T. 2018, A&A, 609, A50

Duric, N. 2004, Advanced Astrophysics (New York: Springer)

Edwards, G. H., Keller, C. B., Newton, E. R., & Stewart, C. W. 2024, Nature Astronomy, 8, 1264

Emsenhuber, A., Asphaug, E., Cambioni, S., et al. 2024, PSJ, 5, 59

Emsenhuber, A., Mordasini, C., Burn, R., et al. 2021, A&A, 656, A69

Ercolano, B. & Pascucci, I. 2017, Royal Society Open Science, 4, 170114

Fabrycky, D. C., Lissauer, J. J., Ragozzine, D., et al. 2014, ApJ, 790, 146

Facchini, S., Benisty, M., Bae, J., et al. 2020, A&A, 639, A121

Facchini, S., Clarke, C. J., & Bisbas, T. G. 2016, MNRAS, 457, 3593

Facchini, S., Teague, R., Bae, J., et al. 2021, AJ, 162, 99

Fang, T., Bi, R., Zhang, H., et al. 2025, MNRAS, 537, L14

Fedele, D., Tazzari, M., Booth, R., et al. 2018, A&A, 610, A24

Fitzmaurice, E., Martin, D. V., & Fabrycky, D. C. 2022, MNRAS, 512, 5023

Flaccomio, E., Micela, G., & Sciortino, S. 2012, A&A, 548, A85

Flaherty, K., Hughes, A. M., Simon, J. B., et al. 2020, ApJ, 895, 109

Flock, M., Ruge, J. P., Dzyurkevich, N., et al. 2015, A&A, 574, A68

Flock, M., Turner, N. J., Mulders, G. D., et al. 2019, A&A, 630, A147

Flock, M., Turner, N. J., Nelson, R. P., et al. 2020, ApJ, 897, 155

Foreman-Mackey, D. 2016, The Journal of Open Source Software, 1, 24

Foreman-Mackey, D., Hogg, D. W., Lang, D., & Goodman, J. 2013, PASP, 125, 306

Forgan, D. H., Hall, C., Meru, F., & Rice, W. K. M. 2018, MNRAS, 474, 5036

Fortney, J. J., Marley, M. S., & Barnes, J. W. 2007, ApJ, 659, 1661

Francis, L. & van der Marel, N. 2020, ApJ, 892, 111

Franz, R., Picogna, G., Ercolano, B., et al. 2022, A&A, 659, A90

Fujii, M., Iwasawa, M., Funato, Y., & Makino, J. 2007, PASJ, 59, 1095

Fujii, M. S. & Portegies Zwart, S. 2011, Science, 334, 1380

Fulton, B. J. & Petigura, E. A. 2018, AJ, 156, 264

Fulton, B. J., Petigura, E. A., Howard, A. W., et al. 2017, AJ, 154, 109

Fung, J. & Chiang, E. 2016, ApJ, 832, 105

Gammie, C. F. 1996, ApJ, 457, 355

Gan, T., Cadieux, C., Jahandar, F., et al. 2023a, AJ, 166, 165

Gan, T., Wang, S. X., Wang, S., et al. 2023b, AJ, 165, 17

Gárate, M., Pinilla, P., Haworth, T. J., & Facchini, S. 2024, A&A, 681, A84

Garrido-Deutelmoser, J., Petrovich, C., Charalambous, C., Guzmán, V. V., & Zhang, K. 2023a, arXiv e-prints, arXiv:2301.13260

Garrido-Deutelmoser, J., Petrovich, C., Charalambous, C., Guzmán, V. V., & Zhang, K. 2023b, ApJ, 945, L37

Ge, J., Zhang, H., Zang, W., et al. 2022, arXiv e-prints, arXiv:2206.06693

Gerosa, F. A., Bec, J., Méheut, H., & Kapoor, A. U. 2024, A&A, 685, L4

Ghosh, T. & Chatterjee, S. 2022, arXiv e-prints, arXiv:2209.05138

Gillon, M., Jehin, E., Lederer, S. M., et al. 2016, Nature, 533, 221

Gillon, M., Meadows, V., Agol, E., et al. 2020, in Bulletin of the American Astronomical Society, Vol. 52, 0208

Gillon, M., Triaud, A. H. M. J., Demory, B.-O., et al. 2017, Nature, 542, 456

Ginzburg, S., Schlichting, H. E., & Sari, R. 2018, MNRAS, 476, 759

Goldberg, M. & Batygin, K. 2021, AJ, 162, 16

Goldberg, M. & Batygin, K. 2022, arXiv e-prints, arXiv:2211.16725

Goldberg, M., Batygin, K., & Morbidelli, A. 2022, ICARUS, 388, 115206

Goldreich, P. & Schlichting, H. E. 2014, AJ, 147, 32

Goldreich, P. & Soter, S. 1966, ICARUS, 5, 375

Goldreich, P. & Tremaine, S. 1979, ApJ, 233, 857

Goldreich, P. & Tremaine, S. 1980, ApJ, 241, 425

Goździewski, K. & Migaszewski, C. 2020, ApJ, 902, L40

Goździewski, K., Migaszewski, C., Panichi, F., & Szuszkiewicz, E. 2016, MNRAS, 455, L104

Grimm, S. L., Demory, B.-O., Gillon, M., et al. 2018, A&A, 613, A68

Griveaud, P., Crida, A., Petit, A. C., Lega, E., & Morbidelli, A. 2024, A&A, 688, A202

Guilera, O. M., Cuello, N., Montesinos, M., et al. 2019, MNRAS, 486, 5690

Guilera, O. M., Miller Bertolami, M. M., Masset, F., et al. 2021, MNRAS, 507, 3638

Gurrutxaga, N., Johansen, A., Lambrechts, M., & Appelgren, J. 2024, A&A, 682, A43

Haffert, S. Y., Bohn, A. J., de Boer, J., et al. 2019, Nature Astronomy, 3, 749

Hamer, J. H. & Schlaufman, K. C. 2024, AJ, 167, 55

Hammond, I., Christiaens, V., Price, D. J., et al. 2023, MNRAS, 522, L51

Hansen, B. M. S. 2009, ApJ, 703, 1131

Hara, N. C., Bouchy, F., Stalport, M., et al. 2020, A&A, 636, L6

Harrison, T. M. 2009, Annual Review of Earth and Planetary Sciences, 37, 479

Hartmann, L., Herczeg, G., & Calvet, N. 2016, ARA&A, 54, 135

Haworth, T. J. 2021, MNRAS, 503, 4172

Haworth, T. J., Facchini, S., Clarke, C. J., & Mohanty, S. 2018, MNRAS, 475, 5460

Hayashi, C. 1981, Progress of Theoretical Physics Supplement, 70, 35

Hayya, J., Armstrong, D., & Gressis, N. 1975, Management Science, 21, 1338

He, M. Y. & Weiss, L. M. 2023, AJ, 166, 36

Hinkley, D. V. 1969, Biometrika, 56, 635

Hu, Q., Huang, Y., Gladman, B., & Zhu, W. 2025a, arXiv e-prints, arXiv:2505.16317

Hu, X., Zhu, Z., Okuzumi, S., et al. 2019, ApJ, 885, 36

Hu, Z., Dai, F., Zhu, W., et al. 2025b, ApJ, 995, 206

Huang, J., Andrews, S. M., Dullemond, C. P., et al. 2020, ApJ, 891, 48

Huang, S. & Ormel, C. W. 2022, MNRAS, 511, 3814

Huang, S. & Ormel, C. W. 2023, MNRAS, 522, 828

Huang, S., Ormel, C. W., Portegies Zwart, S., Kokubo, E., & Yi, T. 2025, ApJ, 988, 137

Huang, S., Portegies Zwart, S., & Wilhelm, M. J. C. 2024, A&A, 689, A338

Hyodo, R., Ida, S., & Charnoz, S. 2019, A&A, 629, A90

Ida, S. & Guillot, T. 2016, A&A, 596, L3

Ida, S. & Lin, D. N. C. 2004, ApJ, 604, 388

Ida, S., Muto, T., Matsumura, S., & Brasser, R. 2020, MNRAS, 494, 5666

Ida, S., Tanaka, H., Johansen, A., Kanagawa, K. D., & Tanigawa, T. 2018, ApJ, 864, 77

Ikoma, M., Nakazawa, K., & Emori, H. 2000, ApJ, 537, 1013

Isella, A., Huang, J., Andrews, S. M., et al. 2018, ApJ, 869, L49

Ito, T. & Tanikawa, K. 2002, MNRAS, 336, 483

Izidoro, A., Bitsch, B., Raymond, S. N., et al. 2021, A&A, 650, A152

Izidoro, A., Ogihara, M., Raymond, S. N., et al. 2017, MNRAS, 470, 1750

Izidoro, A., Schlichting, H. E., Isella, A., et al. 2022, ApJ, 939, L19

Jacobson, S. A., Morbidelli, A., Raymond, S. N., et al. 2014, Nature, 508, 84

Jeans, J. H. 1902, Philosophical Transactions of the Royal Society of London Series A, 199, 1

Jiang, H. & Ormel, C. W. 2021, MNRAS, 505, 1162

Jiang, H. & Ormel, C. W. 2023, MNRAS, 518, 3877

Johansen, A. & Bitsch, B. 2019, A&A, 631, A70

Johansen, A. & Dorn, C. 2022, A&A, 662, A19

Johansen, A., Ida, S., & Brasser, R. 2019, A&A, 622, A202

Johansen, A. & Lambrechts, M. 2017, Annual Review of Earth and Planetary Sciences, 45, 359

Johansen, A., Olson, P., & Sharp, Z. 2024, arXiv e-prints, arXiv:2411.17043

Johansen, A., Ronnet, T., Bizzarro, M., et al. 2021, Science Advances, 7, eabc0444

Johansen, A., Ronnet, T., Schiller, M., Deng, Z., & Bizzarro, M. 2023, A&A, 671, A74

Johansen, A., Youdin, A., & Klahr, H. 2009, ApJ, 697, 1269

Johnston, H. F., Panić, O., & Liu, B. 2024, MNRAS, 527, 2303

Kaib, N. A. & Chambers, J. E. 2016, MNRAS, 455, 3561

Kaib, N. A. & Raymond, S. N. 2025, ICARUS, 439, 116632

Kajtazi, K., Petit, A. C., & Johansen, A. 2022, arXiv e-prints, arXiv:2211.06181

Kama, M., Min, M., & Dominik, C. 2009, A&A, 506, 1199

Kanagawa, K. D., Tanaka, H., Muto, T., & Tanigawa, T. 2017, PASJ, 69, 97

Kanagawa, K. D., Tanaka, H., Muto, T., Tanigawa, T., & Takeuchi, T. 2015, MNRAS, 448, 994

Kanagawa, K. D., Tanaka, H., & Szuszkiewicz, E. 2018, ApJ, 861, 140

Kelling, T., Wurm, G., & Köster, M. 2014, ApJ, 783, 111

Kenyon, S. J. & Hartmann, L. 1995, ApJS, 101, 117

Keppler, M., Benisty, M., Müller, A., et al. 2018, A&A, 617, A44

Keppler, M., Teague, R., Bae, J., et al. 2019, A&A, 625, A118

Kley, W. & Nelson, R. P. 2012, ARA&A, 50, 211

Kobayashi, H. & Dauphas, N. 2013, ICARUS, 225, 122

Kokubo, E., Hoshino, H., Matsumoto, Y., & Sari, R. 2025, ApJ, 991, L49

Kokubo, E. & Ida, S. 1998, ICARUS, 131, 171

Kokubo, E. & Ida, S. 2002, ApJ, 581, 666

Königl, A., Romanova, M. M., & Lovelace, R. V. E. 2011, MNRAS, 416, 757

Krijt, S., Ormel, C. W., Dominik, C., & Tielens, A. G. G. M. 2016, A&A, 586, A20

Krumholz, M. R. & Forbes, J. C. 2015, Astronomy and Computing, 11, 1

Krumholz, M. R., McKee, C. F., & Bland-Hawthorn, J. 2019, ARA&A, 57, 227

Kruss, M., Demirci, T., Koester, M., Kelling, T., & Wurm, G. 2016, ApJ, 827, 110

Kubli, N., Mayer, L., & Deng, H. 2023, MNRAS, 525, 2731

Kurtovic, N. T., Pinilla, P., Penzlin, A. B. T., et al. 2022, A&A, 664, A151

Kuwahara, A. & Kurokawa, H. 2020, A&A, 643, A21

Kuwahara, A., Kurokawa, H., Tanigawa, T., & Ida, S. 2022, A&A, 665, A122

Lada, C. J. & Lada, E. A. 2003, ARA&A, 41, 57

Lambrechts, M. & Johansen, A. 2012, A&A, 544, A32

Lambrechts, M., Johansen, A., & Morbidelli, A. 2014, A&A, 572, A35

Lamers, H. J. G. L. M., Gieles, M., Bastian, N., et al. 2005, A&A, 441, 117

Laskar, J. 1997, A&A, 317, L75

Lau, T. C. H., Lee, M. H., Brasser, R., & Matsumura, S. 2024, A&A, 683, A204

Laune, J. T., Rodet, L., & Lai, D. 2022, MNRAS, 517, 4472

Lee, E. J. & Chiang, E. 2017, ApJ, 842, 40

Lee, M. H. & Peale, S. J. 2002, ApJ, 567, 596

Leemker, M., Booth, A. S., van Dishoeck, E. F., et al. 2022, A&A, 663, A23

Leemker, M., Booth, A. S., van Dishoeck, E. F., Wölfer, L., & Dent, B. 2024, A&A, 687, A299

Leleu, A., Alibert, Y., Hara, N. C., et al. 2021, arXiv e-prints, arXiv:2101.09260

Leleu, A., Delisle, J.-B., Burn, R., et al. 2024, A&A, 687, L1

Levison, H. F., Morbidelli, A., Tsiganis, K., Nesvorný, D., & Gomes, R. 2011, AJ, 142, 152

Levison, H. F., Morbidelli, A., Van Laerhoven, C., Gomes, R., & Tsiganis, K. 2008, ICARUS, 196, 258

Li, J., O'Connor, C. E., & Rasio, F. A. 2025, arXiv e-prints, arXiv:2510.18955

Li, R., Chiang, E., Choksi, N., & Dai, F. 2024, arXiv e-prints, arXiv:2408.10206

Li, Y.-P., Li, H., Li, S., & Lin, D. N. C. 2019, ApJ, 886, 62

Lichtenberg, T., Golabek, G. J., Burn, R., et al. 2019, Nature Astronomy, 3, 307

Lim, O., Albert, L., Artigau, E., et al. 2021, Atmospheric reconnaissance of the TRAPPIST-1 planets, JWST Proposal. Cycle 1

Lin, D. N. C. & Papaloizou, J. 1979, MNRAS, 186, 799

Lin, D. N. C. & Papaloizou, J. C. B. 1993, in Protostars and Planets III, ed. E. H. Levy & J. I. Lunine, 749

Lin, Y.-C., Matsumoto, Y., & Gu, P.-G. 2021a, ApJ, 907, 81

Lin, Z., MacDonald, R. J., Kaltenegger, L., & Wilson, D. J. 2021b, MNRAS, 505, 3562

Lincowski, A. P., Meadows, V. S., Crisp, D., et al. 2018, ApJ, 867, 76

Lissauer, J. J. 1993, ARA&A, 31, 129

Lithwick, Y. & Wu, Y. 2012, ApJ, 756, L11

Lithwick, Y., Xie, J., & Wu, Y. 2012, ApJ, 761, 122

Liu, B., Lambrechts, M., Johansen, A., & Liu, F. 2019, A&A, 632, A7

Liu, B. & Ormel, C. W. 2018, A&A, 615, A138

Liu, B., Ormel, C. W., & Lin, D. N. C. 2017, A&A, 601, A15

Liu, B., Raymond, S. N., & Jacobson, S. A. 2022, Nature, 604, 643

Lock, S. J., Stewart, S. T., Petaev, M. I., et al. 2018, Journal of Geophysical Research (Planets), 123, 910

Long, F., Pinilla, P., Herczeg, G. J., et al. 2018, ApJ, 869, 17

Long, M., Romanova, M. M., & Lovelace, R. V. E. 2005, ApJ, 634, 1214

Lopez, T. A., Barros, S. C. C., Santerne, A., et al. 2019, A&A, 631, A90

Lu, C. X., Schlaufman, K. C., & Cheng, S. 2020, AJ, 160, 253

Luger, R., Sestovic, M., Kruse, E., et al. 2017, Nature Astronomy, 1, 0129

Luque, R., Osborn, H. P., Leleu, A., et al. 2023, Nature, 623, 932

Luque, R. & Pallé, E. 2022, Science, 377, 1211

Lynden-Bell, D. & Kalnajs, A. J. 1972, MNRAS, 157, 1

Lynden-Bell, D. & Pringle, J. E. 1974, MNRAS, 168, 603

Maas, B., Huang, S., & Portegies Zwart, S. 2025, arXiv e-prints, arXiv:2506.02253

MacDonald, M. G., Ragozzine, D., Fabrycky, D. C., et al. 2016, AJ, 152, 105

MacDonald, M. G., Shakespeare, C. J., & Ragozzine, D. 2021, arXiv e-prints, arXiv:2107.05597

Mah, J. 2018, HKU Theses Online (HKUTO)

Makino, J. 1991, PASJ, 43, 859

Malamud, U. & Perets, H. 2024, arXiv e-prints, arXiv:2411.08659

Manara, C. F., Ansdell, M., Rosotti, G. P., et al. 2023, in Astronomical Society of the Pacific Conference Series, Vol. 534, Protostars and Planets VII, ed. S. Inutsuka, Y. Aikawa, T. Muto, K. Tomida, & M. Tamura, 539

Manara, C. F., Testi, L., Natta, A., & Alcalá, J. M. 2015, A&A, 579, A66

Marchi, S., Walker, R. J., & Canup, R. M. 2020, Science Advances, 6, eaay2338

Masset, F. S. 2017, MNRAS, 472, 4204

Masset, F. S., Morbidelli, A., Crida, A., & Ferreira, J. 2006, ApJ, 642, 478

Mayor, M. & Queloz, D. 1995, Nature, 378, 355

McNally, C. P., Nelson, R. P., Paardekooper, S.-J., Gressel, O., & Lyra, W. 2017, MNRAS, 472, 1565

Meadows, V., Lincowski, A., Lustig-Yaeger, J., & Crisp, D. 2021, in Bulletin of the American Astronomical Society, Vol. 53, 0302

Miguel, Y. & Brunini, A. 2010, MNRAS, 406, 1935

Miguel, Y., Cridland, A., Ormel, C. W., Fortney, J. J., & Ida, S. 2020, MNRAS, 491, 1998

Mills, S. M., Fabrycky, D. C., Migaszewski, C., et al. 2016, Nature, 533, 509

Moldenhauer, T. W., Kuiper, R., Kley, W., & Ormel, C. W. 2021, A&A, 646, L11

Morbidelli, A. 2020, A&A, 638, A1

Morbidelli, A., Baillié, K., Batygin, K., et al. 2022, Nature Astronomy, 6, 72

Morbidelli, A., Kleine, T., & Nimmo, F. 2024, arXiv e-prints, arXiv:2411.09271

Morbidelli, A., Levison, H. F., Tsiganis, K., & Gomes, R. 2005, Nature, 435, 462

Morbidelli, A., Tsiganis, K., Crida, A., Levison, H. F., & Gomes, R. 2007, AJ, 134, 1790

Mordasini, C., Alibert, Y., Benz, W., & Naef, D. 2009, A&A, 501, 1161

Mordasini, C., Mollière, P., Dittkrist, K. M., Jin, S., & Alibert, Y. 2015, International Journal of Astrobiology, 14, 201

Mori, S., Okuzumi, S., Kunitomo, M., & Bai, X.-N. 2021, ApJ, 916, 72

Mulders, G. D. & Dominik, C. 2012, A&A, 539, A9

Muley, D., Fung, J., & van der Marel, N. 2019, ApJ, 879, L2

Murray, C. D. & Dermott, S. F. 1999, Solar System Dynamics (Cambridge, UK: Cambridge University Press)

Nagasawa, M., Lin, D. N. C., & Ida, S. 2003, ApJ, 586, 1374

Nakagawa, Y., Sekiya, M., & Hayashi, C. 1986, ICARUS, 67, 375

Ndugu, N., Abedigamba, O. P., & Andama, G. 2022, MNRAS, 512, 861

Ndugu, N., Bitsch, B., & Jurua, E. 2018, MNRAS, 474, 886

Nesvorný, D., Morbidelli, A., Bottke, W. F., Deienno, R., & Goldberg, M. 2025, AJ, 170, 180

Nesvorný, D., Vokrouhlický, D., Bottke, W. F., & Levison, H. F. 2018, Nature Astronomy, 2, 878

Nesvorný, D., Vokrouhlický, D., & Deienno, R. 2014, ApJ, 784, 22

Noyelles, B., Frouard, J., Makarov, V. V., & Efroimsky, M. 2014, ICARUS, 241, 26

Öberg, K. I., Guzmán, V. V., Walsh, C., et al. 2021, ApJS, 257, 1

O'Brien, D. P., Morbidelli, A., & Bottke, W. F. 2007, ICARUS, 191, 434

O'Dell, C. R. & Wen, Z. 1994, ApJ, 436, 194

O'Dell, C. R., Wen, Z., & Hu, X. 1993, ApJ, 410, 696

Ogihara, M. & Kobayashi, H. 2013, ApJ, 775, 34

Ogihara, M., Kokubo, E., Suzuki, T. K., & Morbidelli, A. 2018, A&A, 615, A63

Ogihara, M. & Kunitomo, M. 2026, ApJ, 996, 91

Ogihara, M., Morbidelli, A., & Kunitomo, M. 2024, ApJ, 972, 181

Ohashi, S., Kobayashi, H., Nakatani, R., et al. 2021, ApJ, 907, 80

Okamura, T. & Kobayashi, H. 2021, ApJ, 916, 109

Olson, P., Sharp, Z., & Garai, S. 2022, Earth and Planetary Science Letters, 587, 117537

Olson, P. L. & Sharp, Z. D. 2023, Earth and Planetary Science Letters, 622, 118418

Orihara, R., Momose, M., Muto, T., et al. 2023, PASJ, 75, 424

Ormel, C. W. & Huang, Y. 2025, arXiv e-prints, arXiv:2502.04016

Ormel, C. W. & Klahr, H. H. 2010, A&A, 520, A43

Ormel, C. W. & Liu, B. 2018, A&A, 615, A178

Ormel, C. W., Liu, B., & Schoonenberg, D. 2017, A&A, 604, A1

Ormel, C. W., Shi, J.-M., & Kuiper, R. 2015, MNRAS, 447, 3512

Ormel, C. W., Vazan, A., & Brouwers, M. G. 2021, A&A, 647, A175

Owen, J. E., Clarke, C. J., & Ercolano, B. 2012, MNRAS, 422, 1880

Owen, J. E. & Wu, Y. 2013, ApJ, 775, 105

Owen, J. E. & Wu, Y. 2017, ApJ, 847, 29

Paardekooper, S. J., Baruteau, C., Crida, A., & Kley, W. 2010, MNRAS, 401, 1950

Paardekooper, S. J., Baruteau, C., & Kley, W. 2011, MNRAS, 410, 293

Paardekooper, S. J. & Papaloizou, J. C. B. 2009, MNRAS, 394, 2283

Paardekooper, S.-J., Rein, H., & Kley, W. 2013, MNRAS, 434, 3018

Pan, M., Wang, S., & Ji, J. 2020, MNRAS, 496, 4688

Papaloizou, J. C. B. & Larwood, J. D. 2000, MNRAS, 315, 823

Papaloizou, J. C. B. & Szuszkiewicz, E. 2005, MNRAS, 363, 153

Papaloizou, J. C. B., Szuszkiewicz, E., & Terquem, C. 2018, MNRAS, 476, 5032

Pascucci, I., Cabrit, S., Edwards, S., et al. 2023, in Astronomical Society of the Pacific Conference Series, Vol. 534, Astronomical Society of the Pacific Conference Series, ed. S. Inutsuka, Y. Aikawa, T. Muto, K. Tomida, & M. Tamura, 567

Pelupessy, F. I., van Elteren, A., de Vries, N., et al. 2013, A&A, 557, A84

Pérez, S., Casassus, S., Baruteau, C., et al. 2019, AJ, 158, 15

Perri, F. & Cameron, A. G. W. 1974, ICARUS, 22, 416

Petigura, E. A., Benneke, B., Batygin, K., et al. 2018, AJ, 156, 89

Petit, A. C., Pichierri, G., Davies, M. B., & Johansen, A. 2020, A&A, 641, A176

Piaulet, C., Benneke, B., Almenara, J. M., et al. 2022, Nature Astronomy [arXiv:2212.08477]

Pichierri, G., Bitsch, B., & Lega, E. 2022, arXiv e-prints, arXiv:2212.03608

Pichierri, G., Bitsch, B., & Lega, E. 2024, ApJ, 967, 111

Pichierri, G. & Morbidelli, A. 2020, MNRAS, 494, 4950

Picogna, G., Ercolano, B., Owen, J. E., & Weber, M. L. 2019, MNRAS, 487, 691

Pinilla, P., Benisty, M., Waters, R., Bae, J., & Facchini, S. 2024, A&A, 686, A135

Pinilla, P., Pérez, L. M., Andrews, S., et al. 2017, ApJ, 839, 99

Pinte, C., Dent, W. R. F., Ménard, F., et al. 2016, ApJ, 816, 25

Pinte, C., van der Plas, G., Ménard, F., et al. 2019, Nature Astronomy, 3, 1109

Pollack, J. B., Hubickyj, O., Bodenheimer, P., et al. 1996, ICARUS, 124, 62

Portegies Zwart, S., McMillan, S., Harfst, S., et al. 2009, Nature Astronomy, 14, 369

Portegies Zwart, S., McMillan, S. L. W., van Elteren, E., Pelupessy, I., & de Vries, N. 2013a, Computer Physics Communications, 184, 456

Portegies Zwart, S., Pelupessy, I., Martínez-Barbosa, C., van Elteren, A., & McMillan, S. 2020, Communications in Nonlinear Science and Numerical Simulations, 85, 105240

Portegies Zwart, S., Torres, S., Cai, M. X., & Brown, A. G. A. 2021, A&A, 652, A144

Portegies Zwart, S. F. 2016, MNRAS, 457, 313

Portegies Zwart, S. F., McMillan, S. L., van Elteren, A., Pelupessy, F. I., & de Vries, N. 2013b, Computer Physics Communications, 184, 456

Portegies Zwart, S. F., McMillan, S. L. W., & Gieles, M. 2010, ARA&A, 48, 431

Portilla-Revelo, B., Kamp, I., Facchini, S., et al. 2023, A&A, 677, A76

Pringle, J. E. & Rees, M. J. 1972, A&A, 21, 1

Qiao, L., Coleman, G. A. L., & Haworth, T. J. 2023, MNRAS, 522, 1939

Rafikov, R. R. 2017, ApJ, 837, 163

Rafikov, R. R. & De Colle, F. 2006, ApJ, 646, 275

Ramos, X. S., Charalambous, C., Benítez-Llambay, P., & Beaugé, C. 2017, A&A, 602, A101

Rauer, H., Catala, C., Aerts, C., et al. 2014, Experimental Astronomy, 38, 249

Raymond, S. N., Barnes, R., & Mandell, A. M. 2008, MNRAS, 384, 663

Raymond, S. N., Izidoro, A., Bolmont, E., et al. 2021, arXiv e-prints, arXiv:2111.13351

Rein, H. 2012, MNRAS, 427, L21

Rein, H., Hernandez, D. M., Tamayo, D., et al. 2019, MNRAS, 485, 5490

Rein, H. & Liu, S. F. 2012, A&A, 537, A128

Rein, H. & Papaloizou, J. C. B. 2009, A&A, 497, 595

Ribas, Á., Merín, B., Bouy, H., & Maud, L. T. 2014, A&A, 561, A54

Rivera, E. J., Laughlin, G., Butler, R. P., et al. 2010, ApJ, 719, 890

Romanova, M. M., Koldoba, A. V., Ustyugova, G. V., Espaillat, C. C., & Lovelace, R. V. E. 2025, arXiv e-prints, arXiv:2507.15115

Romanova, M. M., Lii, P. S., Koldoba, A. V., et al. 2019, MNRAS, 485, 2666

Roquette, J., Matt, S. P., Winter, A. J., Amard, L., & Stasevic, S. 2021, MNRAS, 508, 3710

Rosotti, G. P., Benisty, M., Juhász, A., et al. 2020, MNRAS, 491, 1335

Rota, A. A., Meijerhof, J. D., van der Marel, N., et al. 2024, A&A, 684, A134

Rowe, J. F., Bryson, S. T., Marcy, G. W., et al. 2014, ApJ, 784, 45

Rowther, S., Nealon, R., Meru, F., et al. 2024, MNRAS, 528, 2490

Ruden, S. P. & Lin, D. N. C. 1986, ApJ, 308, 883

Sagear, S. A., Skinner, J. N., & Muirhead, P. S. 2020, AJ, 160, 19

Sánchez, M. B., de Elía, G. C., & Downes, J. J. 2020, A&A, 637, A78

Schäfer, U., Yang, C.-C., & Johansen, A. 2017, A&A, 597, A69

Schoonenberg, D., Liu, B., Ormel, C. W., & Dorn, C. 2019, A&A, 627, A149

Schoonenberg, D. & Ormel, C. W. 2017, A&A, 602, A21

Schoonenberg, D., Ormel, C. W., & Krijt, S. 2018, A&A, 620, A134

Seager, S., Kuchner, M., Hier-Majumder, C. A., & Militzer, B. 2007, ApJ, 669, 1279

Sellek, A. D., Booth, R. A., & Clarke, C. J. 2020, MNRAS, 492, 1279

Sestovic, M. & Demory, B.-O. 2020, A&A, 641, A170

Shakura, N. I. & Sunyaev, R. A. 1973, A&A, 500, 33

Shakura, N. I. & Sunyaev, R. A. 1976, MNRAS, 175, 613

Siegel, J. & Fabrycky, D. 2021, arXiv e-prints, arXiv:2104.14665

Snellgrove, M. D., Papaloizou, J. C. B., & Nelson, R. P. 2001, A&A, 374, 1092

Speedie, J., Dong, R., Hall, C., et al. 2024, Nature, 633, 58

Spergel, D. N., Kasdin, J., Belikov, R., et al. 2009, in American Astronomical Society Meeting Abstracts, Vol. 213, American Astronomical Society Meeting Abstracts #213, 458.04

Stadler, J., Benisty, M., Izquierdo, A., et al. 2023, A&A, 670, L1

Stammler, S. M. & Birnstiel, T. 2022, ApJ, 935, 35

Steffen, J. H. & Hwang, J. A. 2015, MNRAS, 448, 1956

Stock, K., Cai, M. X., Spurzem, R., Kouwenhoven, M. B. N., & Portegies Zwart, S. 2020, MNRAS, 497, 1807

Suzuki, D., Bennett, D. P., Sumi, T., et al. 2016, ApJ, 833, 145

Tabatabaei, F. S., Minguez, P., Prieto, M. A., & Fernández-Ontiveros, J. A. 2018, Nature Astronomy, 2, 83

Takahashi, S. Z. & Muto, T. 2018, ApJ, 865, 102

Tamayo, D., Rein, H., Petrovich, C., & Murray, N. 2017, ApJ, 840, L19

Tamayo, D., Rein, H., Shi, P., & Hernand ez, D. M. 2020, MNRAS, 491, 2885

Tanaka, H., Takeuchi, T., & Ward, W. R. 2002, ApJ, 565, 1257

Tanaka, H. & Ward, W. R. 2004, ApJ, 602, 388

Tanigawa, T. & Tanaka, H. 2016, ApJ, 823, 48

Terquem, C. & Papaloizou, J. C. B. 2007, ApJ, 654, 1110

Terquem, C. & Papaloizou, J. C. B. 2019, MNRAS, 482, 530

Teske, J., Wang, S. X., Wolfgang, A., et al. 2021, ApJS, 256, 33

Teyssandier, J. & Libert, A.-S. 2020, A&A, 643, A11

Teyssandier, J., Libert, A.-S., & Agol, E. 2021, arXiv e-prints, arXiv:2110.03340

Teyssandier, J., Libert, A. S., & Agol, E. 2022, A&A, 658, A170

Teyssandier, J. & Terquem, C. 2014, MNRAS, 443, 568

Thiemens, M. M., Sprung, P., Fonseca, R. O. C., Leitzke, F. P., & Münker, C. 2019, Nature Geoscience, 12, 696

Thommes, E., Nagasawa, M., & Lin, D. N. C. 2008, ApJ, 676, 728

Timpe, M., Reinhardt, C., Meier, T., Stadel, J., & Moore, B. 2023, ApJ, 959, 38

Toci, C., Lodato, G., Christiaens, V., et al. 2020, MNRAS, 499, 2015

Toomre, A. 1964, ApJ, 139, 1217

Trapman, L., Rosotti, G., Bosman, A. D., Hogerheijde, M. R., & van Dishoeck, E. F. 2020, A&A, 640, A5

Tsiganis, K., Gomes, R., Morbidelli, A., & Levison, H. F. 2005, Nature, 435, 459

van Capelleveen, R. F., Ginski, C., Kenworthy, M. A., et al. 2025, ApJ, 990, L8

van der Marel, N. 2023, European Physical Journal Plus, 138, 225

van der Marel, N. & Mulders, G. D. 2021, AJ, 162, 28

van der Marel, N., van Dishoeck, E. F., Bruderer, S., et al. 2016, A&A, 585, A58

Villenave, M., Stapelfeldt, K. R., Duchêne, G., et al. 2022, ApJ, 930, 11

Visser, R. G. & Ormel, C. W. 2016, A&A, 586, A66

Wall, J. E., Mac Low, M.-M., McMillan, S. L. W., et al. 2020, ApJ, 904, 192

Wall, J. E., McMillan, S. L. W., Mac Low, M.-M., Klessen, R. S., & Portegies Zwart, S. 2019, ApJ, 887, 62

Walsh, K. J., Morbidelli, A., Raymond, S. N., O'Brien, D. P., & Mandell, A. M. 2011, Nature, 475, 206

Wang, J. J., Vigan, A., Lacour, S., et al. 2021a, AJ, 161, 148

Wang, S. & Ji, J. 2014, ApJ, 795, 85

Wang, S., Lin, D. N. C., Zheng, X., & Ji, J. 2021b, AJ, 161, 77

Wang, Y., Ormel, C. W., Huang, P., & Kuiper, R. 2023, MNRAS, 523, 6186

Ward, W. R. 1986, ICARUS, 67, 164

Ward, W. R. 1988, ICARUS, 73, 330

Ward, W. R. 1991, in Lunar and Planetary Science Conference, Vol. 22, Lunar and Planetary Science Conference, 1463

Ward, W. R. 1992, in Lunar and Planetary Science Conference, Vol. 23, Lunar and Planetary Science Conference, 1491

Ward, W. R. 1997, ICARUS, 126, 261

Weder, J., Mordasini, C., & Emsenhuber, A. 2023, A&A, 674, A165

Weidenschilling, S. J. 1977, MNRAS, 180, 57

Weiss, B. P., Bai, X.-N., & Fu, R. R. 2021, Science Advances, 7, eaba5967

Wichittanakom, C., Oudmaijer, R. D., Fairlamb, J. R., et al. 2020, MNRAS, 493, 234

Wiechert, U., Halliday, A. N., Lee, D. C., et al. 2001, Science, 294, 345

Wieczorek, M. A., Correia, A. C. M., Le Feuvre, M., Laskar, J., & Rambaux, N. 2012, Nature Geoscience, 5, 18

Wilhelm, M. J. C. & Portegies Zwart, S. 2022, MNRAS, 509, 44

Wilhelm, M. J. C., Portegies Zwart, S., Cournoyer-Cloutier, C., et al. 2023, MNRAS, 520, 5331

Winter, A. J., Clarke, C. J., Rosotti, G. P., Hacar, A., & Alexander, R. 2019, MNRAS, 490, 5478

Winter, A. J., Haworth, T. J., Coleman, G. A. L., & Nayakshin, S. 2022, MNRAS, 515, 4287

Wölfer, L., Facchini, S., van der Marel, N., et al. 2023, A&A, 670, A154

Wolfgang, A., Rogers, L. A., & Ford, E. B. 2016, ApJ, 825, 19

Woo, J. M. Y., Grimm, S., Brasser, R., & Stadel, J. 2021, ICARUS, 359, 114305

Woo, J. M. Y., Nesvorný, D., Scora, J., & Morbidelli, A. 2024, ICARUS, 417, 116109

Wu, Y. & Chen, Y.-X. 2025, MNRAS, 536, L13

Wu, Y., Chen, Y.-X., Jiang, H., et al. 2023, MNRAS, 523, 2630

Wu, Y., Malhotra, R., & Lithwick, Y. 2024a, arXiv e-prints, arXiv:2405.08893

Wu, Y., Malhotra, R., & Lithwick, Y. 2024b, ApJ, 971, 5

Xie, J.-W. 2013, ApJS, 208, 22

Xie, J.-W. 2014, ApJ, 786, 153

Yang, Y., Liu, H. B., Muto, T., et al. 2023, ApJ, 948, 110

Ye, Y. 2022, Nature, 604, 415

Yi, T., Ormel, C. W., Huang, S., & Petit, A. C. 2025a, A&A, 695, A191

Yi, T., Ormel, C. W., Huang, S., & Petit, A. C. 2025b, arXiv e-prints, arXiv:2502.01736

Youdin, A. N. & Lithwick, Y. 2007, ICARUS, 192, 588

Young, E. D., Shahar, A., & Schlichting, H. E. 2023, Nature, 616, 306

Zang, W., Jung, Y. K., Yang, H., et al. 2023, AJ, 165, 103

Zang, W., Jung, Y. K., Yee, J. C., et al. 2025, Science, 388, 400

Zawadzki, B., Carrera, D., & Ford, E. B. 2021, MNRAS, 503, 1390

Zhang, K., Blake, G. A., & Bergin, E. A. 2015, ApJ, 806, L7

Zhang, K., Booth, A. S., Law, C. J., et al. 2021a, ApJS, 257, 5

Zhang, K., Booth, A. S., Law, C. J., et al. 2021b, ApJS, 257, 5

Zhang, S., Hu, X., Zhu, Z., & Bae, J. 2021c, ApJ, 923, 70

Zhou, Y., Sanghi, A., Bowler, B. P., et al. 2022, ApJ, 934, L13

Zhu, W. & Dong, S. 2021, ARA&A, 59, 291

Zurlo, A., Goździewski, K., Lazzoni, C., et al. 2022, A&A, 666, A133

Summary

The discovery of the first exoplanet, 51 Pegasi b, marked the beginning of a rapidly expanding field. Today, nearly 6,000 exoplanets have been detected, revealing an astonishing diversity of planetary systems. Yet, despite this progress, Earth remains the only known planet hosting life. This contrast raises profound questions about whether life is common in the Universe and how planetary systems, including our own, form and evolve.

Rather than providing a complete picture on their own, observations and theory work in close synergy to advance our understanding of exoplanet systems. Different detection methods probe different regions of parameter space: transit photometry favors close-in planets, radial velocity is most sensitive to massive planets, direct imaging reveals young and widely separated companions, while microlensing and astrometry access other complementary regimes. Together, these techniques offer a partial but expanding view of planetary populations. In this context, theoretical models of planet formation and evolution play a crucial role in interpreting observational data, making predictions, and guiding future surveys. At the same time, new observations continually challenge existing theories, pushing them to evolve and refine our understanding of how planetary systems form.

Planet formation begins with the gravitational collapse of a dense region within a molecular cloud, leading to the formation of a protostar surrounded by a rotating protoplanetary disk. These disks, composed primarily of gas with a small fraction of solids, provide the environment in which planets form. Two main pathways are thought to operate: gravitational instability, which can rapidly form massive objects, and core accretion, in which small dust grains grow into planetesimals, planetary embryos, and eventually full planets. Observations from facilities such as ALMA have revealed that these disks often exhibit rings and gaps, which may indicate the presence of forming planets.

Once formed, planets do not remain at their birth locations. Instead, they interact gravitationally with the surrounding gas disk, leading to orbital migration. Low-mass planets undergo Type I migration, while more massive planets that open gaps in the disk experience slower Type II migration. The migration process is governed by a balance of torques, primarily Lindblad and corotation torques, as well as additional effects such as heating and pebble accretion torques. These processes can drive planets inward, halt their motion, or even cause outward migration, significantly shaping planetary system architectures.

Migration naturally leads to the formation of mean motion resonances, a concept first studied in the context of the Galilean moons by Pierre-Simon Laplace. When planets migrate toward each other, they can become locked in orbital configurations where their periods form simple integer ratios. In such resonances, gravitational interactions accumulate coherently, stabilizing the system and preventing close encounters. Resonances can also involve multiple planets simultaneously, forming resonant chains or three-body resonances that play an important role in compact planetary systems.

Observations show that exoplanet system architectures are highly diverse. While some systems, such as TRAPPIST-1, exhibit resonant chains, many others do not. Statistical studies

reveal that only a small fraction of planet pairs are currently in resonance, though many lie just outside resonant configurations. This has led to competing theories: planets may have formed in resonant chains that later became unstable, formed in gas-poor environments with little migration, or assembled in situ after the gas disk dissipated. Increasing observational evidence suggests that resonant chains may commonly form early and later break due to dynamical instabilities.

Overall, the study of planet formation and system architecture combines observations, theory, and numerical simulations to understand how diverse planetary systems emerge. While significant progress has been made, many fundamental questions remain open, particularly regarding the origins of system diversity and the conditions that lead to habitable planets.

Chapter 2: When, where, and how many exoplanets end up in orbital resonances?
Protoplanetary disks are the birthplaces of planets. As protoplanets exchange angular momentum with the surrounding disk, they migrate. Migration can capture two planets in a stable mean motion resonance, as observed in systems such as PDS70 (2:1 resonance Bae et al. 2019) and TRAPPIST-1 (resonance chain Luger et al. 2017). However, too rapidly migrating planets result in resonance crossing instead of trapping. Here, I have derived the critical migration rate delineating the transition between resonance trapping and crossing, providing a tool for the community to diagnose the birth disk mass of perfect resonance chain planets. Because fast migration typically entails the existence of a massive disk, I also calculated that near-resonant exoplanets were formed in disks with masses comparable to the Minimum Mass Solar Nebula. Around the same time that I archived my paper, Batygin & Petit (2023a) independently derived an equivalent resonance-trapping criterion using a different approach.

Chapter 3: The dynamics of special chain systems and their formation: TRAPPIST-1
Higher-order resonance chains allow us to constrain planet formation timescales. For example, in the TRAPPIST-1 system, the high-order 8:5 and 5:3 resonances of its inner three planets are near-impossible to replicate if the planets stayed within the disk (Teyssandier et al. 2022; Burn et al. 2021). These resonances can only be obtained when the inner planets migrated into a gas-free magnetospheric cavity, where disk torques expand their original 3:2 resonances to the observed higher-order resonances. In addition, the outer planets d, e, and f can neither form too fast nor too slow, otherwise the planets would result in a configuration incompatible with observation. In this way, I offered an approach to constrain the formation timescales of exoplanets from their present-day architectures. Recent magnetohydrodynamic simulations (Romanova et al. 2025) confirmed our proposed cavity migration mechanism. Our proposed pathway for TRAPPIST-1 is also applicable to other resonance chain systems, e.g., TOI-178, and HD158259.

Chapter 4: The dynamics of broken chain systems and their formation: the Solar System
While many systems exhibit resonances, others, including our Solar System, do not. Various mechanisms, such as disk dispersal (Izidoro et al. 2021), stellar flybys (Maas et al. 2025), and planetesimal collisions (Li et al. 2024; Yi et al. 2025a), can disrupt primordial resonances. In the Solar System, the giant planet instability (Morbidelli et al. 2005) perturbs inner terrestrial planets through secular interactions (Kaib & Chambers 2016). Here, the present-day dynamical structure of the Solar terrestrial planets naturally emerges when these planets started in a resonance chain that was destabilized during the giant planet instability, resulting in the Moon-forming impact. Our findings support the view that the Solar terrestrial planets

formed early, in a gas-rich disk, analogous to exoplanet systems. It also offers a new testable way for multi-planet systems to break primordial resonances, as most planet systems exhibit.

Chapter 5: Suppression of giant planet formation in star cluster environments
Observation already revealed that the birth environment of stars significantly impacts the planet-forming disks. The examples are the observed Proplyds in the Orion Nebula (Berné et al. 2024) as well as numerical simulations (Wilhelm et al. 2023). This study introduces a simplified planet population synthesis code that simulates planet formation in the proplyds in an Orion-like cluster, incorporating factors such as pebble accretion and the effects of nearby stellar radiation on protoplanetary disks. The simulations show that clustered environments hinder the formation of giant planets, especially around low-mass stars. Neptune-sized planets on wide orbits are formed instead. The reason is that the short disk life time halt both planet gas accretion and migration. The large population of Neptune-sized planets at Jupiter-like orbits is consistent with recent Microlensing discoveries (Zang et al. 2025).

Chapter 6: Signature of closely-spaced pebble-accreting protoplanets in ALMA disks
While exoplanets on wide orbits are relatively common, not so many protoplanets have been found. It has been shown that the occurrence rate of substructures in disks is comparable to the occurrence rate of exoplanets (van der Marel & Mulders 2021). This study propose many of the protoplanets are too small to be detected. The transition disks are categorized into two distinct groups based on their properties and the types of planets they may host. In Group A, massive gas giants create deep gaps in the gas disk, while in Group B, multiple smaller Neptunian-like planets contribute to the formation of inner dust cavities without creating substantial gas gaps. The characteristics of the dust rings formed in these disks—such as sharp inner edges—can provide critical insights into the underlying planet formation processes. The observational implications of these findings suggest that high-resolution imaging techniques, particularly with the Atacama Large Millimeter/submillimeter Array (ALMA), could further validate these models and enhance our understanding of planet formation in various disk environments.

Outlook: Identifying broken resonance chains
While intact resonant chains are relatively easy to identify through integer period ratios and resonance angles, broken chains are far more subtle and challenging to detect even if many broken-chain theories have been proposed. Nevertheless, they encode critical information about a system's migration history and dynamical evolution. A promising approach is to search for near-integer period ratios as relics of past resonances, as seen in several *Kepler* systems. Future work can combine analytical models and N-body simulations to systematically test whether the architectures of known multi-planet systems are consistent with an origin in resonant chains that were later destabilized. Such studies may also reveal the presence of unseen outer companions, offering testable predictions for upcoming missions such as Gaia.

In addition to orbital architecture, planetary composition provides an independent and powerful probe of resonance disruption. The breaking of resonant chains is expected to trigger dynamical instabilities. If giant impacts have happened, it would leave observable imprints on planetary masses, radii, and atmospheres. By combining dynamical simulations with models of collision outcomes, it is possible to identify candidate post-impact planets and connect their present properties to their formation histories. These predictions can be tested with radial-velocity measurements and atmospheric characterization with facilities such as JWST. Looking ahead, next-generation telescopes on the ground and in space will enable systematic studies of small exoplanets, bringing us closer to understanding how common

Solar System–like architectures are and ultimately addressing the origin of habitable worlds.

Nederlandse samenvatting

De ontdekking van de eerste exoplaneet, 51 Pegasi b, markeerde het begin van een snel groeiend onderzoeksveld. Inmiddels zijn bijna 6.000 exoplaneten ontdekt, wat een verbluffende diversiteit aan planetenstelsels heeft onthuld. Toch blijft de Aarde de enige bekende planeet waarop leven voorkomt. Dit contrast roept fundamentele vragen op over de vraag of leven algemeen voorkomt in het heelal en hoe planetenstelsels, inclusief het onze, ontstaan en evolueren.

In plaats van op zichzelf een volledig beeld te geven, werken waarnemingen en theorie nauw samen om ons begrip van exo-planetenstelsels (planetenstelsels buiten het zonnestelsel) te verdiepen. Verschillende detectiemethoden onderzoeken verschillende delen van de parameterruimte: transitfotometrie is gevoelig voor planeten dicht bij hun ster, radialsnelheidsmetingen voor massieve planeten, directe beeldvorming onthult jonge en ver verwijderde objecten, terwijl microlensing en astrometrie andere complementaire regimes bestrijken. Samen bieden deze technieken een gedeeltelijk maar steeds uitbreidend beeld van planetenpopulaties. In deze context spelen theoretische modellen van planeetvorming en -evolutie een cruciale rol bij het interpreteren van waarnemingen, het doen van voorspellingen en het sturen van toekomstige surveys. Tegelijkertijd dagen nieuwe waarnemingen bestaande theorieën voortdurend uit, waardoor deze verder worden verfijnd.

Planeetvorming begint met de zwaartekrachtinstorting van een dicht gebied binnen een moleculaire wolk, wat leidt tot de vorming van een protoster omgeven door een roterende protoplanetaire schijf. Deze schijven, die voornamelijk uit gas bestaan met een kleine fractie vaste deeltjes, vormen de omgeving waarin planeten ontstaan. Twee hoofdmechanismen worden onderscheiden: gravitatie-instabiliteit, die snel massieve objecten kan vormen, en kernaccretie, waarbij kleine stofdeeltjes uitgroeien tot planetesimalen, baby planeten's en uiteindelijk planeten. Waarnemingen met faciliteiten zoals ALMA hebben aangetoond dat deze schijven vaak ringen en openingen vertonen, wat kan wijzen op de aanwezigheid van zich vormende planeten.

Eenmaal gevormd blijven planeten niet op hun oorspronkelijke locatie. Door zwaartekrachtinteracties met de omringende gasschijf migreren hun banen. Lage-massaplaneten ondergaan zogenoemde type I-migratie, terwijl zwaardere planeten die openingen in de schijf creëren, langzamere type II-migratie ervaren. Dit migratieproces wordt bepaald door een evenwicht van krachten, met name Lindblad- en corotatiekoppels, evenals aanvullende effecten zoals verwarmings- en pebble-accretiekoppels. Deze processen kunnen planeten naar binnen drijven, hun migratie stoppen of zelfs omkeren, en bepalen daarmee in sterke mate de uiteindelijke architectuur van planetenstelsels.

Migratie leidt op natuurlijke wijze tot het ontstaan van baanresonanties, een concept dat voor het eerst werd bestudeerd in de context van de Galileïsche manen door Pierre-Simon Laplace. Wanneer planeten naar elkaar toe migreren, kunnen zij gevangen raken in baanconfiguraties waarbij hun omlooptijden eenvoudige gehele verhoudingen vormen. In zulke resonanties stapelen zwaartekrachtinteracties zich coherent op, wat het systeem

stabiliseert en nauwe ontmoetingen voorkomt. Resonanties kunnen ook meerdere planeten omvatten, wat leidt tot resonantieketens of drie-lichaamresonanties die een belangrijke rol spelen in compacte planetenstelsels.

Waarnemingen tonen aan dat de architecturen van exo-planetenstelsels zeer divers zijn. Sommige systemen, zoals TRAPPIST-1, vertonen resonantieketens, terwijl veel andere dat niet doen. Statistische studies laten zien dat slechts een klein deel van de planeetparen zich momenteel in resonantie bevindt, hoewel veel systemen zich net buiten resonante configuraties bevinden. Dit heeft geleid tot verschillende theorieën: planeten kunnen gevormd zijn in resonantieketens die later instabiel werden, in gasarme omgevingen met weinig migratie, of in situ na het verdwijnen van de gasschijf. Toenemend observationeel bewijs suggereert dat resonantieketens vaak vroeg ontstaan en later worden verbroken door dynamische instabiliteiten.

In het algemeen combineert het onderzoek naar planeetvorming en systeemarchitectuur waarnemingen, theorie en numerieke simulaties om te begrijpen hoe de grote diversiteit aan planetenstelsels ontstaat. Hoewel er aanzienlijke vooruitgang is geboekt, blijven veel fundamentele vragen open, met name over de oorsprong van deze diversiteit en de voorwaarden die leiden tot bewoonbare planeten.

Chapter 2: Wanneer, waar en hoeveel exoplaneten eindigen in baanresonanties?
Protoplanetaire schijven zijn de geboorteplaatsen van planeten. Terwijl protoplaneten impulsmoment uitwisselen met de omringende schijf, migreren zij. Migratie kan twee planeten vangen in een stabiele mean motion resonantie, zoals waargenomen in systemen zoals PDS70 (2:1 resonantie Bae et al. 2019) en TRAPPIST-1 (resonantieketen Luger et al. 2017). Te snelle migratie leidt echter tot het kruisen van resonanties in plaats van vangst. In dit werk heb ik de kritische migratiesnelheid afgeleid die de overgang tussen resonantievangst en kruising bepaalt, en zo een hulpmiddel geleverd om de massa van de oorspronkelijke schijf van perfecte resonantieketens te diagnosticeren. Omdat snelle migratie doorgaans wijst op een massieve schijf, heb ik ook berekend dat bijna-resonante exoplaneten zijn gevormd in schijven met massa's vergelijkbaar met de Minimum Mass Solar Nebula. Rond dezelfde tijd dat mijn artikel verscheen, leidde Batygin & Petit (2023a) onafhankelijk een vergelijkbaar criterium af via een andere methode.

Chapter 3: De dynamica van bijzondere resonantieketens en hun vorming: TRAPPIST-1
Resonantieketens van hogere orde stellen ons in staat om tijdschalen van planeetvorming te bepalen. In het TRAPPIST-1-systeem zijn de hogeorde 8:5- en 5:3-resonanties van de binnenste drie planeten bijvoorbeeld vrijwel onmogelijk te reproduceren indien de planeten binnen de schijf blijven (Teyssandier et al. 2022; Burn et al. 2021). Deze resonanties ontstaan alleen wanneer de binnenste planeten migreren naar een gasvrije magnetosferische holte, waar schijfkoppels hun oorspronkelijke 3:2-resonanties omzetten tot de waargenomen hogere orde. Daarnaast mogen de buitenste planeten d, e en f noch te snel, noch te langzaam gevormd worden, anders ontstaat een configuratie die niet overeenkomt met de waarnemingen. Op deze manier heb ik een methode voorgesteld om vormingstijdschalen af te leiden uit de huidige systeemarchitectuur. Recente magnetohydrodynamische simulaties (Romanova et al. 2025) bevestigen dit mechanisme. Deze vormingsroute is ook toepasbaar op andere resonantieketens, zoals TOI-178 en HD158259.

Chapter 4: De dynamica van gebroken resonantieketens en hun vorming: het Zonnestelsel
Terwijl veel systemen resonanties vertonen, doen andere systemen, waaronder ons Zonne-

stelsel, dat niet. Verschillende mechanismen, zoals het verdwijnen van de schijf (Izidoro et al. 2021), sterpassages (Maas et al. 2025) en botsingen tussen planetesimalen (Li et al. 2024; Yi et al. 2025a), kunnen oorspronkelijke resonanties verstoren. In het Zonnestelsel beïnvloedt de instabiliteit van de reuzenplaneten (Morbidelli et al. 2005) de binnenste planeten via seculaire interacties (Kaib & Chambers 2016). In dit werk laat ik zien dat de huidige dynamische structuur van de terrestrische planeten op natuurlijke wijze ontstaat wanneer zij begonnen in een resonantieketen die werd verstoord tijdens deze instabiliteit, wat uiteindelijk leidde tot de maanvormende botsing. Dit ondersteunt het idee dat de terrestrische planeten vroeg zijn gevormd in een gasrijke schijf, vergelijkbaar met exo-planetenstelsels, en biedt een nieuwe toetsbare verklaring voor het verbreken van resonanties.

Chapter 5: Onderdrukking van reuzenplaneetvorming in sterclusteromgevingen
Waarnemingen tonen aan dat de geboorteomgeving van sterren een sterke invloed heeft op planeetvormende schijven, bijvoorbeeld in de proplyds van de Orionnevel (Berné et al. 2024) en in numerieke simulaties (Wilhelm et al. 2023). In dit werk wordt een vereenvoudigd populatiesynthesemodel geïntroduceerd om planeetvorming in dergelijke omgevingen te simuleren, inclusief kiezelopveging en de invloed van nabijgelegen sterrenstraling. De resultaten tonen aan dat clusteromgevingen de vorming van reuzenplaneten onderdrukken, vooral rond lichte sterren. In plaats daarvan ontstaan Neptunus-achtige planeten op wijde banen. De korte levensduur van de schijf stopt zowel gasaccretie als migratie. Dit komt overeen met recente microlensingwaarnemingen (Zang et al. 2025).

Chapter 6: Signaturen van dicht opeengepakte, kiezelopveging protoplaneten in ALMA-schijven
Hoewel exoplaneten op wijde banen relatief vaak voorkomen, zijn er nog maar weinig protoplaneten direct waargenomen. Studies tonen aan dat de frequentie van substructuren in schijven vergelijkbaar is met die van exoplaneten (van der Marel & Mulders 2021). Dit werk stelt dat veel protoplaneten te klein zijn om direct te detecteren. Overgangsschijven kunnen in twee groepen worden verdeeld: systemen met massieve gasreuzen die diepe gaten vormen, en systemen met meerdere kleinere Neptunus-achtige planeten die stofholtes creëren zonder duidelijke gasgaten. De eigenschappen van de stofringen bieden belangrijke aanwijzingen voor planeetvorming. Waarnemingen met hoge resolutie, met name met ALMA, kunnen deze modellen testen.

Outlook: Identificatie van gebroken resonantieketens
Hoewel intacte resonantieketens relatief eenvoudig te herkennen zijn, zijn gebroken ketens subtieler en moeilijker te detecteren. Toch bevatten zij cruciale informatie over de migratiegeschiedenis en dynamische evolutie van planetensystemen. Een veelbelovende aanpak is het zoeken naar bijna-integer periodeverhoudingen als overblijfselen van vroegere resonanties. Toekomstig werk kan analytische modellen en N-body-simulaties combineren om te testen of waargenomen systemen afkomstig zijn van instabiel geworden resonantieketens. Dit kan ook wijzen op onzichtbare buitenste planeten, te testen met toekomstige missies zoals Gaia.

Naast baanarchitectuur biedt ook de samenstelling van planeten een krachtige diagnose. Het verbreken van resonantieketens kan leiden tot dynamische instabiliteiten en catastrophale botsingen, die sporen achterlaten in massa, straal en atmosfeer van planeten. Door simulaties te combineren met botsingsmodellen kunnen kandidaten worden geïdentificeerd en vergeleken met waarnemingen via radiale snelheden en atmosferische studies met bijvoorbeeld JWST. Toekomstige telescopen zullen systematische studies mogelijk maken en ons dichter brengen bij het begrijpen van de oorsprong van bewoonbare werelden.

List of Publications

1. **Huang S.**, Ormel C., Portegies Zwart S., Kokubo E., Yi T., 2025, **ApJ**, 988, 137
   A Resonant Beginning for the Solar System's Terrestrial Planets.
2. **Huang S.**, van der Marel N. & Portegies Zwart S., 2024, **A&A**, 691, A155
   Origin of transition disk cavities: Pebble-accreting protoplanets vs Super-Jupiters.
3. **Huang S.**, Portegies Zwart S., C. & Wilhelm M., 2024, **A&A**, 689, A338
   Suppression of giant planet formation around low-mass stars in clustered environments.
4. **Huang S.** & Ormel C., 2023, **MNRAS**, 522, 828
   When, where, and how many planets end up in first-order resonances?
5. **Huang S.** & Ormel C., 2022, **MNRAS**, 511, 3814
   The dynamics of the TRAPPIST-1 system in the context of its formation.

Curriculum Vitæ

I was born on October 22 in a village near Hefei, the capital of Anhui Province, China. As a child, I was rather mischievous and enjoyed simple games such as playing marbles with friends. Somewhat unexpectedly, I passed the entrance exam to a prestigious junior middle school in Hefei. During this period, my interest in science grew significantly. I still remember a remark from my history teacher: "History is a vase in the hands of those who manipulate it." Although I now view this statement more critically, it left a strong impression on me at the time and contributed to my preference for subjects grounded in objective reasoning like science.

After Gaokao (the entrance exam of Chinese Universities), I choose physics in Hohai University in Nanjing from 2016 to 2020 as a bachelor student. While studying the basic physics courses, I was keen on doing some cool scientific researches. Under the guidance of Prof. Hua Zou, my initial project involved applying machine learning techniques to predict deformation of the CCD in the LAMOST telescope due to temperature variations. While implementing neural networks was relatively straightforward, the project sparked my interest in astronomy and motivated me to pursue the field further.

In 2019, I attended a summer camp organized by the Department of Astronomy at Tsinghua University. At that time, my background in astronomy was still limited, mostly based on fundamental physics and my own research experience. Nevertheless, Prof. Chris Ormel recognized my enthusiasm for scientific research and offered me a position as a graduate student at Tsinghua University to study planet formation. This was an opportunity I readily accepted. Coincidentally, that same year saw both the awarding of the Nobel Prize in Physics for discoveries in exoplanet research and the outbreak of the COVID-19 pandemic.

During the pandemic when I started my graduate work, I used planet-planet dynamical interaction as a tool to constrain the planet formation and evolution processes. Although opportunities for international collaboration were limited during this period, I later grasped one of the few chances and joined the CSC joint PhD program between Tsinghua University and Leiden Observatory. From 2022 to 2024, I spent a very good time at Leiden University as a joint PhD student. Under the supervision of Prof. Simon Portegies Zwart, I studied how planet formation is influenced by stellar dynamics and photoevaporation in young star clusters.

As I move forward in my academic career, I have been awarded the TDLI postdoctoral fellowship at Shanghai Jiao Tong University. Starting in July 2026, I will begin this new position, where I aim to investigate the effects of planet giant impacts and identify exoplanetary systems that have possibly experienced such events.

Acknowledgments

Looking back over my PhD, I am amazed at how far I have come. The achievement I am most proud of is neither the handful of publications I have written nor the many scientific presentations I have given. Rather, I cherish the interactions with so many friends and the joy I have found both in life and in science. As someone who has never been particularly good at expressing himself, I could not have imagined this growth before starting my PhD.

I would like to sincerely thank the support staff, including the secretaries and IT helpdesk at the Sterrewacht and Tsinghua DoA, for ensuring that everything runs smoothly. Especially as a joint degree CSC student, I have relied on your assistance more often than most.

I am deeply grateful to my two advisors in the Joint PhD program, Chris and Simon, for their invaluable guidance and encouragement throughout this project. At the start of my PhD, I have grown tremendously thanks to Chris. Your insights during our discussions have helped me cultivate an intuition for many physical processes in astronomy as a theorist. The thought-provoking questions you consistently raise have greatly deepened my understanding of the research. On the other hand, Simon's research interests are as broad as the local Universe. And you have always been excited to discuss ideas with me, some are very wild. You would always help analyze their feasibility with me and encourage me to explore them further. I am honored to have worked with both of you.

I am grateful to my collaborators, Eiichiro, Maite, Nienke, and Tian, for the exciting science we have carried out together. I truly enjoyed working with you. I would also like to thank the master's student Brent, who chose to work on research projects with me.

I am thankful to the many staff members I interacted with at Tsinghua DoA and Leiden Observatory, including Antony, Huan, Junjie, Nienke, Sharon, Takayuki, Wei (Zhu), Xuening, and Yamila. I would also like to acknowledge the support from Huub, Koen, Shude, and Wei (Cui) for the CSC program.

I also benefited greatly from many stimulating scientific discussions with Anders, Antoine, Beibei, Betram, Carsten, Haiyang, Ida-san, Ruobin, Sijme-Jan, Yaping, and Yinhao. And Erwan—I still owe you a beer and a hotpot. I would like to extend my appreciation to the previous and current PhD students and postdocs in the Tsinghua DoA PSF group and the Leiden Pangolin group.

I greatly appreciate the hospitality of my talk and visit hosts: Andre, Christoph, Daniel, Eric, Fei, Hongping, DJ, Konstantin, Ramo, and Shangfei.

I would express gratitude to many fellow students Jinyi, Sai, Tong, and Yunhao, and others. I especially enjoyed being with Ben and Xinyu for the CSC adventure, and Daming additionally for the northern lights in Norway.

Finally, I would like to express my deepest gratitude to my parents. Your unconditional love, encouragement, and constant support have made everything possible. Last but not least, I want to thank my girlfriend, Tianjiao, for her patience throughout this journey. With your companionship, every step I take feels more confident and less hesitant. I look forward to the many adventures that await us.